CENTRO INTERNACIONAL DE ESTUDOS
DE DOUTORAMENTO E AVANZADOS
DA USC (CIEDUS)

TESE DE DOUTORAMENTO

Study of the $B^0 \to \rho(770)^0 K^*(892)^0$ decay with an amplitude analysis of $B^0 \to (\pi^+\pi^-)(K^+\pi^-)$ decays

María Vieites Díaz

ESCOLA DE DOUTORAMENTO INTERNACIONAL

PROGRAMA DE DOUTORAMENTO EN FÍSICA NUCLEAR E DE PARTÍCULAS

SANTIAGO DE COMPOSTELA

2019

USC
UNIVERSIDADE
DE SANTIAGO
DE COMPOSTELA

DECLARACIÓNDA AUTORA DA TESE

Study of the $B^0 \to \rho(770)^0 K^*(892)^0$ decay with an amplitude analysis of $B^0 \to (\pi^+\pi^-)(K^+\pi^-)$ decays

Dna. María Vieites Díaz

Presento a miña tese, seguindo o procedemento axeitado ao Regulamento, e declaro que:

1) A tese abarca os resultados da elaboración do meu traballo.
2) De selo caso, na tese faise referencia ás colaboracións que tivo este traballo.
3) A tese é a versión definitiva presentada para a súa defensa e coincide coa versión enviada en formato electrónico.
4) Confirmo que a tese non incorre en ningún tipo de plaxio doutros autores nin de traballos presentados por min para a obtención doutros títulos.

En Santiago de Compostela, a 21 de febreiro de 2019

Asdo. María Vieites Díaz

USC
UNIVERSIDADE
DE SANTIAGO
DE COMPOSTELA

AUTORIZACIÓN DO DIRECTOR / TITOR DA TESE

Study of the $B^0 \to \rho(770)^0 K^*(892)^0$ decay with an amplitude analysis of $B^0 \to (\pi^+\pi^-)(K^+\pi^-)$ decays

D. Máximo Pló Casasús

D. Cibrán Santamarina Ríos

INFORMAN:

Que a presente tese, correspóndese co traballo realizado por Dna. María Vieites Díaz, baixo a nosa dirección, e autorizamos a súa presentación, considerando que reúne os requisitos esixidos no Regulamento de Estudos de Doutoramento da USC, e que como directores desta non incorre nas causas de abstención establecidas na Lei 40/2015.

En Santiago de Compostela, a 21 de febreiro de 2019

Asdo. Máximo Pló Casasús

Asdo. Cibrán Santamarina Ríos

USC
UNIVERSIDADE
DE SANTIAGO
DE COMPOSTELA

Nothing in life is to be feared, it is only to be understood. Now is the time to understand more, so that we may fear less.

Marie Skłodowska-Curie

[...] You look at science (or at least talk of it) as some sort of demoralising invention of man, something apart from real life, and which must be cautiously guarded and kept separate from everyday existence. But science and everyday life cannot and should not be separated. Science, for me, gives a partial explanation of life.

Rosalind Franklin

USC
UNIVERSIDADE
DE SANTIAGO
DE COMPOSTELA

Acknowledgements

First of all, I would like to thank my advisors, Máximo Pló Casasús and Cibrán Santamarina Ríos, for all the time they have devoted to my education in the past years. I also want to thank Abraham Gallas for his support since I first joined the LHCb group in Santiago.

Special thanks go to Xabier Cid, who showed me the very basics of LHCb analysis during the last year of my Bachelor and many more things as one of my supervisors for my Summer Student project at LHCb. My gratitude also goes to Sean Benson and Paula Álvarez, whom have kindly agreed to write the expert's reports for the International Mention of my PhD. I also want to thank Patrick Owen, with whom I had the pleasure to collaborate after joining the semi-leptonics working group.

Many people provided me with very valuable and much appreciated feedback during the many months I had "Minuit gives up" showing in my terminal. In particular, I am very grateful to Diego Martinez, who also introduced me to the MultiNest algorithm and to some of the software tools I then used in the analysis. During this period, I also shared many useful conversations with Antonio Romero, Cibrán, Marcos Seco, Jeremy Dalseno, and, especially, with Julián García.

I would like to thank the Charmless working group members and, especially, Sean, Stefano Perazzini, Thomas Latham and Wenbin Quian, who were the group conveners during my *MC liaison* time and with whom it has been a pleasure to work. My gratitude also goes to the Simulation working group, where I learnt many things regarding the LHCb simulation software, and to Svende Braun, who was *MC liaison* for the semi-leptonics group and was always happy to discuss and help clarifying our tasks after the simulation group meetings.

I would also like to thank the seniors in Santiago, especially Cibrán and Abraham, for their always encouraging support to do things during my PhD that allowed me to acquire not only analysis skills but many others relevant for my development as a researcher. Working in Santiago has been a pleasure and I have all the members of the group to thank for this. I was able to share teaching duties with Máximo, Cibrán, Pablo, Juan, Xabier and Abraham, and I have really enjoyed doing so.

I thank the financial support provided by the "Programa de Formación de Profesorado Universitario" of the "Ministerio de Educación, Cultura y Deporte" and by "Axudas Predoutorais" of "Xunta de Galicia". I would also like to thank "Fundación Barrié" for the funding for a six month stay at CERN.

From a more personal side, I want to thank several people with whom I am very happy to have shared my time at CERN. In particular, Jessica, Carla, Svende, Suzanne and Giulio, for talking life and physics regardless of the time and place. Special thanks to Paul, for many shared moments and for his everyday support.

Seguindo co ámbito personal, quero agradecer á xente coa que compartín despacho durante o doutoramento. Primeiro Álvaro, Toño, Julián, Brais e Carlos e despois, tamén

Óscar, Bea, Julián (Lomba) e Alessandra, axudaron a facer máis levadeiro o día a día. Tamén ao resto de estudantes do grupo: Miguel, Miriam, Antonio, Adrián e Alexandre, con quen tamén compartín tempo en Santiago e durante estadías no CERN. Quero agradecer especialmente a Julián, con quen coincidín dende que comezamos a estudar física en Santiago, por moitas conversas compartidas.

O día a día tampouco sería o mesmo sen as comidas en Fonseca. Gustaríame agradecer a todos os habituais do grupo (Toño, Juan, Álvaro, Julián, Eliseo, Abraham, Pablo, Cibrán, Óscar, Bea, Alessandra, ...) pola diversión das comidas e por todo o coñecemento de temas (moi) variados que adquirín. Cibrán, Abraham, Xabier, Álvaro (e as súas recomedacións de películas) merecen un recoñecemento especial.

Quero agradecerlle a Cris todas as viaxes, actividades e experiencias que levamos compartindo e disfrutando dende a nosa chegada a Santiago. Gracias a Andrea (Rodil), tamén por moitos anos compartidos xuntas. Tamén quero agradecer ao meu grupo de amizades en Ribadeo, especialmente a Antía, Iria e Andrea, por seguir aturándome despois de tantos anos.

Para rematar, quero agradecer a miña nai, Teresa, e a meu pai, Antonio, por escoitarme sempre e por axudarme a conseguir a confianza e a seguridade en min mesma necesaria para rematar todas as etapas ata agora e continuar coas seguintes.

María

Abstract

This thesis is devoted to the study of the $B^0 \to \rho(770)^0 K^*(892)^0$ decay mode for which $3\,\text{fb}^{-1}$ of proton-proton collision data collected by the LHCb experiment at centre-of-mass energies of 7 and 8 TeV were analysed.

The details of an amplitude analysis of $B^0 \to (\pi^+\pi^-)(K^+\pi^-)$ decays performed in the two-body invariant mass regions corresponding to $300 < m(\pi^+\pi^-) < 1100\,\text{MeV}/c^2$ and $750 < m(K^+\pi^-) < 1200\,\text{MeV}/c^2$ are documented and its results are discussed.

Particular emphasis is placed in the measurements of the *CP* averages and asymmetries for the magnitudes and phase differences of the contributing amplitudes. The presented results correspond to the first measurements of most of these observables. In particular, the *CP*-averaged longitudinal polarisation fractions of the vector-vector modes are found to be $\tilde{f}^0_{\rho K^*} = 0.164 \pm 0.015 \pm 0.022$ and $\tilde{f}^0_{\omega K^*} = 0.68 \pm 0.17 \pm 0.16$, and their *CP* asymmetries, $\mathcal{A}^0_{\rho K^*} = -0.62 \pm 0.09 \pm 0.09$ and $\mathcal{A}^0_{\omega K^*} = -0.13 \pm 0.27 \pm 0.13$, where the first uncertainty is statistical and the second systematic. Consequently, the first observation of direct *CP* violation in amplitude analyses of vector-vector decays is reported.

USC
UNIVERSIDADE
DE SANTIAGO
DE COMPOSTELA

Resumo

Nesta tese preséntanse os resultados do estudo do modo de desintegración $B^0 \to \rho(770)^0 K^*(892)^0$, para o que se analizaron $3\,\mathrm{fb}^{-1}$ de datos recollidos polo detector LHCb. Estes datos foron tomados durante os anos 2011 e 2012 cunha enerxía no centro de masas de $\sqrt{s} = 7$ e $\sqrt{s} = 8$ TeV, respectivamente.

Documéntanse os detalles e coméntanse as conclusións da análise de amplitudes de eventos $B^0 \to (\pi^+\pi^-)(K^+\pi^-)$, realizada nas rexións de masa invariante de dous corpos correspondentes a $300 < m(\pi^+\pi^-) < 1100\,\mathrm{MeV}/c^2$ e $750 < m(K^+\pi^-) < 1200\,\mathrm{MeV}/c^2$, respectivamente.

O traballo focalízase na determinación dos valores promediados en sabor e das correspondentes asimetrías *CP* para as fraccións de polarización e as diferenzas de fase das canles vectoriais accesibles. En particular, obtéñense os valores $\tilde{f}^0_{\rho K^*} = 0.164 \pm 0.015 \pm 0.022$ e $\tilde{f}^0_{\omega K^*} = 0.68 \pm 0.17 \pm 0.16$, coas correspondentes asimetrías *CP*, $\mathcal{A}^0_{\rho K^*} = -0.62 \pm 0.09 \pm 0.09$ e $\mathcal{A}^0_{\omega K^*} = -0.13 \pm 0.27 \pm 0.13$, onde a primeira incerteza é estatística e a segunda sistemática. Como consecuencia destas medidas, repórtase a primeira observación de violación da simetría *CP* en distribucións angulares de decaementos vector-vector.

USC
UNIVERSIDADE
DE SANTIAGO
DE COMPOSTELA

INDEX

Introduction

The Standard Model (SM) of Particle Physics is a gauge theory describing the weak, strong and electromagnetic interactions. It relies on the Glashow-Salam-Weinberg Electroweak model [1–3] and on Quantum Cromodynamics (QCD), first described by Gross, Wilczek, and Politzer [4]. Up to date, it has proven to be the most successful theory describing fundamental particles and how they interact. However, the formulations of some very well known phenomena, such as the gravitational interaction or the flavour oscillations present in the neutrino sector, still find their explanations beyond the SM framework and, in the case of gravity, using a different paradigm. Furthermore, the existence of dark matter has been proven by cosmological observations and the question on its particular nature remains unaddressed. In addition, there are certain phenomenologies, such as the different behaviours that matter and antimatter have under some conditions, which are only partially understood on account of the SM predictions.

This thesis presents an experimental analysis performed with data recorded by the LHCb experiment, installed in the Large Hadron Collider (LHC) in the surroundings of Geneva area, Switzerland. Experimental high energy physics allows the study of the properties of unstable particles, both composite and elementary. At the LHC matter and antimatter are produced, enabling thorough searches of new phenomena in the boundaries of what might be expected as predicted by the SM. This particular topic is referred to as violation of the CP invariance [5].

The CP transformation combines charge conjugation (C) with parity (P). Under C, particles and antiparticles are exchanged, by conjugating all internal quantum numbers. Under P, the handedness of space is reversed, $\vec{x} \to -\vec{x}$. Most phenomena in nature are C-symmetric and P-symmetric, thus, CP-symmetric. In particular, these symmetries are respected by the gravitational, electromagnetic, and strong interactions. On the other hand, the weak interaction was found to violate P and C in the strongest possible way [6]. However, the combination of these two operators, CP, is also preserved in most of the weak processes, challenging the explanation for the matter-antimatter asymmetry mentioned before. Therefore, the study of processes mediated by the weak interaction is one of our best tools to go deeper in the understanding of the composition of our universe.

The decays of B mesons occur via quark flavour transitions, mediated by the electroweak interaction, and are thus particularly interesting to study CP violating effects. The first decay in which direct CP violation was observed in B mesons was $B^0 \to K^+\pi^-$ [7, 8]. The neutral mode $B^0 \to \pi^0 K^0$ receives contributions from at least three SM diagrams, allowing for several interference patterns to arise. This rich phenomenology in the electro-weak sector is shared with the vector counterpart of the $B^0 \to \pi^0 K^0$,

the $B^0 \to \rho(770)^0 K^*(892)^0$ decay mode. Furthermore, since the latter corresponds to a pseudo-scalar meson decay into two vector particles, there are three accessible final states, depending on the orbital angular momentum between the decay products, thus, giving access to even more observables.

The goal of this thesis is to measure a set of *CP*-violating observables using B^0 meson decays reconstructed in the $(\pi^+\pi^-)(K^+\pi^-)$ quasi-two-body final state, with particular focus on the $B^0 \to \rho(770)^0 K^*(892)^0$ decay (hereafter, denoted by $B^0 \to \rho^0 K^{*0}$). The analysis uses data recorded by the LHCb experiment during its operation in 2011 and 2012, when the LHC delivered proton-proton collision data at $\sqrt{s} = 7$ and 8 TeV, respectively. The structure of the document is as follows. Chapter 1 summarises the most important aspects for the theoretical framework related to this study, which include the formalism upon which the decay rate is written and the general strategy that was followed to perform the analysis. The experimental setup, including a brief description of the plans for the LHCb detector upgrade, is introduced in Chapter 2. A summary of several stand-alone analysis tools that were used at different analysis steps is presented in Chapter 3. The selection of $B^0 \to (\pi^+\pi^-)(K^+\pi^-)$ candidates is explained in Chapter 4, along with the description and the results of the four-body invariant mass fit. The details of the amplitude analysis and the different sources of systematic uncertainties are discussed in Chapter 5. This chapter also presents the results of the amplitude analysis. Finally, the conclusions of the work are drawn in Chapter 6.

1

Theoretical principles

In this chapter the relevant theoretical aspects for the $B^0 \to \rho^0 K^{*0}$ analysis are discussed. The Standard Model of Particle Physics is briefly introduced, following the scheme presented in [9] and [10]. A greater level of details are discussed for the CKM matrix and *CP* violation phenomenology, particularising for the decay channel under study. Finally, the phenomenology of the $B^0 \to \rho^0 K^{*0}$ decay channel is summarised.

1.1 The Standard Model of Particle Physics

The Standard Model (SM) is the agreed quantum gauge theory describing the interactions and properties of the fundamental particles. These can be classified according to the value of their spin in fermions and bosons. The first correspond to the matter particles, which have spin 1/2, and are further divided into quarks and leptons, depending on the type of interactions they are sensitive to. Bosons have integer spin values and, within the nomenclature of a gauge theory, they are referred to as the carriers of the various interactions.

The SM is based on the symmetry group $SU(3)_C \otimes SU(2)_L \otimes U(1)_Y$, where C denotes the colour charge of the strong interaction, L the left chirality of the weak interaction and Y the hypercharge of the electromagnetic interaction. Quarks have all three charges and therefore all gauge bosons couple to them. These are eight massless gluons and one massless photon for the strong and electromagnetic interactions, respectively, and three massive particles, $W^{\pm}$ and Z, for the weak interaction. Leptons do not have colour charge, and can not, therefore, couple to gluons. Neutrinos are a particular type of leptons, which,

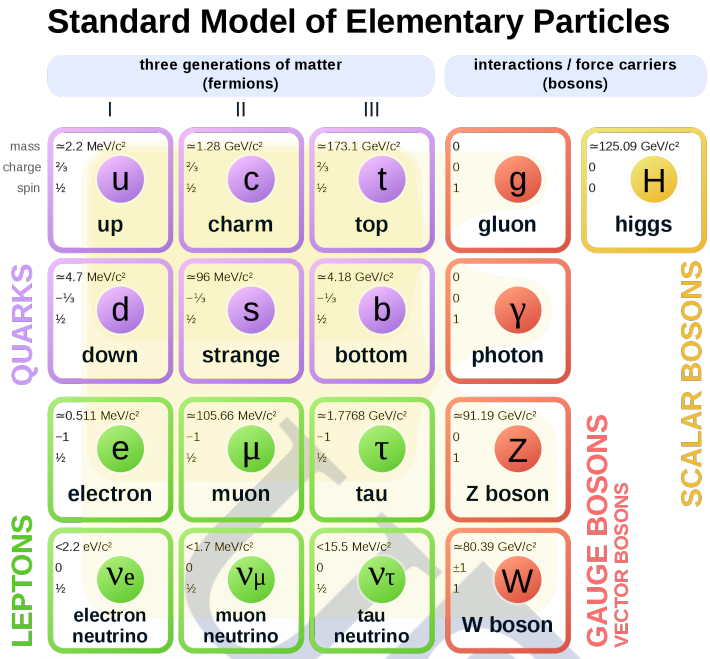

Figure 1.1: Fundamental particles in the Standard Model of Particle Physics. Leptons and quarks are the fermionic constituents of matter, organised in a 3-fold structure (first three columns) of families. The fourth column shows the gauge bosons, which are the force carriers associated to the strong, electromagnetic and weak interactions, respectively. The Higgs boson, arising from the spontaneous symmetry breaking of the electroweak sector, appears in the fifth column. Figure taken from [11].

in addition, lack electromagnetic charge. Therefore, they can only couple to the mediators of the weak interaction. If charged, the gauge bosons can also self-couple, which explains some of the very contrasting features exhibited by the different interactions. The fermionic particles are organised in a 3-fold family structure, as illustrated in Figure 1.1, along with a summary of all the fundamental particles in the SM. Within this framework, the three families share the same gauge charge assignments, and only differ in their mass and their flavour quantum numbers. Finally, all fermions have antimatter partners with conjugated values for their charges but identical mass.

The strong interaction is described by Quantum Chromodynamics (QCD) which establishes the basis for the interactions among quarks and gluons. Unlike the rest of the SM fundamental particles, neither quarks nor gluons can be observed as free particles. These particles always appear in Nature as the constituents of bound states called hadrons. Most hadrons are composed of either two ($q\bar{q}$) or three (qqq) quarks and are referred to as mesons and baryons, respectively (other compositions are referred to as exotic, an updated review on the topic can be found in [12]). A new quantum number, *colour*, has to be introduced in order to satisfy the Fermi-Dirac statistics for hadrons. Each quark

can therefore appear in three different colours (red, green, blue) and the postulation that only colourless states are observable justifies the aforementioned requirement for quarks to always manifest in bound states.

The electromagnetic and weak interactions are unified in the Glashow-Weinberg-Salam model into the electroweak theory. The gauge symmetry is spontaneously broken by the Higgs mechanism [13], resulting in the electromagnetic subgroup, $SU(2)_L \otimes U(1)_Y \rightarrow U(1)_{QED}$. The Higgs boson, the only scalar fundamental particle in the SM, appears in the model as a consequence of this spontaneous symmetry breaking. This mechanism generates the masses of the $W^{\pm}$ and Z^0 bosons, as well as the masses of the fermions. Furthermore, since the mass eigenstates of the quarks do not coincide with their weak eigenstates, the Higgs mechanism also gives rise to the quark mixing phenomenology, which allows for the existence of quark flavour changing processes.

1.1.1 The CKM matrix

The relation between the quark weak and mass eigenstates is given by a rotation matrix for the down type quarks:

$$\begin{pmatrix} \mathrm{d} \\ \mathrm{s} \\ \mathrm{b} \end{pmatrix}_{\text{weak}} = \begin{pmatrix} V_{ud} & V_{us} & V_{ub} \\ V_{cd} & V_{cs} & V_{cb} \\ V_{td} & V_{ts} & V_{tb} \end{pmatrix} \begin{pmatrix} \mathrm{d} \\ \mathrm{s} \\ \mathrm{b} \end{pmatrix}_{\text{mass}} \tag{1.1}$$

which is known as the CKM matrix [14], named after Cabibbo (who first elaborated the formalism for two family of quarks) and Kobayashi and Maskawa (who formulated the extension to three families). If both mass and flavour basis are complete, and provided that there are three (and only three) quark families in Nature, then, the CKM matrix must be unitary. This represents one of the the most powerful closure tests of the SM and its only prediction imposing constraints to the values of the matrix elements. A general unitary matrix of dimension D can be characterised by D^2 real parameters, $D(D-1)/2$ moduli and $D(D+1)/2$ phases. Therefore, by imposing unitarity of the CKM matrix, it can be deduced that 3 moduli and 6 phases need to be determined for its characterisation. Nonetheless, absolute phases are not physical due to a rotation invariance of the mathematical description of the quark fields, which means that 5 of the phases can be reabsorbed by redefinition of the theory elements and are not observable. The resulting four free parameters are referred to as three quark mixing angles, θ_{ij}, and one complex phase, δ. This phase is of key relevance when studying *CP*-conjugated processes.

A given quark flavour transition, $i \rightarrow j$, will be more or less favourable depending on the value of the involved CKM matrix element, V_{ij}. When considering the *CP* conjugated process, $\bar{i} \rightarrow \bar{j}$, the relevant parameter is the corresponding complex conjugate, V_{ij}^*, of the aforementioned CKM matrix element. Without the existence of the irreducible complex phase in the matrix parameterisation, $V_{ij} = V_{ij}^*$ would be satisfied for all elements, preventing the existence of *CP* violation within the SM.

A natural parameterisation that shows the hierarchy (hence the strength of the mixing among families) of the CKM matrix was introduced by Wolfenstein [5]:

$$V^{CKM} = \begin{pmatrix} 1-\frac{\lambda^2}{2} & \lambda & A\lambda^3(\rho-i\eta) \\ -\lambda & 1-\frac{\lambda^2}{2} & A\lambda^2 \\ A\lambda^3(1-\rho-i\eta) & -A\lambda^2 & 1 \end{pmatrix} + \mathcal{O}(\lambda^4), \tag{1.2}$$

where λ, A, ρ and η are given by

$$\lambda = \frac{|V_{us}|}{\sqrt{|V_{ud}^2 + |V_{us}^2}}, \qquad A\lambda^2 = \lambda \left|\frac{V_{cb}}{V_{us}}\right|, \qquad A\lambda^3(\rho+i\eta) = V_{ub}^*. \tag{1.3}$$

The definition of $A\lambda^3(\rho+i\eta)$ relates to the third family of quarks, therefore justifying the expectation for sizeable *CP*-violating effects in processes involving the b quark.

1.1.2 CP violation

There are several types of processes that allow for manifestations of *CP*-violating phenomenologies. As previously mentioned, these effects are expected to be most sizeable in processes involving b quarks. In particular, the fact that B mesons are quite long-living particles allows for the measurement of the three types of phenomena sensitive to *CP*-violating effects:

- *CP* violation in the mixing,
- *CP* violation in the decay,
- *CP* violation in the interference between mixing and decay.

Particularising the examples for the B meson sector, the first type of process may occur when both, $B^0_{(s)}$ and $\overline{B}^0_{(s)}$ mesons, decay to a common final state. The reason for this mixing is that $B^0/\overline{B}^0$ mesons are flavour eigenstates, which are different from the physical mass eigenstates. Both basis are related by a rotation matrix which is constructed as a linear combination of the mass and width matrices of the B mesons, thus, containing elements that must be identical if CPT invariance is assumed. Adopting the usual notation in this cases, *CP* symmetry is violated if $|q/p| \neq 1$, were q and p are the relative amount of each flavour eigenstate in the mass eigenstates.

The second *CP* violation type is usually referred to as direct *CP* violation and it is the only source of *CP* violation for charged B mesons or b-baryons. Direct *CP* violation accounts for the differences that may arise between the relative amplitudes for the $B \to f$ and $\overline{B} \to \overline{f}$ processes. The total amplitudes of these transitions can be written as a coherent sum of the contributing decay amplitudes:

$$A_f = \sum_j |a_j| e^{i(\delta_j+\phi_j)} \qquad \text{and} \qquad \overline{A}_{\overline{f}} = \sum_j |a_j| e^{i(\delta_j-\phi_j)}, \tag{1.4}$$

where j runs over all the possible decay paths, which are characterised by their strength a_j, a *CP*-conserving phase, δ_j and a *CP*-violating phase, ϕ_j. This last term changes sign when entering the description of the *CP* conjugate decay. A related observable (*CP* asymmetry) can be defined as

$$a_{CP} = \frac{\Gamma(B \to f) - \Gamma(\overline{B} \to \overline{f})}{\Gamma(B \to f) + \Gamma(\overline{B} \to \overline{f})} = \frac{|\overline{A}_{\overline{f}}/A_f| - 1}{|\overline{A}_{\overline{f}}/A_f| + 1} \propto 2 \sum_{i,j} |a_i a_j| \sin(\delta_i - \delta_j) \sin(\phi_i - \phi_j), \tag{1.5}$$

from where the conditions enabling *CP*-violating effects can be deduced: a process has to receive contributions from at least two decay amplitudes (a_i, a_j) with non-zero strong $(\delta_i - \delta_j)$ and weak $(\phi_i - \phi_j)$ phase difference. As mentioned before, the weak phase difference originates from the phase in the CKM matrix, which creates a difference between V_{ij} and V_{ij}^*. On the other side, the strong phase difference emerges from hadronic effects (phase motion associated to resonances, re-scattering, ...). Since QCD is invariant under *CP* transformation, these phases appear with the same sign for conjugated processes and therefore dynamical differences are required.

Finally, since both processes described above can occur simultaneously, *CP* asymmetry may arise too in the interference between the mixing and the decay. In these cases the interfering amplitudes are those corresponding to the processes $B^0 \to f$ and $B^0 \to \overline{B}^0 \to f$.

The violation of the *CP* symmetry is one of the conditions A. Sakharov [15] deemed necessary to be fulfilled in order to explain the different production rates of matter and antimatter in physical processes. The complete set of the so-called "Sakharov conditions" are:

- Baryon number violation.
- *C*- and *CP*-symmetries violation.
- Interactions out of thermal equilibrium.

The first of them is a direct requirement for the mere existence of the asymmetry. The second must exist in order to prevent the asymmetry to be counterbalanced by the processes where antimatter production rates are larger than the corresponding rates for matter. Finally, the departure from equilibrium requirement arises as a consequence from the second condition. The violation of *CP* symmetry implies that time-reversal (T) needs to be broken too, motivated by the overall constraint of maintaining the CPT invariance. From the thermodynamic point of view, breaking T implies an irreversible process, which must therefore be out of equilibrium. While the Sakharov conditions are fulfilled in the SM, the explanation of matter and antimatter asymmetry is not met quantitatively, as the magnitude of the observed asymmetry in the known Universe is well beyond the SM expectations. Nevertheless, this discrepancy hints at new phenomena contributing to *CP*-violating processes, hence motivating experimental searches in this regard.

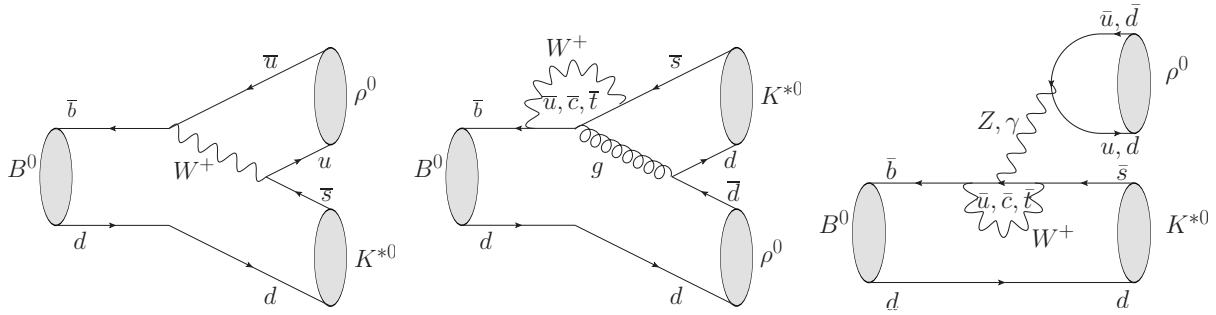

Figure 1.2: Leading Feynman diagrams in the $B^0 \to \rho^0 K^{*0}$ decay, from left to right: doubly Cabibbo-suppressed tree, gluonic-penguin and electroweak-penguin diagrams.

1.2 The $B^0 \to \rho^0 K^{*0}$ decay channel

1.2.1 Introduction

As explained in the previous sections, direct *CP* violation manifests through the difference between partial widths of a decay and its *CP* conjugate. This phenomenon has been observed in several processes, and in particular within B physics, for the family of $B \to \pi K$ decays. A closure test for the SM can be performed by measuring the branching ratios and *CP* asymmetries for all these decays, since the use of isospin relations (if ignoring subdominant contributions) overconstraints the predictions for this set of observables. The lack of agreement between experimental measurements and theoretical predictions on these constraints is commonly referred to as the "$K\pi$ puzzle". Much more information about the relative strength of all the contributing amplitudes can be obtained by analysing the vector counterparts of these channels, as the decay dynamics can be scrutinised in terms of the anisotropic distributions of the decay products.

In particular, for the vector-vector (VV) neutral mode, $B^0 \to \rho^0 K^{*0}$, the tree level contribution, $b \to u\overline{u}s$ depends on the CKM matrix elements $V_{ub}V_{us}^*$. This amplitude is doubly Cabibbo suppressed (mediated by two off-diagonal terms in the CKM matrix) and higher order diagrams dominate the decay (see Figure 1.2). Such contributions originate from the $b \to d\overline{d}s$ ($V_{tb}V_{ts}^*$) process that may proceed either via colour-allowed electroweak-penguin or gluonic-penguin transitions.

As anticipated, these decays are not isotropic and the decay products may be polarised. This behaviour arises due to the chiral structure of the quark operators and its study helps gaining a better understanding of QCD. Furthermore, the aforementioned electroweak-penguin amplitude contributes with different signs to the total decay rate depending on which helicity amplitude is considered. This allows for several interference patterns in the decay and plays an important role in its polarisation since both penguin amplitudes are comparable in magnitude. A more detailed discussion on these phenomena can be found in Ref. [16]. The angular analysis of VV decays also gives access to T-odd triple product asymmetries (TPA), which are observables suitable for comparison with

theoretical predictions, such as those in Ref. [17].

In the past, the theoretical approach to the study of B decays into light-vector mesons was influenced by the idea that quark helicity conservation and the V−A nature of the weak interaction induce large longitudinal polarisation fractions, of order $f^0 \sim 0.9$. However, this prediction holds only for decays dominated by tree diagrams [18], whilst in penguin-dominated decays this hypothesis is not fulfilled [19, 20]. A summary of the latest experimental results as of May 2018 is shown in Figure 1.2.1. Low values of longitudinal polarisation fractions in penguin-dominated decays could be accounted by the SM invoking a strong-interaction effect, both in the QCD factorisation (QCDF) [16] and perturbative (pQCD) [21] frameworks. This so-called polarisation puzzle might be resolved by combining measurements from all the $B \to \rho K^*$ modes ($B^0 \to \rho^0 K^{*0}$, $B^0 \to \rho^- K^{*+}$, $B^+ \to \rho^0 K^{*+}$ and $B^+ \to \rho^+ K^{*0}$). This would allow also to probe physics beyond the SM [22, 23].

Regarding previous experimental results, the decay mode $B^0 \to \rho^0 K^{*0}$ and its scalar-vector counterpart $B^0 \to f_0(980) K^{*0}$ have previously been studied by the BaBar [25] and Belle [26] collaborations, although the latter only targeted the measurements of the branching fractions. The BaBar collaboration performed an angular analysis of the $B^0 \to \rho^0 K^{*0}$ mode integrating over one of the helicity angles (ϕ) due to the limited size of their available data sample. They determined the longitudinal polarisation fraction of the *CP*-averaged $B^0 \to \rho^0 K^{*0}$ decay to be $f^0 = 0.40 \pm 0.08 \pm 0.11$. Both BaBar and Belle collaborations pursued the measurement of the *CP*-averaged longitudinal polarisation of $B^0 \to \omega(\to \pi^+\pi^-\pi^0) K^{*0}$ decays, yielding $f^0 = 0.72 \pm 0.14 \pm 0.02$ [27] and $f^0 = 0.56 \pm 0.29^{+0.18}_{-0.08}$ [28], respectively.

In the following sections the dependence of the $B^0 \to (\pi^+\pi^-)(K^+\pi^-)$ decay rate on the two-body invariant masses and the helicity angles is described, including the characterisation of the functions involved. The `PDF` used in the amplitude fit is discussed and its parameters are related to physical observables suitable for comparison with other experimental measurements and theoretical predictions, when available.

1.2.2 $B^0 \to \rho^0 K^{*0}$ decay rate

Analytical expression

The analytical expression for the decay rate of $B^0 \to (\pi^+\pi^-)(K^+\pi^-)$ events is built following the helicity formalism described in Ref. [16]. In the $B^0 \to \rho^0 K^{*0}$ decay, the parent particle has a intrinsic spin of $S_M = 0$, while the decay products have both $S_1 = S_2 = 1$. This leads to a total angular momentum $J_M = 0$ in the B^0 rest frame, which, due to total angular momentum conservation, implies that the orbital momentum and the coupled spin vector must satisfy $L_{12} = S_{12}$ in the final system. The combined spin of a two spin-1 particles system can either be $S_{12} = 0, 1$ or 2, thus, for each of this configurations, L_{12} must be, accordingly, 0, 1 or 2, in order to fulfil the $J_M = 0$ requirement. This configuration leads to three possible helicity values, $h = -1, 0$ or 1, hence, to three

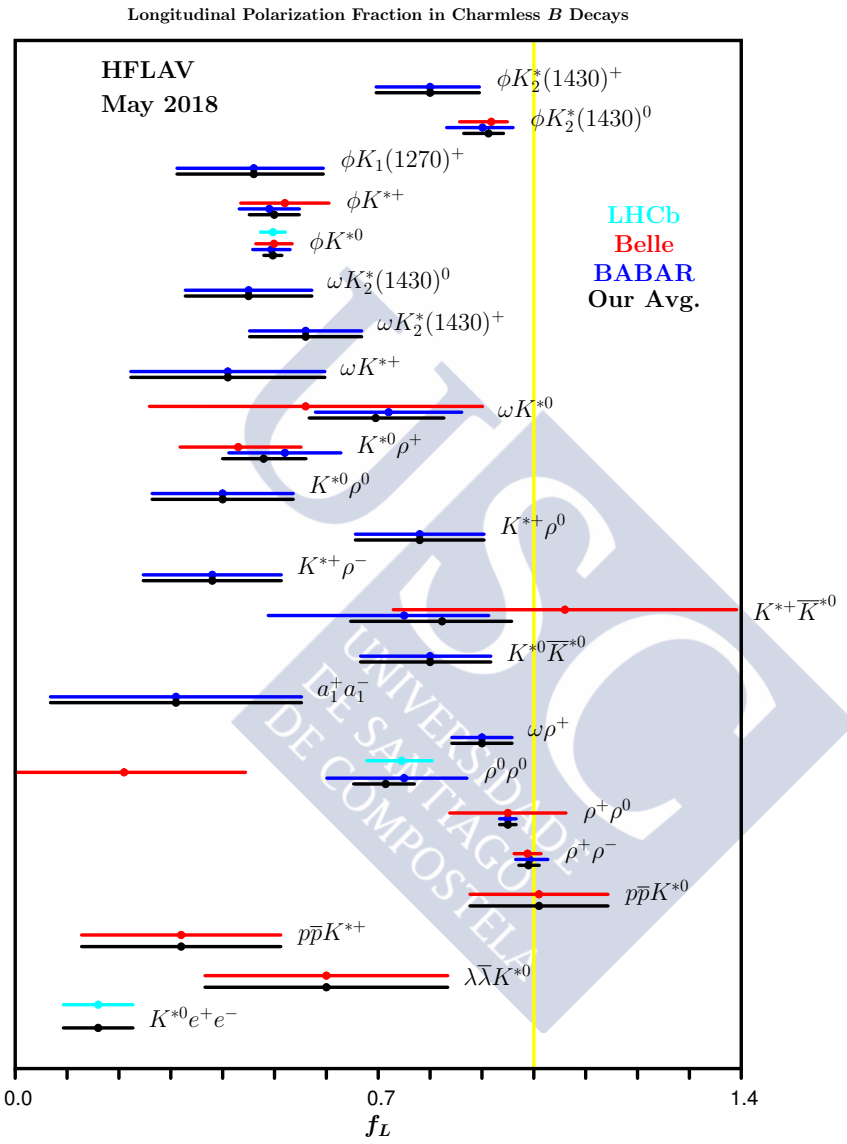

Figure 1.3: Experimental results on the longitudinal polarisation fractions for charmless B meson decays as of May 2018. Figure taken from [24].

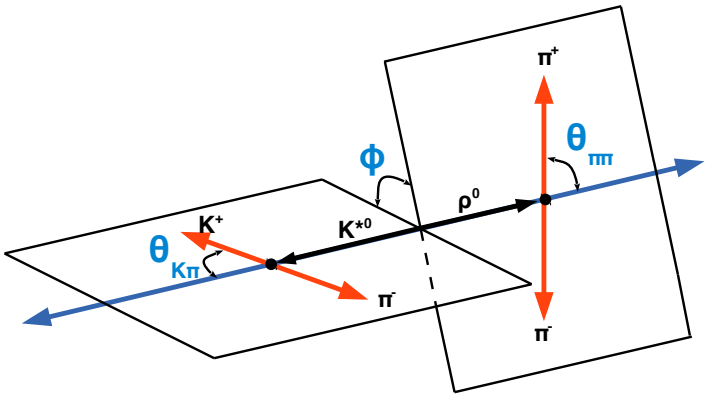

Figure 1.4: Definition of the helicity angles in the $B^0 \to \rho^0 K^{*0}$ decay, where the indexes from Equation 1.8 have been substituted according to $i = 1, 2, 4 \equiv \pi$ e $i = 3 \equiv K$.

complex amplitudes: one longitudinal, H_0; and two transverse $H_{\pm 1}$. The helicity basis is defined by these three amplitudes, (H_0, H_{+1}, H_{-1}), which correspond to the helicity states. The use of this basis results convenient to perform theoretical computations, given the dependency of the hadronic matrix element (see Ref. [16] for details) on the helicity states. However, in experimental analyses, this basis is usually rotated into the transversity basis, which elements have definite parity. The relation between both sets of amplitudes is:

$$P\text{-even} : A^0 = H^0,$$

$$P\text{-even} : A^{||} = \frac{H^+ + H^-}{\sqrt{2}},$$

$$P\text{-odd} : A^{\perp} = \frac{H^+ - H^-}{\sqrt{2}}.$$

As derived in [29], the differential decay rate of a pseudoscalar B^0 meson into two vector particles can be written as:

$$\frac{d\Gamma}{d\Omega} \propto |A^0 F^0(\Omega) + A^{||} F^{||}(\Omega) + A^{\perp} F^{\perp}(\Omega)|^2, \tag{1.6}$$

where the $F^{\lambda}(\Omega)$ ($\lambda = 0, ||$ or $\perp$) functions describe the angular distributions of the final state particles. These are given as combinations of spherical harmonics depending on the helicity angles, which are depicted in Figure 1.4 and, in the present analysis, are defined as follows:

- θ_{12} is the angle between the π^+ direction in the $(\pi^{\pm}\pi^{\mp})$ rest frame and the ρ^0 direction in the B^0 rest frame.

- θ_{34} is the angle between the kaon direction in the $(K^{\pm}\pi^{\mp})$ rest frame and the K^{*0} direction in the B^0 rest frame.

- ϕ is the angle between the $(\pi^{\pm}\pi^{\mp})$ and the $(K^{\pm}\pi^{\mp})$ decay planes.

The Isobar model is used to parameterise the total decay amplitude, this meaning that the overall rate is built from a coherent sum over all the contributing resonances (in a quasi-2-body approach, which includes the nonresonant pairs). Within the aforementioned formalism, the total amplitude can be written in a compact way as:

$$A_T = \sum_i \mathcal{A}_i = \sum_i A_i \cdot g_i(\theta_{12}, \theta_{34}, \phi) \cdot M_i(m_{12}, m_{34}), \tag{1.7}$$

where the A_i represent the strength of each component, the g_i functions are combinations of spherical harmonics, describing the angular distribution of states with a definite spin, and the $M(m_{12}, m_{34})$ functions have been included to explicitly account for the effective masses of the $\pi^{\pm}\pi^{\mp}$and $K^{\pm}\pi^{\mp}$pairs and distinguish resonances with the same angular dependence. The sum index, i, runs over all contributing waves, which are briefly motivated in the following paragraphs and listed in Table 1.1.

In the considered region of the $(\pi^{\pm}\pi^{\mp})$ invariant mass spectrum ($300 < m(\pi^+\pi^-) < 1100\,\mathrm{MeV}/c^2$) the scalar ($S$, spin-0) resonances $f_0(500)$ and $f_0(980)$ have been previously established and are expected to contribute in addition to the vector resonance ω, together with the ρ^0 meson. There is also clear evidence [30] of the existence of a higher mass spin-0 resonance, the $f_0(1370)$, although its nominal mass and width have not yet been measured with great precision.

The $(K^{\pm}\pi^{\mp})$ invariant mass spectrum up to $\sim$1.2 GeV/c^2 is dominated by two equally relevant structures: the spin-1 $K^*(892)^0$ resonance and the spin-0 state, which shall include both a resonant ($K_0^*(1430)$) and a nonresonant component. It should be noted that in this nonresonant case, the $(K^{\pm}\pi^{\mp})$ pair is expected to only be produced in the $J_{(K\pi)} = 0$ state due to kinematic reasons. Since no orbital momentum is induced between the final state particles, as far as perturbative QCD holds [31], the $J_{K\pi} = L_{K\pi} = 0$ assumption is reasonable since it is the most kinematically favoured.

All these intermediate states contribute to the final $(\pi^{\pm}\pi^{\mp})(K^{\pm}\pi^{\mp})$ observed distribution, both VV decays with three amplitudes each ($A^0, A^{||}$ and $A^{\perp}$) and the rest of them with only one. The angular and mass functions corresponding to each of these 14 amplitudes are shown in Table 1.1.

Bringing all the previous factors together, the differential decay rate is obtained by squaring the sum of all the amplitudes in Table 1.1:

$$\begin{aligned} \frac{d^5\Gamma}{dm_{12}^2 dm_{34}^2 d\cos\theta_{12} d\cos\theta_{34} d\phi} &\propto |A_T(\theta_{12}, \theta_{34}, \phi, m_{12}, m_{34})|^2 = \\ &= \left| \sum_{i=1}^{14} A_i \cdot g_i \cdot M_i \right|^2 = \sum_{i=1}^{14} \sum_{j=1}^{14} (A_i \cdot g_i \cdot M_i)(A_j \cdot g_j \cdot M_j)^*. \end{aligned} \tag{1.8}$$

The fitting model (`PDF`) is proportional to the decay rate described in Equation 1.8. Each complex amplitude in the fit contributes with two free parameters (magnitude and

Table 1.1: Partial waves contributing to the total amplitude and their angular and mass dependences.

i	Type	A_i	$g_i(\theta_{12}, \theta_{34}, \phi)$	$M_i(m_{12}, m_{34})$
1		$A^0_{\rho K^*}$	$\cos\theta_{12}\cos\theta_{34}$	$M_\rho(m_{12})M_{K^*}(m_{34})$
2	V_1V	$A^{\parallel}_{\rho K^*}$	$\frac{1}{\sqrt{2}}\sin\theta_{12}\sin\theta_{34}\cos\phi$	$M_\rho(m_{12})M_{K^*}(m_{34})$
3		$A^{\perp}_{\rho K^*}$	$\frac{i}{\sqrt{2}}\sin\theta_{12}\sin\theta_{34}\sin\phi$	$M_\rho(m_{12})M_{K^*}(m_{34})$
4		$A^0_{\omega K^*}$	$\cos\theta_{12}\cos\theta_{34}$	$M_\omega(m_{12})M_{K^*}(m_{34})$
5	V_2V	$A^{\parallel}_{\omega K^*}$	$\frac{1}{\sqrt{2}}\sin\theta_{12}\sin\theta_{34}\cos\phi$	$M_\omega(m_{12})M_{K^*}(m_{34})$
6		$A^{\perp}_{\omega K^*}$	$\frac{i}{\sqrt{2}}\sin\theta_{12}\sin\theta_{34}\sin\phi$	$M_\omega(m_{12})M_{K^*}(m_{34})$
7	V_1S	$A^0_{\rho(K\pi)}$	$\frac{1}{\sqrt{3}}\cos\theta_{12}$	$M_\rho(m_{12})M_{(K\pi)}(m_{34})$
8	V_2S	$A^0_{\omega(K\pi)}$	$\frac{1}{\sqrt{3}}\cos\theta_{12}$	$M_\omega(m_{12})M_{(K\pi)}(m_{34})$
9	S_1V	$A^0_{f_0(500)K^*}$	$\frac{1}{\sqrt{3}}\cos\theta_{34}$	$M_{f_0(500)}(m_{12})M_{K^*}(m_{34})$
10	S_2V	$A^0_{f_0(980)K^*}$	$\frac{1}{\sqrt{3}}\cos\theta_{34}$	$M_{f_0(980)}(m_{12})M_{K^*}(m_{34})$
11	S_3V	$A^0_{f_0(1370)K^*}$	$\frac{1}{\sqrt{3}}\cos\theta_{34}$	$M_{f_0(1370)}(m_{12})M_{K^*}(m_{34})$
12	S_1S	$A^0_{f_0(500)(K\pi)}$	$\frac{1}{3}$	$M_{f_0(500)}(m_{12})M_{(K\pi)}(m_{34})$
13	S_2S	$A^0_{f_0(980)(K\pi)}$	$\frac{1}{3}$	$M_{f_0(980)}(m_{12})M_{(K\pi)}(m_{34})$
14	S_3S	$A^0_{f_0(1370)(K\pi)}$	$\frac{1}{3}$	$M_{f_0(1370)}(m_{12})M_{(K\pi)}(m_{34})$

phase or real and imaginary part), therefore, one complex quantity has to be constrained by the normalisation of the PDF. This is implemented in the fit by fixing the values of two parameters to some reference constants. Given that many of the considered amplitudes are expected to have small values of $|A_i|^2$, it was decided to perform the baseline fit in terms of real and imaginary parts, instead of moduli and phases (more details are given in Section 5.1.4, when discussing the technical advantages of each parameterisation). The $V_1S(\rho(K\pi))$ contribution was found to be a sizeable fit component, so the normalisation of the PDF is ensured by forcing

$$A^{Re}_{\rho(K\pi)} = 2, \text{ and } A^{Im}_{\rho(K\pi)} = 0. \tag{1.9}$$

Therefore, the parameters that are determined from the fit correspond to the relative strength of each contribution to the decay rate with respect to that of the $V_1S(\rho(K\pi))$. From the amplitudes A_i, modelling B^0 decays, and $\overline{A}_i$, describing $\overline{B}^0$ decays, other physically meaningful observables can be derived (summarised in Table 1.2). In particular, for the VV decays $B^0 \to \rho^0 K^{*0}$ and $B^0 \to \omega K^*(892)^0$, these quantities are the polarisation

fractions

$$f_{VV}^{\lambda} = \frac{|A_{VV}^{\lambda}|^2}{|A_{VV}^{0}|^2 + |A_{VV}^{||}|^2 + |A_{VV}^{\perp}|^2}\,, \qquad \lambda = 0, ||, \perp \tag{1.10}$$

with their *CP* averages, $\tilde{f}$, and asymmetries, $\mathcal{A}$,

$$\tilde{f}_{VV}^{\lambda} = \frac{1}{2}(f_{VV}^{\lambda} + \overline{f}_{VV}^{\lambda})\,, \qquad \mathcal{A}_{VV}^{\lambda} = \frac{\overline{f}_{VV}^{\lambda} - f_{VV}^{\lambda}}{\overline{f}_{VV}^{\lambda} + f_{VV}^{\lambda}}\,, \tag{1.11}$$

and the phase differences, measured with respect to the reference channel, $B^0 \to \rho^0(K\pi)$,

$$\delta_{VV}^{0} \equiv (\delta_{VV}^{0} - \delta_{\rho(K\pi)}) = \arg(A_{VV}^{0}/A_{\rho(K\pi)}). \tag{1.12}$$

For comparison with theoretical predictions it is also convenient to compute the phase differences among the different VV amplitudes,

$$\delta_{VV}^{||-0,\perp-0} \equiv (\delta_{VV}^{||,\perp} - \delta_{VV}^{0}) = \arg(A_{VV}^{||,\perp}/A_{VV}^{0}). \tag{1.13}$$

From these sets of observables, the phase differences of the *CP* average, $\frac{1}{2}(\delta_{\overline{B}} + \delta_B)$, and *CP* difference, $\frac{1}{2}(\delta_{\overline{B}} - \delta_B)$, are obtained. Ambiguities in this definition are resolved by choosing the smallest value of the *CP*-violating phase.

From the polarisation fractions obtained for the VV waves, other observables, called triple-product correlations [17,32] can also be computed. These quantities depend on the polarisation vectors and are odd under time-reversal. They can be obtained from the perpendicular polarisation fractions and the phase differences as

$$\mathcal{A}_T^1 = f_\perp f_0 \sin(\delta_\perp - \delta_0), \quad \mathcal{A}_T^2 = f_\perp f_{||} \sin(\delta_\perp - \delta_{||}), \tag{1.14}$$

for both the B^0 ($\mathcal{A}_T^1$) and the $\overline{B}^0$ ($\overline{\mathcal{A}}_T^1$) samples. Non-zero values of these observables can not be uniquely identified with a *CP*-violating process, however, the so called Triple Product Asymmetries (TPA) can be built when comparing $\mathcal{A}_T^1$ and $\mathcal{A}_T^2$ with $\overline{\mathcal{A}}_T^1$ and $\overline{\mathcal{A}}_T^1$:

$$\mathcal{A}_{T-true}^{k} = \frac{\mathcal{A}_T^k - \overline{\mathcal{A}}_T^k}{2}, \qquad \mathcal{A}_{T-fake}^{k} = \frac{\mathcal{A}_T^k + \overline{\mathcal{A}}_T^k}{2}, \tag{1.15}$$

where $k = 1, 2$ and the *true* or *fake* labels refer to whether the asymmetry is due a genuine *CP* asymmetry or due to effects from final state interactions, respectively. It should be noted that observing a TPA value consistent with zero would not rule out the presence of *CP*-violating effects, since negligible *CP* averaged phase differences would suppress the asymmetries.

Table 1.2: Summary of the fit parameters and their definitions ($\lambda = 0, ||, \perp$; i runs over all the contributing waves but the normalisation $V_1 S(\rho(K\pi))$)

Parameter	Definition
f^{λ}	$\frac{1}{2}\left(\frac{\lvert\overline{A}^{\lambda}_{\rho K^*}\rvert^2}{\sum_\lambda \lvert\overline{A}^{\lambda}_{\rho K^*}\rvert^2} + \frac{\lvert A^{\lambda}_{\rho K^*}\rvert^2}{\sum_\lambda \lvert A^{\lambda}_{\rho K^*}\rvert^2}\right)$
$\lvert A_i^{av}\rvert^2$	$\frac{1}{2}\left(\lvert\overline{A}_i\rvert^2 + \lvert A_i\rvert^2\right)$
δ_i^{av}	$\frac{1}{2}\left(\overline{\delta}_i + \delta_i\right)$
$f^{\lambda,\mathcal{CP}}$	$\frac{\overline{f}^{\lambda} - f^{\lambda}}{\overline{f}^{\lambda} + f^{\lambda}}$
$\mathcal{A}_i^{\mathcal{CP}}$	$\frac{\lvert\overline{A}_i\rvert^2 - \lvert A_i\rvert^2}{\lvert\overline{A}_i\rvert^2 + \lvert A_i\rvert^2}$
$\delta_i^{\mathcal{CP}}$	$\frac{1}{2}\left(\overline{\delta}_i - \delta_i\right)$
Normalisation	**Constraint**
A_i^{Re}	$A^{Re}_{\rho(K\pi)} = \overline{A}^{Re}_{\rho(K\pi)} = 2$
A_i^{Im}	$A^{Im}_{\rho(K\pi)} = \overline{A}^{Im}_{\rho(K\pi)} = 0$

Resonances lineshape

The dependence of the PDFon the two-body invariant masses was introduced in Equation 1.7 through the $M(m_{12}, m_{34})$ functions. These terms can be written as:

$$\begin{aligned} M(m_{12}, m_{34}) = B_{L_B}(p, p_0, d_B) \left(\frac{p}{m_B}\right)^{L_B} \\ \times B_R(q_{12}, q_0, d_R) \left(\frac{q_{12}}{m_R}\right)^{L_R} \times \mathcal{R}(m_{12}) \\ \times B_{R'}(q_{34}, q'_0, d_{R'}) \left(\frac{q_{34}}{m_{R'}}\right)^{L_{R'}} \times \mathcal{R}'(m_{34}) \\ \times \Phi_4(m_{12}, m_{34}) \end{aligned} \tag{1.16}$$

Where $\mathcal{R}(m_{ij})$ is the dynamical function describing each resonance and depends on the invariant mass of the 2-body system (m_{ij}) and Φ_4 is the phase-space density, included in order to account for the kinematics of the 4-body decay. The other factors in the equation above account for the finite size of the involved particles and for the centrifugal barriers arising from non zero relative angular momentum between the decay products. These effects are parametrised as proportional to $q^L \cdot B_L(q, q_0, d_R)$, where q stands for the momentum of the daughter particle in its mother's rest frame (Equation 1.38), q_0 is this momentum evaluated at the nominal mass of the daughter particle, d_R is the effective radius of the resonance ($R^{(\prime)}$) and the $B_L(q, q_0, d_R)$ function represents the Blatt-Weisskopf barrier penetration factor, depending on the relative angular momentum between the decay products, L:

$$B_L(q, q_0, d_R) = \begin{cases} 1 \text{ for } L = 0, \\ \sqrt{\frac{1+(d_R q_0)^2}{1+(d_R q)^2}} \text{ for } L = 1. \end{cases} \tag{1.17}$$

Details on this formalism can be found in [33] and [34]. The different nature of the resonances taken into account in the present study motivates different choices for the functional form of $\mathcal{R}(m_{ij})$ in Equation 1.16. All these propagators are described in the following, together with the values of the different constants that they may depend on. The central values of these constants are used to perform the nominal fit, while the corresponding uncertainties define the range of the variations introduced to study systematic uncertainties.

Relativistic Breit-Wigner

This propagator is used in the nominal fit model to describe the $K^*(892)^0$, ω, $f_0(500)$ and the $f_0(1370)$ resonances with the parameters summarised in Table 1.3. This function is defined as

$$BW(m, L) = \frac{m_0 \Gamma_0}{m_0^2 - m^2 - i m_0 \Gamma_L(m)}, \tag{1.18}$$

Table 1.3: Values [5] of the parameters used in the parametrisations of the $K^*(892)^0$, ω, $f_0(500)$ and the $f_0(1370)$ resonances when described with a relativistic Breit-Wigner mass propagator (nominal fit values).

Variable	$K^*(892)^0$	ω	$f_0(500)$	$f_0(1370)$
m_0 [MeV/c^2]	895.8± 0.2	782.65±0.12	475±32	1350±6
Γ_0 [MeV/c^2]	47.4±0.5	8.49±0.08	337±67	350±11
d_R [(MeV/c^2)$^{-1}$]	0.0034±0.0005	0.0034±0.0005	-	-
L	1	1	0	0
Particle masses [MeV/c^2]				
$m_B = 5279.61$		$m_\pi = 139.57018$		$m_K = 493.677$

where

$$\Gamma_L(m) = \Gamma_0 \left(\frac{m_0}{m}\right) B_L(q, q_0, d_R)^2 \left(\frac{q}{q_0}\right)^{2L+1}, \tag{1.19}$$

being m_0 and Γ_0 the nominal mass and natural width of the resonance.

Gounaris-Sakurai

The formalism resulting in the Breit-Wigner function described above uses the narrow width-approximation, making this distribution unsuitable for the description of the ρ^0 resonance, due to its large width. Instead, the Gounaris-Sakurai [35] parametrisation is used to describe this broad resonance. This function takes the form:

$$GS(m) \propto \frac{1}{m_{\rho^0}^2 - m^2 + \Gamma_{\rho^0}\frac{m_{\rho^0}^2}{q_{\rho^0}^3}[q^2(h - h_{\rho^0}) - (m^2 - m_{\rho^0}^2)q_{\rho^0}^2 h'_{\rho^0}] - i m_{\rho^0}\Gamma(m)} \tag{1.20}$$

with

$$q \equiv q(m) = (m^2/4 - m_\pi^2)^{1/2} \tag{1.21}$$

$$h(m) = \frac{2}{\pi}\frac{q}{m}\log\left(\frac{m + 2q}{2m_\pi}\right) \tag{1.22}$$

$$h'(m) \equiv \frac{dh(m)}{dm^2} \tag{1.23}$$

$$q_{\rho^0} = q(m_{\rho^0}) \tag{1.24}$$

$$h_{\rho^0} = h(m_{\rho^0}) \tag{1.25}$$

$$\Gamma(m) = \Gamma_1(m) \tag{1.26}$$

$$\tag{1.27}$$

where m is the $\pi^+\pi^-$ invariant mass, $\Gamma_{\rho^0} = 147.8\pm0.9$ MeV/c^2 is the ρ^0 natural width, $m_{\rho^0}= 775.26 \pm 0.25$ MeV/c^2 is the ρ^0 nominal mass and $d_R = 0.0053\pm0.0008$ MeV/c^2 $^{-1}$ [5] the effective radius of this meson.

Flatté

The pole mass of the $f_0(980)$ resonance is very close to the kinematic threshold for the opening of its decay to two kaons. Due to unitarity constraints, this effect significantly distorts the lineshape of the $f_0(980)$ resonance in the two pion invariant mass spectrum. On account of this, the Flatté parametrisation is used to describe this resonance in the analysis. The definition of this function [36, 37] is given by:

$$F(m) = \frac{m_0(g_{\pi\pi}\rho_{\pi\pi}(m_0) + g_{KK}\rho_{KK}(m_0))}{m_0^2 - m^2 - im_0(g_{\pi\pi}\rho_{\pi\pi}(m) + g_{KK}\rho_{KK}(m))} \tag{1.28}$$

$$\rho_{XX}(m) = 2\frac{q_{XX}(m)}{m} = \begin{cases} \sqrt{1 - 4\frac{m_X^2}{m^2}} \text{ for } m > 2m_X, \\ i\sqrt{4\frac{m_X^2}{m^2} - 1} \text{ for } m \leq 2m_X, \end{cases} \tag{1.29}$$

where $m_X = m_K, m_\pi$, accordingly. The resonance mass is $m_{f(980)} = 945 \pm 2$ MeV/c^2 and the strength of the coupling to the decay channels, $g_{\pi\pi} = 199 \pm 30\,\text{MeV}/c^2$ and $g_{KK} = (3 \pm 0.1)g_{\pi\pi}$ [38]. The following modification of this line shape was considered during the evolution of the analysis:

$$F'(m) = \frac{m_0(g_{\pi\pi}\rho_{\pi\pi}(m_0) + g_{KK}\rho_{KK}(m_0))}{m_0^2 - m^2 - im_0(g_{\pi\pi}\rho_{\pi\pi}(m) + g_{KK}F_{KK}^2\rho_{KK}(m))}, \tag{1.30}$$

$$\tag{1.31}$$

where $F_{KK} = \exp(-\alpha k^2)$ stands for a form factor that allows to describe a slight increase of the $f_0(980)$ width after the opening of the KK threshold, k being the momentum of each kaon in the KK rest frame. While checking the effect of this modification, the parameter α was fixed to 2.0 GeV^{-2}, following what was done in Ref. [38] motivated by the poor sensitivity of the fit to this value. Given the tiny change introduced by this modification in the parametrisation, the standard Flatté distribution was chosen for the baseline model.

LASS

The $(K^\pm\pi^\mp)$ S-wave is described in the nominal model with the LASS [39] parametrisation, which consists of a K^{*0} resonant term together with an effective-range, nonresonant component to describe the slowly increasing phase as a function of the $(K^\pm\pi^\mp)$ pair invariant mass. The Breit-Wigner parametrisation (Equations 1.18 and 1.19 with the parameters in Table 1.4) is used to describe the shape of the wide $K_0^*(1430)$ resonance, while an effective parametrisation in terms of a scattering length and an effective range parameter models the low invariant mass region:

$$LASS(m) = \frac{1}{\cot\delta_B - i} + e^{2i\delta_B} BW(m, L=0), \tag{1.32}$$

$$\cot\delta_B = \frac{1}{aq} + \frac{1}{2}bq, \tag{1.33}$$

where a is the scattering length and b the effective range of the nonresonant part.

The values of these two parameters reported by the LASS experiment were obtained by fitting scattering data which means that they alone should not be expected to accurately describe an invariant mass distribution originated from the decay of a particle. However, if there are not final state interactions and if staying below inelastic threshold, according to Watson's theorem [40] and as suggested by recent phenomenological work [41], it can be assumed that the variation of the propagator phase will remain identical in both scattering and decay regimes. The elastic scattering threshold is, in principle, established at $m_\eta + m_{(K\pi)} \sim 1180$ MeV/c^2. However, it could be argued that the $m_{\eta'}$ value can replace m_η in the previous equation due to the tiny coupling to the first decay channel. This would shift the elastic threshold to even higher values for the invariant mass of the $K\pi$ system, resulting in an even safer scenario for the assumption of this hypothesis for this work. The simplest way to introduce such a behaviour is to re-shape the propagator module with a real function, namely, an effective form factor. This is obtained from a 1D fit to the $K^\pm\pi^\mp$invariant mass spectrum of the efficiency corrected (implemented with the tool described in Section 3.7) nominal data sample. The set of parameters needed to describe the $(K\pi)$ S-wave is shown in Table 1.4, where the FF_i stand for the coefficients of the modelled form factor:

$$FF(m) = e^{FF_1 \cdot \left(\frac{m}{m_{K^{*0}}} - 1\right)} + e^{FF_2 \cdot \left(\frac{m}{m_{K^{*0}}} - 1\right)^2}. \tag{1.34}$$

Description of the phase-space density

In order to account for the kinematics of the 4-body decay, a phase-space density has to be included in the description of the overall decay rate, as shown in Equation 1.16. Defining P as the four momentum of the mother particle and $\vec{p}_i$ as the four momentum of the daughter particles, the n-body phase-space, Φ_n, is given by:

$$d\Phi_n(\vec{P}; \vec{p}_1, ..., \vec{p}_n) = \delta^{(4)}\left(\vec{P} - \sum_{i=1}^{n} \vec{p}_i\right) \prod_{j=1}^{n} \frac{d^3\vec{p}_j}{(2\pi)^3 2E_j}. \tag{1.35}$$

Since the phase-space density can be recursively calculated, the corresponding to the four-body decay can be written as:

$$d\Phi_4(P; p_1, p_2, p_3, p_4) = (2\pi)^6 d\Phi_2(m_{12}; p_1, p_2) d\Phi_2(m_{34}; p_3, p_4) d\Phi_2(m_B; m_{12}, m_{34}) dm_{12} dm_{34}, \tag{1.36}$$

Table 1.4: LASS parameters (taken from [39]) and form factor coefficients. Given that FF_2 is compatible with 0, the form factor used in the nominal fit only considers the FF_1 term.

Parameter	Value
$m_{K_0^*(1430)}$ [MeV/c^2]	$1435 \pm 5 \pm 5$
$\Gamma_{K_0^*(1430)}$ [MeV/c^2]	$279 \pm 6 \pm 21$
a [MeV/c^2 $^{-1}$]	$1.95 \pm 0.09 \pm 0.06$
b [MeV/c^2 $^{-1}$]	$1.76 \pm 0.36 \pm 0.67$
FF_1	-0.71 ± 0.28
FF_2	1.8 ± 1.9

where $d\Phi_2(P; p_1, p_2) = \frac{1}{4(2\pi)^6} \frac{|\boldsymbol{p}_1|}{M} d\Omega$, being $d\Omega$ the element of solid angle in the mother particle rest frame. Inserting this Φ_2 expression in Equation 1.36, the differential four-body phase-space can be obtained. However, it is convenient to make a re-definition of the angles, masses and momenta, so that the final equation is expressed as a function of the helicity angles ($\theta_{12}, \theta_{34}, \phi$) and of the ($\pi^{\pm}\pi^{\mp}$) and ($K^{\pm}\pi^{\mp}$) invariant masses ($m_{12}, m_{34}$).

Therefore, the final expression for the four-body phase-space for the decay $M \to m_{12}(\to m_1 m_2) m_{34}(\to m_3 m_4)$ is:

$$\Phi_4(m_{12}, m_{34}) \propto q(m_{12}) q(m_{34}) q(M), \tag{1.37}$$

being $q(m_{ij})$ the relative momentum of the daughter particles in their mother's rest frame, which is given by:

$$q(m_{ij}) = \frac{\sqrt{(m_{ij}^2 - (m_i + m_j)^2)(m_{ij}^2 - (m_i - m_j)^2)}}{2m_{ij}}. \tag{1.38}$$

Mass terms normalisation

The global phases in the mass propagators $M_i(m_1, m_2)$ in Equation 1.8 may have an arbitrary offset, therefore, it is chosen to shift them to zero at the nominal mass of the ρ^0, for m_1, and of the $K^*(892)^0$, for m_2, mesons, according to which pair of final state particles is being considered.

In order to identify the squared amplitudes with the amplitudes of each partial wave (i) in the considered mass range, the mass terms are normalised according to:

$$\int_{m_l'}^{m_h'} \int_{m_l}^{m_h} |M_{m_1}^i M_{m_2}^i|^2 \Phi_4 \mathrm{d}m_1^2 \mathrm{d}m_2^2 = 1, \tag{1.39}$$

being m_h and m_l the high and low limits of the mass spectra ($m_l = 300, m_h = 1100$ MeV/c^2 for m_1 and $m'_l = 746, m'_h = 1196$ MeV/c^2 for m_2) and $M^k_{m_{1(2)}} \equiv M^k(m_{1(2)})$ where the index k runs over each of the considered resonances in the $m_{1(2)}$ spectrum.

Invariant mass propagators and phase space factor used in simulation

As it was already anticipated, simulated data samples are used in different steps of the analysis. Both the models and the values of the parameters used in these generations need to be known for some elements of the analysis. When exclusive decay modes are generated (and for the $B^0 \to \rho^0 K^{*0}$ in particular), the intermediate resonances are described with a slightly modified Breit-Wigner shape, as compared to what is given in Equation 1.18. Its expression, directly obtained from the EvtGen code, is:

$$BW^{MC}(m, L) = \frac{\sqrt{m\Gamma_L(m) \cdot m_0\Gamma_0}}{m^2 - m_0^2 - im_0\Gamma_L(m)}, \tag{1.40}$$

where $\Gamma_L(m)$ has the same definition as in Equation 1.19. The projections of these propagators evaluated for the ρ^0 and $K^*(892)^0$ resonances over simulated data (generator level simulation only) are shown in Figure 1.5, as validation.

Likewise, the description of the phase space density is different from the one in Equation 1.37 and it is given by the approximation in which one of the masses of the VV is fixed in each term:

$$\Phi_4^{MC}(m_{(\pi\pi)}, m_{(K\pi)}) \quad \propto \quad q(m_{B^0}, m_\rho, m_{(K\pi)}) \cdot q(m_{B^0}, m_{(\pi\pi)}, m_{K^*}), \tag{1.41}$$

where the dependency of $q(m_{ij})$ on the masses of the decay products (m_i and m_j, from Equation 1.38) has been included to make the approximation explicit.

It should be noted that Equation 1.41 is used to describe the phase space factor in simulation only when the resonances are generated (in particular, with the `SVV_HELAMP` model from EvtGen, as specified in Section 4.1). The same description as used for real data (Equation 1.37) is used otherwise. The input parameters for the Breit-Wigners used in the simulated data samples are shown in Table 1.5.

Table 1.5: Parameters used in the BW parametrisations of the ρ^0 and $K^*(892)^0$ resonances in the simulated data sample (values obtained from EvtGen documentation) together with the values of the B^0, π and K masses used in the phase space computation.

Variable	ρ^0	$K^*(892)^0$
m_0 [MeV/c^2]	775.3	895.81
Γ_0 [MeV/c^2]	149.1	47.4
d_R [MeV/$c^{2\ -1}$]	0.003	0.003
L	1	1
Particle masses [MeV/c^2]		
$m_B = 5279.61$ $m_\pi = 139.57018$ $m_K = 493.677$		

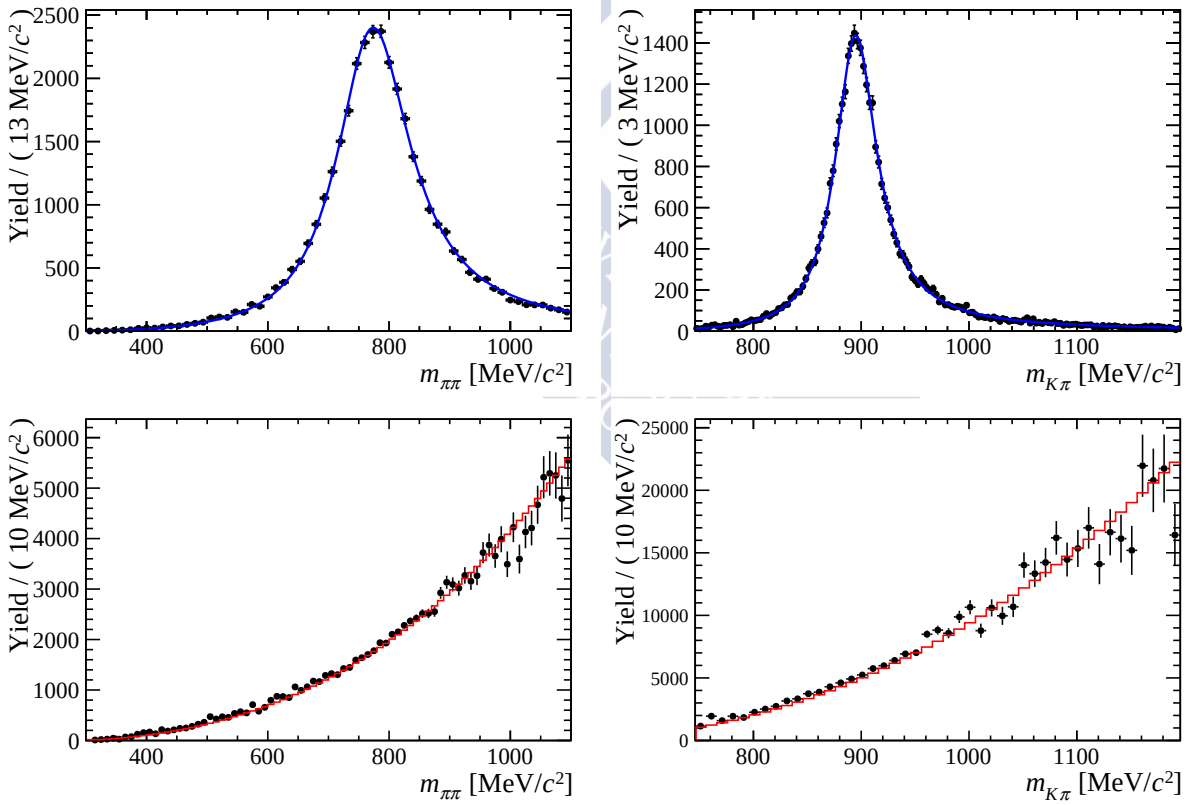

Figure 1.5: Projection of the full generation models ($BW^{MC}+\Phi^{MC}$) used in simulation for the ρ^0 and the $K^*(892)^0$ resonances (upper row) and of the phase-space component alone (Φ^{MC}) (lower row) over generator level data (EvtGen output). The model describing the simulated samples is shown with a solid blue (red) line over the data points.

1.3 Summary of the analysis strategy

The PDF that has been built in the previous sections describes the decay of a B^0 meson into the $(\pi^{\pm}\pi^{\mp})(K^{\pm}\pi^{\mp})$ final state. In order to also account for the charge conjugate decay, each amplitude has to be transformed accounting for its parity as $\overline{A}_i \to \eta_i A_i$, when describing the decay of a $\overline{B}^0$ meson. These correspond to $\eta = -1$ for the perpendicular amplitudes and $\eta = 1$ for the remaining contributions. The resulting B^0 and $\overline{B}^0$ models are fitted to two data sub-samples, split according to the sign of the electrical charge of the kaon in the final state, allowing to measure the contributing amplitudes (that were listed in Table 1.1) in each sub-sample, as indicated in Section 1.2.2.

The normalisation of the fitting PDF has to account for the acceptance of the LHCb detector. This effect is tackled using simulated events and will be discussed in detail in Section 3.4, but it can be anticipated that the acceptance of the signal events depends on their kinematic distributions. To account for this, the analysed data sample will be further split into four new categories: Year×Trigger. The first, refers to the data taking period, and is motivated by the different $\sqrt{s}$ between 2011 and 2012 data. The second, stands for the path the event followed in order to be selected by the different triggers. It accounts for the fact that only signal candidates that triggered themselves must satisfy a requirement in their transverse momentum. The final fits to the B^0 and $\overline{B}^0$ data samples are therefore performed simultaneously each on these 4 kinematic categories. In this work, they will be referred to as "fitting categories" and will be labelled following the naming schema Flavour||Year||Trigger (where only Year||Trigger appear, it should be understood that B^0 and $\overline{B}^0$ samples have been merged).

An statistical unfolding technique (described in Section 3.2) is used to obtain a background subtracted sample taking as input the four-body invariant mass distribution of the events fulfilling the selection requirements. The fit to the angular distributions and the two-body invariant masses (5D fit) is performed on this background subtracted data sample and, as anticipated, the acceptance effects are described using simulated events, following the method detailed in Section 3.4.

The *CP* averages and asymmetries of the contributing amplitudes, which were reported in Table 1.2, are obtained from the fit parameters (real and imaginary parts of each amplitude), accounting for correlations among parameters when estimating their uncertainties. These are further discussed in Section 5.1.5 and Section 5.2 for the statistical and systematic uncertainties, respectively.

Details from the first part of the analysis, corresponding to the selection of $B^0 \to (\pi^+\pi^-)(K^+\pi^-)$ candidates, are given in Chapter 4, while those on the amplitude analysis of the selected data sample are discussed in Chapter 5.

USC
UNIVERSIDADE
DE SANTIAGO
DE COMPOSTELA

2

The LHCb experiment at the LHC

The LHCb (Large Hadron Collider beauty) [42] experiment is an excellent facility to study $B-$physics hosted at the European laboratory for particle physics (CERN) [43]. LHCb was designed to study heavy flavour and BSM physics, searching for its indirect evidences in rare decays and *CP* violation effects. The excellent performance of the detector and the experience gained during its early operation allowed the LHCb collaboration to expand the physics case that was originally planned. As a consequence, rare kaon decays (strange physics), cross-section measurements in the forward region of electro-weak mediated processes or proton-ion and ion-ion collisions among others, have become relevant parts of the collaboration physics program.

2.1 The LHC

The Large Hadron Collider (LHC) is a two-ring superconducting proton-proton collider that has been designed to operate at the TeV scale in the centre-of-mass energy. Upon design, it was hoped that at these energies, direct observations of New Physics (NP) at mass-scales of ~ 1 TeV were likely to be made, addressing the hierarchy problem in the SM. Other than this, the possibilities for discovering the Higgs boson, performing high precision measurements in the B physics sector and studying a new phase of matter produced in heavy-ion collisions strongly influenced the design and experimental conditions during the first years of operation of the LHC.

The LHC, shown within the CERN accelerators complex in Figure 2.1, has been deployed in the 27 km tunnel that previously housed the LEP(*Large Electron Positron*)

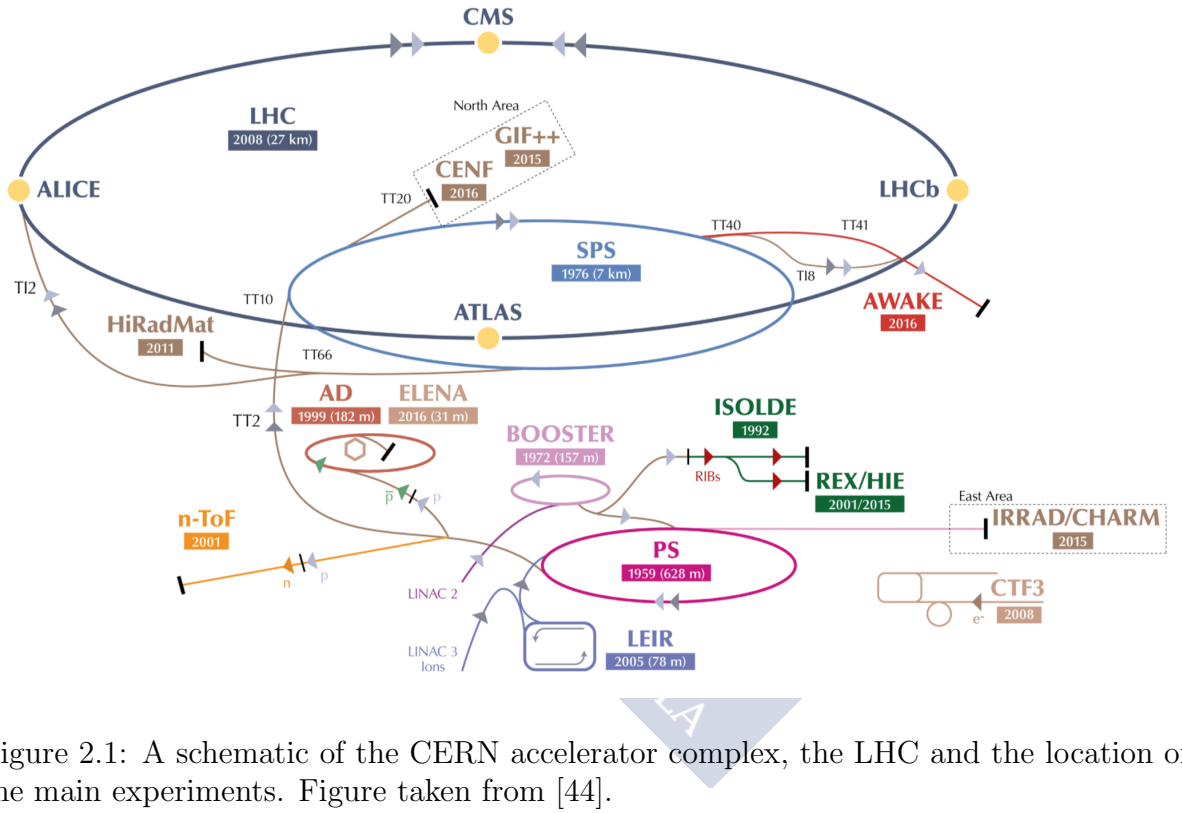

Figure 2.1: A schematic of the CERN accelerator complex, the LHC and the location of the main experiments. Figure taken from [44].

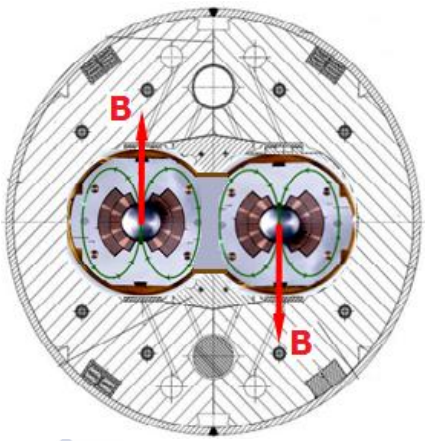

Figure 2.2: The niobium-titanium coils create the magnetic fields to guide the two counter-rotating proton beams in separate magnetic channels but within the same physical structure. The coils are surrounded by non-magnetic "collars" of austenitic steel, a material that combines the required properties of good thermal contraction and magnetic permeability. The collars hold the coils in place against the strong magnetic forces that arise when the coils are at full field. Figure taken from [46].

[45] collider. The accelerator has now completed two of its projected data-taking periods. These are characterised by different experimental conditions and are interleaved with scheduled technical stops, meant for the installation and test of the different upgrades, during which the accelerator is shut down.

The physics dedicated runs have been characterised by the accelerator delivering data at three different beam energies: $\sqrt{s} = 7$ TeV, for a short period in 2010 and during 2011, $\sqrt{s} = 8$ TeV in 2012 and $\sqrt{s} = 13$ TeV for the period from early 2015 to late 2018. The data analysed in this thesis were recorded during 2011 and 2012, which defines the so called Run I period.

Protons, obtained from ionised hydrogen, are injected into the LHC from the Super Proton Synchrotron (SPS) at an energy of 450 GeV. For the nominal operating conditions, Radio Frequency (RF) cavities accelerate the protons to 6.5 TeV and superconducting magnets, with a maximum field of 8.3 T, bend the protons within the orbit. Both LHC rings are incorporated into a single magnetic structure with two sets of coils in a common yoke and cryostat, which contains superfluid helium at a temperature of 1.9 K. Figure 2.2 shows the magnetic field profile inside the yoke. The beams are arranged into bunches separated by a minimum time-shift of 25 ns and cross at four interaction points, where the main LHC experiments are located. The bunch–crossing rate of 40 MHz imposes high demands on the speed of the detector elements and readout electronics for all experiments.

The four major LHC experiments, shown schematically in Figure 2.3, are ALICE [47], ATLAS [48], CMS [49] and LHCb [50]. Figure 2.1 shows the location of each experiment along the LHC ring. ATLAS (*A Toroidal LHC Apparatus*) and CMS (*Compact Muon*

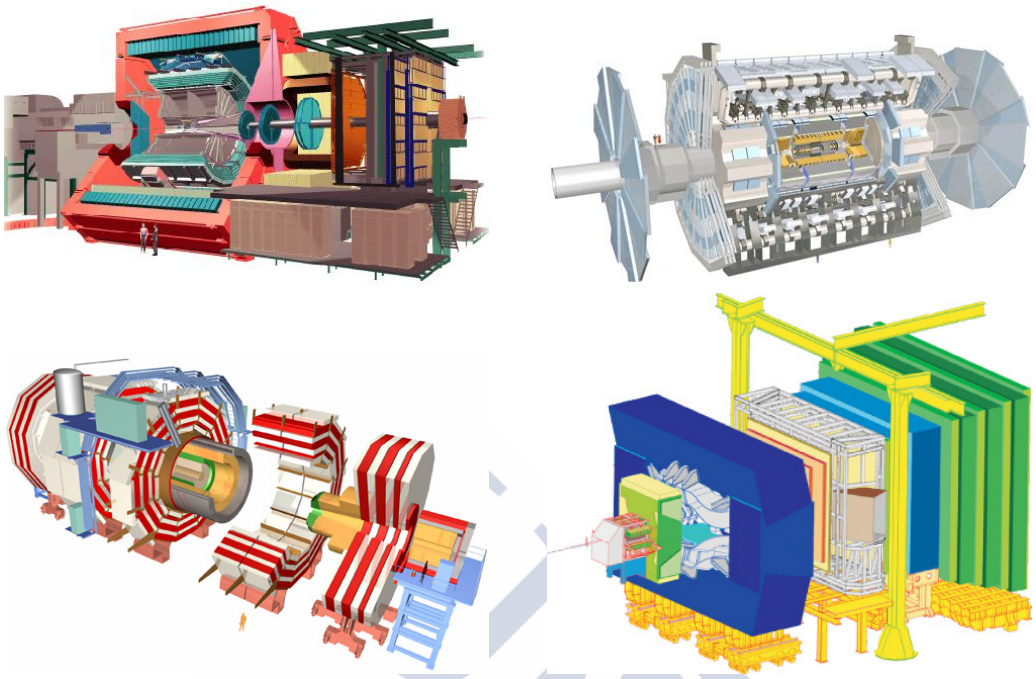

Figure 2.3: Schemas of the four main experiments at CERN (not to the same scale), taken from [43]. Top left ALICE, top right, ATLAS, bottom left, CMS and bottom right, LHCb.

Solenoid) are two general-purpose detectors (GPD), whose main physics goals are the profuse study of the recently discovered Higgs boson and the search for supersymmetric particles, among other research topics. The other two experiments mentioned above, ALICE (*A Large Ion Collider Experiment*) and LHCb (*Large Hadron Collider beauty*), have specific tasks and have been optimised accordingly. The former is focused on the study of strongly interacting matter at extreme energy densities produced by heavy-ion collisions, and aims to perform measurements of the phase transition between hadronic matter and the quark-gluon plasma. Hence, it has been designed to cope with the high particle multiplicities that are characteristic for heavy-ion collisions. As anticipated, LHCb was engineered to study B physics and will be characterised in more detail in the following section.

2.2 The LHCb detector

As already mentioned, the LHCb experiment focuses on $b$physics and it is located at CERN laboratory. This experiment re–uses the DELPHI (*Detector with Lepton, Photon and Hadron Identification*, one of the four main experiments at LEP) cavern at interaction point 8, which constrains the total length of the detector to $\sim$20 m. In the following paragraphs some general information and the detector layout will be introduced.

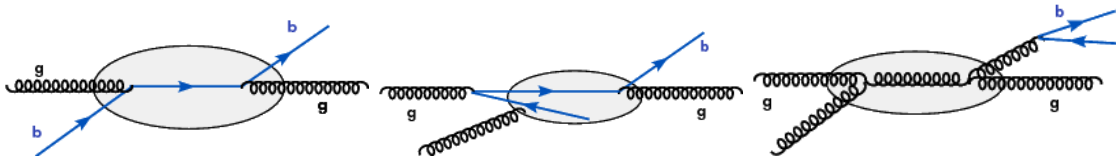

Figure 2.4: From left to right, the Feynman diagrams for: flavour creation, flavour excitation and gluon splitting processes.

In order to better understand the motivations for the relatively non-standard LHCb detector design, it is convenient to summarise how the physics processes that we aim to measure are originated. In proton–proton collisions, $b\bar{b}$ pairs are produced by three main mechanisms, see Figure 2.4, namely:

- Flavour creation ($2 \to 2$): a $b\bar{b}$ pair is produced by gluon fusion or by annihilation of light quarks.
- Flavour excitation ($2 \to 3$): this mechanism corresponds to the scattering of a b-quark (or $\bar{b}$-quark) out of the initial-state into the final-state by a gluon or by a light quark/anti-quark. With this configuration a large asymmetry in the transverse momentum of the two b-quarks is observed.
- Gluon splitting ($2 \to 3$): the $b\bar{b}$ pair is created within a parton shower or during the fragmentation process of a gluon or a light quark or antiquark. This process leads to small opening angles of the pair, and hence, small transverse momentum.

At LHC energies, the parton distribution functions of the proton are such that it is most favourable that partons with very different momenta interact, resulting in a major contribution from the $2 \to 3$ processes to the $b\bar{b}$ production yields. As a consequence, the two B hadrons from the $b\bar{b}$ pair produced in a pp collision are likely to fly in the same forward or backward cone (see Figure 2.5). The LHCb detector has been consequently designed as a single-arm forward spectrometer with an angular coverage from, approximately, 10 mrad to 300 (250) mrad in the bending (non-bending) plane, thus having a large acceptance for B events with a relatively small detection surface. The general detector layout can be seen in Figure 2.6.

In the LHCb detector and at nominal operation conditions, the mean flight distance of B hadrons before decay is expected to be (11.8 ± 0.2) mm. Consequently, a good vertex resolution allows to separate most B decay vertices from the production vertex. This feature is essential in the identification of background decays which typically originate directly in the primary pp collision. Other pp collisions within the same bunch crossing, also called underlying event, can significantly reduce the ability to identify the B decay vertex and its corresponding production vertex, especially when there are on average 27 collisions in the event of a bunch crossing. For this reason, the luminosity at the LHCb interaction point is limited, by defocusing the beams in the transverse plane, to

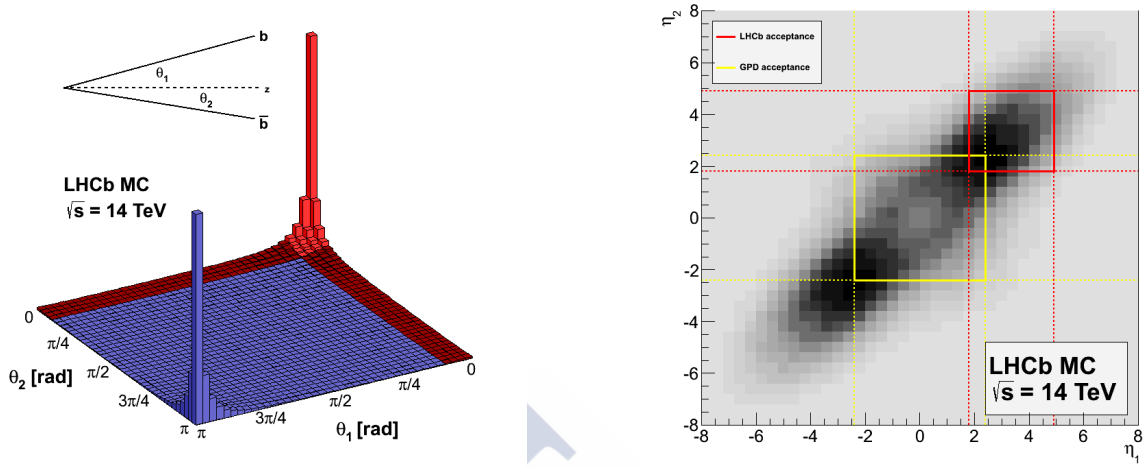

Figure 2.5: Left: angular distribution of b and $\bar{b}$ quarks in collisions at $\sqrt{s} = 7TeV$. Right: acceptances in the pseudorapidity plane for LHCb and the GPD.

$2 - 5 \cdot 10^{32} cm^{-2} s^{-1}$, smaller than the LHC nominal $10^{34} cm^{-2} s^{-1}$. Under these conditions, an average of 2 collisions per bunch crossing were produced during the Run I period. This has the positive consequence that the decrease in instantaneous luminosity caused by the beams degradation can be mitigated by tuning the defocusing of the beams. This process is called luminosity levelling and allows for having a constant luminosity through the whole run or, at least, until the defocusing potential is exhausted and the beams collide "heads on".

In the following sections each of the LHCb subdetectors are be presented. They can be categorised into tracking detectors and particle identification (PID) detectors. The Vertex Locator (VELO), placed short after the interaction point; the Tracker Turicensis (TT), before the magnet; and the T-Stations (T1,T2 and T3), after the magnet, are the major components of the tracking system. On the other hand, two Ring-Imaging Cherenkov (RICH) detectors, the electromagnetic and hadronic calorimeters and the muon chambers integrate the PID system. In addition, since it is impossible to save data from every collision, a trigger system is used to make a real time decision on whether to record or not the detector readout. The trigger combines information from several subdetectors to identify experimental signatures characteristic from signal events. For this purpose, it is subdivided into three independent levels, denoted as Level-0 (L0), Level-1, and High-Level Trigger (HLT).

The bending power of the magnet mentioned above is represented by the total integrated field, which is $\int \vec{B} \mathrm{d}\vec{l} = 4.2$ Tm. This dipole is composed by an iron yoke surrounded by two identical coils of conical saddle shape produced of pure Al-99.7. These coils are carved following the detector acceptance shape, which helps reducing the electrical power requirements while still providing the desired intensity of the magnetic field. Charged

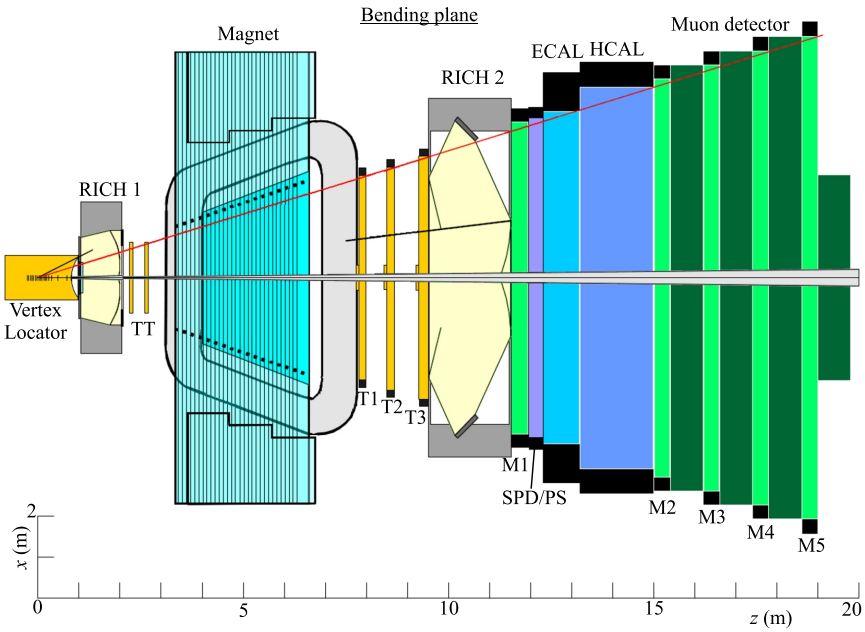

Figure 2.6: The LHCb setup [50] with the different subdetectors shown in the bending plane (xz) of the magnet.

particles are bent in the $\vec{B}$ field of this magnet enabling for the measurement of their momenta. The difference between the track slope in the VELO and the track slope in the T-stations is inversely proportional to the momentum of each particle. The non-uniformity of the magnetic field is mapped to a high accuracy and kept below $\pm 5\%$ in the detector acceptance region in order to obtain a momentum resolution better than 0.5% for particles with momentum around 200 GeV. It should be noted that the presence of this dipole magnet in the LHC ring affects the orbits of both circulating beams. These effects must be compensated to avoid the degradation of the beam conditions, which is the reason why three compensator magnets are placed in the surroundings of the detector. All four magnets are operated by the CERN Control Centre. Finally, it should be noted that in order to control the systematic effects arising from the detector performance, the polarity of the magnetic field is inverted periodically.

Many of the LHCb measurements are dominated by the size of the available data samples. This, along with the great performance of the detector and its potential to cope with more challenging operating conditions than those that was originally planned for, motivated the proposal for a major detector upgrade to be installed during the long shut down (LS2) that is currently ongoing. The objective is that from 2021 onwards, LHCb would be able to collect data at a rate corresponding to an integrated luminosity of 5 fb^{-1} per year, operating at instantaneous luminosity of 2 $\times 10^{33}\text{cm}^{-2}\text{s}^{-1}$. The implications of this upgrade for the different parts of the detector are briefly discussed in the corresponding sections.

Figure 2.7: Left: a lateral view of the VELO detector. Right: real picture of the VELO sensors.

2.2.1 Tracking detectors

VELO

The Vertex Locator (VELO) [51] is a silicon microstrip detector formed by 21 stations, placed along and perpendicular to the beam axis where there is negligible magnetic field. It is an all-silicon design capable to measure the decay lengths of B and D mesons to a precision of between 220 and 375 μm and locate the primary vertex to 10 μm in the transverse (xy) plane and 42 μm in the z direction. The resolution on the impact parameter of tracks to the primary vertex is about 20 μm [1]. In the finest pitched region of the VELO, the highest resolution is achieved, leading to a spatial cluster resolution of about 4 μm for 100 mrad tracks.

Each of the stations is composed by a pair of silicon sensors mounted back-to-back, these two sensors having different designs: one measures the r polar coordinate with circular strips centred around the beam axis, the other measures the ϕ coordinate with straight, radial strips. Figure 2.7 shows a lateral view of the detector and a picture of one of its modules. The radius of each module is about 42 mm, allowing to cover the pseudorapidity range $1.6 < \eta < 4.9$ for particles emerging from primary vertices in the range -10.6 cm$< z <$10.6 cm.

The sensitive area of the sensors starts 8.2 mm away from the beam axis, such that the first measurement of the track is as close to the primary vertex as possible. The shorter is the extrapolation of a track from its first measurement to the interaction region, the smaller is the uncertainty on the reconstructed position of the vertex. This distance is smaller than the beam aperture required by the LHC machine during injection, hence, in order to avoid the beam being steered into the vertex detector and the consequent radiation damage, the two VELO halves are retractable. Therefore, the whole subdetector is installed on a mechanical structure that allows the two halves to be shifted away from the beam in the horizontal direction during filling and beam tuning periods.

To protect the integrity of the primary LHC vacuum system, the sensors are separated

[1] The coordinate axes are defined in Figure 2.6

from the beam volume by a 0.3 mm aluminium shield (known as RF-foil). This foil also provides with mechanical support and suppresses side effects on the sensors caused by the beam current (and vice-versa), as it allows a mirror current to travel parallel with the beam. Unfortunately, the presence of the RF-foil implies that extra material is present for particles produced in the pp interaction point to scatter before reaching the sensors. This obviously degrades the accuracy with which their production vertex can be determined and also places the most important constraints in terms of material budget for the design of the RF-foil.

A new VELO [52] was designed in order to cope with the higher luminosity conditions after the general LHC upgrade scheduled for the long technical stop that is currently ongoing. The upgraded LHCb VELO silicon vertex detector is a lightweight hybrid pixel detector containing 41 million of 55 $\mu m \times 55 \mu m$ pixels and capable of 40 MHz readout at a luminosity of $2 \cdot 10^{33} \mathrm{cm}^{-2}\mathrm{s}^{-1}$. The track reconstruction speed and precision are enhanced relative to the current VELO detector even at the high occupancy conditions of the upgrade. This improvement relies on the pixel geometry and a closest distance of approach to the LHC beams of just 5.1 mm for the first sensitive pixel.

Tracker Turicensis and T-Stations

The Tracker Turicensis (TT) tracking station is the most downstream of these subdetectors before the magnet in the LHCb detector. Beyond the magnet are the inner and outer trackers (OT) [53], together known as the Tracking Stations (T-stations) [54]. Three layers of these T-stations, labelled as T1, T2 and T3 in Figure 2.6, together with the TT, provide the main momentum measurement for tracks in LHCb. The TT is roughly 150 cm wide and 130 cm high and covers the full acceptance of the experiment. The IT covers a 120 cm wide and 40 cm high cross shaped region in the centre of the three tracking stations. Figure 2.8 shows the detailed geometry of these detectors. As for the OT, the total active area of a station is $6{\times}5$ m^2. In terms of angular aperture, the inner and outer trackers collectively cover an acceptance of 300 mrad in x and 250 mrad in y.

Since the TT and the three inner tracker modules share the same silicon microstrips technology, both are typically grouped in what is called the Silicon Tracker (ST). The four ST stations use planar 500 μm silicon microstrip sensors with a strip pitch of about 200 μm (giving a single hit resolution of 50 μm). The OT is a drift-time detector using as counting gas a mixture of Argon (70%) and CO_2 (30%), with which a drift time below 50 ns and a drift-coordinate resolution of 200 μm is achieved. In order to get a 3D reconstruction, the first and the last T-stations are instrumented with vertical strips while the second (third) has its strips rotated by an stereo angle of $5°(-5°)$.

These subdetectors have currently ended their operation time. More stringent radiation hardness requirements and the need for a faster read-out are the main reasons motivating their replacement for the operation after the spectrometer upgrade. The TT will be replaced with the Upstream Tracker (UT), using single-sided silicon strip sensors providing high granularity to cope with the higher occupancy that will characterise the

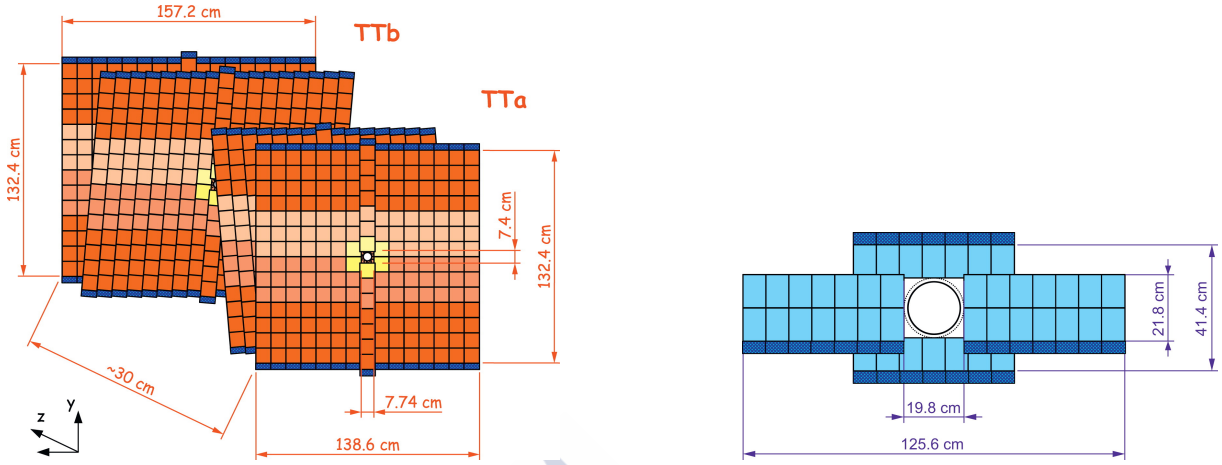

Figure 2.8: Layout of the TT (left), where the different colours indicate different types of readout sectors and a single layer of the IT (right), where the light blue area corresponds to individual sensors. In both figures dark blue coloured regions correspond to the readout electronics. Figures taken from [54].

experimental conditions. On the other side, the outer and inner tracker stations will be replaced with the Scintillating Fibre Tracker (SciFi), composed of 2.5 m long fibres read out by silicon photo-multipliers (SiPMs) outside the acceptance. More information on the upgrade of both detectors can be found in [55].

2.2.2 Particle identification detectors

A very important fraction of the LHCb physics analyses involve the study of exclusive decay channels. In order to be able to distinguish among kinetically and topologically similar decays, excellent PID performance is required. This is achieved by combining information from the systems described in the following sections.

RICH detectors

These detectors [56] identify particles by making use of the Cherenkov radiation emitted by relativistic charged particles passing through a medium with a velocity greater than the speed of light in that medium, see Figure 2.9. Photons propagate with an opening angle dependent on the particle velocity (v) and the refractive index (n) of the radiator according to $\cos\theta_c = c/vn$, provided $c/vn < 1$. Measuring this velocity and using the momentum of the reconstructed track, the mass, and thus the particle type, can be hypothesized.

LHCb uses two RICH detectors, aiming at different momentum ranges. The upstream detector, RICH1, using C_4F_{10} gas as radiator, covers the low momentum charged particle range $\sim 1 - 60$ GeV/c while the downstream detector, RICH2 (CF_4), covers the high

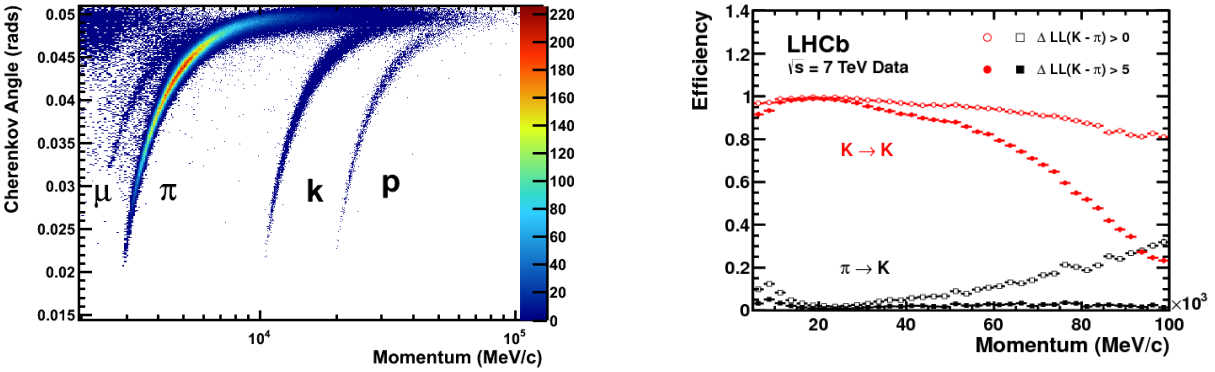

Figure 2.9: RICH detector performances (figures taken from [56]): (left) reconstructed Cherenkov angle as a function of track momentum in the C_4F_{10} radiator and (right) kaon identification efficiency and pion misidentification rate measured on data as a function of track momentum.

momentum range from $\sim$ 15 GeV/c up to and beyond 100 GeV/c. Their angular acceptances are 250 mrad and 120 mrad, respectively. In both RICH detectors the focusing of Cherenkov light is accomplished using a combination of spherical and flat mirrors to reflect the image out of the spectrometer acceptance. These photons are then detected by Hybrid Photon Detectors (HPD), which are protected from the dipole field by magnetic shielding, in the wavelength range 200−600 nm. The replacement of these HPDs by Multi-anode Photomultiplier Tubes (MaPMTs) represents the major change for the upgrade of these two detectors [57]. In addition, the radius of curvature of the primary mirror in the RICH1 will also be changed from the current 2710 mm to 3650 mm in order to prevent degradation of the PID performance associated to the higher occupancy of the detector.

Calorimetry

The calorimeter system performs several vital functions: rapidly renders the transverse energy estimates in the initial stages of the trigger for every event, provides positional information for electrons, photons and hadrons and gives positive particle identification of electrons, neutral pions and photons.

At LHCb there are two main calorimeters [58]: the electromagnetic calorimeter (ECAL) measures the energy of electrons and photons, while the hadronic calorimeter (HCAL) is dedicated to long-lived hadrons. Each is broadly based on a similar principle of detecting scintillation light from traversing charged particles and transmitting photons through wavelength-shifting fibres to a photo-multiplier tube. In order to accurately distinguish electrons over the wide $\pi^{\pm}$ and π^0 background, two other calorimeter systems, the Preshower Detector (PS) and Scintillator Pad Detector (SPD) are placed in front of the ECAL.

The most downstream scintillator (the PS) distinguishes incident charged particles from neutrals; its inclusion is motivated by the requirement for electron identification in the trigger where track information is initially unavailable. Next, a 15 mm lead sheet causes single electrons and photons to preferentially shower, while charged pions are highly likely to pass through since they have a much longer interaction length. Finally, the second row of scintillators (the SPD) detects the electromagnetic showers, again through scintillation light. Combining information from the ECAL, PS and SPD allows electron identification at the first level of the trigger (L0). This involvement of the calorimetry system in the trigger of the experiment will be the most affected by the detector upgrade, as all readout electronics will have to be replaced following the removal of the L0 stage. Furthermore, the PS and SPD will no longer be needed, as their main purpose was to provide this hardware trigger response. The granularity of both ECAL and HCAL was found to be satisfactory even for the detector operation at the increased instantaneous luminosity and therefore the calorimeter modules will be kept.

Muon system

The muon system is used both in the L0 trigger, to select muons with a high transverse momentum, and in the offline reconstruction, to identify muons. These detectors [59] are instrumented with multiwire proportional chambers (MWPC's), which fulfil both the requirement from the trigger to collect the signal within 20 ns and the requirement for radiation hardness.

This system is composed of five stations: the first one, M1, is placed before the calorimeter system, while the other four stations, M2–M5, are located directly behind the HCAL and are separated by 80 cm thick iron plates, this shielding acting as absorber for the hadronic background. An additional iron shield protects M5 against particles emerging from the opposite LHC beam. The inner and outer angular acceptances of the muon system are 20 (16) mrad and 306 (258) mrad in the bending (non-bending) plane, similar to those of the tracking system. Muons crossing all five stations must have a momentum greater than 6 GeV/c.

The most relevant changes for this detector after the upgrade comprise the removal of the first station, M1, and the installation of new Off Detector Electronics boards, faster and much more radiation tolerant read-out electronics, that will replace the current scheme.

2.2.3 The Trigger system

As mentioned before, events cannot be recorded to permanent storage at the 40 MHz bunch crossing rate, therefore a trigger system [60] is developed to reduce the collected amount of data retaining as much interesting b hadron decays as possible. The main strategy of the trigger is to identify the two signatures of B meson decays: the large B mass produces decay products with a high transverse momentum, and the long B lifetime

produces tracks with a high impact parameter with respect to the primary interaction vertex.

At LHCb, events are selected (triggered) in successive stages (levels) which process an increasing amount of information from the subdetectors. The first level, namely L0, is a hardware trigger, implemented using custom made electronics to reduce the input rate to a maximum of 1 MHz. At this rate, the whole detector can be read out. The second trigger level (High Level Trigger, HLT) is a C++ application running on an Event Filter Farm (EFF) composed of several thousands of multi-CPU nodes. It reduces the L0 output rate to a maximum rate of about 3 kHz. The HLT selected events are then saved on permanent storage. The HLT is divided into two parts: HLT1 and HLT2. HLT1 reduces the input rate to about 40 kHz using a partial reconstruction of data to optimise computing time. At the HLT2 level, events are reconstructed and selected by a set of inclusive and exclusive algorithms. The reconstruction performed in HLT2 is as similar as possible to the one performed offline, with the limitations originating from computing time requirements. At this level of reconstruction, the trigger signals are associated with reconstructed particles, whose decay chain may be inferred. This way, the events causing the trigger response can be categorised according to whether the decision was due to the signal candidate (Triggered On Signal, `TOS`), other particles produced in the *pp* collision (Triggered Independent of Signal, `TIS`), or a combination of both. Because no trigger requirements are imposed in the `TIS` samples their kinematic distributions will be less biased and their acceptance rate will also differ from that of the `TOS` events.

When operating at the higher luminosities foreseen for the next LHC runs, the L0 trigger rate from the calorimeters would saturate the 1 MHz bandwidth imposed by the rest of the trigger system. A possible solution would be to increase its firing threshold, but, although this would maintain an acceptable efficiency for the dimuon events, the efficiency on fully hadronic decays would decrease below an acceptable rate. Instead, it was decided to remove the L0 trigger stage and process all events with an HLT farm. Parts of this scheme were already implemented for Run II, where the selected events by L0 were buffered to the HLT farm for the detector calibration and alignment to be performed before further stages of the trigger were executed (therefore HLT and L0 ran asynchronously). As anticipated in the previous sections, this requires the front end electronics of all the systems involved in the trigger to be capable of working at full LHC non-empty bunch crossing rate.

2.3 Generation of simulated samples in LHCb

Simulated data samples are widely used in HEP data analysis. Many important analysis steps such as the description of the detector acceptance effects, the optimisation and characterisation of the signal selection process or the description of the backgrounds usually rely on simulated data. Knowing beforehand which is the nature of the processes under study represents an obvious advantage when trying to understand the features

observed in real data. To achieve this, the LHCb collaboration has designed a simulation framework [61] called Gauss, which manages the creation of simulated events by interfacing to multiple external applications. The general workflow for event simulation is:

1. The desired particle is generated by the so-called production tool. In the case of the B^0 or B_s^0 meson decays, this is done by the Pythia [62, 63] generator, with a customised configuration [64] for LHCb. Generated events may be categorised in minimum bias (all elastic, diffractive or inelastic events are kept), inclusive (at least one b hadron is produced within the detector acceptance) or exclusive (a specific particle is generated within acceptance).

2. EvtGen [65] is used to decay the particle generated in the previous step. In case of an exclusive production, the desired chain is imposed for the signal particle. All remaining unstable particles are decayed independently. The Photos [66] package is interleaved with EvtGen to account for final-state radiation in the simulated samples.

3. At this step, generator level requirements may be imposed on any of the particles from the decay chain. This is particularly relevant when optimising CPU and disk usage and dealing with rare processes or when trying to accumulate statistics in a given phase space region. In case the signal candidate flies in the negative z direction, the event is mirrored to optimise the use of available CPU resources.

4. The produced particles are then transported through the detector simulation. The interaction of the generated particles with the detector, and its response, are implemented using the Geant4 toolkit [67] as described in Ref. [68].

The output of this process is digitalised and saved in a format as close as possible to which is used to store the real data. Therefore, starting from the trigger, a common process chain in the consequent steps can be used for both simulated and real data. This is illustrated in the flow chart shown in Figure 2.10. The so-called *stripping* process is rather specific to the LHCb framework. In this step, data are filtered further through a set of selections and the output files are grouped into streams, which share similar requirements. Analysts have only access to the output of the stripping step, which, on the one side is a safety measurement as it prevents any accidental access to raw data and on the other, optimises computing time as the data relevant for one analysis is usually fully contained within a single stream.

It should be remarked that the decay dynamics is fully implemented in the EvtGen by using different models. These control the kinematic distributions of the final state particles by using different decay models. For instance, the two-body invariant masses of a $B^0 \to (\pi^+\pi^-)(K^+\pi^-)$ sample would be generated according to their phase space density, while the corresponding distributions for $B^0 \to \rho^0(\to \pi^+\pi^-)K^*(K^+\pi^-)$ must reproduce the characteristics of the intermediate resonances.

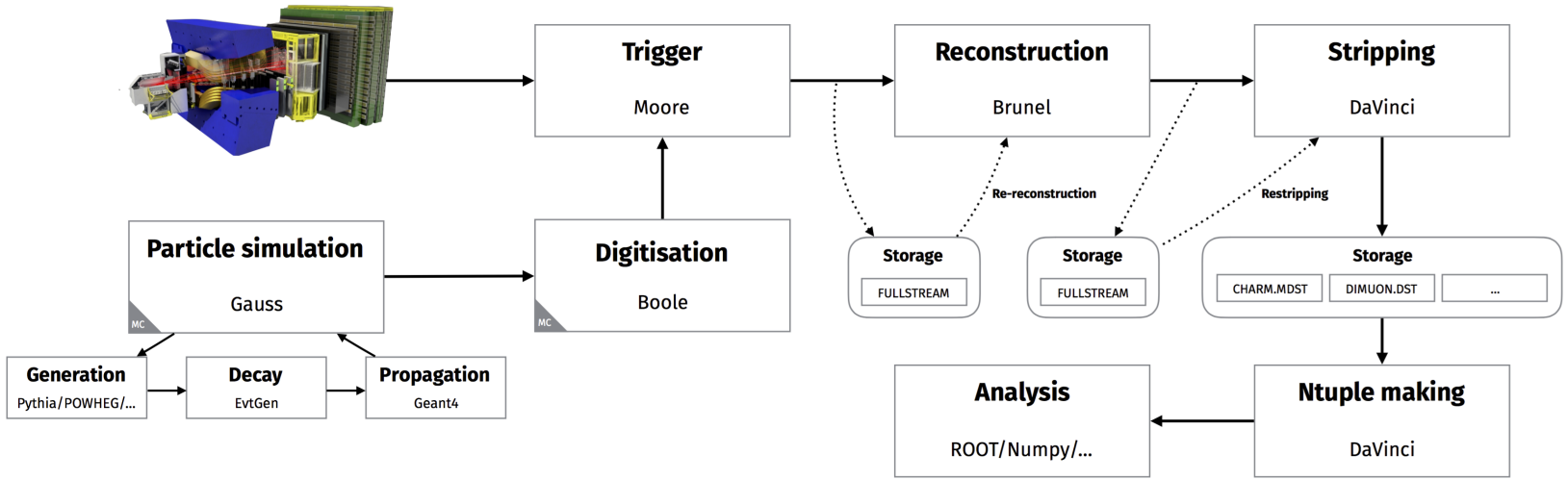

Figure 2.10: Schema of the LHCb data flow, shared for real and simulated data from the trigger step onwards. Figure from the LHCb Starterkit documentation.

USC
UNIVERSIDADE
DE SANTIAGO
DE COMPOSTELA

3

Tools and analysis techniques

In this chapter the stand-alone tools and analysis techniques that were used at different steps of this work are briefly introduced. Some of these tools were developed as part of the LHCb simulation project and some are available under Creative Commons Attribution Licenses or other open access sources.

3.1 Boosted decision trees

One of the multiple applications of machine learning techniques in HEP consists in the characterisation of multidimensional distributions. In particular, the decision tree method [69] uses variables that behave differently for signal and background. Not only the distribution of each variable but also the different correlations among them in each sample, are used to train the discriminator to distinguish between signal and background candidates. This training is achieved by recursively splitting the initial (signal+background) sample according to different requirements on each input variable. The goal in each splitting (tree node) is to maximise the separation power between events labelled as signal or background, respectively. Iterating this procedure, events will follow different paths (branches) passing through several nodes until each sample reaches the minimum allowed size or until it contains only one type of events. These final sub-samples are called the tree leafs. Each leaf receives a score (and a signal/background label) depending on its composition: below 1 if there are more background than signal events and larger than 1 otherwise. Figure 3.1 shows a scheme of this process.

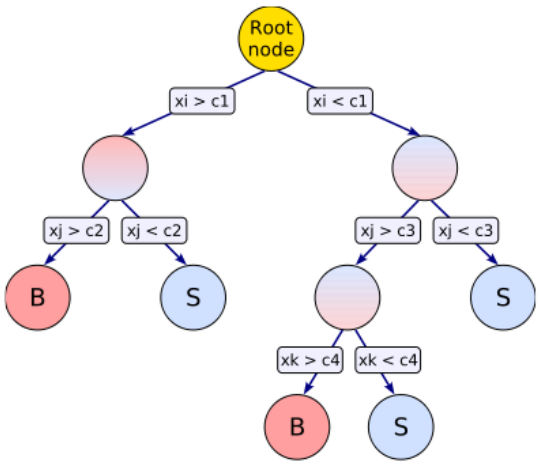

Figure 3.1: Decision tree flow schema, taken from *TMVA Users Guide v4.0.3*.

A trained tree can be tested by making events from alternative signal and background samples (different from those used in the training) pass through it and studying if they land on leafs correctly labelled as either signal or background, according to which sample the event originally belonged to. Such tests show that the output of the decision tree is highly dependent on the training sample composition. Therefore, a small change in the training samples could potentially lead to very different tree structures (nodes, branches and leafs) and performances. This instability is avoided by the use of the boosting method [70]: the composition of the tree leafs is studied and signal (background) events landing on leafs labelled as signal (background) are given a weight of 1 (-1). Misplaced events (belonging to the initial signal sample but landing on background leafs, or vice versa) get increased (boosted) weights. A second tree is then trained with the new set of weights. This procedure can be iterated many (order of hundreds) times to obtain a final per event weight (the renormalised sum of all the scores obtained by an event) that varies from -1 (certain background origin) to 1 (certain signal) according to the most likely event classification. The resulting classifier is referred to as Boosted Decision Tree (BDT).

Once the boosting is performed, an overtraining test needs to be done. This phenomenon occurs, in general, when a machine learning problem has too few degrees of freedom, because too many model parameters of an algorithm were adjusted to too few data points. The usual test consists in running the trained trees over some control samples ("unknown" simulated or data samples) and compare their classifier scores to those obtained in the original sample.

The multivariate analysis used for the work presented in this thesis was implemented using the ROOT package Toolkit for Multivariate Data Analysis (TMVA) [71] which serves as an interface to the BDT algorithm. This is used to reduce the background component arising from the random combinations of four tracks that fulfil the selection criteria, as explained in Section 4.2.

3.2 *sPlot*: statistical unfolding

This technique [72] allows the user to perform a statistical unfolding of a data sample effectively identifying the different species of events present in the sample. The method is embedded in `RooFit`, so the usual syntax and interfaces from this framework apply.

An amplitude analysis such and the one presented in this thesis serves as an example of use-case for this technique: the goal of the analysis is to perform a multidimensional fit on a set of observables ($\vec{x}$) for which the background distributions are unknown. On the contrary, there is a different set of observables ($\vec{y}$), uncorrelated with $\vec{x}$, for which both signal and background distributions are well established. The former are referred to as control variables ($\vec{x}$), while the latter represent the discriminating variables ($\vec{y}$). The *sPlot* technique allows the shapes of the background components on the control variables to be inferred by making use of their known shapes in the discriminant variables. In order to achieve this, per-event weights, usually in the -1 to 1 range, are assigned to the data sample. These weights, commonly referred to as *sWeights*, follow a distribution such that the negatively weighted events effectively cancel the positively weighted for all components in the data sample, except for the one labelled as signal.

For the analysis presented in this thesis, a single variable provides the discriminating power for the different event species present in the data sample. This is the invariant mass of the B meson candidate resulting from the combination of the four final state particles. As shown in Section 4.3.2, this observable is not correlated with the variables used in the amplitude analysis.

3.3 Strategy for the combination of two simulated data samples

There are diverse reasons to combine simulated data samples, the increase of the available sample size likely being the most common. This operation might be reduced to a plain aggregation in the case that uniform distributions were produced, but it requires a more careful treatment if different models were used at the generation level. In such cases, the total generation efficiencies and the total number of generated (not reconstructed) events need to be combined with the appropriately normalised generation models in order to consistently combine the samples.

For the analysis presented in this thesis, two simulated data samples with different EvtGen generation models are combined in order to simultaneously achieve a satisfactory coverage of the considered phase-space, also accumulating simulated events in the areas of interest, populated by the vector-vector candidates. The first EvtGen model describes the phase-space density alone and is referred to as `PHSP`. The second model, forces the decay of the B^0 meson via the $B^0 \to \rho^0 K^{*0}$ resonant channel (labelled as VV, after the vector-vector phenomenology).

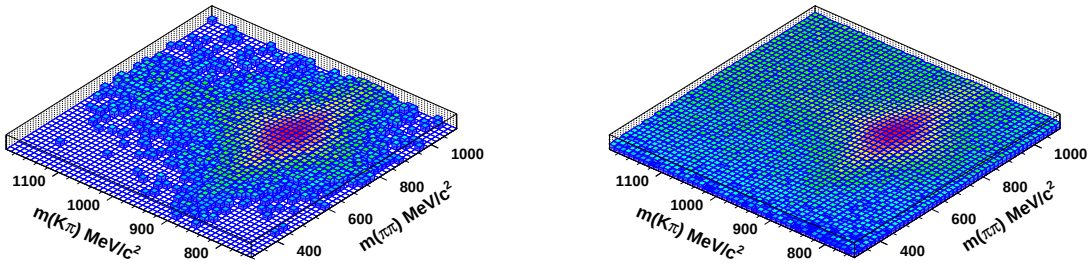

Figure 3.2: 2D histogram of the $m_{(\pi\pi)} \times m_{(K\pi)}$ plane, for theVV sample alone (left) and when combined with the pure phase-space density sample (right).

Defining N^{PHSP} and N^{VV} as the generation yields from each simulated sample and being $\texttt{PDF}^{PHSP}$ and $\texttt{PDF}^{VV}$ the corresponding generation models, the combined PDF is obtained from the weighted combination:

$$\texttt{PDF}^{Comb} = \frac{N^{PHSP}}{N^{PHSP}+N^{VV}} \times \texttt{PDF}^{PHSP} + \frac{N^{VV}}{N^{PHSP}+N^{VV}} \times \texttt{PDF}^{VV}. \tag{3.1}$$

This $\texttt{PDF}^{Comb}$ is used to describe the simulated sample resulting from the combination of Truth-matched events (via PID_TRUE) from the SVV_HELAMP and PHSP simulated samples described in Section 4.1. As shown in Figure 3.2, when compared with the exclusive VV sample, a much better coverage of the edges at the $m_{(\pi\pi)} \times m_{(K\pi)}$ plane is achieved by using this combined sample.

3.4 Normalisation weights

This technique [73] exploits that the acceptance is independent from the physical parameters (λ_j) appearing in the fitting model. Thus, since the fit procedure minimises the logarithm of the likelihood function, the following factorisation is possible:

$$\begin{aligned} \sum_{j=1}^{n} \frac{\partial}{\partial\lambda_j} \ln\mathcal{L} = \sum_{j=1}^{n} \frac{\partial}{\partial\lambda_j} \sum_{e} \ln \frac{\mathcal{P}(X_e;\lambda_i)\varepsilon(X_e)}{\int \mathcal{P}(X;\lambda_i)\varepsilon(X)d^5X} = \\ \sum_{j=1}^{n} \frac{\partial}{\partial\lambda_j} \sum_{e} \ln \frac{\mathcal{P}(X_e;\lambda_i)}{\int \mathcal{P}(X;\lambda_i)\varepsilon(X)d^5X} = 0, \end{aligned} \tag{3.2}$$

since $\sum_{j=1}^{n} \frac{\partial}{\partial\lambda_j} \log(\varepsilon(X)) = 0$. In Equation 3.2, λ_j is a set of n physical parameters the probability density function ($\mathcal{P}(X;\lambda)$) depends on, X stands for the kinematic variables $(\theta_1, \theta_2, \phi, m_1, m_2)$ used in the analysis, $\mathcal{L}$ is the likelihood function and $\varepsilon(X)$ represents the unknown acceptance function.

In Equation 3.2, only the integral in the denominator depends on the acceptance effects. This integral corresponds to

$$\int \mathcal{P}(X;\lambda_i)\varepsilon(X)d^5X = \int \Phi_4 \sum_{i=1}^{n}\sum_{j=1}^{i}(A_i \cdot g_i \cdot M_i)(A_j \cdot g_j \cdot M_j)^*\varepsilon(X)d^5X. \tag{3.3}$$

This expression can be rewritten as follows:

$$\int \Phi_4 \sum_{i=1}^{14}\sum_{j=1}^{i}(A_i \cdot g_i \cdot M_i)(A_j \cdot g_j \cdot M_j)^*\varepsilon(X)d^5X = \sum_{i=1}^{14}\sum_{j=1}^{i} A_i A_j^* w_{ij}, \tag{3.4}$$

where the normalisation weights, w_{ij}, have been introduced.

The w_{ij} integrals account for the acceptance effects and can be calculated with a simulated data sample, as long as the generation `PDF` is known. This is the case of a simulated data sample.

3.5 Analysing the output from MultiNest

The `pyMultiNest` [74] package implements the MultiNest algorithm [75–77]. This is a multimodal nested sampling algorithm which allows to perform fits to data distributions without relying on the smoothness of the likelihood function. By doing so, this fitting approach solves the known problems that arise when performing a weighted maximum likelihood fit, such as the one needed for the analysis presented in this thesis. The MultiNest algorithm is fully parallelised but, more importantly, presents two very convenient qualities for the analysis at hand:

- It has been optimised to perform well in distributions with an unknown number of modes (were each mode could be a local minimum of the likelihood function).
- It is robust against pronounced degeneracies between parameters.

In order to find the minimum of the likelihood function, a decision has to be made on where to evaluate the function at each iteration such that $\mathcal{L}_i > \mathcal{L}_{i-1}$. The algorithm uses a set of active points, meaning that this is the subset of points at which the likelihood is being evaluated for the *i-th* iteration. At each step, the covariance matrix of the active points is used to build a D-dimensional ellipsoid. New points are drawn within the bounds of this ellipsoid, always requiring that the condition $\mathcal{L}_i > \mathcal{L}_{i-1}$ is fulfilled. The MultiNest algorithm is prepared to deal with several overlapping ellipsoids at the same time, therefore, overtaking the efficiency of its predecessors when dealing with multimodal distributions. The power of the algorithm consists in achieving a high acceptance rate for the trial points when iterating the aforementioned process.

As usual in sampling algorithms, the output produced by MultiNest can be treated as a table with columns that contain the sample probability, the $-2\log(\mathcal{L})$ value for a set

of parameter values and each of these parameter values (a total of $2+N_{params}$ columns). One of the output files produced by `pyMultiNest` is a text file containing such table. The sample probability is defined such that the following expressions hold when summing over all the rows (i) in the aforementioned table. For a variable X which takes the values x_i with sample probabilities p_i:

$$\mu_X = \sum_i^n p_i \cdot x_i, \qquad Var(X) \equiv \sigma_X^2 = \left(\sum_i^n p_i \cdot x_i^2\right) - \mu_X^2. \tag{3.5}$$

Therefore, the covariance (Σ) and correlation (C) matrices are obtained from their standard definitions:

$$\Sigma_{XY} = cov(X,Y) = E(X \cdot Y) - \mu_X \cdot \mu_Y = \sum_i^n \sum_{j>i}^n p_i \cdot x_i \cdot y_j - \mu_X \mu_Y, \tag{3.6}$$

$$C_{XY} = \frac{cov(X,Y)}{\sigma_X \cdot \sigma_Y}. \tag{3.7}$$

It should be noted that, if directly accessing the MultiNest output with its default configuration, a Bayesian interpretation of the fit results would be obtained. The `Ipanema` [78] framework implements flat distributions for the priors of all parameters, which ensures, as proven by the Bayes theorem, that the Maximum A Posteriori (MAP) coincides with the Maximum Likelihood Estimate (MLE) that would be obtained performing a frequentist analysis.

The application `Superplot` [79] provides the user with a convenient tool for making one and two dimensional projections of the likelihood function, as well as with an interface for an easy interpretation of the text files produced by `pyMultiNest`.

3.6 The PIDCalib package

As introduced in Section 2.2.2, the PID information is obtained by combining many sub-detector responses. In most of the cases these may depend on the detector occupancy, which varies from event to event, on the kinematics of the considered particles and on many experimental conditions (the beam parameters, the gas pressure inside the RICH or the physical alignment of all the involved systems, for instance), which may differ among data-taking runs. Accounting for all these effects in simulation would be extremely complicated and not always possible, therefore, the LHCb collaboration has decided to use data-driven methods to characterise these PID variables. To do so, decays with very clean signatures are used to obtain calibration samples of different stable charged particles. These samples are considered PID-unbiased as the PID information itself is not required for the identification or the particles involved. The PID efficiency is assumed to depend and to be fully determined by some set of variables, in particular, track momentum

and transverse momentum, pseudorapidity and the event multiplicity. The tracks in the calibration samples are used to build efficiency maps in different bins of these variables, the precise set of which as well as the granularity of the map is analysis dependent. The *Particle IDentification and Calibration* (PIDCalib) [80] software package provides the user with the necessary set of tools and calibration samples to build these maps, allowing for the correct estimation of the efficiencies of the PID selection requirements applied to the analysed data samples. Within the work presented in this thesis, the PIDCalib package is used to correct for differences between real and simulated data samples before pursuing the description of the detector acceptance with the latter.

3.7 Gradient Boost Reweighter

As commented in Section 3.1, the BDT technique may be used as classifier, this is, the goal would be to identify the features that make two samples different and then classify events according to their probability of belonging to one or another sample. The same machinery can be used to achieve a regression-like behaviour, where the output weights are computed such that one of the distributions (original) reproduces the features of the other (target). If treating with one dimensional distributions, the relevant set of weights can be obtained by simply dividing the original by the target histograms. However, if the analysed sample has more dimensions, the correlations among variables need to be accounted for, since achieving a good agreement between both distributions in several 1D projections does not ensure compatible multidimensional distributions, as illustrated by Figure 3.3.

The `GBReweighter` [81] method is available in the `hep_ml` software package and provides the user with a convenient implementation of the algorithm for its use with the regression-like behaviour.

Differences between data and simulation can be corrected for using the methods implemented with the `GBReweighter`. For this, *sWeighted* data are used as target distribution and official LHCb simulation productions, as original. The distributions of a set of variables are studied in both samples and this information is then used by `GBReweighter` to produce the correction weights that will be applied to the simulated samples. As detailed in Section 5.2.6, for the analysis presented in this thesis, this method is used to improve the description in the simulation of the event multiplicity and the momentum of the B-meson candidate.

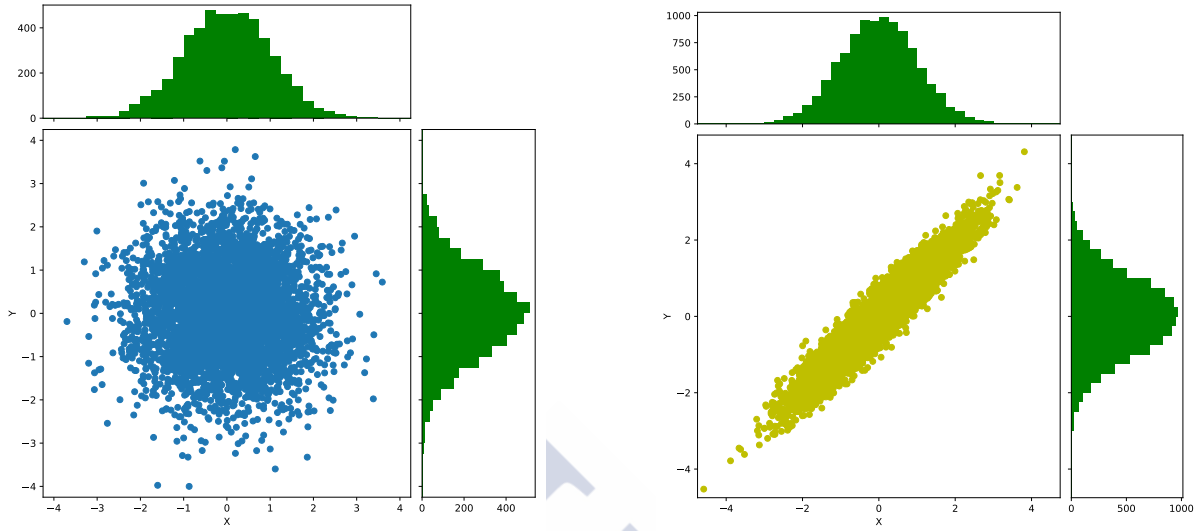

Figure 3.3: Illustration of two different distributions (uncorrelated and correlated 2D Gaussian) that share identical 1D projections.

3.8 Generate a random multidimensional distribution of correlated numbers

The generation of correlated random numbers with a multi-dimensional Gaussian distribution (defined by the collection of means, μ_j, and the covariance matrix, C_{ij}, for i dimensions) may be computed using linear algebra with matrices or, directly, with the `multivariate_normal` method available in `NumPy` [82].

If implemented using matrices, for each μ_j, its uncorrelated uncertainty can be identified with the square root of the corresponding eigenvalue (λ_i) in the diagonal space ($s_{\mu_i}^{diagonal} = \sqrt{\lambda_i}$). This covariance matrix (C) has to be diagonalised to get to the diagonal space:

$$C = UDU^T, \tag{3.8}$$

being D the diagonal matrix generated with C's eigenvalues (λ_i) and U, the matrix of C's eigenvectors. A random number following a Gaussian distribution with $\mu = 0$ and $\sigma = \sqrt{\lambda_i}$ is generated and stored in a column vector $R^{diagonal}$. Finally, this vector needs to be rotated back into the correlated space:

$$\vec{R} = U\vec{R}^{diagonal}. \tag{3.9}$$

A new set of numbers (ν_j), randomised accounting for the correlations among them, can be computed by adding to each μ_j (the original central value) a given shift R_i originated from the uncorrelated uncertainty on μ_j.

4

Selection of $B^0 \to (\pi^+\pi^-)(K^+\pi^-)$ candidates

The model introduced in Section 1.2 exclusively describes the distribution of $B^0 \to (\pi^+\pi^-)(K^+\pi^-)$ events, which implies that all the possible backgrounds need to be subtracted or cancelled before performing the fit. The following sections describe the technical implementation and the physical motivations for the different analysis steps that are needed in order to obtain such background subtracted data sample.

4.1 Characterisation of the simulated and real data samples

As already mentioned, this analysis is performed with the full data sample recorded by the LHCb experiment during its Run I period, corresponding to years 2011 and 2012, an integrated luminosity of $\int \mathcal{L} = 945 \pm 33$ pb^{-1} and $\int \mathcal{L} = 2052 \pm 102$ pb^{-1} and centre-of-mass energies of 7 and 8 TeV, respectively. These conditions need to be known to the data-processing chain and reproduced during the generation of the simulated data samples. This information is propagated to the Gauss framework by making use of specific tags defining the experimental (CondDB) and the detector (DDDB) conditions.

Following the technical naming scheme that was introduced in Section 2.3, the 2012 (2011) data have been reconstructed (see Table 4.1) and stripped with DaVinci v33r8 using the Reco14-Stripping20r0p2 (Reco14-Stripping20r1p2) versions of the corresponding

Table 4.1: Database tags used to process the data and simulated samples. For the simulated data, the CondDB tag indicates the "down" magnet polarity (*md* as opposed to *mu* for the reversed polarity).

Sample	DDDB tag	CondDB tag
Collision11	head-20111102	cond-20130125
Collision12	dddb-20120831	cond-20130125
MC2011	head-20111102	sim-20111111-vc-md100
MC2012	dddb-20120831	sim-20121025-vc-md100

software packages. The same reconstruction and stripping versions are employed for the corresponding simulated data samples.

Two different EvtGen models are used to generate the samples needed for the analysis, depending on whether or not the simulated B^0 mesons decay through intermediate resonances. If no constraints are applied, the decay model is referred to as `PHSP` and is generated according to the phase-space density (Φ_4) described in Equation 1.37. In the case where the exclusive $B^0 \to \rho^0 K^{*0}$ channel is simulated, because of the characteristics of the amplitude analysis, it is convenient to express the decay rate in terms of the helicity formalism described in Section 1.2.2. This is implemented in the EvtGen `SVV_HELAMP` model, resulting in the decay rate

$$\begin{aligned} \texttt{PDF}^{VV} \propto & \left(A_0 \cos\theta_{12}\cos\theta_{34} + \frac{A_{||}}{\sqrt{2}}\sin\theta_{12}\sin\theta_{34}\cos\phi + i\frac{A_{\perp}}{\sqrt{2}}\sin\theta_{12}\sin\theta_{34}\sin\phi\right) \\ & \times \left(BW^{MC}(m_{12}, L=1)\cdot BW^{MC}(m_{34}, L=1)\Phi_4^{MC}(m_{12}, m_{34})\right), \end{aligned} \tag{4.1}$$

where the lineshapes of the corresponding Breit-Wigner and phase-space distributions have been described, together with the invariant mass propagators used in the analysis, in Equations 1.40 and 1.41.

Two $B^0 \to \rho^0 K^{*0}$ simulated data samples, referred to as `SVV_HELAMP(1)` and `SVV_HELAMP(2)`, were generated using different values for the set of generation parameters, A_λ, which are listed in Table 4.2. The first sample was produced with a combination of A_λ values such that the generation model evaluates to zero at $\phi = n\pi$ (n, an integer). In order to avoid this, the second set of parameters, used to generate `SVV_HELAMP(2)`, was chosen to maximise the interference among the three $(0, ||, \perp)$ waves in the decay amplitude and therefore ensure full coverage of the phase space in the angular dimensions. Furthermore, to achieve a better description of the acceptance in the 2-body invariant mass dimensions, the $B^0 \to \rho^0 K^{*0}$ `SVV_HELAMP(2)` and the `PHSP` (in bold in Table 4.3) simulated data samples are merged following the technique described in Section 3.3. The total number of generated events in each sample, which needed to compute the relative weight between both distributions, is also included in Table 4.3.

Table 4.2: Generation parameters used with the SVV_HELAMP models for the $B^0 \to \rho^0 K^{*0}$ samples. For convenience, both helicity (H_i) and transverse ($|A_\lambda|$) amplitudes are quoted.

	SVV_HELAMP(1)				SVV_HELAMP(2)			
$(H_i,\|A_\lambda\|^2)$	$\|H_i\|$	Phase	$\|A_\lambda\|^2$	Phase	$\|H_i\|$	Phase	$\|A_\lambda\|^2$	Phase
$(H_0,\|A_0\|^2)$	1.	0.	0.4142	0.	0.57735	0.	0.3333	0.
$(H_+,\|A_\|\|^2)$	1.	0.	0.5857	0.	0.8121	1.39	0.2969	1.30
$(H_-,\|A_\perp\|^2)$	1.	0.	0.	0.	0.0846	-0.74	0.3699	1.47

Table 4.3: Number of generated signal events for each simulated sample.

Event type	Signal Mode	MC2011	MC2012
11104041	$B^0 \to \rho(770)^0 K^*(892)^0$ (SVV_HELAMP(1))	3070994	4021486
11104042	$B^0 \to \rho(770)^0 K^*(892)^0$ (SVV_HELAMP(2))	1780251	3811888
11104090	$B^0 \to \rho(770)^0 K^*(892)^0$ (PHSP)	2036274	3997696
13104093	$B_s^0 \to K^*(892)^0 \overline{K}^*(892)^0$ (PHSP)	4141211	4161257
13104001	$B_s^0 \to K^*(892)^0 \overline{K}^*(892)^0$ (SVV_HELAMP)	1004357	2037039

4.2 Event selection

In this section, the selection process for the analysed data sample is introduced. The event selection is based on the decay topology of the B^0 meson, where it decays into two light vector mesons in a well defined secondary vertex (SV). Events fulfilling the trigger requirements are first filtered by the BetaSBs2Q2Body4piLine stripping line, and preselected with very soft PID and sanity cuts to allow the reconstruction of each light meson under a given mass hypothesis. On top of this, remaining background events are suppressed by performing a multivariate analysis using the BDT technique that was described in Section 3.1. Since no significant differences were observed, the same preselection cuts have been used in both 2011 and 2012 data, although two different BDTs were trained, one for each sample. Once the full selection has been applied, a fraction of 0.1% of multiple candidates was found. Among these, the candidate with the highest BDT output value was kept in the analysed sample.

4.2.1 Pre-selection: online and first offline requirements

Selected events were required to be triggered on signal (TOS) by the hadron trigger (L0HadronDecision_TOS) or triggered independent of signal (TIS) globally by the

Table 4.4: Summary on trigger requirements.

Trigger lines	
L0	L0HadronDecision_TOS or L0Global_TIS
	and
HLT1	HLT1TrackAllL0Decision_TOS
	and
HLT2	Hlt2Topo2BodyBBDTDecision_TOS or Hlt2Topo3BodyBBDTDecision_TOS or Hlt2Topo4BodyBBDTDecision_TOS

L0 trigger (L0Global_TIS). Furthermore, all events are required to be TOS on the HLT1TrackAllL0Decision tigger at the HLT1 stage, and at any of the 2-, 3- or 4-body topological triggers used at the HLT2 level.

These trigger requirements are summarised in Table 4.4, where it can also be seen that the only difference in the trigger path the events may follow appears at the L0 level. This splitting will define the fitting categories: TIS events (note that the TIS&TOS overlap is included here) and TOSnotTIS. By including the overlapping region with the TIS events, the momentum spectrum in this sample is kept as complete as possible, and therefore, the induced momentum bias is minimal.

The stripping of the studied mode has been performed with the quasi two-body (Q2B) decay stripping line StrippingBetaSBs2Q2Body4piLine. This line mainly selects B^0 meson decay products by requiring a displaced secondary vertex and tracks with a high transverse momentum and large impact parameter (IP). As it was mentioned, these are the main signatures of the B^0 meson decays, the SV being displaced due to the relatively large life of the meson and the decay products having a large p_T as a result of their low mass as compared to the B^0 meson. In particular, this line searches for a reconstructed displaced vertex formed by four hadrons (reconstructed under a π hypothesis) for which both pairs are satisfying the invariant mass and p_{T} requirements: $m_{\pi\pi} < 1.1\,\mathrm{GeV}/c^2$ and $p_{\mathrm{T}} > 500\,\mathrm{MeV}/c$ for each track. The complete stripping selections are gathered in Table 4.5.

Once events have been triggered and stripped, final state particles have to be well identified in order to correctly reconstruct their invariant mass and achieve further discrimination power. All the offline selections that are introduced in the following paragraphs are summarised in Table 4.6.

The Probability Neural Network (ProbNN) [83] variables are giving the ID information for each particle. These variables assign a probability (therefore, their value is restricted to the range $[0, 1]$) for each particle to be a kaon (ProbNNK), a pion (ProbNNpi), a proton (ProbNNp), an electron (ProbNNe) or a muon (ProbNNmu). In this analysis, the final state

Table 4.5: Stripping selection requirements.

Variable Definition	`StrippingBetaSBs2Q2Body4piLine`
B candidates selection cuts	
Mass of B	$4.5 < M_{B^0} < 5.7\,\mathrm{GeV}/c^2$
DIRA	$B_{\mathrm{PV\ DIRA}} > 0.99$
IPχ^2 wrt PV	IP$\chi^2 < 20$
χ^2/ndof of B vertex fit	$\chi^2/\mathrm{ndf}(B^0\,\mathrm{vtx}) < 12$
Vector meson selection Cuts	
Transverse momentum magnitude	$p_{\mathrm{T}} > 900\,\mathrm{MeV}/c$
Momentum magnitude	$p > 1\,\mathrm{GeV}/c$
Mass of the resonance candidate	$M_{\pi\pi} < 1.1\,\mathrm{GeV}/c^2$
χ^2/ndf of resonance vertex fit	$\chi^2_{(\pi\pi)\,\mathrm{vtx}} < 12$
Hadron selection Cuts	
Minimal p_{T}	$p_{\mathrm{T}} > 500\,\mathrm{MeV}/c$
Track ghost probability	`GhostProb` < 0.8
Track χ^2/ndof	$\chi^2/\mathrm{ndf} < 4$
χ^2_{IP} wrt PV	$\chi^2_{\mathrm{IP}} > 16$

particle with the highest `ProbNNK` value is assumed to be the kaon candidate, whereas the three remaining particles are assumed to be pions. This identification allows to reconstruct the two-body masses by matching up the assigned kaon with the oppositely charged pion for the $K^*(892)^0$ candidate and to merge the remaining pion pair to build the ρ^0 candidate. The exchange of the same sign pions does not produce a combination fulfilling the invariant mass requirements on both quasi-two-body systems. Misidentified particles are reduced by requiring each particle to be its assigned type with a probability larger than 0.2 (this is, `ProbNNk`>0.2 for the kaon candidate and `ProbNNpi`>0.2 for the three pion candidates). A fiducial requirement on the momentum of each track ($p_i < 100$GeV) is applied as the K/π separation power from the RICH drops dramatically above this threshold [84].

Further requirements are applied in order to reduce combinatorial backgrounds or poorly reconstructed tracks. Decays with charmonium resonances are rejected by applying a muon veto to each final state track. The secondary vertex is tighter defined and a large flying distance is required for the B^0 candidate. Moreover, all final state tracks are required to have a large impact parameter, to leave some signal in the calorimeter and to

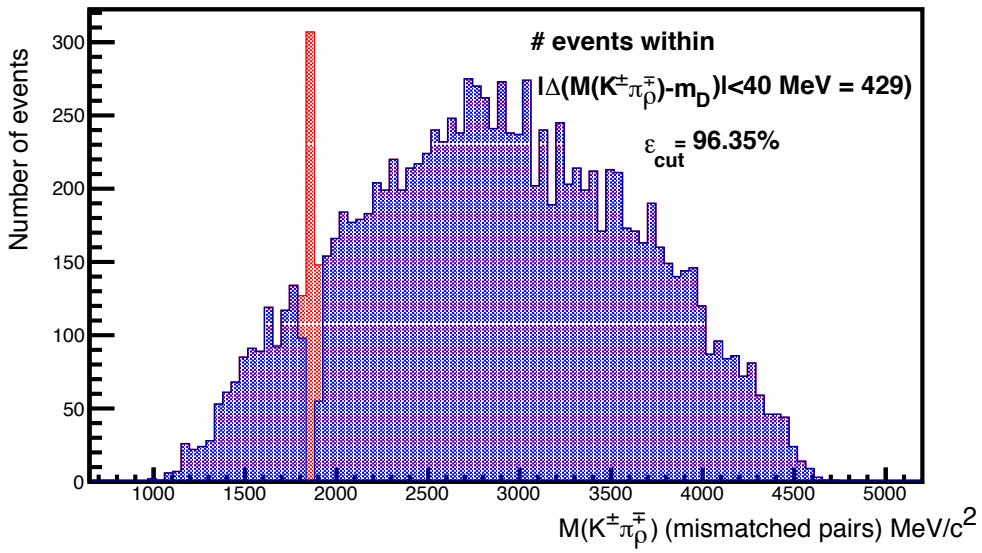

Figure 4.1: 2-body invariant mass spectrum of mismatched $K^{\pm}\pi^{\mp}$pairs. The $\pm$20 MeV window around the D^0 peak is highlighted.

have a probability of being *ghost tracks* (artifacts from the tracking algorithms) smaller than 50%.

This preselected data sample has a large contribution originating from B^0 decays to a $\pi^{\pm}$ and an oppositely charged $D^{\mp}$ meson, where this charmed meson decays into $K^{\pm}\pi^{\pm}\pi^{\mp}$, thus mimicking the signal. Contamination from other decay modes proceeding via broad 3-body resonances (like $a_1(1200)^- \to \pi^+\pi^-\pi^-$) is also possible. These events are removed from the analysed sample by imposing $|\cos(\theta_{\pi\pi})| < 0.8$, as the angular spectrum of these 3-body resonances peaks on the edges of the $\cos(\theta_{\pi\pi})$ variable. In addition, a significant background contribution coming from the $B^0 \to \overline{D}^0(K^+\pi^-)\pi^+\pi^-(X)$ decay is seen when studying mismatched pairs of the final state particles. In these cases, the D^0 meson is reconstructed with the kaon candidate and the opposite charged pion which was firstly assumed to be originated in the ρ^0 decay. In order to minimize this background source, these events are reconstructed under the correct matching hypothesis and, again, those falling within a mass window of 20 MeV/c^2 around the best known mass of the D meson (1864.84 ± 0.05 MeV/c^2 [5]), are rejected. The effect of this cut in the 2-body invariant mass spectrum for the mismatched $K^{\pm}\pi^{\mp}$pairs can be seen in Figure 4.1.

4.2.2 Multivariate analysis

As anticipated in Section 3.1, in this analysis the TMVA toolkit was used to exploit machine learning techniques to discriminate between signal and background. The different multivariate methods provided in this package are trained by defining two data samples, one of signal events and the other with a background like composition. The usual choice

Table 4.6: Off-line preselection cuts. The particle with the highest `ProbNNK` among the four final state tracks is assumed to be the K candidate.

Variable definition	Requirement
Fiducial requirements	
Track momentum	`allTracks_p` < 100 GeV
Any calorimetry signal	`allTracks_PIDk` > -500
SV isolation	`B0_SMALLESTDELTACHI2` > -1
SV quality	`B0_DOCA` $\in [0, 0.5]$ mm
PV sanity requirement	`B0_IPCHI2_OWNPV` > 0
PV sanity requirement	`B0_FDCHI2_OWNPV` > 0
PV sanity requirement	`B0_FD_OWNPV` < 50 mm
B^0 pointing to PV	`B0_IP_OWNPV` < 0.2 mm
PID requirements	
K candidate ID	`ProbNNk` > 0.2
π candidates ID	`ProbNNpi` > 0.2
μ ID veto	`allTracks_isMuon` $== 0$
Invariant mass requirements	
4-body	m$(K\pi\pi\pi) > 4800$ MeV
2-body	$m(K\pi) \in m_{K^*(892)} \pm 300$ MeV
$D^\mp$ veto	Abs(m$((K^\pm\pi^\mp)\pi^{1,2}_\rho)$ - $m_{D^\mp}) > 40$ MeV
D^0 veto	Abs(m$(\mathrm{K}^\pm\pi^\mp_\rho)$ - $m_{D^0}) > 20$ MeV

consists of a simulated data sample to describe the signal and a sample composed of real data events that will not be included in the analysis but are mimicking the expected background in the surroundings of the signal region.

The right side band (SB) ($M(K\pi\pi\pi) > 5540$MeV) of each four-body mass spectrum was used as the background sample to train the BDTs (one for 2011 data and other for 2012), while the signal samples were the corresponding simulated data for the $B^0 \to \rho^0 K^{*0}$ (the `SVV_HELAMP(1)` sample was used, for historical reasons). Both samples were randomly split in two, using one of the sub-samples for training and the other for testing the BDT (these samples are composed of 27791 events for the 2011 BDT and of 34440 for the 2012 one). The discrimination power of the BDT is achieved by using kinematic and topological variables, which have been shown to work best against the combinatorial background.

Table 4.7 shows the variables used in the BDT, together with a short description

Table 4.7: Kinematical and topological variables used in the BDT.

Variable	Description
`log10(B0_PT)`	B^0 transverse momentum
`log10(Rho_lessIPS)`	less $(\pi^{\pm}\|\|\pi^{\mp})$ IP significance w.r.t the PV
`log10(Kst_lessIPS)`	less $(K^{\pm}\|\|\pi^{\mp})$ IP significance w.r.t the PV
`B0_IPCHI2_OWNPV`	B^0 IP significance w.r.t the PV
`B0_ENDVERTEX_CHI2`	SV vertex fit
`log10(B0_FDCHI2_OWNPV)`	B^0 flying distance w.r.t its PV
`log10(2.+B0_SMALLESTDELTACHI2)`	Isolation of the SV

of each. Topological variables were chosen such that a clearly displaced and well reconstructed SV is appearing in the event. This is enhanced by requiring the two light vector mesons to have a large impact parameter and by taking into account the goodness of the SV fit (with its χ^2 value) and its isolation (distance to the closest track not belonging to the decay vertex, with the `SMALLESDELTACHI2` variable). In addition, the B^0 meson p_{T}, its flying distance, and its IP value were considered.

The distribution of the variables considered in the BDT for the 2011 (2012) signal and background samples can be seen in Figure 4.2 (Figure 4.3), while Figure 4.4 shows the correlation matrices for the variables used in the BDTs. The different correlation for a given variable between signal and background, as well as the non-linearity of the correlations between these variables, justifies employing a multivariate BDT technique. As explained in Section 3.1, an overtraining test has to be performed to ensure the stability of the BDT response. This check (performed through a Kolmogorov-Smirnov test), as well as the output BDT classifier distribution, can be seen in Figure 4.5, where the classifier value for the test sample is drawn superimposed to its value in the training sample for both BDTs. No signs of overtraining are observed in any of the classifiers.

4.2.3 Choice of the PID and BDT working points

The final goal of the analysis is to perform a fit in a background subtracted sample, which will be obtained using the *sPlot* technique on the $m(K^{\pm}\pi^{\mp}\pi^{\pm}\pi^{\mp})$ invariant mass distribution. This method works best when used against the combinatorial background, but is harder to control if many other background contributions have to be accounted for. Therefore, a requirement on the BDT output value, `BDTcut=0.06`, was chosen such that the efficiency on the training/testing background samples is $\sim$1% (see Figure 4.6) while it remains $\geq$90% for the signal. This was found to be a good compromise between low signal loss and low contribution from the combinatorial background for the 4-body invariant mass fit. Figure 4.7 shows that this requirement is very close to the optimal

choice in terms of estimated signal purity and significance. The PID selection criterium was chosen to minimise the number of peaking background contributions that will have to be accounted for in the 4-body invariant mass fit. Different combinations of pions, kaons and protons, from either B^0, B_s^0 or Λ_b^0 decays, are expected in the analysed data sample. These background components are reduced to negligible contributions (with two exceptions, commented below) by requiring:

- Kaon: (preselection cut, `ProbNNk`>0.2) and `ProbNNk`×(1-`ProbbNNpi`)>0.3
- Pions: (preselection cut, `ProbNNpi`>0.2) and `ProbNNpi`×(1-`ProbbNNk`)>0.3

The requirement on the kaon candidate removes four pion contributions (like the originated from $B^0 \to \rho^0\rho^0$ decay), while any combination in which a $\phi(\to K^+K^-)$ meson is present is very suppressed by both the PID constraints on the pions and the considered 2-body invariant mass windows. A contribution from the $\Lambda_b^0 \to (K^-\pi^+)(p\pi^-)$ decay remains present in the analysed data sample after this selection and a dedicated PID requirement (`ProbNNp`<0.35) is used to strongly suppress it. This requisite on the `ProbNNp` value is placed only on one of the pions used to build the ρ^0 candidate, as the other match lies outside the considered 2-body invariant mass ranges. Contributions from the $\Lambda_b^0 \to p\pi\pi\pi$ mode were searched for and not observed under their correct mass hypothesis (either proton to kaon misidentification or double proton to pion and kaon to pion). It was found that all except for the combinatorial contribution and a $B_s^0 \to (K^+\pi^-)(K^-\pi^+)$ component could be neglected in the nominal model for the 4-body invariant mass fit by applying the full selection discussed above. Figure 4.8 shows where these PID requirements are on a background rejection versus signal efficiency plot, together with a comparison with the achieved performance when using one of the `ProbNN` variables alone, instead of combinations of them.

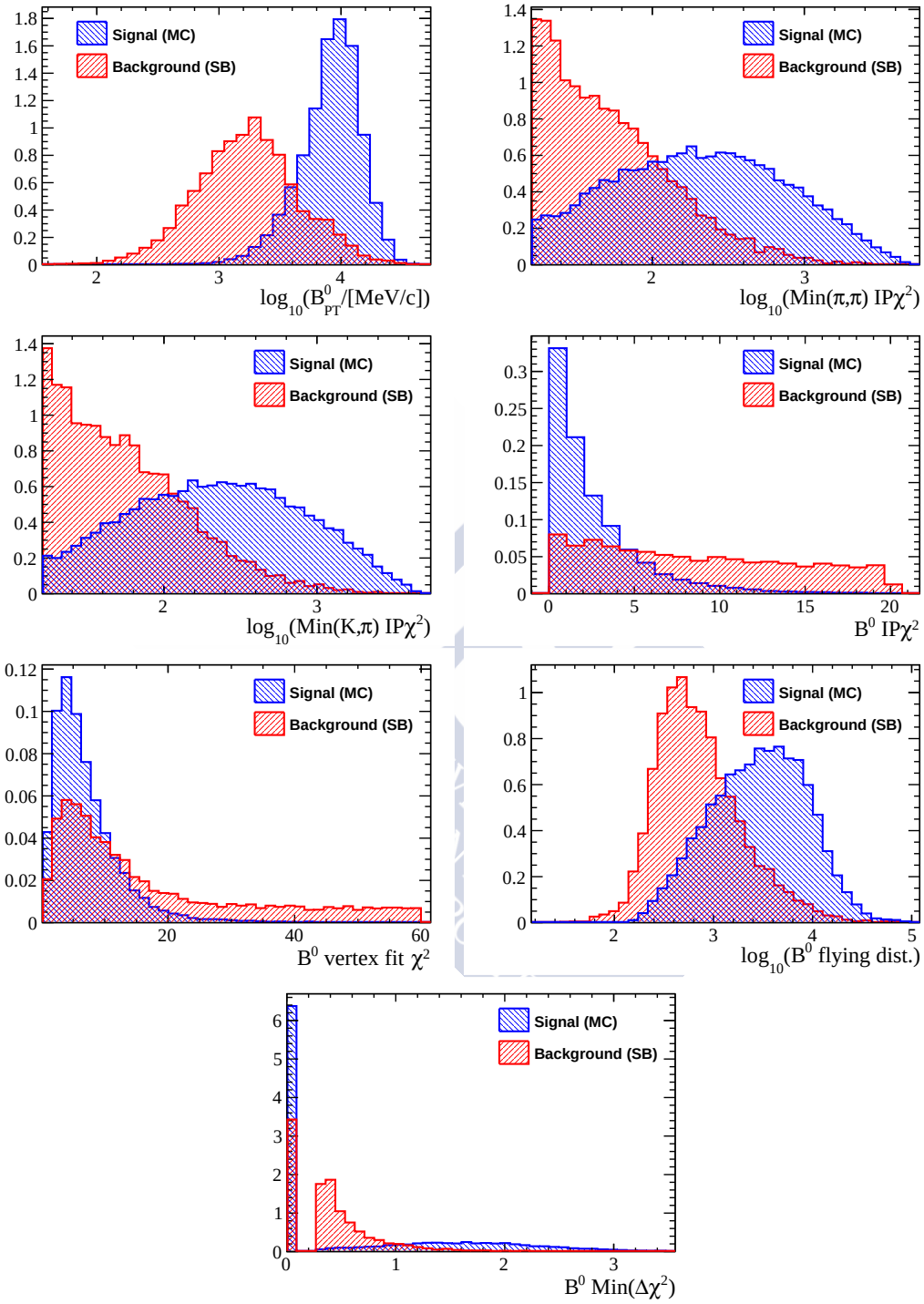

Figure 4.2: The distributions in the signal and background samples of each input variable to the 2011 BDT are shown. Variables are appearing in the same order as in Table 4.7. Simulated data were employed as the signal sample (blue) while one of the sub-samples from the right side band of the four body invariant mass spectrum was used as background (red).

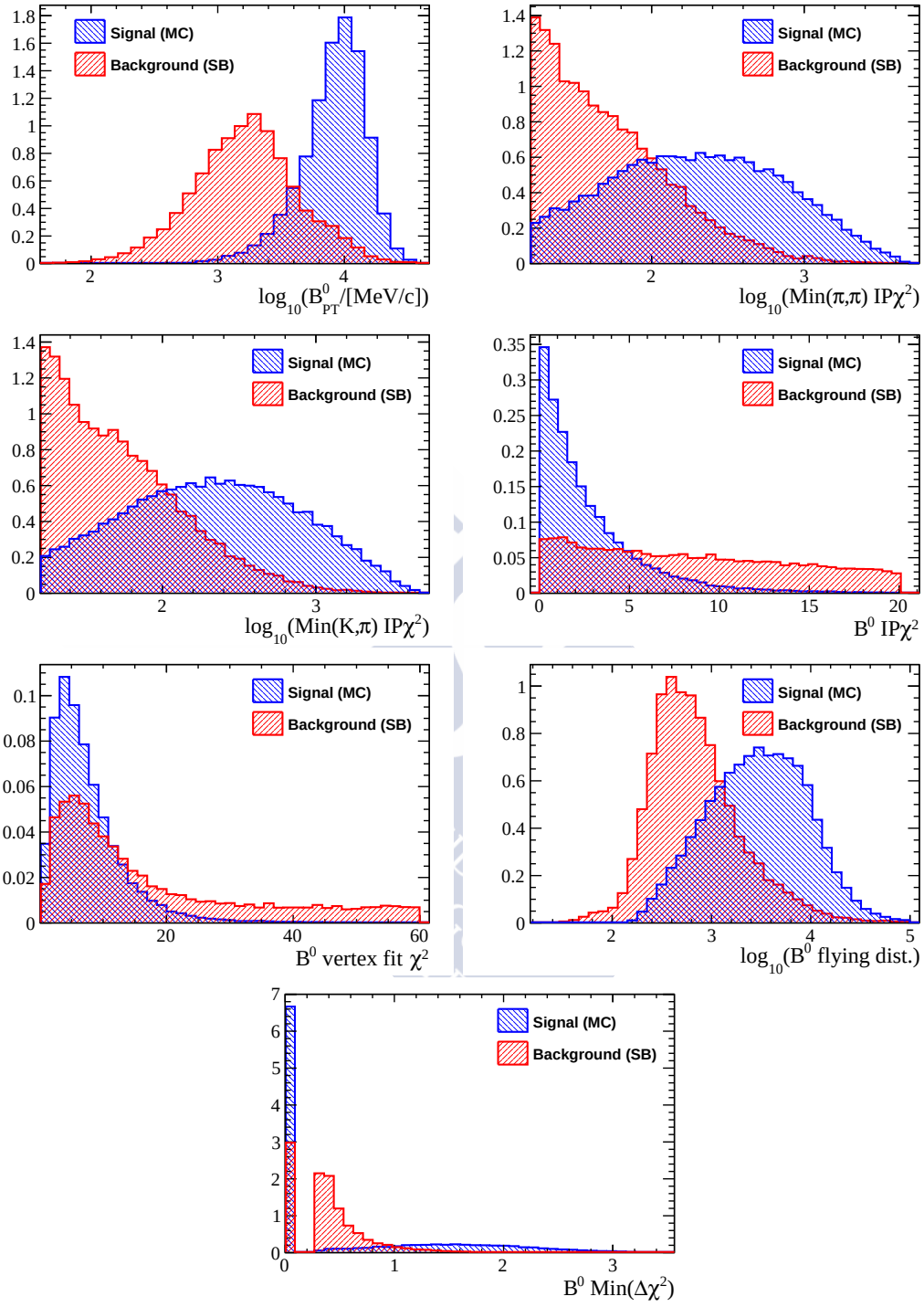

Figure 4.3: The distributions in the signal and background samples of each input variable to the 2012 BDT are shown. Variables are appearing in the same order as in Table 4.7. Simulated data were employed as the signal sample (blue) while one of the sub-samples from the right side band of the four body invariant mass spectrum was used as background (red).

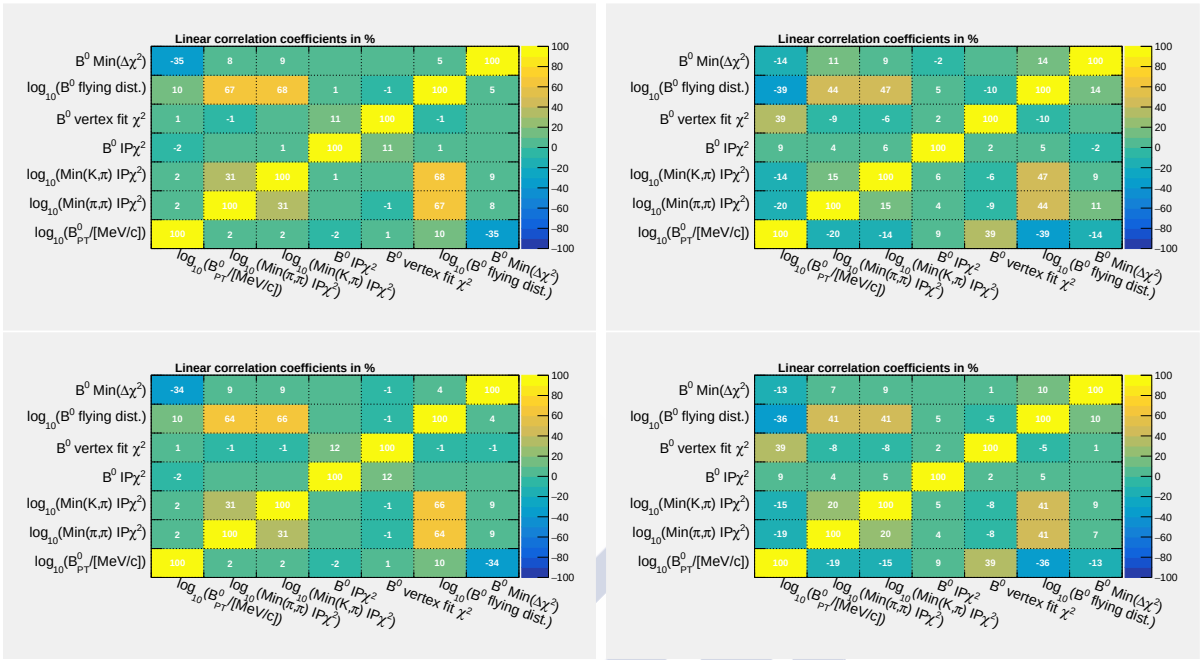

Figure 4.4: Correlation coefficients between the input variables for signal (left) and background (right) for the 2011 (top) and 2012 (bottom) BDTs.

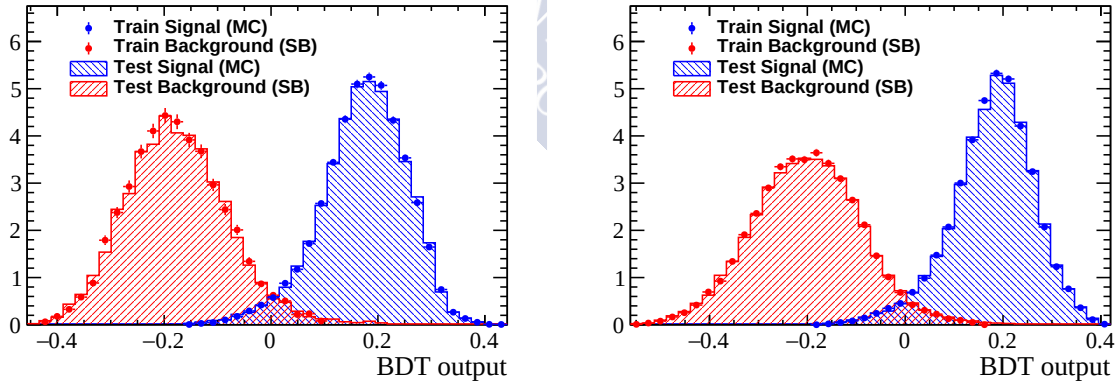

Figure 4.5: BDT classifier output and overtraining test for the 2011 (left) and 2012 (right) samples. In the figure, the BDT response is shown in blue for signal (simulated data) and red for background in both samples, the training samples are represented with small markers and the testing ones with filled histograms. The results of the Kolmogorov-Smirnov tests are, for 2011 and 2012 BDTs, respectively: signal (background) probability: 0.93 (0.700) and signal (background) probability: 0.541 (0.587).

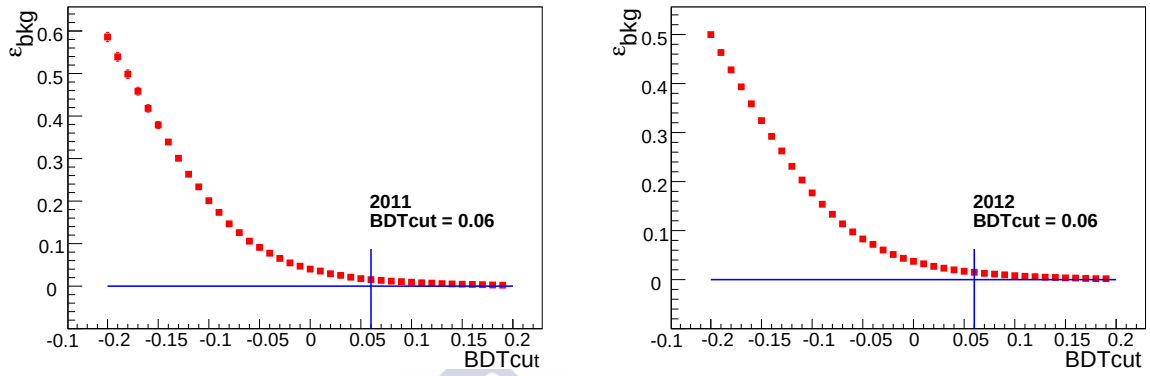

Figure 4.6: Efficiency selecting background events in the background sample used in the BDT testing as a function of the requirement applied in the BDT variable. The result for 2011 (2012) is shown in the left (right) plot. The threshold that reduces this efficiency to a $\leq 1\%$ value is set as our working point. This cut has a efficiency on both (2011 and 2012) signal samples greater than 90%.

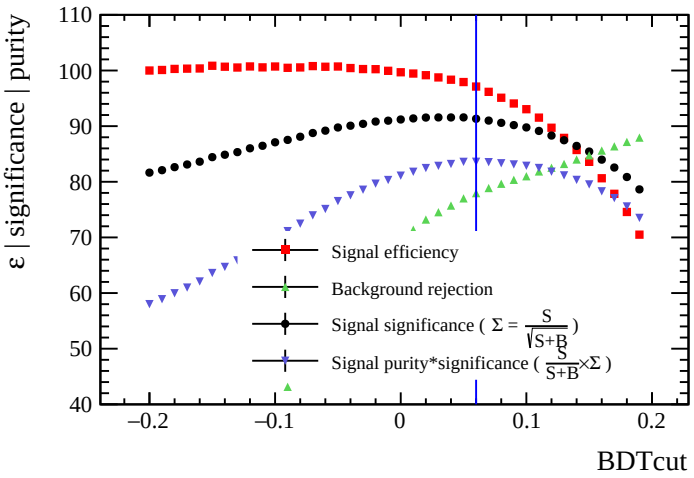

Figure 4.7: BDT cut working point with respect to: the signal efficiency, the combinatorial background rejection and the signal significance and purity times significance figures of merit for the 2012 data sample.

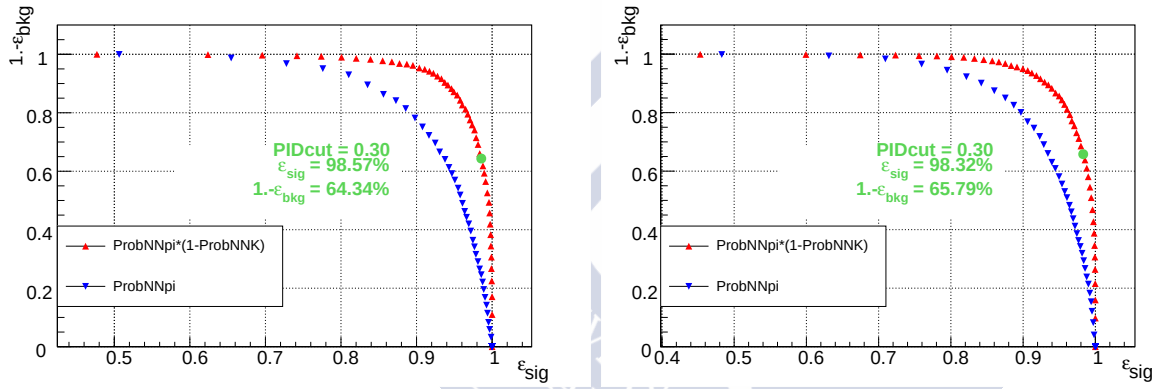

Figure 4.8: $B_s^0 \to K^*(892)^0\overline{K}^*(892)^0$ background rejection versus $B^0 \to \rho^0 K^{*0}$ signal efficiency as a function of the PID cut applied in both simulated data samples. Events are required to be truth-matched (`TRUE_ID`) and fulfil all the selection criteria. The result obtained from the 2011(2012) simulated data samples is shown on the left (right).

4.3 Backgrounds subtraction

Once the event selection is applied, the analysed data sample is highly dominated by signal events. However, two background components with non negligible contributions remain present. These are the combinatorial background and the $B_s^0 \to K^*(892)^0\overline{K}^*(892)^0$ reflection. While for the former the *sFit* technique is expected to perform accurately and completely subtract these events, the latter requires a bit more elaboration. There are two main reasons for the $B_s^0 \to K^*(892)^0\overline{K}^*(892)^0$ component implying extra work. First, the kaon to pion misidentification shifts the reconstructed mass of these events into the complicated region between the B^0 and B_s^0 signal peaks; and, second, the $B_s^0 \to K^*(892)^0\overline{K}^*(892)^0$ shape in the $K^\pm\pi^\mp\pi^\pm\pi^\mp$ invariant mass spectrum is wide enough not to allow the fit to be accurate in the determination of its yield. The strategy used to cancel the $B_s^0 \to K^*(892)^0\overline{K}^*(892)^0$ contribution consists of the use of simulated events, injected to the data sample with negative weights, thus effectively removing this background component. The *sFit* procedure can be applied as usual afterwards to suppress the combinatorial background. Details on the procedure followed are given below.

4.3.1 Treatment of the $B_s^0 \to K^*(892)^0\overline{K}^*(892)^0$ reflection

The $B_s^0 \to K^*(892)^0\overline{K}^*(892)^0$ decay mimics the $B^0 \to \rho^0 K^{*0}$ as for what kinematic and topological distributions are concerned. This includes all the variables that were used in the BDT which was, indeed, trained to prefer a generic quasi-two-body decay over a random combination of tracks. Although a slight preference from the BDT to select events matching the $B^0 \to \rho^0 K^{*0}$ kinematics is expected (due to the simulated data sample used in the training), the final composition of the selected data sample will be mostly determined by the imposed PID requirements. This implies that a good estimation on the number of $B_s^0 \to K^*(892)^0\overline{K}^*(892)^0$ events present in the analysed data sample (Sample1) has to be obtained. This is accomplished using the following strategy:

1. Choose PID cuts corresponding to the $K\pi K\pi$ final state ($\text{PID}_{K\pi K\pi}$, from Table 4.8), while leaving the rest of selection cuts untouched. This defines Sample2.

2. Fit the resulting four body invariant mass spectrum, $m(K^+\pi^-K^-\pi^+)$, accounting for the $B_s^0 \to K^*(892)^0\overline{K}^*(892)^0$, $B^0 \to K^*(892)^0\overline{K}^*(892)^0$, missID $B^0 \to \rho^0 K^{*0}$ and the combinatorial background.

3. Obtain the $B_s^0 \to K^*(892)^0\overline{K}^*(892)^0$ yield in Sample2 ($N^{B_s\to K\pi K\pi}|_{PID_{K\pi K\pi}}$) from the previous fit.

4. Compute the ratio of the $B_s^0 \to K^*(892)^0\overline{K}^*(892)^0$ selection efficiencies (that reduces to ratio of PID efficiencies) between Sample1 ($\text{PID}_{K\pi\pi\pi}$) and Sample2 ($\text{PID}_{K\pi K\pi}$).

Table 4.8: Definition of the PID selection cuts $\text{PID}_{K\pi\pi\pi}$ and $\text{PID}_{K\pi K\pi}$, used in Sample1 and Sample2, respectively. To further suppress the $B^0 \to \rho^0 K^{*0}$ component in Sample 2, the PID requirement on the second kaon (particle 3) is tightened with respect to its nominal value.

	$\text{PID}_{K\pi\pi\pi}$ Sample1$\equiv B^0_{(s)} \to (K\pi)(\pi\pi)$	$\text{PID}_{K\pi K\pi}$ Sample2$\equiv B^0_{(s)} \to (K\pi)(K\pi)$
particle1	ProbNNK(1-ProbNNpi)> 0.3	ProbNNK(1-ProbNNpi)> 0.3
particle2	ProbNNpi(1-ProbNNK)> 0.3	ProbNNpi(1-ProbNNK)> 0.3
particle3	ProbNNpi(1-ProbNNK)> 0.3	ProbNNK(1-ProbNNpi)> 0.45
particle4	ProbNNpi(1-ProbNNK)> 0.3	ProbNNpi(1-ProbNNK)> 0.3

5. Obtain the $B^0_s \to K^*(892)^0\overline{K}^*(892)^0$ yield in Sample1 ($N^{B_s\to K\pi K\pi}|_{PID_{K\pi\pi\pi}}$) as a function of $N^{B_s\to K\pi K\pi}|_{PID_{K\pi K\pi}}$ and the ratio of selection efficiencies:

$$N^{B_s\to K\pi K\pi}|_{PID_{K\pi\pi\pi}} = \frac{\varepsilon_{PID_{K\pi\pi\pi}}}{\varepsilon_{PID_{K\pi K\pi}}} \cdot N^{B_s\to K\pi K\pi}|_{PID_{K\pi K\pi}}.$$

The aforementioned efficiencies can not be directly obtained from the available simulated samples as the PID distributions are known to be mismodelled. The reason for this effect and some other details are discussed, along with the systematic effects they may induce in the analysis, in Section 5.2. To solve this, the PIDCalib [80] software package has been developed and is maintained by the PID physics performance working group of the LHCb collaboration, providing a set of tools (briefly described in Section 3.6) that allow these effects to be corrected for.

Both sets of PID cuts are summarized in Table 4.8. Their efficiencies on the $B^0_s \to K^*(892)^0\overline{K}^*(892)^0$ samples are computed using the PIDCalib software package, the results of these computations are shown in Table 4.9 and were obtained with the binning scheme detailed in Table 4.10. It should be noted that the aim for Sample2 was to obtain the cleanest possible $B^0_s \to K^*(892)^0\overline{K}^*(892)^0$ sample. Therefore, the $\text{PID}_{K\pi K\pi}$ cuts were chosen to be the least efficient on $B^0 \to \rho^0 K^{*0}$ (not the most efficient on $B^0_s \to K^*(892)^0\overline{K}^*(892)^0$).

Figure 4.9 shows the fit to the $(K^\pm\pi^\mp)(K^\mp\pi^\pm)$ invariant mass spectra, for 2011 and 2012 data, together with the different components that were considered in the fit. Two Hypatia [85] functions are used to fit the B^0 and B^0_s peaks, the shape of both functions being the same and all their parameters, except their means, being fixed to those obtained from a fit to simulated data. Despite the tight PID cuts, $B^0 \to \rho^0 K^{*0}$ events pollute this sample, and a Crystal Ball (CB) [86] distribution is used to model this component. Except for its mean value, the rest of the CB parameters are also taken from simulation. The results of these fits to simulated data, both for the Hypatia and the Crystal Ball functions, are shown in Figures 4.10, 4.11 and Table 4.11.

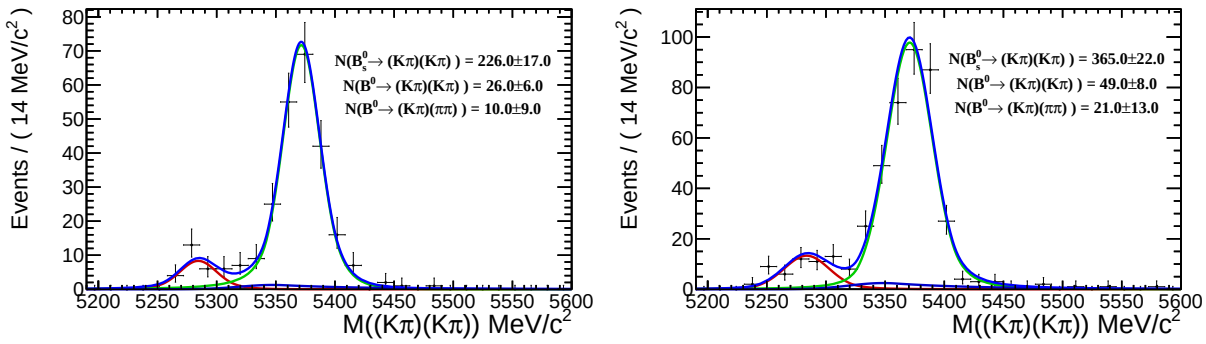

Figure 4.9: Fits to the $(K^{\pm}\pi^{\mp})(K^{\mp}\pi^{\pm})$ invariant mass spectra, for 2011 (left) and 2012 (right) data, in Sample 2. The $B^0_s \to K^*(892)^0\overline{K}^*(892)^0$ is shown in light green, the $B^0 \to K^*(892)^0\overline{K}^*(892)^0$ in red and the broad pollution below the peaks (dark blue) corresponds to the remaining $B^0 \to \rho^0 K^{*0}$ events in these samples.

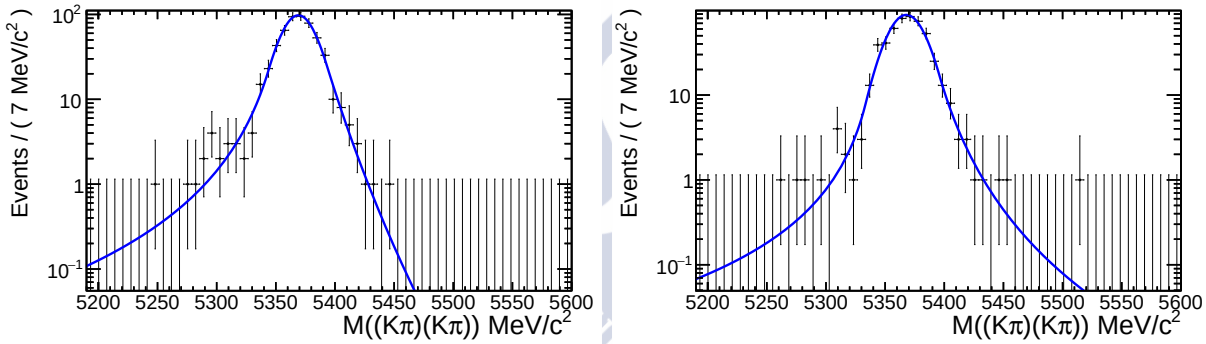

Figure 4.10: Hypatia fit to the $B^0_s \to K^*(892)^0\overline{K}^*(892)^0$ simulated samples, corresponding to 2011 and 2012 conditions, are shown in the left and right plots, respectively. The same set of parameters is used to describe the B^0_s and the B^0 line shapes.

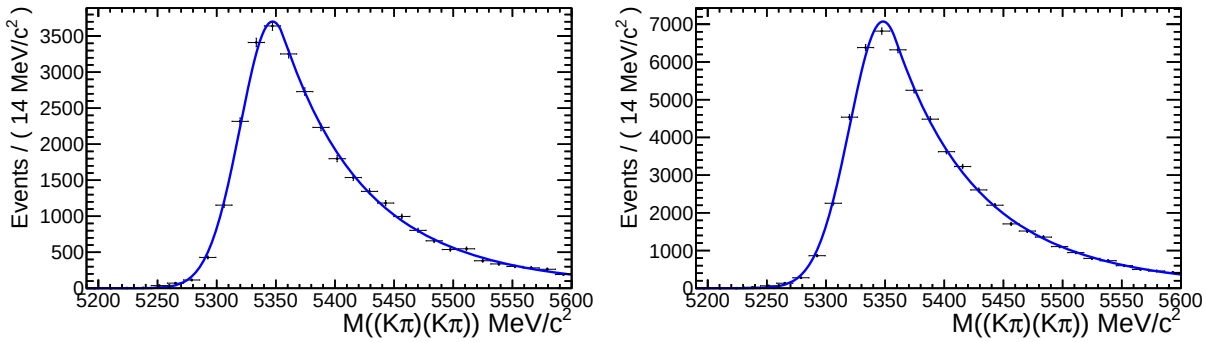

Figure 4.11: CB fit to the $B^0 \to \rho^0 K^{*0}$ simulated data reconstructed as $K^{\pm}\pi^{\mp}K^{\mp}\pi^{\pm}$, 2011 and 2012 samples are shown in the left and right plots, respectively.

Table 4.9: $\text{PID}_{K\pi\pi\pi}$ and $\text{PID}_{K\pi K\pi}$ cuts efficiency on the $B_s^0 \to K^*(892)^0\overline{K}^*(892)^0$ and $B^0 \to \rho^0 K^{*0}$ simulated data samples. These efficiencies were computed splitting the sample by year and magnet polarity (as required by the PIDCalib software). The samples are only separated according to the year for the final computation (averaged in magnet polarity). The correction histograms were built in terms of the momentum and pseudorapidity of each track.

`Sample|Cut`	2011 (%)	2012 (%)
$B^0 \to \rho^0 K^{*0}$ $\|\varepsilon(\text{PID}_{K\pi\pi\pi})$	67.35	67.39
$B^0 \to \rho^0 K^{*0}$ $\|\varepsilon(\text{PID}_{K\pi K\pi})$	0.074	0.086
$B_s^0 \to K^*(892)^0\overline{K}^*(892)^0$ $\|\varepsilon(\text{PID}_{K\pi\pi\pi})$	10.22	9.90
$B_s^0 \to K^*(892)^0\overline{K}^*(892)^0$ $\|\varepsilon(\text{PID}_{K\pi K\pi})$	5.75	5.90

The estimated $B_s^0 \to K^*(892)^0\overline{K}^*(892)^0$ yields shown in Figure 4.9 were averaged in `Flavour&Trigger` categories due to the smallness of the samples. In order to estimate this yield per fitting category, the fractions of N(`TIS`)/N(`TOSnotTIS`) and of N(B)/N($\overline{B}$) found in the $B_s^0 \to K^*(892)^0\overline{K}^*(892)^0$ simulated data are assumed to hold for real data. The final number of events that will be subtracted from each sub-sample is shown in Table 4.12.

To properly cancel this contribution, helicity angles and 2-body invariant mass distributions from the pure phase space simulated sample are weighted with a PDF whose physical parameters are taken from the LHCb analysis of the $B_s^0 \to K^*(892)^0\overline{K}^*(892)^0$ decay described in Ref. [87]. The analytical expression of this $\texttt{PDF}_{K^*K^*}$ is:

$$\begin{aligned}\frac{d^5\Gamma}{\Gamma d\Omega dm_1 dm_2} \propto \Big[&\frac{A_0}{\Gamma_L}\cos\theta_1\cos\theta_2 + \frac{A_{||}}{\sqrt{2}\Gamma_L}\sin\theta_1\sin\theta_2\cos\phi \\ &+ i\frac{A_\perp}{\sqrt{2}\Gamma_H}\sin\theta_1\sin\theta_2\sin\phi\Big]\mathcal{M}_1(m_1)\mathcal{M}_1(m_2) \\ &- \frac{A_{s+}}{\sqrt{6}\Gamma_H}\left(\cos\theta_1\mathcal{M}_1(m_1)\mathcal{M}_\prime(m_2) + \cos\theta_2\mathcal{M}_0(m_1)\mathcal{M}_1(m_2)\right) \\ &- \frac{A_{s-}}{\sqrt{6}\Gamma_L}\left(\cos\theta_1\mathcal{M}_1(m_1)\mathcal{M}_\prime(m_2) - \cos\theta_2\mathcal{M}_0(m_1)\mathcal{M}_1(m_2)\right) \\ &- \frac{A_{ss}}{3\Gamma_L}\mathcal{M}_0(m_1)\mathcal{M}_0(m_2)]^2\Phi_4(m_1,m_2)\end{aligned} \tag{4.2}$$

where $\mathcal{M}_1(m_i) \equiv BW(m_i, L=1)$ and $\mathcal{M}_0(m_i) \equiv LASS(m_i)$ from Section 1.2.2 and the physical amplitudes are multiplied by the lifetime of each mass eigenstate, Γ_L or Γ_H, to account for the fact that the $\texttt{PDF}_{K^*K^*}$ is time-integrated.

Table 4.10: Binning scheme used to run the PIDCalib software. Alternative schema were investigated and no significant changes on the PID efficiencies were seen.

Bin	$\Delta(\mathrm{p_T})$ (GeV/c)	$\Delta(\eta)$
1	[0-12]	[1.5,2.4]
2	[12,16]	[2.4,3.0]
3	[16,19]	[3.0,3.5]
4	[19,22]	[3.5,5.0]
5	[22,25]	-
6	[25,29]	-
7	[29,33]	-
8	[33,37]	-
9	[37,41]	-
10	[41,47]	-
11	[47,60]	-
12	[60,100]	-

4.3.2 *sPlot* technique applied to the combinatorial background

As explained in Section 3.2, the use of this method requires the variable in which the *sFit* is performed to be uncorrelated with the final analysis variables. This requirement was proven to be fulfilled in this analysis by plotting the four-body invariant mass in bins of each of the analysis variables ($m_{1(2)}, \cos\theta_{1(2)}, \phi$). The relevant plots are shown in Figures 4.12 and 4.13. No significant correlations were found, proving the usability of the *sFit* technique for this analysis.

Once the $B_s^0 \to K^*(892)^0\overline{K}^*(892)^0$ component has been suppressed, the *sFit* technique is used to effectively cancel the combinatorial background. The four body invariant mass spectrum limits are redefined leaving the partially reconstructed backgrounds outside of the fitted region and the yields of each component are the only free variables in the fit. The set of *sWeights* that are used in the final fit are corrected by the normalisation factor $\chi = \sum_i w_i / \sum_i w_i^2$ to account for the known shortcoming of the *sFit* method of underestimating the statistical uncertainties [72].

Table 4.11: Values for the parameters defining the Hypatia and CB shapes in the $M(K\pi K\pi)$ invariant mass spectrum. The $B_s^0 \to K^*(892)^0\overline{K}^*(892)^0$ and $B^0 \to K^*(892)^0\overline{K}^*(892)^0$ line shapes are modelled with two identical Hypatia functions, except for their mean values ($\mu_{B_s^0} = \mu_{B^0} + 87.13$ [5]). The $B^0 \to \rho^0 K^{*0}$ reflection is parametrised with a CB.

	Hypatia		CB	
	2011	2012	2011	2012
μ	5369.08 ± 0.72	5367.88 ± 0.76	5347.26 ± 0.54	5348.26 ± 0.41
σ	15.54 ± 2.25	15.86 ± 0.66	27.35 ± 0.33	28.3 ± 0.25
a_1	1.63 ± 0.29	2.16 ± 0.33	−0.39 ± 0.01	−0.4 ± 0.01
n_1	2.71 ± 2.37	2.09 ± 1.03	8.82 ± 1.9	9.26 ± 1.51
a_2	1.55 ± 0.22	1.78 ± 0.3	-	-
n_2	13.81 ± 7.88	3.84 ± 2.08	-	-
λ	−7.08 ± 6.14	−14.0 ± 3.9	-	-

Table 4.12: Number of $B_s^0 \to K^*(892)^0\overline{K}^*(892)^0$ events to be subtracted from each subsample according to the fitting categories splitting. The fraction of events per category is also shown.

Sample≡ B	2011		2012	
	TIS	TOSnotTIS	TIS	TOSnotTIS
(%)	27.02	23.68	26.15	23.87
$N^{B_s \to K\pi K\pi}$	100	89	156	144
Sample≡ $\overline{B}$	2011		2012	
	TIS	TOSnotTIS	TIS	TOSnotTIS
(%)	25.96	23.32	26.76	23.21
$N^{B_s \to K\pi K\pi}$	96	85	162	144

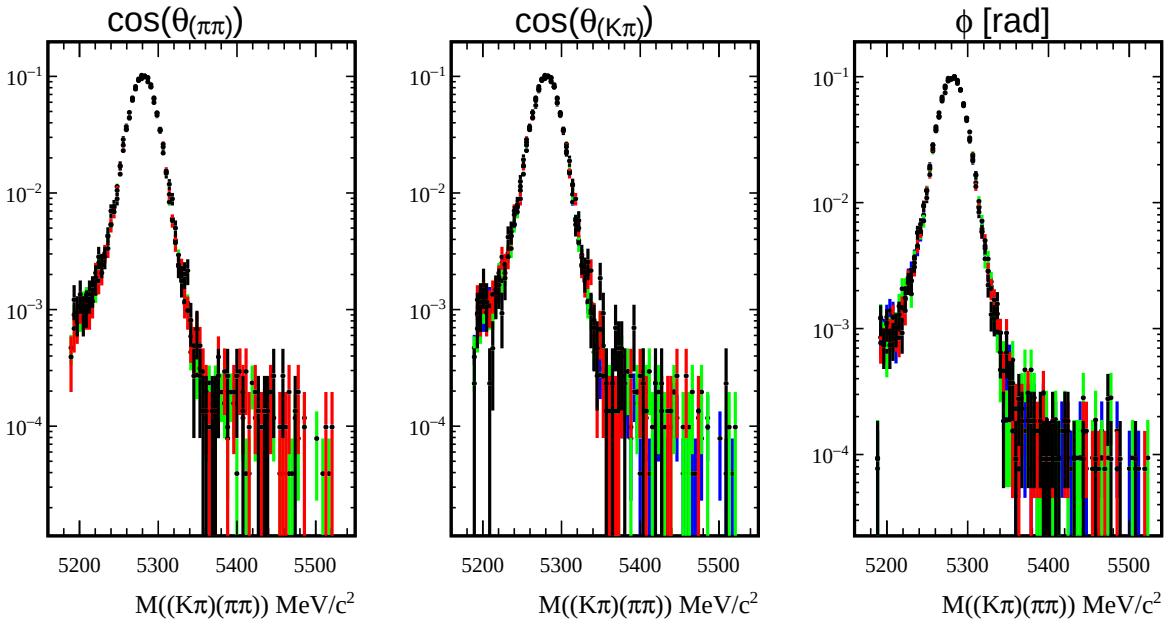

Figure 4.12: Four-body invariant mass distribution in bins of $\cos\theta_{(\pi\pi)}, \cos\theta_{(K\pi)}$ and ϕ. The binning schema are: $\text{abs}(\cos\theta_{(\pi\pi)}) = [0., 0.4], [0.4, 0.6], [0.6, 0.8]$, $\text{abs}(\cos\theta_{(\text{K}\pi)}) = [0., 0.4], [0.4, 0.6], [0.6, 0.8], [0.8, 1.]$ and $\pi/2$ intervals in ϕ. For each plot, the distribution in bin number [1,2,3,4] is drawn with a solid [black,red,green,blue] line, respectively.

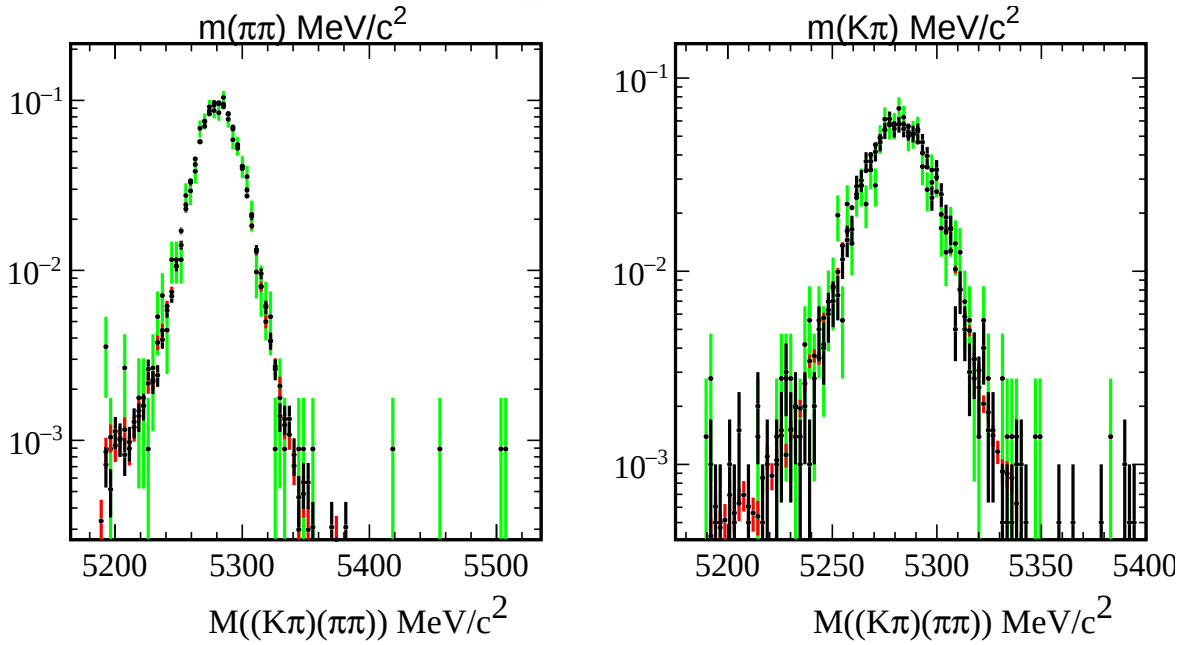

Figure 4.13: Four-body invariant mass distribution in bins of 250 MeV/c^2 in each of the 2-body invariant masses, $m_{(\pi\pi)}$ and $m_{(K\pi)}$. For each plot, the distribution in bin number [1,2,3,4] is drawn with a solid [black,red,green,blue] line, respectively.

4.4 Four-body invariant mass fit model

As introduced in Section 1.3, the four-body invariant mass spectrum is studied in order to obtain a background subtracted data sample, which will be used as input to the amplitude fit. Despite having fulfilled all the selection requirements, the candidates originating from the random combination of tracks (combinatorial background) do not show any peaking structure in the four-body invariant mass spectrum, much unlike genuine signal candidates. This characteristic maximises the efficiency of the *sPlot* technique when used to cancel the combinatorial background contribution and motivates the characterisation of all the contributions to this spectrum, which are described below.

4.4.1 Possible contributions to the spectrum

Once the full selection has been performed, the resulting sample is dominated by signal events. However, some contributions from misidentified particles, partially reconstructed and combinatorial backgrounds remain. In addition, during the analysis process, contributions from known decay channels were searched for in order to stablish whether their polluted the signal sample or not. The different shapes used to describe these components in the fit are also discussed.

- $\boldsymbol{B^0 \to (\pi^+\pi^-)(K^+\pi^-)}$: the signal peak is modelled with an Hypatia distribution, which is a generalisation of the so-called Crystall-Ball function that marginalises over the per-event mass resolution on the experimental distribution, improving the description of the no-longer Gaussian core of the CB function. Its parameters, except for the mean (μ_B) and sigma (σ) are fixed to the values obtained in a fit to simulated events (see Section 4.4.2), fulfilling the same selection criteria as real data.

- $\boldsymbol{B_s^0 \to (\pi^+\pi^-)(K^-\pi^+)}$: the B_s^0 and B^0 peaks may be accurately described by the same set of Hypatia parameters, provided that the central value of the distribution is shifted to account for the invariant mass difference between both mesons ($m_{B_s^0} - m_{B^0} = 87.13 \pm 0.19$ MeV/c^2 from the PDG [5]).

- **Partially reconstructed background**: all the decays in which a final state particle is missed can be described as a single contribution. Its shape can be parameterised with an ARGUS [88] function convolved with a Gaussian distribution, to consider resolution effects. The sigma of the Gaussian distribution is shared with the one from the signal Hypatias. The kinematic distributions of these events are highly correlated with those from the signal, which prevents the use of the *sPlot* technique to remove this contribution. Therefore the $M(K^\pm\pi^\mp\pi^\pm\pi^\mp) < 5200$ MeV/c^2 region is excluded from the nominal fit. Nonetheless, a control fit in the full invariant mass range is performed to ensure a good understanding of the components of the spectrum. Figure 4.14 and Table 4.13 show the results of this check.

- **Combinatorial background**: this contribution originates from the random combination of four tracks fulfilling all the selection criteria whose invariant mass value falls within the considered range in the analysis. As anticipated, this contribution does not have any peaking structure and it is therefore modelled with an exponential function, whose yield and decay parameter are allowed to float in the fit. Again, different values of these two parameters are allowed for each `Year||Trigger` sample.

- $\boldsymbol{B_s^0 \to (K^+\pi^-)(K^-\pi^+)}$: before employing negative weights to remove this background, the performance of the *sPlot* technique to remove this component was checked. For this, the invariant mass shape of these events was modelled with a CB distribution whose parameters are obtained from a fit to the corresponding simulated sample, once all selection criteria have been applied. The projections and numerical results of these fits are shown in Figure 4.16 and Table 4.15, respectively.

- $\boldsymbol{\Lambda_b^0 \to p\pi K\pi}$: this background component spans widely in the upper side of the four-body invariant mass spectrum, which hinders its effective separation from the combinatorial background contribution. This motivated the use of a dedicated PID requirement on one of the final state pions used to build the ρ^0 candidate, as explained in Section 4.2.3.

- **Other exclusive channels**: with the exception of the PID requirements, the selection that has been applied to the data sample favours any type of 4-body decays in the quasi-two-body approach, mostly due to the topological constraints applied. Therefore, contributions from decays such as $B_s \to \rho^0\rho^0$ or $B^0 \to \phi K^*(892)^0$ were included in the fit and the results compared before and after the PID criteria. It was concluded that these components were reduced to negligible levels with the PID selection. The shapes of the relevant distributions were taken from fits to simulated samples of each of the studied decay modes.

The baseline of the four-body invariant mass model is therefore composed of the $B^0 \to \rho^0 K^{*0}$, $B_s \to \rho(770)^0 K^*(892)^0$ and the combinatorial background contributions, as the partially reconstructed backgrounds need to be removed from the analysed sample in order to fulfil the requisites for using the *sPlot* technique.

4.4.2 Shapes of the B^0 and B_s^0 signal peaks from simulation

The `SVV_HELAMP(1)` sample was split according to `Year||Trigger` categories and the parameters describing the Hypatia function were obtained from the corresponding fits to the simulated data sample. These values are then used as a fixed input for the four-body invariant mass fit to describe the $B^0 \to \rho(770)^0 K^*(892)^0$ and $B_s \to \rho(770)^0 K^*(892)^0$ peaks (note that the sigma and the mean value of the peaks are not shown, as their values are taken from data not from simulation). The results of these four fits are shown in Figure 4.15 and in Table 4.14.

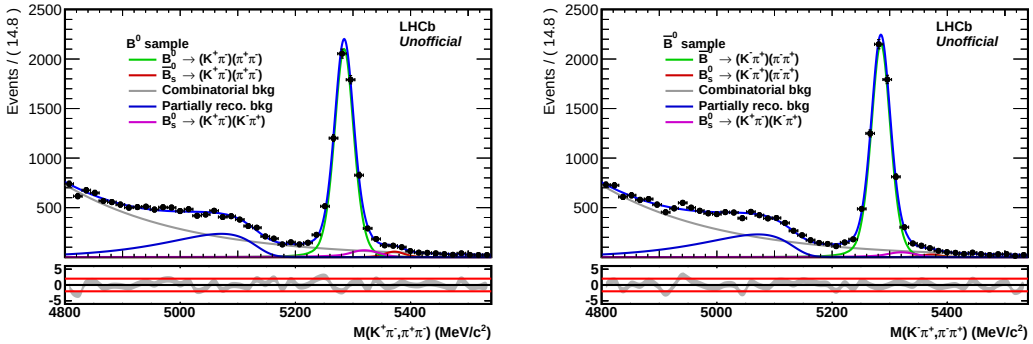

Figure 4.14: Fit to $M(K\pi\pi\pi)$ including the partially reconstructed background. The parameters of the combinatorial background and the mass and width of the signal peaks are fixed to the values obtained in this fit in order to obtain the *sWeights*.

As the amplitude fit is performed in 8 (`Flavour||Year||Trigger`) categories, in order for the *sWeights* to be correctly normalised, the four-body invariant mass fit must be split accordingly. However, there is no reason for the Hypatia parameters to depend on the flavour of the B^0 meson, so only four sets of parameters (for the trigger and year categories) are determined from simulation. Table 4.14 shows the four (`Year||Trigger`) sets of Hypatia parameters used to describe this contribution.

4.4.3 Four-body invariant mass fit results

The fit described in the previous sections is used to extract one set of *sWeights* for each fitting category. A two-step strategy is used: first, the fit shown in Figure 4.14 is performed letting all the parameters (mean value of the signal peak, its width, the combinatorial and partially reconstructed backgrounds parameters and all the yields) free to vary. On the second step, all parameters except the yields are fixed to the results obtained in the first fit and the low mass limit is shifted up to 5190 MeV/c^2. The *sWeights* are obtained from this last fit. Figure 4.17 shows this last fit results for the B^0 and $\overline{B}^0$ datasets, respectively. Table 4.16 shows the results obtained for each free parameter in each of the eight fits. For completeness of the results, the direct raw *CP* asymmetry in $B^0 \to (K^+\pi^-)(\pi^+\pi^-)$ events is computed below (only the statistical uncertainty is reported) using the results reported in Table 4.16:

$$\mathcal{A}_{rawCP}^{B\to K\pi\pi\pi} = \frac{N\left(B^0 \to (K^+\pi^-)(\pi^+\pi^-)\right) - N\left(\overline{B}^0 \to (K^-\pi^+)(\pi^+\pi^-)\right)}{N\left(B^0 \to (K^+\pi^-)(\pi^+\pi^-)\right) + N\left(\overline{B}^0 \to (K^-\pi^+)(\pi^+\pi^-)\right)} \tag{4.3}$$

$$\mathcal{A}_{rawCP}^{B\to K\pi\pi\pi} = -0.011 \pm 0.010 \tag{4.4}$$

Table 4.13: Results from the fit to $M(K\pi\pi\pi)$ including the partially reconstructed background.

	Common parameters			
m_{B^0}	5284.63 ± 0.21			
σ	19.46 ± 0.26			
	TIS	TOSnotTIS	TIS	TOSnotTIS
p_{comb}	−0.00447 ± 0.00013	−0.00481 ± 0.00018	−0.00485 ± 9e-05	−0.00475 ± 0.00012
	B			
	2011		2012	
	TIS	TOSnotTIS	TIS	TOSnotTIS
$N(B^0)$	1111 ± 40	742 ± 33	2771 ± 64	1704 ± 50
$N(B_s^0)$	15 ± 10	20 ± 8	86 ± 16	43 ± 12
$N(comb)$	2050 ± 72	1095 ± 55	4333 ± 112	2631 ± 87
$N(Part.)$	500 ± 53	410 ± 42	1350 ± 87	849 ± 67
$N(B_s^0 \to K^*\overline{K}^*)$	88 ± 29	115 ± 26	51 ± 45	131 ± 39
	Bbar			
	2011		2012	
	TIS	TOSnotTIS	TIS	TOSnotTIS
$N(B^0)$	1133 ± 40	768 ± 32	2876 ± 66	1707 ± 50
$N(B_s^0)$	0 ± 8	9 ± 7	55 ± 15	11 ± 10
$N(comb)$	1827 ± 69	1162 ± 55	4500 ± 113	2542 ± 83
$N(Part.)$	622 ± 53	330 ± 41	1311 ± 87	769 ± 63
$N(B_s^0 \to K^*\overline{K}^*)$	99 ± 29	39 ± 22	7 ± 140	131 ± 37

Table 4.14: Hypatia parameters used to describe the $B^0 \to \rho^0 K^{*0}$ and $B_s^0 \to \rho^0 K^{*0}$ peaks.

Variables	11TIS	11TOSnTIS	12TIS	12TOSnTIS
a_1	2.31 ± 0.16	2.18 ± 0.13	2.15 ± 0.09	2.21 ± 0.07
a_2	3.03 ± 0.18	2.72 ± 0.26	2.92 ± 0.13	2.76 ± 0.19
λ	−4.02 ± 0.49	−6.02 ± 1.07	−4.83 ± 0.57	−5.16 ± 0.79
n_1	1.61 ± 0.40	1.82 ± 0.43	2.20 ± 0.29	2.12 ± 0.22
n_2	2.19 ± 0.34	2.07 ± 0.43	2.04 ± 0.22	2.66 ± 0.40

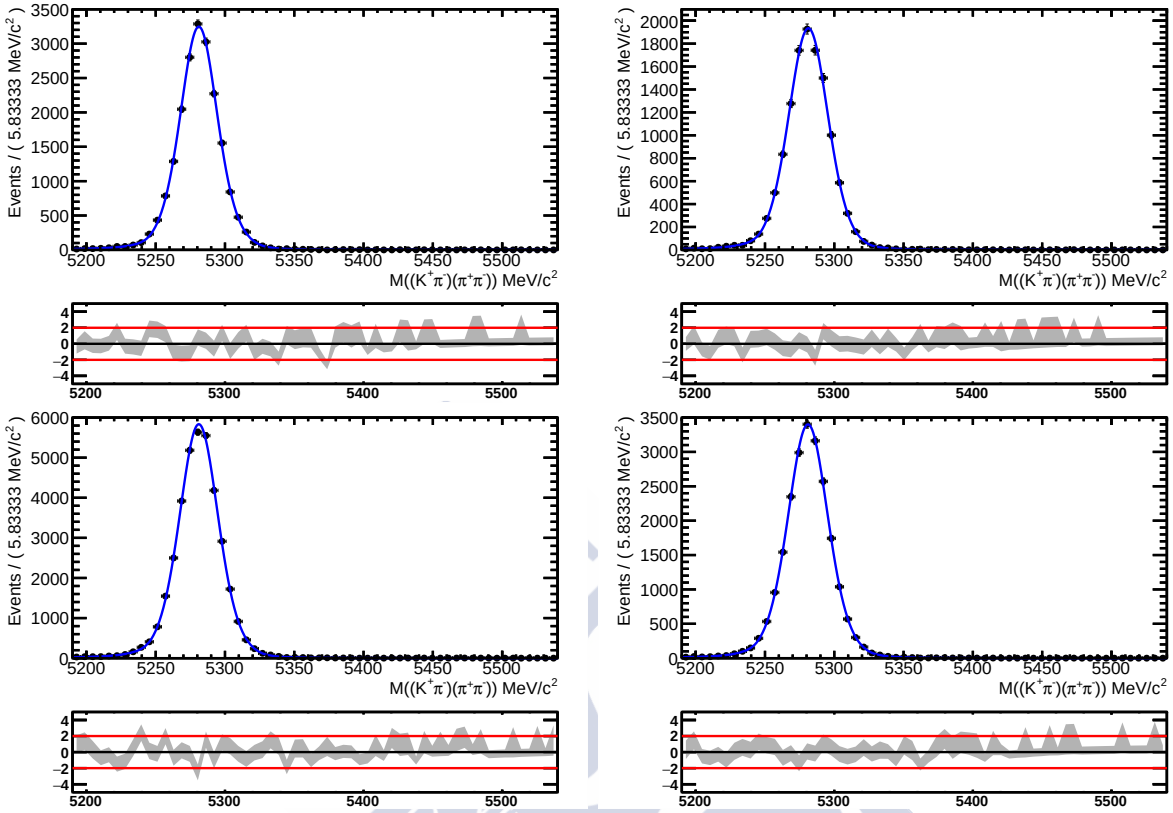

Figure 4.15: Fits to simulated $B^0 \to \rho^0 K^{*0}$ events per `Year||Trigger` categories. Results for 2011(12) are shown on the top (bottom) row, with the `TIS`(`TOSnotTIS`) on the left (right)side. The fitted values are shown in Table 4.14.

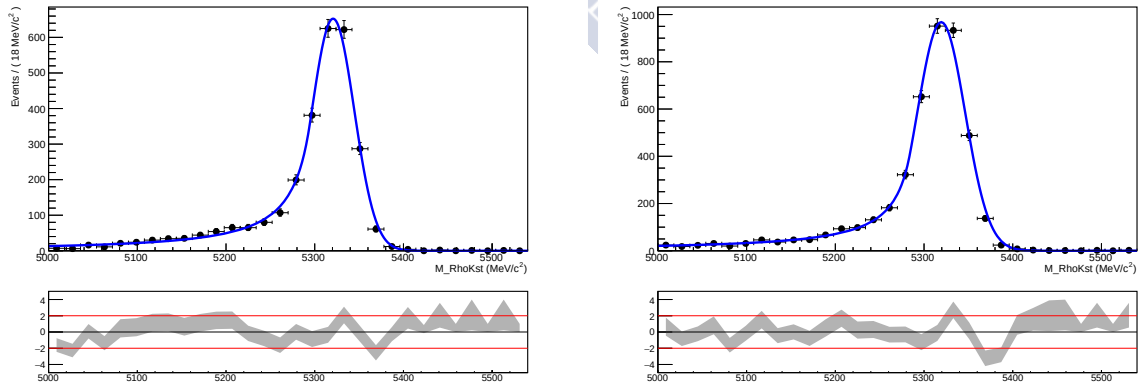

Figure 4.16: Fit to simulated $B_s^0 \to K^*(892)^0\overline{K}^*(892)^0$ events per `Year` categories (2011MC on the left and 2012MC on the right). The fitted values are shown in Table 4.15.

Table 4.15: CB parameters used to describe the $B_s^0 \to K^*(892)^0\overline{K}^*(892)^0$ peak.

Variables	2011MC	2012MC
m	5320.69 ± 0.78	5319.38 ± 0.61
σ	23.87 ± 0.58	26.92 ± 0.48
a	1.11 ± 0.07	1.31 ± 0.06
l	1.38 ± 0.15	1.18 ± 0.10

Table 4.16: Results of the simultaneous fit to the 8 `Flavour||Year||Trigger` categories. The values for the B meson mass, its σ and the parameters describing the combinatorial background are fixed to their fitted values according to this table before performing the *sPlot*.

Fixed parameters				
m_{B^0}	5284.63 ± 0.18			
σ	17.59 ± 0.17			
	TIS	TOSnotTIS	TIS	TOSnotTIS
p_{comb}	−0.00441 ± 0.00055	−0.00557 ± 0.00087	−0.00452 ± 0.00040	−0.00559 ± 0.00057
B				
	2011		2012	
	TIS	TOSnotTIS	TIS	TOSnotTIS
$N(B^0)$	985 ± 34	615 ± 27	2451 ± 54	1422 ± 41
$N(B_s^0)$	20 ± 9	7 ± 5	62 ± 13	30 ± 9
$N(comb)$	249 ± 23	134 ± 17	487 ± 35	250 ± 24
Bbar				
	2011		2012	
	TIS	TOSnotTIS	TIS	TOSnotTIS
$N(B^0)$	1013 ± 34	620 ± 26	2521 ± 53	1439 ± 40
$N(B_s^0)$	4 ± 7	6 ± 4	46 ± 13	12 ± 7
$N(comb)$	204 ± 22	69 ± 12	437 ± 32	220 ± 23

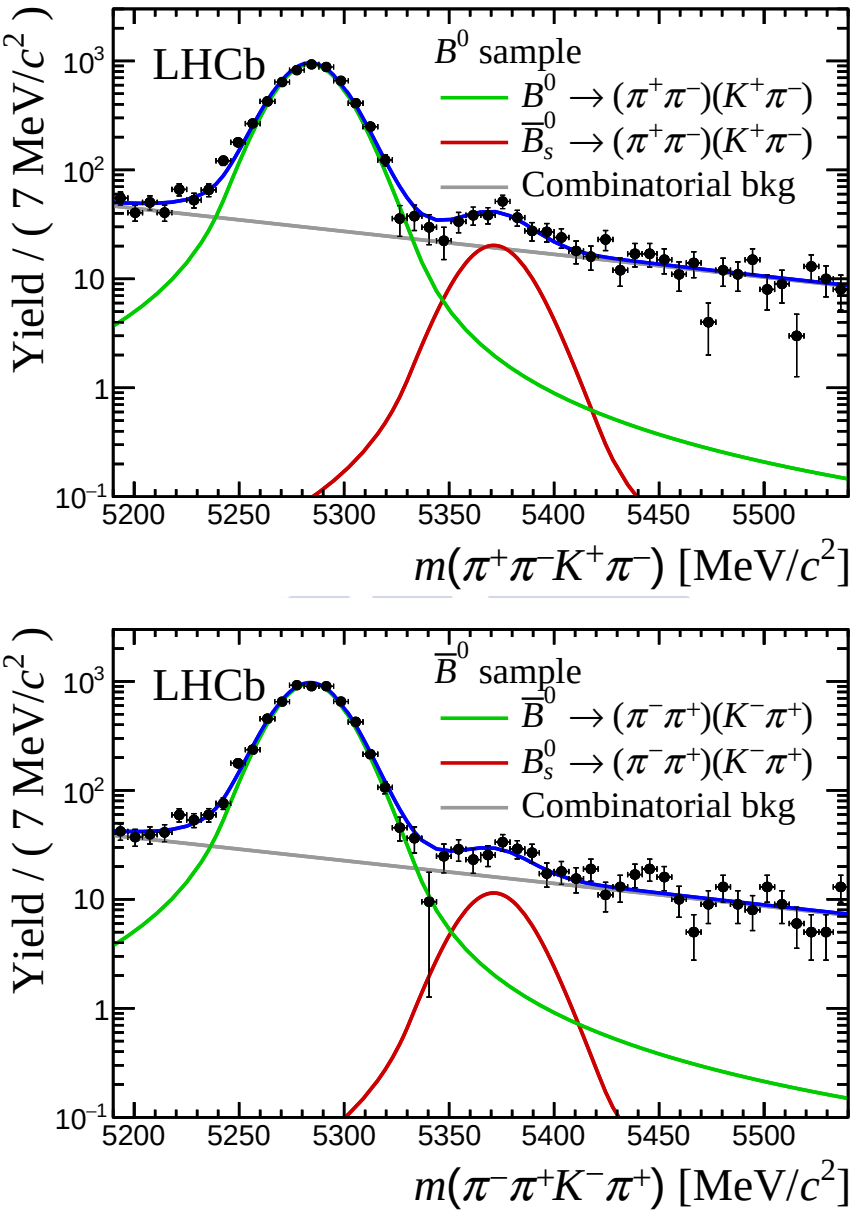

Figure 4.17: Four-body mass spectra fits for B^0 (top) and $\bar{B}^0$ (bottom).

USC
UNIVERSIDADE
DE SANTIAGO
DE COMPOSTELA

5

Amplitude analysis of $B^0 \to (\pi^+\pi^-)(K^+\pi^-)$ events

In this Chapter the details of the amplitude analysis of the B^0 decay to the $(\pi^+\pi^-)(K^+\pi^-)$ final state in the two-body invariant mass windows $300 < m(\pi^+\pi^-) < 1100\,\text{MeV}/c^2$ and $750 < m(K^+\pi^-) < 1200\,\text{MeV}/c^2$ are presented. In the considered $(\pi^+\pi^-)$ invariant-mass range the vector resonances ρ^0 and ω are expected to contribute, together with the scalar resonances $f_0(500)$, $f_0(980)$ and $f_0(1370)$. The $(K^+\pi^-)$ spectrum is dominated by the vector $K^*(892)^0$ resonance, but contributions due to the nonresonant $(K^+\pi^-)$ interaction and the $K_0^*(1430)^0$ state will also be accounted for.

Section 5.2 is devoted to discuss the systematic uncertainties, including their nature and estimating their impact on the reported measurements. By performing the amplitude fit, a measurement of the *CP* asymmetries for the different amplitudes is made, whereas no attempt is done to measure the overall branching fraction or the global direct *CP* asymmetry. The focus of the analysis is on the polarisation fractions of the vector-vector modes as well as the relative phases of the different contributions. The discussion of these results closes the chapter.

5.1 Engine of the 5D fit

In this section, practical and implementation details regarding the fitting `PDF` introduced in Section 1.2.2 are discussed. The strategy followed to deal with the acceptance

effects is explained and the fitting framework is validated in terms of fits to simulated data samples and the study of pseudoexperiments (or toy MC) generated with the fitting `PDF`.

5.1.1 Acceptance effects

The angular distributions are affected by selection requirements and by the detector geometry, and thus the angular acceptance must be determined. Its analytical form is unknown and it is expected to depend on all the kinematic variables in a complicated way. In order to account for its effects the normalisation weights method [73] is commonly used in LHCb analyses.

Particularising Equation 3.4 from Chapter 3 for this analysis,

$$\int \Phi_4 \sum_{i=1}^{14} \sum_{j=1}^{i} (A_i \cdot g_i \cdot M_i)(A_j \cdot g_j \cdot M_j)^* \varepsilon(X) d^5X = \sum_{i=1}^{14} \sum_{j=1}^{i} A_i A_j^* w_{ij}, \tag{5.1}$$

It can be noted that 105 complex numbers have to be calculated in order to use this method. These correspond to 210 real parameters that should be obtained from integrals (approximated by sums) performed with the events in the simulated data sample.

In order to get a better description of the considered phase space (wider than that populated by the ρ^0 and $K^*(892)^0$ resonances), the two simulated data samples documented in Section 4.1 are combined following the method described in Section 3.3.

As introduced in Equation 3.4, the normalisation weights represent integrals in the 5D space. These are needed to perform the fit, but, in order to visualise 1D distributions (or to generate toy experiments), 4D integrals are required instead. Model visualisation can be achieved by reweighting the simulated data samples with the set of amplitudes resulting from the fit, however, toy MC experiment generation requires an analytical treatment of the acceptance. For this purpose, a factorised acceptance is defined as:

$$\varepsilon(X) \sim \varepsilon_1(\cos\theta_{12}) \cdot \varepsilon_2(\cos\theta_{34}) \cdot \varepsilon_3(\phi) \cdot \varepsilon_4(m_{12}) \cdot \varepsilon_5(m_{34}), \tag{5.2}$$

where each term can be extracted from a fit to the correspondent projection of the simulated events, provided that the generation model has been accounted for. The approximation $\varepsilon_3(\phi) = \varepsilon_4(m_{12}) = \varepsilon_5(m_{34}) = C$ is applied, as the 1D projections of the acceptance (see Figure 5.1) are reasonably flat. On the other hand, $\varepsilon_1(\cos\theta_{12})$ and $\varepsilon_2(\cos\theta_{34})$ are parametrized with a 4^{th}-order polynomial depending on, respectively, $\cos\theta_{12}$ and $\cos\theta_{34}$. The function $\varepsilon_2(\cos\theta_{34})$ is expected to be asymmetric due to the K/π mass difference. On the other hand, $\varepsilon_1(\cos\theta_{12})$ should have been symmetric, as both particles in m_{12} are pions. However, since there is a requirement (removal of D decays) on the mismatched $(K^\pm\pi^\mp)$ pairs, the $\cos\theta_{12}$ spectrum becomes asymmetric too. Both acceptances are parametrised as:

$$\varepsilon(\theta_{ij}) = 1 + a \cdot \cos\theta_{ij} + b \cdot \cos^2\theta_{ij} + c \cdot \cos^3\theta_{ij} + d \cdot \cos^4\theta_{ij}, \tag{5.3}$$

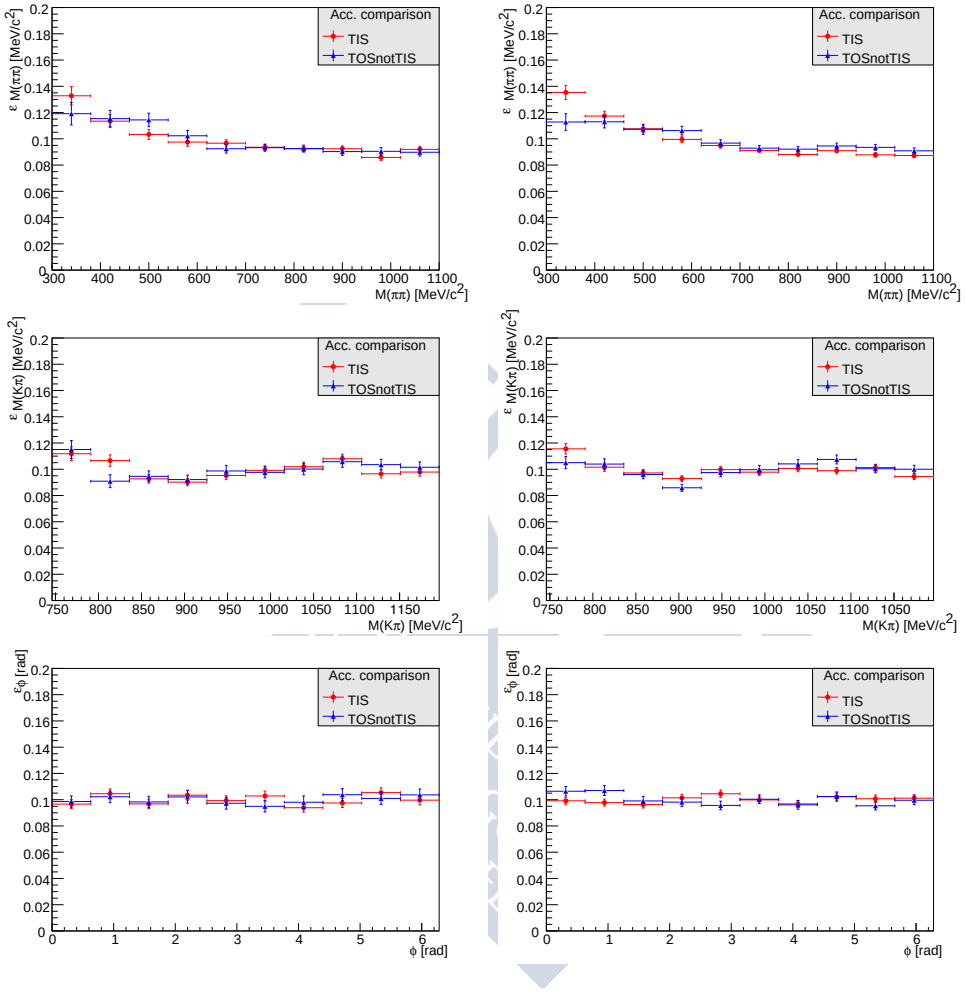

Figure 5.1: Projections of the LHCb acceptance on the two-body invariant masses and the angle ϕ, split by year, 2011 (left) and 2012 (right) and trigger category (`TIS` in red and `TOSnoTIS` in blue). The used simulated data sample was the combination of `SVV_HELAMP(2)` and phase space. These projections have illustrative purposes only, as the acceptance is assumed to be flat on these variables for toy-generation and toy-visualisation purposes.

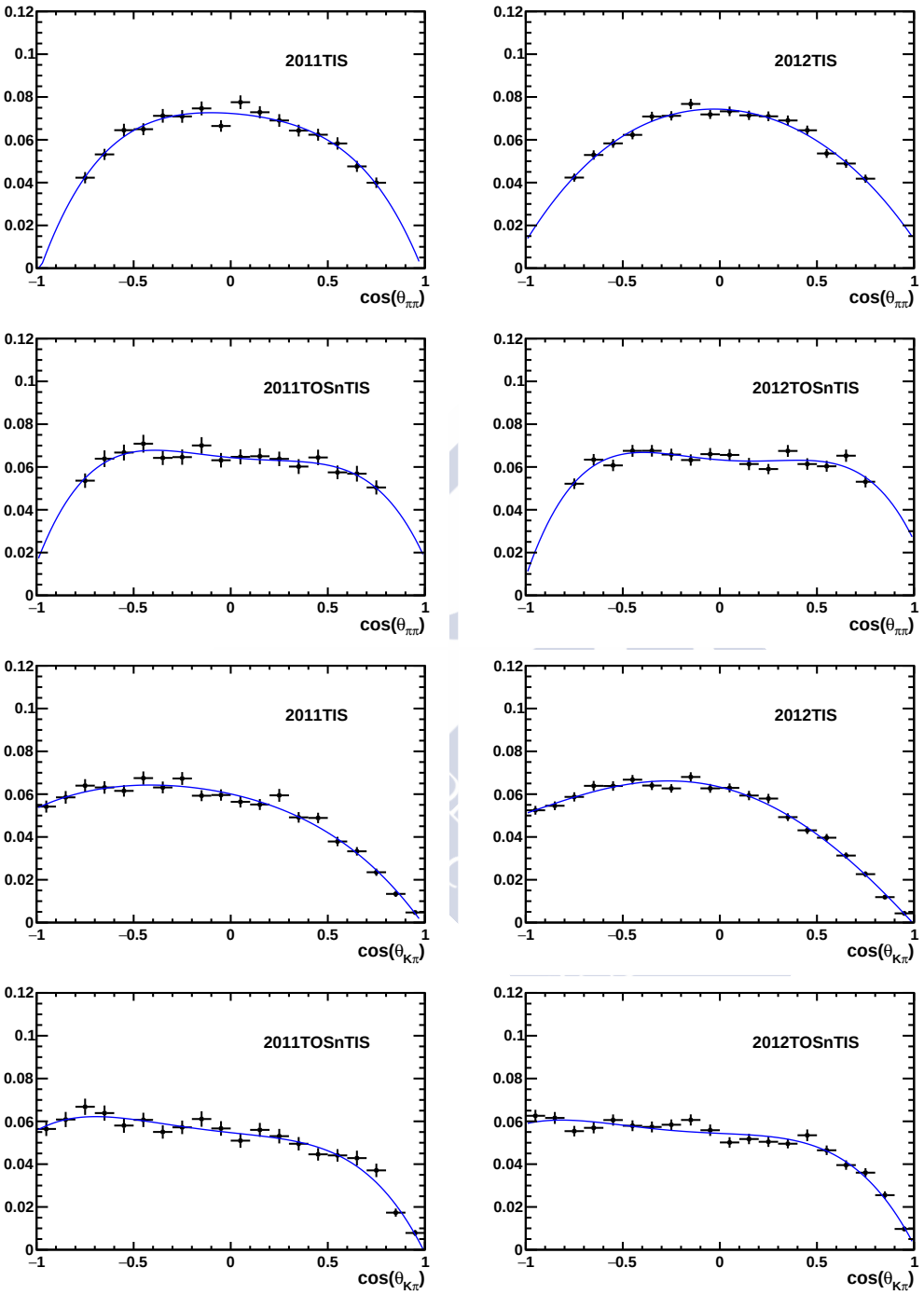

Figure 5.2: Projections of the LHCb acceptance on the $cos\theta_{K\pi}$ and $cos\theta_{\pi\pi}$ variables per year and trigger categories. The simulated data sample used was the combination of `SVV_HELAMP(2)` and phase space. This shape is parametrised with a fourth order polynomial only for visualisation purposes. The results for the fits are shown in Table 5.1.

Table 5.1: Coefficients of the fourth-order polynomials used to describe the factorised acceptance in $\cos\theta_{12}$ and $\cos\theta_{34}$.

	2011			
	TIS		TOSnotTIS	
	$\cos\theta_{12}$	$\cos\theta_{34}$	$\cos\theta_{12}$	$\cos\theta_{34}$
a	-0.087 ± 0.054	-0.336 ± 0.042	-0.133 ± 0.076	-0.182 ± 0.056
b	$-0.40\ \pm0.19$	$-0.44\ \pm0.10$	$0.21\ \pm0.26$	$0.06\ \pm0.15$
c	$0.10\ \pm0.13$	-0.124 ± 0.060	$0.15\ \pm0.18$	-0.342 ± 0.081
d	$-0.66\ \pm0.33$	$-0.14\ \pm0.11$	$-0.96\ \pm0.46$	$-0.56\ \pm0.17$
	2012			
	TIS		TOSnotTIS	
	$\cos\theta_{12}$	$\cos\theta_{34}$	$\cos\theta_{12}$	$\cos\theta_{34}$
a	-0.042 ± 0.040	-0.347 ± 0.030	-0.111 ± 0.058	-0.077 ± 0.043
b	$-0.71\ \pm0.14$	-0.693 ± 0.075	$0.33\ \pm0.20$	$0.02\ \pm0.11$
c	0.049 ± 0.092	-0.062 ± 0.042	$0.25\ \pm0.14$	-0.444 ± 0.064
d	$-0.12\ \pm0.24$	$0.09\ \pm0.78$	$-1.07\ \pm0.36$	$-0.46\ \pm0.13$

the coefficients being determined from simulation. These coefficients are shown in Table 5.1 and the corresponding fits are shown in Figure 5.2.

It should be emphasised that the normalisation weights account for the normalisation of the fitting PDF within the LHCb acceptance, therefore, they must be computed separately for each fitting category with different kinematic properties. However, there is no reason why the kinematic distributions for the B^0 or $\overline{B}^0$ samples should be different (apart from polarisation induced effects due to B^0-$\overline{B}^0$ asymmetries, which would be beyond the sensitivity achievable with the considered simulated sample size). Therefore, four sets of normalisation weights for the four `Year||Trigger` categories are computed.

5.1.2 Visualisation of the fitting model

The acceptance effects induced by the detector and the selection requirements must be taken into account when making projections of the fitted model onto different slices of the data sample. This can be implemented following two different approaches, which make use of different assumptions.

On the one side, the parametric acceptance described in the previous section may be used to shape the PDF according to the acceptance effects, making it suitable for direct comparison with data. It should be reminded that this approach makes strong assumptions on how the acceptance on one variable affects the acceptance on the others. In particular, all five observables are assumed to factorise and a one-dimensional function is fitted to each projection, disregarding all correlations. While this is a strong assumption,

a posteriori comparisons prove that a satisfactory agreement is achieved between the data and the fitted model projections. This validates the use of the parametric acceptance description for the generation of pseudo-experiments and other self-consistency checks of the model.

On the other hand, simulated data samples can be used to extract the acceptance effects on an event-per-event basis. Consequently, this approach accounts for the correlations among observables by construction, but does not provide with an analytical description of these effects. From the technical point of view, the implementation of this method is very similar to what is done to compute the normalisation weights described in the previous section. The difference arises on the function that is used to re-weight the simulated data sample with: for this application, the only function used is the signal `PDF` where the physical parameters are fixed to the values yielded by the amplitude fit. It should be noted that, in order to follow this approach, all data-simulation corrections need to be applied beforehand. The use of this visualisation method assumes that the simulated data correctly models all features in data, from the kinematic distributions to the correlations among the observables. These are the same assumptions that were previously tested in order to validate the use of the normalisation weights technique to compute the normalisation integral of the `PDF`. Therefore, this is the preferred method of visualisation since the overall approach is made much more consistent by not using different assumptions at different levels of the analysis.

5.1.3 Checks for the combination of the simulated data samples

The normalisation weights and the coefficients for the factorised acceptance functions are computed in the combined (`SVV_HELAMP` + `PHSP`) sample in the nominal fitting framework. This has a direct impact in the precision the normalisation weights are computed with, and thus, in the fit performance and accuracy. To check that nothing unexpected is arising from this combination, the normalisation weights are computed separately in each sample and the obtained results are compared with the nominal version. Figure 5.3 shows the pull distributions for these comparisons, where no big deviations are seen. The spread in the pulls is expected due to the large uncertainties that the normalisation weights related to the S-waves have in the `SVV_HELAMP` sample.

5.1.4 Parameterisations

The parametrisation of the complex amplitudes of the `PDF` introduced in Equation 1.8 can be done in several ways. The squared moduli of the complex amplitudes is the most similar parameter to a branching ratio in an amplitude analysis, thus appealing to be used as reference for comparison of experimental and theoretical results. Theoretical works usually predict the values of the polarisation fractions and the phase difference among the different amplitudes. However, from the mathematical point of view of the fitting framework, these parameters result in poor fit performances for various reasons.

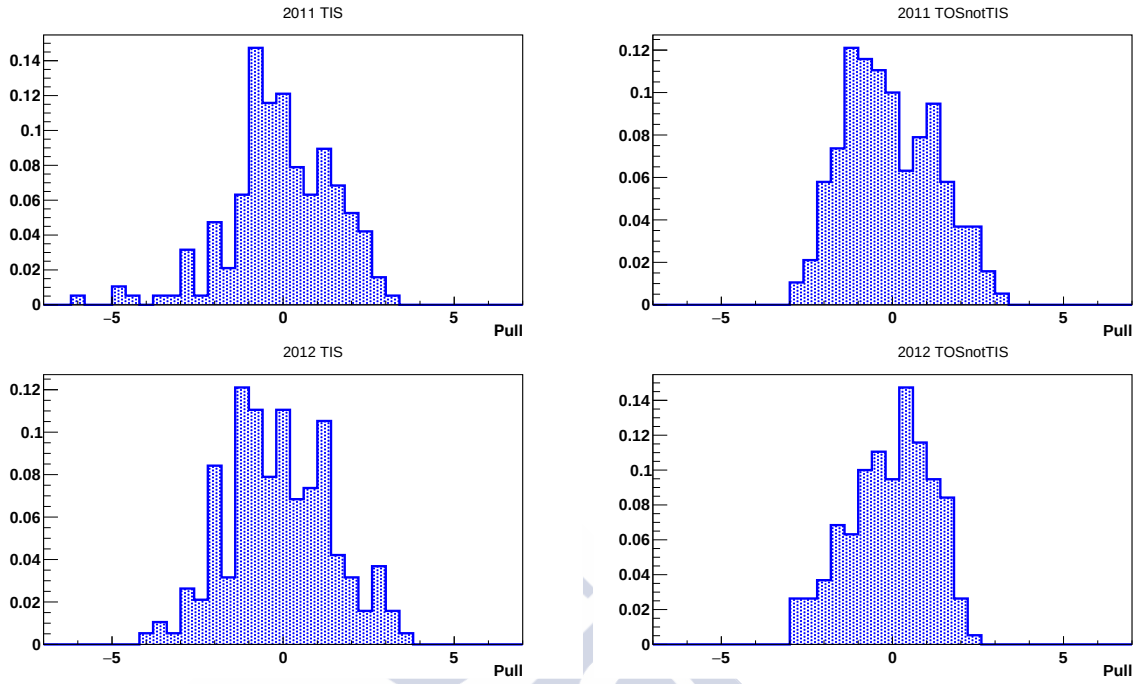

Figure 5.3: Pull distributions for the normalisation weights computed with the two simulated data sub-samples when compared with the nominal (combined) one.

On the one side, their values are, by definition, constrained to the range between 0 and 1. While these values are perfectly valid, the study of the fit convergence and stability in the boundary of a parameter phase space is complicated and results in non-gaussian behaviour of the pull distributions and, in occasions, unreliable estimation of the uncertainties. The normalisation condition of the PDF would naturally arise from the normalisation condition of the three polarisation fractions, which, by construction, must add up to unity. This again is a valid choice, although problematic from the mathematical point of view in the boundaries of the physical regions. Finally, all these problems are aggravated once the phases are taken into account, since, in case of small values of an amplitude, the fit sensitivity on its corresponding phase is very poor. This results in unconstrained degrees of freedom that can badly affect the convergence of the fit.

In order to mitigate these effects and achieve better fit performances, polar coordinates are reparameterised in the cartesian basis. With this choice, the sensitivity on the phases is no longer determined by the magnitude of the corresponding amplitude, since both the real and imaginary part of these amplitude are parameters of the fit and both the phase and the magnitude are determined as a function of these. The normalisation condition in this case is imposed by fixing the real and imaginary part of one of the contributing amplitudes. This also provides an easy way of changing the overall scale of the fit parameters (setting the global reference to different values).

Therefore, the real ($Re(A_i)$) and imaginary ($Im(A_i)$) parts of the complex amplitudes

(A) of each considered wave (i) are the fit parameters. The modulus ($|A^i|^2$) and phase (δ^i) for each wave are also parameters of interest and can be derived from the aforementioned real and imaginary parts of each A^i. The same applies for the polarisation fractions of the two vector-vector modes (f_λ^{VjV}), the phase difference ($\Delta(\delta_{||}^{V1V} - \delta_{\perp}^{V1V})$) between the parallel and perpendicular amplitudes of the $B^0 \to \rho^0 K^{*0}$ mode and all the *CP*-averages and asymmetries that are computed. Due to the high correlations at play, these reparameterisations into the final set of observables (also referred to as derived quantities) deserve special attention when computing the uncertainties of the different observables. More details are given in Sections 5.1.5 and 5.2, regarding the statistical and systematic uncertainties, respectively. It can be anticipated that the need to account for correlations implies that the extended set of observables will need to be considered in both cases, rather than the fit parameters alone.

5.1.5 Fitting frameworks

Given the complexity of the fit presented in this document and due to the modest performance `RooFit` displayed when working with weighted maximum likelihood fits in many dimensions, alternative fitting frameworks were searched for, aiming to improve computing time and the stability of the results.

For historical reasons, the analysis first relied on the `RooFit` framework, using Minuit as minimisation algorithm. The many layers of the `RooFit` interface and its use of CPUs, even if parallelisation is available, turns this fitter into a robust but rather slow one (as orientation, one fit to a toy MC sample with similar size as the analysed data sample takes ∼15min). The robustness of the results gets compromised when introducing weighted data samples, as the shape of the $\log(\mathcal{L})$ function is no longer smooth. Minuit relies on the values of the partial derivatives of this function to reach the minimum and to estimate the parameter errors, therefore, its convergence criteria might be challenging to fulfil in weighted fits. This situation gets more complicated as the fit dimensions and the number of free parameters increase.

Issues related with long computing time were tackled by implementing the fitting `PDF` in the `Ipanema` framework which allows to parallelise over the cores of Graphical Processing Units (GPU), rather than conventional CPUs. This results in a computing time of ∼8s when using Minuit to fit a toy MC sample containing as many events as the nominal data sample. This framework is implemented using pyCUDA [89] and includes minimisation algorithms other than Minuit. In particular, it serves as interface with the MultiNest package [75–77], which, as introduced in Section 3.5, uses nested sampling to calculate the most likely values of the fitted parameters. Not relying on partial derivatives of the $\log(\mathcal{L})$ function, the MultiNest method is unaffected by the difficulties Minuit may encounter in fits to weighted data samples.

In the following, the validation of the three fitting frameworks is presented. This consists of the results of the fit to the simulated data sample generated with the `SVV_HELAMP(2)` model and of the pull distributions study for each minimiser (Minuit (GPU)

and MultiNest).

The analysis relies on MultiNest to perform all the fits to weighted data samples, namely, the nominal fit and some of those needed to asses systematic uncertainties depending on different aspects of the data sample. The `RooFit` framework profits from years of use and has several very useful built-in implementations. Efficient toy MC generation, persistence and input/output handling of objects being the most profitable features for this work. Finally, the `pyCUDA` based fit offers the best time-wise performance, which makes it ideal to compute all the systematic uncertainties based on toy MC studies.

As explained in the previous section, the fit performance and stability greatly improves if changing the parametrisation of the fit variables from the polar ($|A|e^{i\delta}$) to the cartesian ($Re(A_i), Im(A_i)$) basis. The two main reasons for this choice were, firstly, that the cartesian parametrisation significantly reduces correlation among variables, which eases fit convergence; and, secondly, that the existence of amplitudes with tiny values of $|A|^2$ spoils any sensitivity on the corresponding phase. Therefore, the fit parameters for which the pull distributions are computed in the sections below are the real and imaginary parts of each amplitude. To also obtain an estimation on the biases induced when the fit parameters are expressed in the other basis ($|A|^2, \delta$), as well as on other parameters of interest ($f_\lambda^{V1V}, f_\lambda^{V2V}$, $\lambda = 0, ||, \perp$), the correlation matrix among all the fit variables is used to compute, for each fit result, the statistical uncertainty on each derived quantity (modulus, phases and f_λ^i). This provides $\mu_i \pm \sigma_i$ for every variable, regardless of it being directly obtained from the fit result of from a combination of fit parameters, which allows to compute the pull distribution for all of them.

Minuit Fitter (CPU, `RooFit`)

Fit to simulated sample The simulated data sample generated with the `SVV_HELAMP(2)` model is used in a self-consistency check to first, obtain a dedicated set of normalisation weights, and then be fitted back using these to account for the acceptance effects. This fit validates the implementation of the fitting framework and the normalisation weights technique. The ρ^0 and $K^*(892)^0$ resonances are described with the $BW^{MC}(m, L = 1)$ and $\Phi_4^{MC}(m)$ models detailed in Section 1.2.2.

The fit projections superimposed to the simulated data are shown in Figure 5.4. Table 5.2 shows the comparison between the generated and the fitted values of the physical parameters in this simulated sample. In order to fully validate the fitting framework, this fit was performed in the 8 `Flavour||Year||Trigger` fitting categories, the corresponding normalisation weights shown in Table 5.3.

Minuit Fitter (GPU)

Fit to simulated data sample The same strategy as described in the previous section is followed. The `pyCUDA` based fit results are shown in Table 5.4.

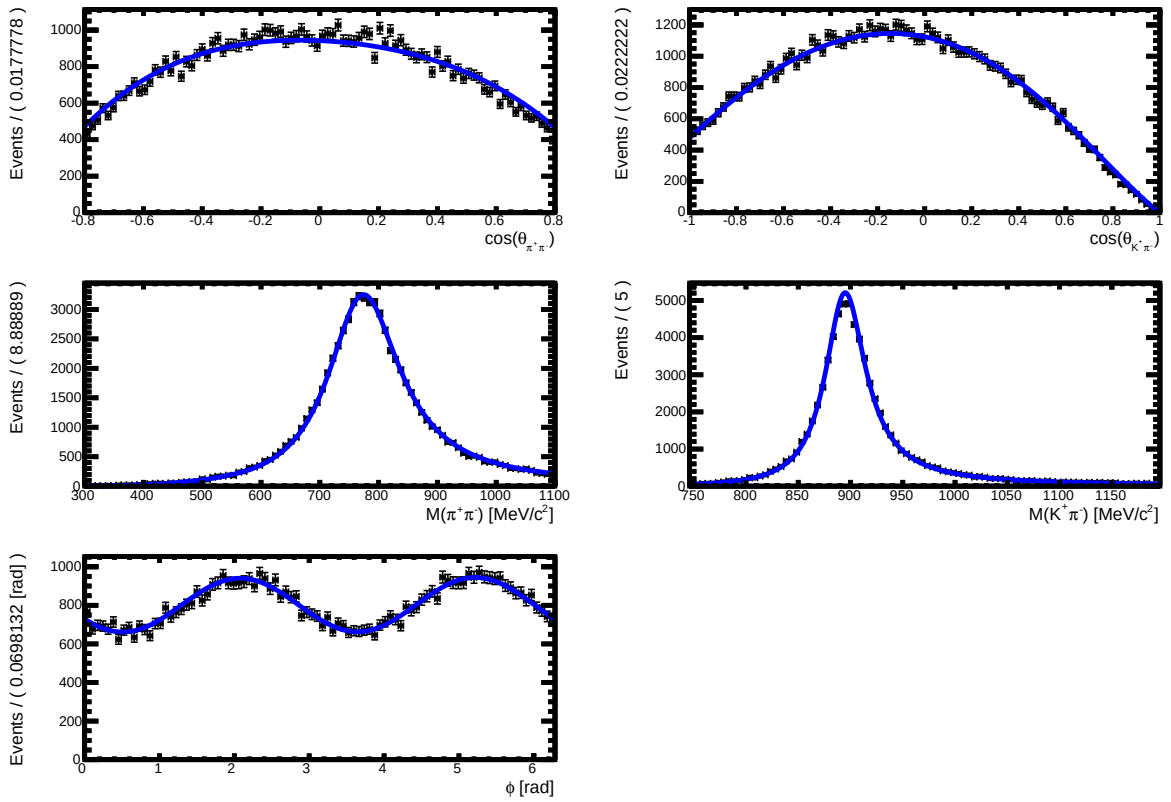

Figure 5.4: Projections of the fit (solid blue line) to the `SVV_HELAMP(2)` simulated data sample (black dots) performed with the normalisation weights in Table 5.3. The results shown are summed over all the fitting categories.

Table 5.2: Results from the fit to the `SVV_HELAMP(2)` simulated data sample. Generation values are shown for reference. The phase δ_0 is taken as a reference and $|A_\perp|^2 = 1 - \sum_{\lambda=0,||} |A_\lambda|^2$ is obtained from the normalisation condition.

Parameter	Generated	Fitted
$\|A_0\|^2$	0.3333	0.3333 ± 0.0029
$\|A_{\|\|}\|^2$	0.2969	0.2969 ± 0.0023
$\|A_\perp\|^2$	0.3699	0.3698 ± 0.0024
$\delta_{\|\|}$	1.30	1.2968 ± 0.0092
$\delta_\perp$	1.47	1.4736 ± 0.0093

Biases check Induced fit biases during the minimisation are studied with simplified toy MC samples. First, N datasets (of a sample size similar to the signal one) experiments are generated according to the presented model and with initial values taken from the results of the nominal fit (x_{gen}). These are then fitted back with the same `PDF` and the pull distribution, as defined below, is computed,

$$x_{pull} = \frac{x_{fitted} - x_{gen}}{\sigma_x}. \tag{5.4}$$

From the definition above, these distributions are expected to behave as Gaussians with $\mu = 0$ and $\sigma = 1$.

A total of 800 toy MC experiments were generated with the `Roofit` framework and fitted back with the `PDF` implemented using `pyCUDA`. All results agree with the expectations and no significant biases are seen.

MultiNest fitter (GPU)

Fit to simulated data sample The same strategy as described in the previous section is followed. The results obtained with MultiNest are shown in Table 5.5. The statistical uncertainty on the derived quantities is obtained from the spread of their corresponding pull distributions, in order to account for the correlations among the fit parameters in their estimation.

Biases check The set of 800 toys described in the previous section are now fitted back with MultiNest, all the results showing reasonable agreement with the expectations and not introducing significant biases from the fitting method. Figures 5.5, 5.6 and 5.7 summarise the values obtained for the mean and sigma for each pull distribution.

Table 5.3: Normalisation weights used in the fit to the `SVV_HELAMP(2)` sample. The PDF terms correspond to those in Equation 1.8 when only the 3 waves (0,|| and $\perp$) of the ρ^0 $K^*(892)^0$ mode are considered. B^0 and $\overline{B}^0$ samples share the same set of normalisation weights.

$A_iA_j^*$	w_{ij}			
	2011		2012	
	`TIS`	`TOSnotTIS`	`TIS`	`TOSnotTIS`
$\|A_0\|^2$	1.000 ± 0.025	1.000 ± 0.031	1.000 ± 0.026	1.000 ± 0.019
$\|A_{\|\|}\|^2$	3.230 ± 0.024	2.451 ± 0.024	3.221 ± 0.017	2.431 ± 0.018
$\|A_\perp\|^2$	3.179 ± 0.029	2.398 ± 0.031	3.263 ± 0.029	2.419 ± 0.021
$A_0A_{\|\|}^*$	0.031 ± 0.027	−0.002 ± 0.029	−0.003± 0.019	−0.036 ± 0.021
$A_\perp A_0^*$	−0.009 ± 0.043	0.030 ± 0.051	−0.051 ± 0.050	0.025 ± 0.031
$A_\perp A_{\|\|}^*$	0.097 ± 0.042	0.029 ± 0.041	0.010 ± 0.030	−0.010 ± 0.030

Table 5.4: Results from the fit to the `SVV_HELAMP(2)` simulated data sample with the `pyCUDA` based fit. Generation values are shown for reference. The phase δ_0 is taken as a reference and $|A_\perp|^2 = 1 - \sum_{\lambda=0,||} |A_\lambda|^2$ is obtained from the normalisation condition.

Parameter	Generated	Fitted
$\|A_0\|^2$	0.3333	0.3334 ± 0.0029
$\|A_{\|\|}\|^2$	0.2969	0.2968 ± 0.0023
$\|A_\perp\|^2$	0.3699	0.3698 ± 0.0024
$\delta_{\|\|}$	1.30	1.2968 ± 0.0092
$\delta_\perp$	1.47	1.4735 ± 0.0093

Table 5.5: Results from the fit to the `SVV_HELAMP(2)` simulated data sample with MultiNest. Generation values are shown for reference. The phase δ_0 is taken as a reference and $|A_\perp|^2 = 1 - \sum_{\lambda=0,||} |A_\lambda|^2$ is obtained from the normalisation condition.

Parameter	Generated	Fitted
$\|A_0\|^2$	0.3333	0.3333 ± 0.0030
$\|A_{\|\|}\|^2$	0.2969	0.2969 ± 0.0023
$\|A_\perp\|^2$	0.3699	0.3698 ± 0.0024
$\delta_{\|\|}$	1.30	1.297 ± 0.009
$\delta_\perp$	1.47	1.474 ± 0.009

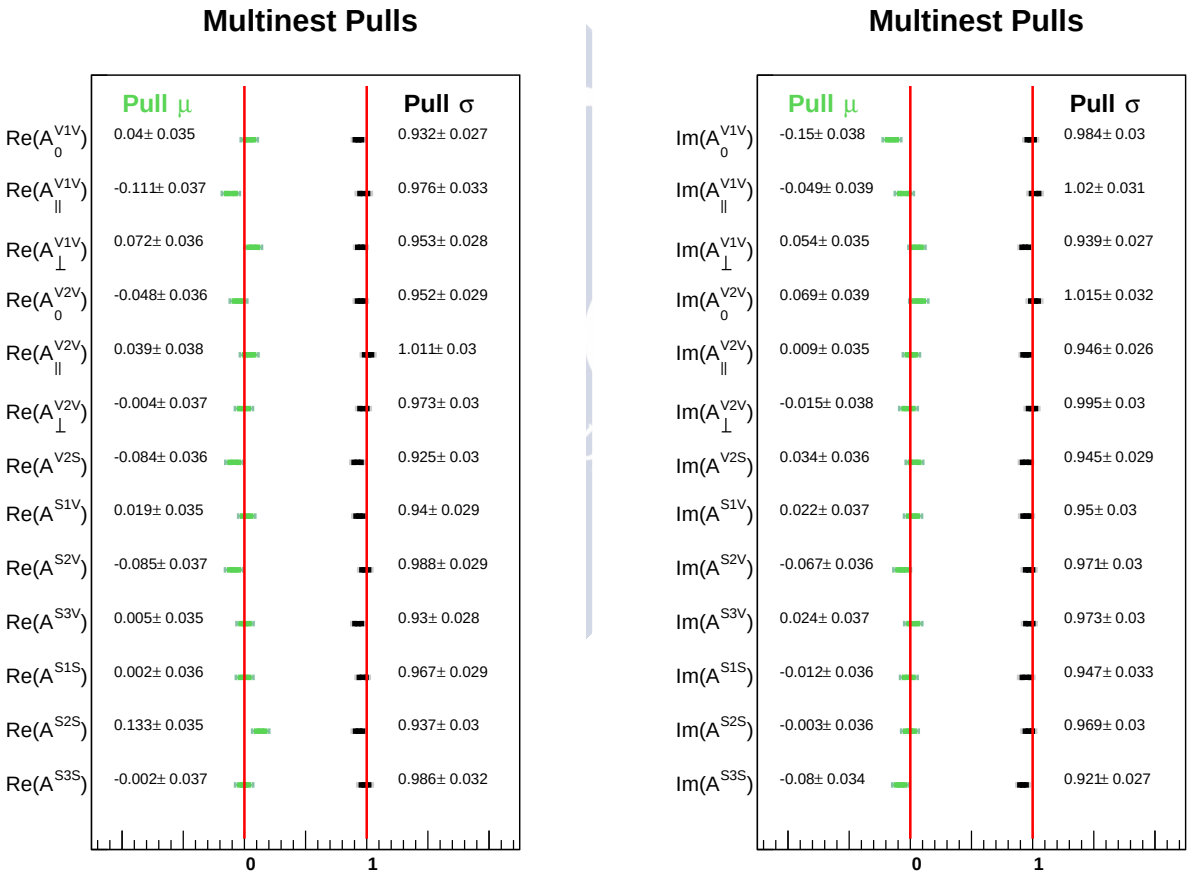

Figure 5.5: Summary of the results obtained using MultiNest from the study of the pull distributions for each fit parameter.

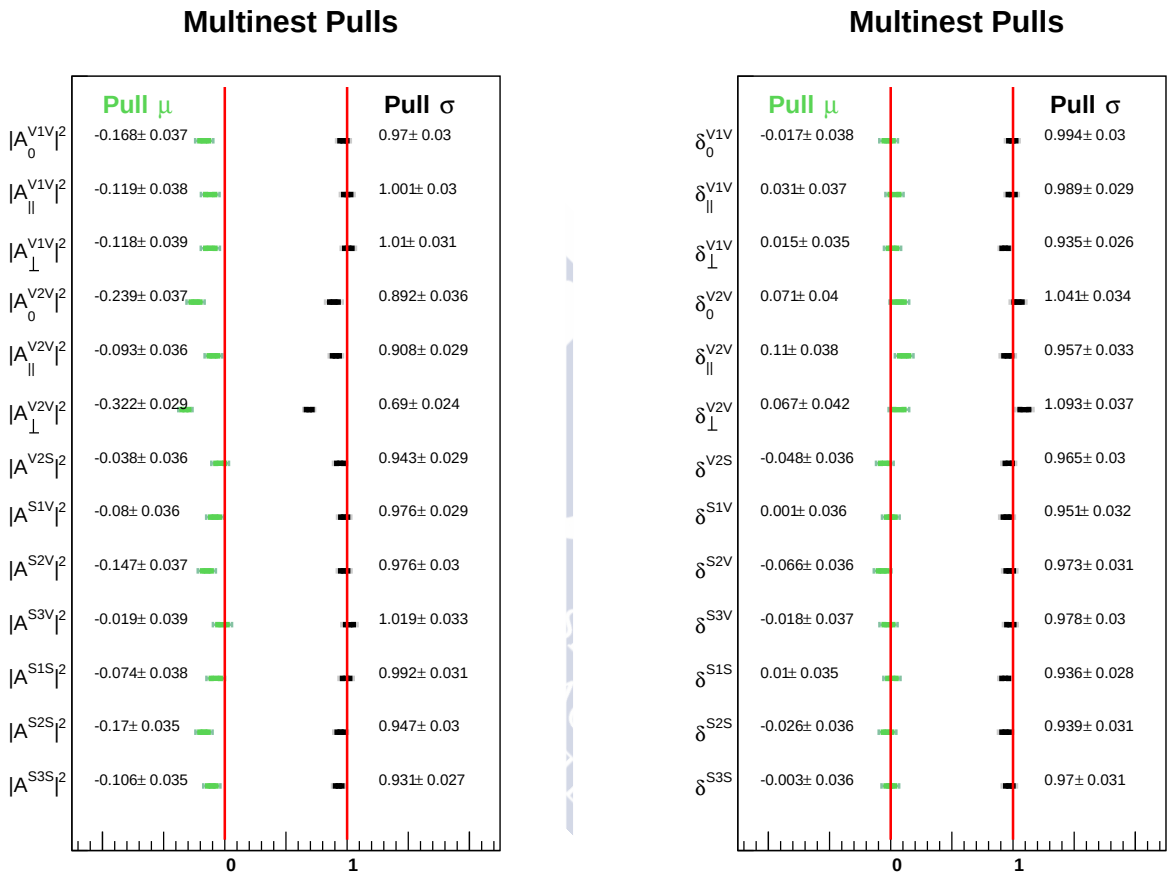

Figure 5.6: Summary of the results obtained using MultiNest from the study of the pull distributions for the derived magnitudes and phases of each amplitude.

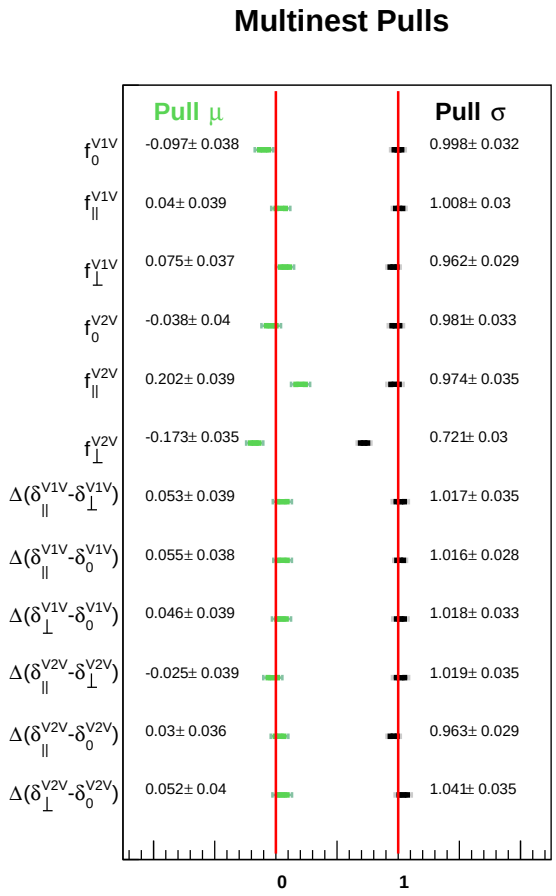

Figure 5.7: Summary of the results obtained using MultiNest from the study of the pull distributions for the VV observables redefined in their own reference system.

5.2 Systematic uncertainties

During the model building phase and the design of the analysis chain, several compromises are made that can potentially induce a bias in the final results. These effects are referred to as systematic uncertainties and are, as introduced, completely dependent on the analysis strategy.

In the paragraphs below, the different sources of systematic uncertainties that were studied are described and their values are summarised at the end of the section. In each sub-section, the corresponding systematic uncertainty, together with the method that was used to asses it, are explained. As already mentioned, the systematic uncertainties are evaluated for the *CP*-averages and asymmetries in addition to the fit parameters, ensuring the correct propagation of the correlations among variables in the estimation of the uncertainty. To facilitate the reading and comparison of the different values, the results are summarised in Section 5.2.7 where Tables 5.14, 5.15 and 5.16 comprise the systematic uncertainties on the fit parameters and Tables 5.17 and 5.18, for the *CP*-averages and asymmetries. The combination of the systematic uncertainties is also discussed in this section. The statistical uncertainty on each parameter, obtained as explained in Section 5.1.5, is shown in the same tables for reference.

From the technical point of view, the propagation of the correlated uncertainties is implemented using the `correlated_values` method from the `uncertainties` [90] python package. The generation correlated random numbers following a multi-dimensional Gaussian distribution (defined by the collection of means, μ_j, and the covariance matrix, C_{ij}, for i dimensions) may be computed using linear algebra with matrices or, directly, with the `multivariate_normal` method available in `NumPy`, as introduced in Chapter 3.

5.2.1 Parameters used in the description of the resonances lineshape

Two main assumptions were made when defining the description of the two-body invariant mass lineshape, resulting in two sources of uncertainties that need to be evaluated. The first systematic uncertainty arises from the fact that all the parameters modelling the mass propagators (such as the nominal mass value and width of a Breit-Wigner distribution) are kept constant in the fit. This implies that the shape of a given resonance is fixed and thus, can not be varied in the fitting process, consequently inducing model-dependency in the results. There are several factors that motivate this choice. On the technical side, keeping these values constant in the fitting process eliminates nuisance parameters, thus simplifying the `PDF`, but, much more relevant, this also implies that the mass normalisation integrals can be computed just once, as they depend on nothing else that these parameters and the two-body invariant mass range. Nevertheless, although the use of a GPU to run the fit would solve the timing issues arising from the need of computing all these integrals per minimisation step, the size of the available data sample

together with the abundance of resonances in the $\pi^+\pi^-$ were proven to be the limiting factors for implementing this approach.

The second uncertainty, originates from the assumptions made with regard to the orbital angular momentum induced between the intermediate resonances in the decay. This choice was first assumed as, historically, it has been the standard approach to deal with these barriers. However, the detailed study of *CP*-asymmetries for each contribution required that this effect was evaluated likewise. In the nominal fit, it is assumed that the decay only proceeds via the most kinematically favoured channel, which implies that no $L = 1$ or $L = 2$ orbital angular momenta are considered. It is also assumed that the three polarisation amplitudes $(0, ||, \perp)$ of the VV modes share the same relative angular momentum value. However, as introduced in the discussion in Section 1.2.2, the VV perpendicular amplitude, $A_\perp$ corresponds to a state with $L = 1$, while the longitudinal and parallel amplitudes, A_0 and $A_{||}$, receive contributions from states with $L = 0$ and $L = 2$. The same conservation laws impose that all the vector-scalar (or scalar-vector) contributions also correspond to states with $L = 1$. These non-zero values influence the two-body invariant mass shape by giving rise to angular momentum barriers as described by Equation 1.16. Given the size of the analysed data sample and the presumably small effect of this perturbation, the resulting systematic uncertainty would likely be negligible, but the lack of previous estimations of this effects motivated the study.

Varying the mass, widths and meson radii in the mass propagators

To asses the influence that the choice on the value of each parameter has, as well as the impact of keeping it fixed, the results of several fits to one toy-MC sample are studied. This sample is generated with one particular value and fitted back 200 times using different values for the constant of interest.

In order to asses these systematic uncertainties, one pseudoexperiment is generated with the default values for all the constant parameters (c_k) in the mass propagators descriptions. The number of events that are generated correspond to those of real data used in the analysis. This pseudoexperiment is then fitted back a certain number of times scanning different values of one constant at a time. By generating only one pseudoexperiment and studying the distribution of the fitted results, the statistical fluctuations associated to the generation of pseudoexperiments do not affect the estimation of this systematic uncertainty.

The systematic on a given fit parameter, A_i, arising from the choice of the value of a given constant, c_k,used in the nominal fit is computed as follows: the toy MC sample previously described is fitted back two hundred times with the `pyCUDA` fitter and using 200 different values for c_k. The distribution of all the values obtained for A_i is fitted with a Gaussian `PDF` which σ is taken as the systematic in A_i due to the choice on the c_k value in the nominal fit. If the RMS of the distribution is larger than its sigma, then this value is used instead of the fitted σ to assign the systematic uncertainty. The same procedure is followed to compute the systematic uncertainties for each A_i due to each mass propagator

Table 5.6: Summary of the central values of the mass propagators parameters and their uncertainties, as introduced in Section 1.2.2.

Variable	Value
m_ρ [MeV/c^2]	775.26 ±0.25
Γ_ρ [MeV/c^2]	147.8 ±0.9
r_{0_ρ}[(MeV/c^2)$^{-1}$]	0.0053±0.0008
m_{K^*} [MeV/c^2]	895.8 ±0.2
Γ_{K^*} [MeV/c^2]	47.4 ±0.5
$r_{0_{K^*}}$[(MeV/c^2)$^{-1}$]	0.003±0.0005
m_ω [MeV/c^2]	782.65 ±0.12
Γ_ω [MeV/c^2]	8.49 ±0.08
r_{0_ω}[(MeV/c^2)$^{-1}$]	0.003 ±0.0005
$m_{f_0(500)}$ [MeV/c^2]	475 ±32
$\Gamma_{f_0(500)}$ [MeV/c^2]	337 ±67
$m_{f_0(1370)}$ [MeV/c^2]	1475 ±6
$\Gamma_{f_0(1370)}$ [MeV/c^2]	113 ±11
$m_{f_0(980)}$ [MeV/c^2]	945 ±2
$g_{\pi\pi}$ [1/MeV/c^2]	199±30
$R\frac{g_{KK}}{g_{\pi\pi}}$	3 ±0.01
FF_1	-0.71 ± 0.5

parameter which was kept constant in the nominal fit. These are the mean, width and range parameter for the ρ, $K^*(892)^0$, ω resonances; the mean and width for the $f_0(500)$ and $f_0(1370)$; the mean and g_{ii} coupling factors for the $f_0(980)$; and the form factor value used in the parametrisation of the nonresonant $K^\pm\pi^\mp$system. The central values of these parameters, together with the sigma of the Gaussian distribution used to vary them, are summarised in Table 5.6. The resulting systematics are shown in Tables 5.7 and 5.8. In the summary tables all these sources have been combined into a single systematic labelled as *Props.*, which was obtained by adding in quadrature all the computed quantities.

Angular momentum barrier factors

Four different scenarios are contemplated in order to evaluate this systematic uncertainty. These correspond to the different combinations for L values shown in Table 5.9 and introduced at the beginning of the section. One fit is performed on each scenario and the difference between the nominal and varied fit results is assigned as systematic uncertainty (labelled as *Ang.Barriers* in the summary tables).

Table 5.7: Breakdown (I) of all the contributions to the systematic uncertainty included in *Props*. This set of toy-based systematic uncertainties has no flavour dependence and is therefore common to the B^0 and $\overline{B}^0$ samples.

Parameter	m_ρ	Γ_ρ	m_{K*}	Γ_{K*}	$m_{f_0(500)}$	$\Gamma_{f_0(500)}$	$m_{f_0(1370)}$	$\Gamma_{f_0(1370)}$
$Re(A^0_{V1V})$	0.0012	3.8e-05	0.022	0.00051	0.0048	0.0033	4e-05	2.1e-05
$Im(A^0_{V1V})$	7.8e-05	0.00064	0.0057	0.0017	0.0019	0.0026	1.4e-05	7.9e-05
$Re(A^{\|\|}_{V1V})$	4.7e-05	0.00021	0.014	0.0021	0.0023	0.0006	4.1e-05	2.6e-05
$Im(A^{\|\|}_{V1V})$	4.5e-05	0.0002	0.017	0.0032	0.0026	0.0009	3.4e-05	9.5e-06
$Re(A^\perp_{V1V})$	0.00023	0.00023	0.021	0.00089	0.0018	0.0008	6.2e-06	6.3e-05
$Im(A^\perp_{V1V})$	1.4e-05	0.00016	0.02	0.0025	0.0032	0.00064	5.4e-05	3.1e-05
$Re(A^0_{V2V})$	0.0049	0.0014	0.0048	0.0031	0.0016	0.00093	3.9e-05	2e-05
$Im(A^0_{V2V})$	0.0025	0.0015	0.0034	0.0012	0.00093	0.0005	3.2e-05	1.5e-05
$Re(A^{\|\|}_{V2V})$	0.0012	0.0021	0.00036	0.00047	0.00046	0.00015	2.3e-05	1.2e-05
$Im(A^{\|\|}_{V2V})$	0.0054	0.00026	0.00097	0.00024	0.00071	3.2e-05	3.5e-06	8.4e-06
$Re(A^\perp_{V2V})$	0.0013	0.0023	0.0007	0.00015	0.00047	0.00085	2.8e-05	1.1e-05
$Im(A^\perp_{V2V})$	0.0057	0.00038	0.00012	3.5e-05	0.00049	0.00046	9.8e-06	2.9e-05
$Re(A_{V2S})$	0.0058	0.0043	0.0014	0.00085	0.0026	0.00057	1.1e-05	4.1e-05
$Im(A_{V2S})$	0.0098	0.0031	0.00047	0.00035	0.0011	0.00087	5e-05	6.2e-05
$Re(A_{S1V})$	0.0059	0.0049	0.0091	0.0012	0.099	0.019	0.0011	0.0014
$Im(A_{S1V})$	0.0041	0.0014	0.017	0.0044	0.1	0.034	0.0014	0.0007
$Re(A_{S2V})$	0.0011	0.0026	0.018	0.0018	0.023	0.011	0.00029	0.00092
$Im(A_{S2V})$	0.0065	0.0052	0.046	0.0058	0.031	0.032	0.00046	8e-05
$Re(A_{S3V})$	0.00093	0.0046	0.018	0.00053	0.023	0.049	0.00028	0.0049
$Im(A_{S3V})$	0.0034	0.0035	0.03	0.0018	0.076	0.014	0.0016	0.0046
$Re(A_{S1S})$	0.0029	0.0025	0.0076	0.0007	0.018	0.013	0.001	0.00061
$Im(A_{S1S})$	0.0015	0.0026	0.0051	0.0025	0.062	0.012	0.00027	0.00054
$Re(A_{S2S})$	0.00091	0.0003	0.0042	0.0054	0.0063	0.011	0.0005	0.00019
$Im(A_{S2S})$	0.0052	0.0035	0.0044	0.0037	0.01	0.00085	2.4e-05	0.00049
$Re(A_{S3S})$	0.004	0.0006	0.0034	0.002	0.013	0.022	0.0012	0.0015
$Im(A_{S3S})$	0.0015	0.0011	0.0021	0.0062	0.022	0.01	0.00031	0.0022
$\|A^0_{V1V}\|^2$	6.5e-05	0.00091	0.005	0.0025	0.0022	0.0041	1.6e-05	0.00012
$\|A^{\|\|}_{V1V}\|^2$	0.00011	2e-05	0.0033	0.0061	0.0011	0.0005	1.3e-05	3.8e-05
$\|A^\perp_{V1V}\|^2$	0.00029	5.4e-05	0.0021	0.0046	0.0022	0.0019	7.2e-05	0.00012
$\|A^0_{V2V}\|^2$	0.0015	0.00031	0.0018	5.2e-05	0.00049	8.9e-05	1.6e-05	5.4e-06
$\|A^{\|\|}_{V2V}\|^2$	0.00024	0.00018	3.3e-05	5.2e-05	1.3e-05	1e-05	2e-06	1.3e-06
$\|A^\perp_{V2V}\|^2$	0.00029	2.5e-05	1.2e-05	4.3e-06	3e-05	3.5e-05	9.6e-07	1.5e-06
$\|A_{V2S}\|^2$	0.0039	0.00063	0.00026	4.1e-05	0.00026	0.00024	1.8e-05	1.7e-05
$\|A_{S1V}\|^2$	0.0026	0.0042	0.0098	0.0058	0.023	0.051	0.0027	0.0023
$\|A_{S2V}\|^2$	0.0061	0.00045	0.016	0.015	0.064	0.082	0.0016	0.003
$\|A_{S3V}\|^2$	0.0022	0.0054	0.0046	0.0012	0.071	0.093	0.0026	0.0048
$\|A_{S1S}\|^2$	0.0016	0.0012	0.0041	9.9e-05	0.0046	0.0096	0.00062	0.00031
$\|A_{S2S}\|^2$	0.0049	0.0027	0.0063	0.013	0.008	0.022	0.001	0.00069
$\|A_{S3S}\|^2$	0.001	0.001	0.00073	0.0033	0.012	0.019	0.00043	0.00077
δ^0_{V1V}	0.0017	0.00014	0.031	0.00049	0.0069	0.0042	5.7e-05	2.2e-05
$\delta^{\|\|}_{V1V}$	9.4e-06	0.00036	0.027	0.00095	0.0043	0.0013	6.4e-05	1.9e-05
$\delta^\perp_{V1V}$	0.00018	0.00029	0.03	0.001	0.0037	0.0002	4.2e-05	3.6e-05
δ^0_{V2V}	0.02	0.01	0.018	0.018	0.0072	0.0057	0.00015	0.00011
$\delta^{\|\|}_{V2V}$	0.1	0.022	0.02	0.0021	0.017	0.0022	0.00024	0.0001
$\delta^\perp_{V2V}$	0.059	0.091	0.027	0.0052	0.011	0.026	0.00091	0.00042
δ_{V2S}	0.018	0.028	0.0073	0.0052	0.015	0.0044	8e-05	0.00032
δ_{S1V}	0.0091	0.0056	0.024	0.0033	0.19	0.026	0.00045	0.00054
δ_{S2V}	0.0036	0.0033	0.028	0.0025	0.019	0.014	0.00017	0.00019
δ_{S3V}	0.0027	0.0043	0.028	0.0015	0.06	0.028	0.001	0.0052
δ_{S1S}	0.0065	0.0094	0.021	0.0078	0.2	0.028	0.0015	0.002
δ_{S2S}	0.0045	0.0031	0.005	0.0019	0.011	0.0021	0.00015	0.00039
δ_{S3S}	0.0094	0.00034	0.009	0.012	0.051	0.027	0.0028	0.006
f^0_{V1V}	4.4e-05	0.00033	0.0013	0.00035	0.00072	0.0012	4.7e-06	2.5e-05
$f^{\|\|}_{V1V}$	7.1e-05	0.00015	8.2e-05	0.00089	0.00075	0.00084	1.7e-05	2.5e-05
$f^\perp_{V1V}$	0.00011	0.00017	0.0013	0.00054	0.00029	0.00042	1.9e-05	7.8e-06
f^0_{V2V}	0.0098	0.0032	0.0033	0.0012	0.00033	0.00092	0.00011	3.7e-05
$f^{\|\|}_{V2V}$	0.0029	0.0041	0.0027	0.0013	0.00085	0.00042	8.1e-05	4e-05
$f^\perp_{V2V}$	0.0069	0.00092	0.0006	0.00016	0.00061	0.00099	3.3e-05	4.2e-05
$\Delta(\delta^{\|\|}_{V1V} - \delta^\perp_{V1V})$	0.00018	0.00065	0.0034	6.4e-05	0.00082	0.0015	2.4e-05	2e-05
$\Delta(\delta^{\|\|}_{V1V} - \delta^0_{V1V})$	0.0017	0.00022	0.0039	0.0014	0.0029	0.0055	9.6e-06	1.8e-05
$\Delta(\delta^\perp_{V1V} - \delta^0_{V1V})$	0.0018	0.00043	0.00054	0.0015	0.0035	0.004	1.9e-05	3e-05
$\Delta(\delta^{\|\|}_{V2V} - \delta^\perp_{V2V})$	0.15	0.069	0.0081	0.0031	0.0074	0.025	0.0012	0.0005
$\Delta(\delta^{\|\|}_{V2V} - \delta^0_{V2V})$	0.08	0.012	0.0028	0.021	0.012	0.0048	0.00014	0.00017
$\Delta(\delta^\perp_{V2V} - \delta^0_{V2V})$	0.076	0.081	0.01	0.024	0.0064	0.021	0.001	0.00035

Table 5.8: Breakdown (II) of all the contributions to the systematic uncertainty included in *Props*. This set of toy-based systematic uncertainties has no flavour dependence and is therefore common to the B^0 and $\overline{B}^0$ samples.

Parameter	m_ω	Γ_ω	$m_{f_0(980)}$	$r0_\rho$	$r0_{K^*}$	$r0_\omega$	$R\frac{g_{KK}}{g_{\pi\pi}}$	$g_{\pi\pi}$	FF_1
$Re(A^0_{V1V})$	0.0032	0.0022	0.0002	0.00063	0.0029	0.00011	2.4e-05	1.4e-05	0.016
$Im(A^0_{V1V})$	0.0027	0.0013	0.00061	0.00017	0.0001	0.00013	8e-06	0.00014	0.0033
$Re(A^{\|\|}_{V1V})$	0.00044	0.00068	0.0003	9.1e-05	0.0017	1.2e-05	1.2e-05	7.4e-05	0.017
$Im(A^{\|\|}_{V1V})$	0.0029	0.00086	0.00038	8.7e-05	0.0032	0.00011	3.8e-05	1.3e-05	0.011
$Re(A^\perp_{V1V})$	0.00062	0.00077	0.00016	0.00023	0.003	1.3e-05	1.4e-05	7.1e-05	0.016
$Im(A^\perp_{V1V})$	0.0021	0.00014	0.00045	3.3e-05	0.0033	9.6e-05	1.4e-05	7.3e-05	0.017
$Re(A^0_{V2V})$	0.013	0.00066	0.00023	4.8e-05	0.0011	0.00011	2e-05	4.9e-05	0.0033
$Im(A^0_{V2V})$	0.0047	0.0009	0.00034	0.0004	0.00084	5.4e-05	9.8e-06	6e-05	0.0065
$Re(A^{\|\|}_{V2V})$	0.0017	0.00032	0.00019	0.00011	0.00032	3.8e-05	1.8e-05	8.1e-05	0.0029
$Im(A^{\|\|}_{V2V})$	0.0037	0.00063	0.00012	0.00025	0.00014	1.5e-05	1.6e-05	8.2e-06	0.00068
$Re(A^\perp_{V2V})$	0.0029	0.00046	0.00011	0.00016	0.00018	4.4e-06	7.6e-06	3.1e-05	0.00064
$Im(A^\perp_{V2V})$	0.00037	0.00039	0.0001	0.00025	0.00011	1.9e-05	8e-06	3.6e-05	0.0009
$Re(A_{V2S})$	0.014	0.0022	0.0003	0.00074	7.4e-05	0.0002	9e-06	6.5e-05	0.0016
$Im(A_{V2S})$	0.0084	0.00089	8.8e-05	0.00021	1.5e-05	5.4e-05	5.1e-06	3.2e-05	0.0029
$Re(A_{S1V})$	0.0023	0.001	0.0065	0.006	0.0014	0.00032	0.00037	0.0024	0.024
$Im(A_{S1V})$	0.0021	0.00014	0.0051	0.0021	0.0036	0.00019	0.0002	0.00015	0.0025
$Re(A_{S2V})$	0.0044	0.0018	0.0037	0.0032	0.0028	0.00021	0.0011	0.0027	0.027
$Im(A_{S2V})$	0.0051	0.00019	0.027	0.0053	0.0094	0.00017	0.0019	0.0041	0.031
$Re(A_{S3V})$	0.0024	0.0013	0.017	0.00023	0.0025	0.00038	0.00072	0.00037	0.0074
$Im(A_{S3V})$	0.0039	0.00023	0.01	0.0032	0.0051	0.00018	0.00011	0.0046	0.016
$Re(A_{S1S})$	0.0016	0.00055	0.00095	0.0045	0.00043	9.2e-05	0.00018	0.00091	0.0051
$Im(A_{S1S})$	0.0001	0.00016	0.0032	0.0014	0.00072	0.00026	0.0002	9.5e-05	0.0035
$Re(A_{S2S})$	0.0033	0.0012	0.0019	0.00079	0.00058	9.4e-05	0.00076	0.0019	0.0032
$Im(A_{S2S})$	0.0027	2.6e-05	0.015	0.004	0.0029	4.1e-05	0.0012	0.0021	0.0043
$Re(A_{S3S})$	0.0014	0.00018	0.0067	0.0028	0.00015	0.00012	0.0007	0.00095	0.0017
$Im(A_{S3S})$	0.0007	0.00042	0.004	0.00044	0.0034	0.00011	0.00024	0.003	0.0048
$\|A^0_{V1V}\|^2$	0.0043	0.0015	0.00084	0.00015	0.00026	0.0002	1.4e-05	0.00021	0.0065
$\|A^{\|\|}_{V1V}\|^2$	0.0031	0.0018	0.00011	2.9e-05	0.0017	0.00011	5.7e-05	0.0001	0.032
$\|A^\perp_{V1V}\|^2$	0.0037	0.0012	0.00083	0.00027	0.00097	0.00015	4e-06	0.00019	0.044
$\|A^0_{V2V}\|^2$	0.00036	0.00039	0.00015	0.00013	0.00044	3.3e-06	3.4e-06	2.6e-05	0.0017
$\|A^{\|\|}_{V2V}\|^2$	0.00012	1.5e-05	8.6e-06	2.4e-05	1.6e-05	3.9e-06	2.4e-06	6.8e-06	0.00027
$\|A^\perp_{V2V}\|^2$	5.8e-05	1e-05	6.7e-06	9e-06	8.3e-06	8.3e-07	4.8e-07	2.2e-06	3.1e-05
$\|A_{V2S}\|^2$	0.0015	8.7e-05	9.5e-06	0.00014	1.1e-05	2.5e-06	1.3e-06	5e-06	0.0011
$\|A_{S1V}\|^2$	0.0048	0.0013	0.012	0.0048	0.0021	0.00018	0.00022	0.0029	0.03
$\|A_{S2V}\|^2$	0.022	0.0059	0.03	0.0023	0.0053	0.00041	0.00064	0.015	0.13
$\|A_{S3V}\|^2$	0.0099	0.0031	0.024	0.0037	0.00098	0.0006	0.0014	0.0049	0.0045
$\|A_{S1S}\|^2$	0.001	0.00033	0.0011	0.0027	0.00039	1.9e-05	8.2e-05	0.00057	0.0038
$\|A_{S2S}\|^2$	0.0084	0.0024	0.0051	0.004	0.0029	0.00017	0.00085	0.0052	0.0088
$\|A_{S3S}\|^2$	0.0012	0.00038	0.0061	0.0017	0.0023	0.00014	0.00019	0.0016	0.0037
δ^0_{V1V}	0.0041	0.0032	0.00035	0.0009	0.0041	0.00013	3.3e-05	7.2e-06	0.022
$\delta^{\|\|}_{V1V}$	0.0028	0.00018	0.00058	0.00015	0.0043	0.0001	2.3e-05	5.3e-05	0.0048
$\delta^\perp_{V1V}$	0.00099	0.00052	0.00019	0.00019	0.0047	5.8e-05	2.1e-05	1.9e-05	0.001
δ^0_{V2V}	0.077	0.0015	0.00057	0.0011	0.004	0.00067	0.00011	0.00015	0.031
$\delta^{\|\|}_{V2V}$	0.078	0.014	0.0042	0.0025	0.0063	0.00026	3.9e-05	0.00089	0.026
$\delta^\perp_{V2V}$	0.11	0.023	0.0027	0.0095	0.0052	0.00044	0.00022	0.00066	0.037
δ_{V2S}	0.089	0.013	0.0017	0.0037	0.00039	0.0012	5.5e-05	0.0004	0.0071
δ_{S1V}	0.00025	0.00072	0.0022	0.0073	0.0047	0.00047	0.00052	0.002	0.018
δ_{S2V}	0.0016	0.00033	0.015	0.0035	0.0055	0.00014	0.0013	0.0015	0.01
δ_{S3V}	0.0018	0.00036	0.014	0.0023	0.0045	0.00028	0.00036	0.0033	0.014
δ_{S1S}	0.00086	0.00087	0.0086	0.0074	0.0018	0.00082	0.00071	0.00092	0.0069
δ_{S2S}	0.0016	0.0003	0.013	0.0034	0.0025	6.1e-05	0.0013	0.0014	0.0033
δ_{S3S}	0.0016	0.00025	0.0078	0.0046	0.005	8e-05	0.0016	0.0059	0.0062
f^0_{V1V}	0.0024	0.0002	0.0002	2.9e-05	0.00042	0.0001	4e-06	6.5e-05	0.011
$f^{\|\|}_{V1V}$	0.0011	0.00017	0.00023	6.9e-05	0.00046	4.3e-05	1.6e-05	9.4e-05	0.0044
$f^\perp_{V1V}$	0.0013	0.00037	3.9e-05	4.4e-05	4.5e-05	6e-05	1.4e-05	3e-05	0.0063
f^0_{V2V}	0.0037	0.00087	0.00072	0.00053	0.0017	0.00013	8e-05	0.00029	0.012
$f^{\|\|}_{V2V}$	0.0023	0.00041	0.00048	0.00036	0.0012	0.00011	6.7e-05	0.00023	0.011
$f^\perp_{V2V}$	0.0014	0.00048	0.00025	0.00017	0.00043	2.2e-05	1.4e-05	7e-05	0.0016
$\Delta(\delta^{\|\|}_{V1V} - \delta^\perp_{V1V})$	0.0018	0.0007	0.00039	0.00035	0.00042	4.6e-05	6e-06	6e-05	0.0039
$\Delta(\delta^{\|\|}_{V1V} - \delta^0_{V1V})$	0.0014	0.003	0.00026	0.00075	0.00022	3e-05	5.6e-05	5.2e-05	0.027
$\Delta(\delta^\perp_{V1V} - \delta^0_{V1V})$	0.0031	0.0037	0.00017	0.0011	0.00063	7.6e-05	5.3e-05	1.4e-05	0.023
$\Delta(\delta^{\|\|}_{V2V} - \delta^\perp_{V2V})$	0.029	0.0087	0.0068	0.012	0.011	0.00021	0.00024	0.0015	0.012
$\Delta(\delta^{\|\|}_{V2V} - \delta^0_{V2V})$	0.0033	0.012	0.0039	0.0036	0.0023	0.00092	0.00014	0.00078	0.055
$\Delta(\delta^\perp_{V2V} - \delta^0_{V2V})$	0.03	0.021	0.0031	0.0085	0.0092	0.0011	0.00023	0.00076	0.063

Table 5.9: Combinations for the angular momentum factors values.

Scenario	$L_\perp$	L_{SV}	$L_{VV_{even}}$
a	1	0	0
b	1	1	0
c	1	1	2
d	1	0	2
nominal	0	0	0

5.2.2 Background subtraction methods

As introduced in Section 4.3, two differentiated techniques are used to subtract the background contributions from the analysed data sample. Each of these methods has a systematic uncertainty associated. On the one hand, the use of simulated events to cancel the $B_s^0 \to K^*(892)^0\overline{K}^*(892)^0$ contribution makes use of several hypotheses. First and foremost, the actual distribution in terms of helicity angles and two-body invariant masses of these events is known to a certain accuracy [87], so the uncertainties on these parameters must be accounted for. Secondly, the estimated yield of the pollution might be affected by different PID efficiencies or data-simulation discrepancies that were not considered in the nominal model. Aiming for a conservative estimate, this yield is varied by twice its uncertainty when addressing the associated systematic uncertainty. On the other hand, to extract the nominal set of *sWeights*, the parameters of the Hypatia functions (describing the B^0 and B_s^0 peaks) are fixed to their values found in fits to simulated data. Therefore, these parameters are known to a certain precision, which also has to be propagated to the final set of observables.

Yield and shape of injected $B_s^0 \to K^*(892)^0\overline{K}^*(892)^0$ events

Several sources of systematic uncertainties may arise from the method that was used to estimate the number and shape of $B_s^0 \to K^*(892)^0\overline{K}^*(892)^0$ misidentified events in the selected sample. Therefore, the estimated peaking background yield is varied by a 2σ factor to asses a global systematic effect, where σ represents the uncertainty on the initial estimation. Furthermore, the physical weights that are given to the $B_s^0 \to K^*(892)^0\overline{K}^*(892)^0$ injected events are recomputed varying their values within their total uncertainty following a Gaussian distribution. Both effects are taken into account simultaneously by generating two hundred sets of negative weights according to the variations mentioned above. The four-body invariant mass fit is consequently repeated as many times to obtain the corresponding varied sets of *sWeights*, which allows for the computation of the final set of observables by running the amplitude fit with each set of weights. In order to evaluate the associated systematic uncertainty, the distribution of fit results obtained

for each fit parameter α is fitted to a Gaussian PDF. The fitted σ of each one of these distributions, or their RMS if larger, is taken as systematic and labelled in the summary tables as *negWeights*.

Description of B^0 and B_s^0 peaks, Hypatia parameters

The four parameters describing the right- and left-side tails of the Hypatia distribution (shown in Table 4.14) are obtained from a fit to simulated data samples fulfilling the same selection criteria as real data. These parameters are varied according to their uncertainties obtained from the aforementioned fit in order to generate two hundred sets of *sWeights*. The MultiNest fitter is used to fit these data samples and study the distribution of the fit results in order to assess the corresponding systematic uncertainty. Following the same data treatment that was explained in the previous section, the distribution of fit results for each fit parameter α is fitted to a Gaussian PDF, whose σ (or the RMS, if larger) is assigned as the systematic uncertainty on α due to the choice of parameters made for the description of the $B_{(s)}$ peaks. This contribution to the total systematic uncertainty is labelled in the summary tables as *sWeights*.

5.2.3 Description of the detector acceptance

The normalisation weights technique is used to compute the integrals of the terms of the PDFwithin the limits of the LHCb detector acceptance. This description is obtained from simulated data and its accuracy is therefore affected by the sample size that was used to compute these integrals.

For each normalisation weight, its uncorrelated uncertainty can be identified with the square root of the corresponding eigenvalue (λ_i) in the diagonal space ($s_{nw_i}^{diagonal} = \sqrt{\lambda_i}$). Using the nomenclature introduced in Chapter 3, a new set of normalisation weights can be computed by adding to each nw_i (μ_j, the nominal value) a given shift R_i originated from the uncorrelated uncertainty on each normalisation weight. This procedure is repeated two hundred times and the pull distribution for each parameter of interest is obtained.

The systematic uncertainty is assigned by comparing the pull mean and width with those obtained in Section 5.1, computed with the nominal set of normalisation weights. Since the widths of all distributions are found to be compatible with unity, only the shift in the mean value of the pull is used to compute the systematic uncertainty. These uncertainties are obtained by scaling the induced shift on each parameter by their corresponding statistical uncertainty and are labelled in the summary tables as *normWeights*.

5.2.4 Neglected contributions in the model

Effect of neglecting masses and angles resolution in the fit

The experimental resolution on the fit observables ($m_{\pi\pi}, m_{K\pi}, \cos\theta_{\pi\pi}, \cos\theta_{K\pi}, \phi$) is neglected in the nominal model, but its effect is studied with pseudoexperiments in order

Table 5.10: Mean values of the 5-dimensional resolution (Δ_i) distribution found in the 2012 simulated data sample.

Variable	μ_i
$m_{\pi\pi}$ [MeV/c^2]	-0.176 ± 0.023
$m_{K\pi}$ [MeV/c^2]	-0.103 ± 0.016
$\cos\theta_{\pi\pi}$	$(\ 1.5 \pm 1.9)10^{-6}$
$\cos\theta_{K\pi}$	$(-8.9 \pm 2.1)10^{-5}$
$\phi[rad]$	-0.0050 ± 0.0055

to assign a systematic uncertainty. To study its influence in the fit parameters, the resolution on the 5 fit variables is obtained from simulation, applying MC-Truth matching to the combined `PHSP+SVV_HELAMP(2)` sample. The 5D distribution is treated as a whole to account for the correlations among the fit variables. The procedure used to compute the systematic uncertainty is described below, where N stands for the number of events in each toy:

- For each one of the five variables, x_i, compute the distribution of the difference between the generated and reconstructed quantities: $\Delta_i = x_i^{gen} - x_i^{rec}$
- Obtain the mean values, μ_i of the Δ_i distributions (shown in Table 5.10)
- Obtain the covariance matrix $C_{ij} = \frac{1}{N-1}\sum_{ev}^{N}(\Delta_i - \mu_i)\cdot(\Delta_j - \mu_j)$ of the Δ_i distributions (shown in Table 5.11, Table 5.12 displays the correlation matrix, for completeness)
- Generate N sets of five random numbers (ϵ_i^{ev}) following the multi-dimensional (5D) Gaussian distribution defined by the μ_i and the C_{ij}. Figure 5.8 shows the 1D projections on each variable of this 5D distribution.
- For each event (ev) in the data sample, for each fit observable (i), add the corresponding ϵ_i^{ev} to the generated value, x_i^{ev} to obtain the smeared toy-MC.

Each toy MC is fitted twice, once before the smearing is applied (therefore, fitting x_i^{ev}) and once afterwards (fitting $x_i^{ev} + \epsilon_i^{ev}$). The distribution of the differences between the corresponding fit results (λ), $\Delta_\alpha = \lambda_\alpha^{rec} - \lambda_\alpha^{smeared}$, for each fit parameter α, is fitted to a Gaussian PDF. Since the smearing does also include a systematic shift on each variable, the mean and width of each of these distributions are added in quadrature to asses the systematic uncertainty on the parameter α due to the effect of the experimental resolution in the helicity angles and 2-body invariant masses. The corresponding uncertainty is referred to as *Resolution* in the summary tables.

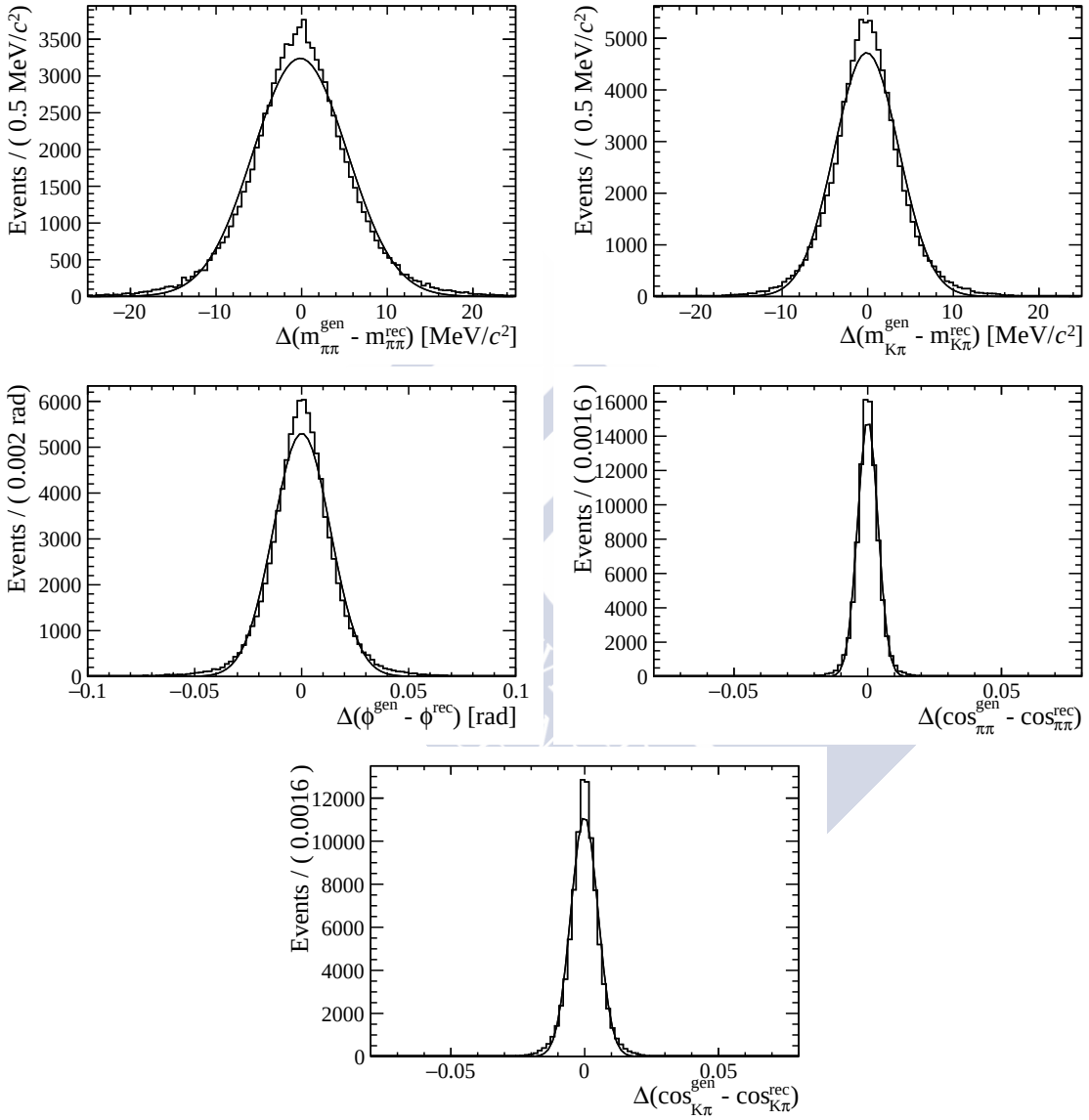

Figure 5.8: 1D projections of the resolution on the two-body invariant masses and the helicity angles obtained from simulation (2012 sample).

Table 5.11: Covariance matrix of the 5-dimensional resolution (Δ_i) distribution found in the 2012 simulated data sample.

	$m_{\pi\pi}$ [MeV/c^2]	$m_{K\pi}$[MeV/c^2]	$\cos\theta_{\pi\pi}$	$\cos\theta_{K\pi}$	ϕ [rad]
$m_{\pi\pi}$ [MeV/c^2]	3.87E+01	3.52E-02	-3.16E-04	-1.43E-05	-2.55E-05
$m_{K\pi}$ [MeV/c^2]	3.52E-02	1.90E+01	-1.10E-04	7.74E-03	-3.89E-03
$\cos\theta_{\pi\pi}$	-3.16E-04	-1.10E-04	2.25E-05	-7.95E-08	-1.38E-06
$\cos\theta_{K\pi}$	-1.43E-05	7.74E-03	-7.95E-08	3.56E-05	2.92E-06
ϕ [rad]	-2.55E-05	-3.89E-03	-1.38E-06	2.92E-06	3.27E-02

Table 5.12: Correlation matrix of the 5-dimensional resolution (Δ_i) distribution found in the 2012 simulated data sample.

	$m_{\pi\pi}$ [MeV/c^2]	$m_{K\pi}$ [MeV/c^2]	$\cos\theta_{\pi\pi}$	$\cos\theta_{K\pi}$	ϕ [rad]
$m_{\pi\pi}$ [MeV/c^2]	9.99E-01	1.30E-03	-1.07E-02	-3.85E-04	-2.27E-05
$m_{K\pi}$ [MeV/c^2]	1.30E-03	9.99E-01	-5.30E-03	2.97E-01	-4.93E-03
$\cos\theta_{\pi\pi}$	-1.07E-02	-5.30E-03	1.00E+00	-2.81E-03	-1.61E-03
$\cos\theta_{K\pi}$	-3.85E-04	2.97E-01	-2.81E-03	1.00E+00	2.70E-03
ϕ [rad]	-2.27E-05	-4.93E-03	-1.61E-03	2.70E-03	9.99E-01

Effect of neglecting the $B^0 \to a_1(1260)^- K^+$ contribution in the model

As anticipated in Section 4.2, decays proceeding via a three-body resonance ($a_1(1260)^-$, $K_1(1270)^-$, ...) are strongly suppressed in the analysed data sample due to the requirements imposed to the two-body invariant mass pairs. This can be seen in the toy example shown in Figure 5.9, where the scatter plot of the invariant mass of two pions (ρ^0 candidate) versus the invariant mass of three pions ($a_1(1260)^-$ candidate) is plotted before and after, the invariant mass window in $m(K\pi)$ is applied. The phase space of the three-body candidate, represented by the red-filled squares, is almost eliminated. Regarding the existence of other contributions, Figure 5.10 shows the projections of the four different combinations of the three-body invariant mass spectra of the fitted `PDF` superimposed to the sweighted data sample. The good agreement between the data (black points) and the fitted model (solid blue line) ratifies the choice of components included in the nominal model. The thresholds of the $m(K\pi\pi)$ spectra in those plots ($\sim$2000 MeV/c^2), are well above the nominal mass of the $K_1(1270)^-$ resonance, so no systematic uncertainty is assigned due to this contribution.

The effect that a small contamination from the $B^0 \to a_1(1260)^- K^+$ decay channel might have in the fitted parameters is studied with toy experiments. In order to establish

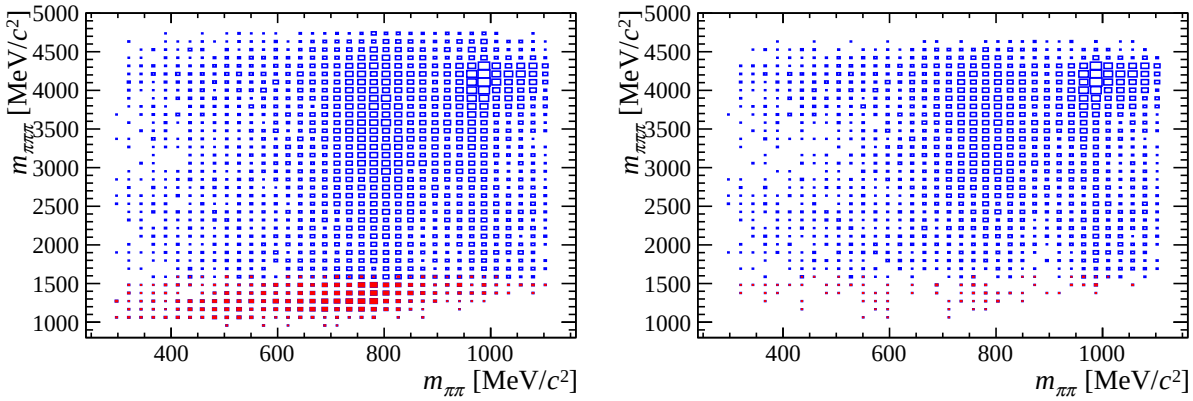

Figure 5.9: Scatter plot of the invariant mass of two pions (ρ^0 candidate) versus the invariant mass of three pions ($a_1(1260)^-$ candidate), plotted before (left) and after (right) the invariant mass window in $m(K\pi)$ is applied. The filled boxes highlight the region within 300 MeV/c^2 of the nominal $a_1(1260)^-$ mass. It should be noted that the $a_1(1260)^-$ decays via $a_1(1260)^- \to \rho^0(\to \pi^+\pi^-)\pi^-$.

the size of the background pollution, four pseudoexperiments are generated in the entire $m(K\pi)$ range with an estimate for the background yield N, with $0.5 \cdot N$, $2 \cdot N$ and $4 \cdot N$. A fifth toy is generated with only signal-like events. After applying the selection cuts in $m(K\pi)$, their $m(3\pi)$ invariant mass spectra is compared with the one found in the sweighted data sample, their ratios being shown in Figure 5.11. The toy generated with the initial estimate for the background pollution ($\sim 4\%$) is found to be the most compatible with data, so this same configuration is used to generate a set of 400 toys. A second set of 400 toys is generated without background pollution to be used as reference.

To estimate the systematic uncertainty, the pull distributions for each parameter are obtained from the 400 previously generated toys. These are then fitted to Gaussian `PDFs` and their mean (μ^i_{syst}) is corrected by the mean of the pull obtained from the signal-only toys (μ^i_{pull}) to obtain the deviation induced by the background pollution on each parameter. The final systematic is computed scaling the difference ($\mu^i_{syst} - \mu^i_{pull}$) by the statistical uncertainty on each parameter:

$$syst^i = (\mu^i_{syst} - \mu^i_{pull}) \cdot stat^i.$$

To account for different phase differences among the $a_1(1240)^-$ pollution and the rest of the components of the model, the whole procedure is repeated three times, assigning a different value (0, $\pi/3$, $2\pi/3$) to the phase difference between the the $a_1(1240)^-$ term and the $A^{\rho(K\pi)}$, used as normalisation. The results of this scan are shown in Table 5.13 and the maximum value obtained for the systematic per parameter is assigned as the systematic uncertainty due to this pollution. This resulting systematic uncertainties are labelled as $a_1(1260)^-$ in the summary tables.

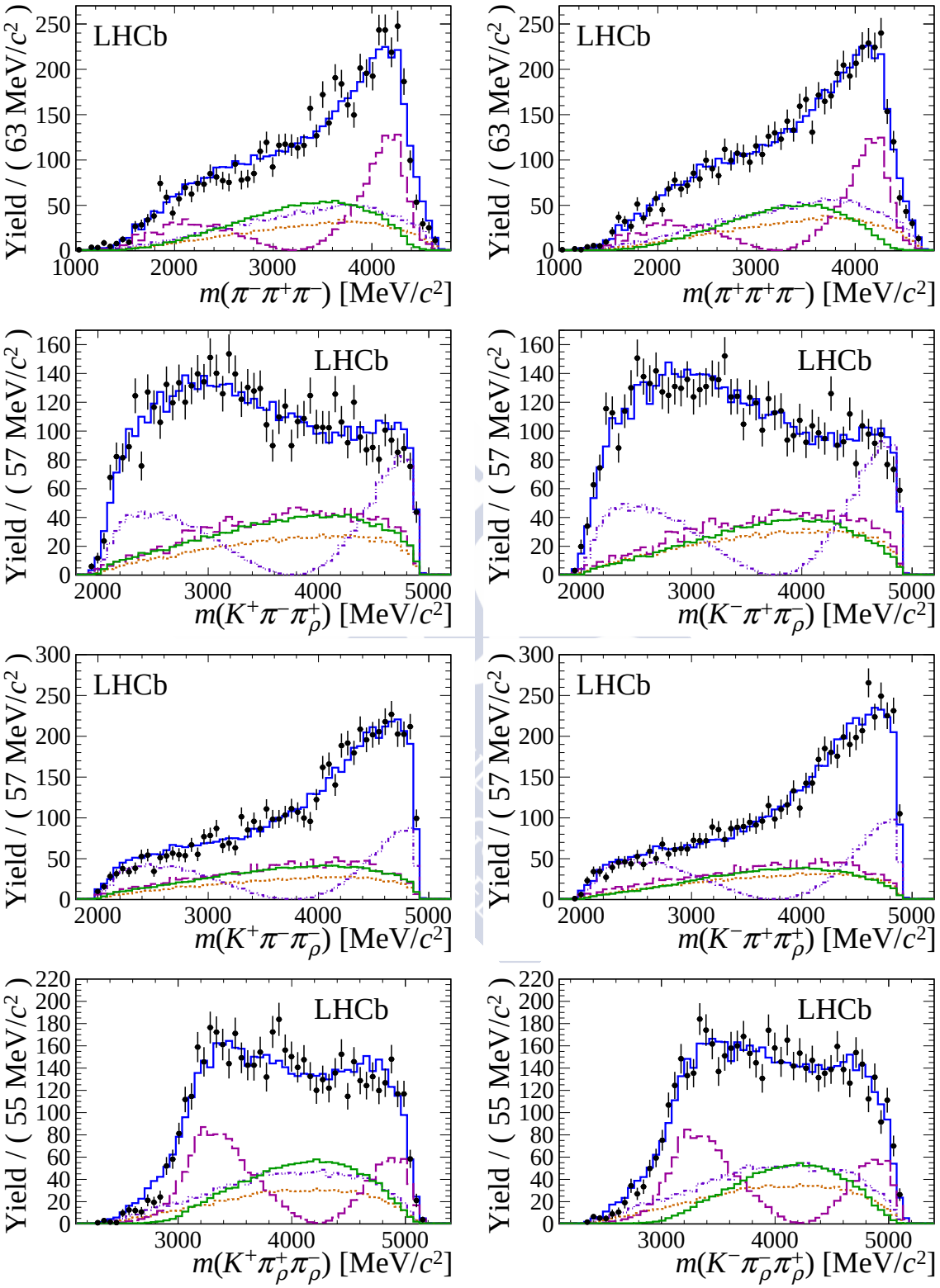

Figure 5.10: The four possible combinations of three-body invariant mass spectra for the fitted model, projected over sweighted data in the B^0 (left) and $\overline{B}^0$ (right) samples.

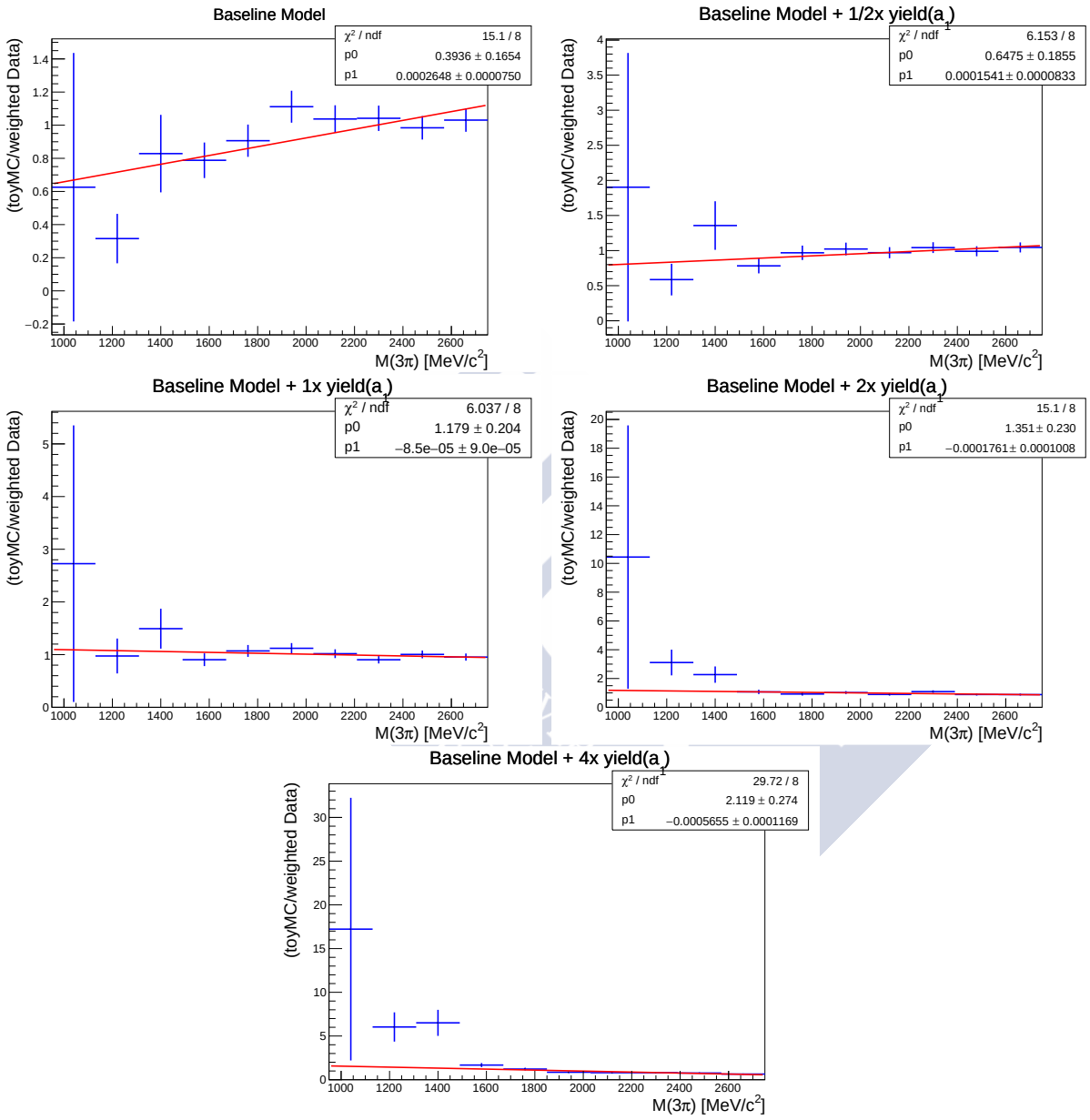

Figure 5.11: Invariant mass of the three pions in the final state. Five pseudoexperiments were generated with different contributions from the $a_1(1260)^-$ decay. The ratio of the number of events in the toy versus the number of weighted candidates found in data is presented for each experiment. A fit to a polynomial of order 1 is superimposed (in red) over each ratio of histograms.

Table 5.13: Scan over three phase differences of the systematic uncertainty due to the $a_1(1240)^-$ pollution, for the fit parameters (left) and the derived quantities (right).

Parameter	0	$\pi/3$	$2\pi/3$
$Re(A^0_{V1V})$	0.059	0.037	0.013
$Im(A^0_{V1V})$	0.014	0.035	0.031
$Re(A^{\|\|}_{V1V})$	0.0035	0.041	0.043
$Im(A^{\|\|}_{V1V})$	0.052	0.046	0.0015
$Re(A^{\perp}_{V1V})$	0.016	0.03	0.011
$Im(A^{\perp}_{V1V})$	0.029	0.018	0.01
$Re(A^0_{V2V})$	0.023	0.018	0.031
$Im(A^0_{V2V})$	0.0033	0.033	0.041
$Re(A^{\|\|}_{V2V})$	0.003	0.007	0.0002
$Im(A^{\|\|}_{V2V})$	0.0024	0.003	0.0064
$Re(A^{\perp}_{V2V})$	0.0013	0.0003	0.0027
$Im(A^{\perp}_{V2V})$	0.0047	0.0027	0.0028
$Re(A_{V2S})$	0.0005	0.018	0.0003
$Im(A_{V2S})$	0.0093	0.023	0.015
$Re(A_{S1V})$	0.031	0.033	0.032
$Im(A_{S1V})$	0.029	0.016	0.0044
$Re(A_{S2V})$	0.0034	0.031	0.021
$Im(A_{S2V})$	0.068	0.034	0.038
$Re(A_{S3V})$	0.018	0.0024	0.0046
$Im(A_{S3V})$	0.069	0.032	0.04
$Re(A_{S1S})$	0.014	0.023	0.023
$Im(A_{S1S})$	0.01	0.0012	0.01
$Re(A_{S2S})$	0.0086	0.0018	0.0083
$Im(A_{S2S})$	0.043	0.03	0.0061
$Re(A_{S3S})$	0.0063	0.0053	0.0063
$Im(A_{S3S})$	0.025	0.017	0.02

Parameter	0	$\pi/3$	$2\pi/3$
$\|A^0_{V1V}\|^2$	0.0044	0.058	0.06
$\|A^{\|\|}_{V1V}\|^2$	0.065	0.0023	0.052
$\|A^{\perp}_{V1V}\|^2$	0.018	0.017	0.019
$\|A^0_{V2V}\|^2$	0.0007	0.0031	0.0031
$\|A^{\|\|}_{V2V}\|^2$	0.0005	0.0001	0.0002
$\|A^{\perp}_{V2V}\|^2$	0	0.0002	0
$\|A_{V2S}\|^2$	0.0009	0.0005	0.0031
$\|A_{S1V}\|^2$	0.013	0.039	0.048
$\|A_{S2V}\|^2$	0.076	0.073	0.13
$\|A_{S3V}\|^2$	0.095	0.037	0.039
$\|A_{S1S}\|^2$	0.0074	0.013	0.018
$\|A_{S2S}\|^2$	0.026	0.022	0.037
$\|A_{S3S}\|^2$	0.019	0.018	0.0036
δ^0_{V1V}	0.17	0.16	0.0059
$\delta^{\|\|}_{V1V}$	0.039	0.06	0.026
$\delta^{\perp}_{V1V}$	0.048	0.048	0.0086
δ^0_{V2V}	0.2	0.4	0.63
$\delta^{\|\|}_{V2V}$	0.021	0.061	0.056
$\delta^{\perp}_{V2V}$	0.021	0.052	0.047
δ_{V2S}	0.043	0.12	0.11
δ_{S1V}	0.067	0.091	0.059
δ_{S2V}	0.04	0.026	0.021
δ_{S3V}	0.039	0.019	0.03
δ_{S1S}	0.044	0.026	0.015
δ_{S2S}	0.046	0.026	0.0081
δ_{S3S}	0.039	0.0017	0.037
f^0_{V1V}	0.011	0.015	0.0005
$f^{\|\|}_{V1V}$	0.02	0.019	0.038
$f^{\perp}_{V1V}$	0.0048	0.031	0.029
f^0_{V2V}	0.0047	0.0094	0.02
$f^{\|\|}_{V2V}$	0.0081	0.009	0.004
$f^{\perp}_{V2V}$	0.0003	0.007	0.0028
$\Delta(\delta^{\|\|}_{V1V} - \delta^{\perp}_{V1V})$	0.001	0.024	0.017
$\Delta(\delta^{\|\|}_{V1V} - \delta^0_{V1V})$	0.035	0.018	0.015
$\Delta(\delta^{\perp}_{V1V} - \delta^0_{V1V})$	0.025	0.032	0.0026
$\Delta(\delta^{\|\|}_{V2V} - \delta^{\perp}_{V2V})$	0.24	0.18	0.1
$\Delta(\delta^{\|\|}_{V2V} - \delta^0_{V2V})$	0.27	0.29	0.32
$\Delta(\delta^{\perp}_{V2V} - \delta^0_{V2V})$	0.11	0.36	0.34

Effect of neglecting the symmetrised ($\pi^{\pm}\pi^{\pm}$) contribution in the model

Among the final state particles there are two identically charged pions which may be exchanged and the PDF re-evaluated. The exchange of these same sign pions produces a combination fulfilling the invariant mass requirements on both quasi-two-body systems with a frequency lower than 0.5%, and therefore this contribution was not considered in the nominal fitting model. The interference between both configurations might, however, give rise to some effect on the fit parameters, which is evaluated using toys and accounted for with the corresponding systematic uncertainty.

To asses this systematic uncertainty, 400 toy experiments are generated taking into account the contribution form the amplitude with swapped pions:

$$\frac{d^5\Gamma}{dm^2_{\pi_1^+\pi^-}dm^2_{K^-\pi_2^+}d\cos\theta_{\pi_1^+\pi^-}d\cos\theta_{K^-\pi_2^+}d\phi} \propto |PDF(m_{\pi_1^+\pi^-}, m_{K^-\pi_2^+}, \cos\theta_{\pi_1^+\pi^-}, \cos\theta_{K^-\pi_2^+}, \phi) + PDF(m_{\pi_2^+\pi^-}, m_{K^-\pi_1^+}, \cos\theta_{\pi_2^+\pi^-}, \cos\theta_{K^-\pi_1^+}, \phi)|^2 \tag{5.5}$$

and fitted with the nominal model

$$\frac{d^5\Gamma}{dm^2_{\pi_1^+\pi^-}dm^2_{K^-\pi_2^+}d\cos\theta_{\pi_1^+\pi^-}d\cos\theta^-_K\pi^+_2 d\phi} \propto |PDF(m_{\pi_1^+\pi^-}, m_{K^-\pi_2^+}, \cos\theta_{\pi_1^+\pi^-}, \cos\theta_{K^-\pi_2^+}, \phi)|^2. \tag{5.6}$$

A pull distribution is obtained for each parameter and fitted to a Gaussian PDF. The resulting mean (μ^i_{syst}) is corrected by the mean value (μ_{pull}) of the pull obtained when generating the nominal model (pulls with the Minuit based fitter), and their difference is used to assign the corresponding systematic uncertainty, scaling the deviation found in number of standard deviations, by the statistical uncertainty on each parameter:

$$syst^i = (\mu^i_{syst} - \mu^i_{pull}) \cdot stat^i.$$

The resulting systematic uncertainties are labelled as *Symm. ($\pi\pi$)* in the summary tables.

5.2.5 Model-induced biases

As anticipated in Section 5.1, even if validated, the fitting model may induce some intrinsic bias to the parameters of interest. These effects were studied as part of the validation process of the fitting model, as it was described in Section 5.1.5. In order to estimate the corresponding systematic uncertainty, the biases in the fit results induced by the fit model are escalated by their corresponding statistical uncertainty and the resulting value is assigned as associated uncertainty. This contribution is labelled as *Fit method* in the summary tables.

5.2.6 Corrections applied to simulation

Simulated data samples are used in the analysis to describe the LHCb detector acceptance, by means of the normalisation weights. Therefore, known differences between data and simulated data distributions must be corrected for in order to obtain the best possible description of the acceptance.

One of this distributions is the momentum of the B^0 meson candidates. Due to the complexity of the description of the hadronisation process and the consequent approximations that are made in order to be able to simulate it, the description of this and other related variables (see Figure 5.12) in simulation is not fully satisfactory. The simulated event multiplicity (number of tracks) distribution is also known not to match what is seen in data and this effect propagates to the PID variables, where the differences between data and simulation are rather significant.

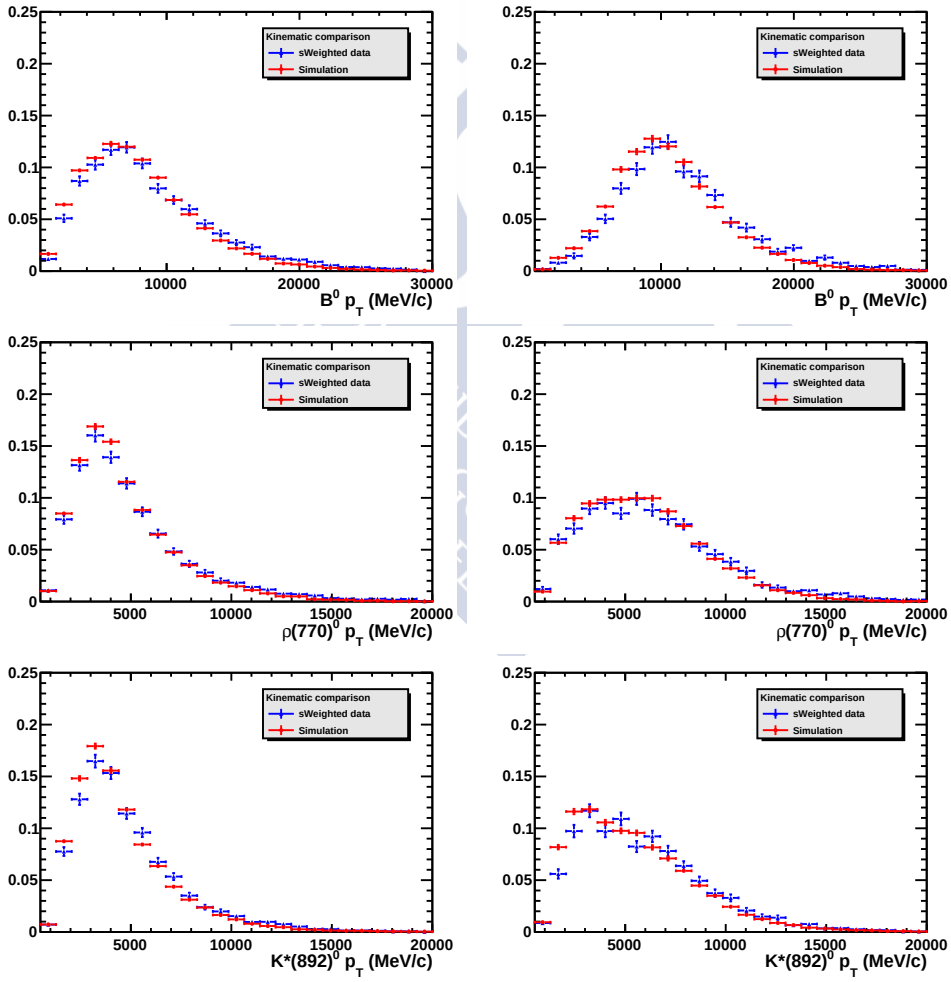

Figure 5.12: Transverse momentum of the B^0, ρ^0 and $K^*(892)^0$ candidates from s-weighted data and simulation. `TIS` sample is shown in the left column and `TOSnTIS` in the right.

In the first place, the PIDCalib package, introduced in Chapter 3, is used to obtain bidimensional efficiency maps, in bins of each track's pseudorapidity and momentum, per data taking year and magnet polarity. These maps are then used to evaluate the efficiency of the PID requirements for each track in the simulated sample and then assign a global per event PID efficiency weight, resulting from multiplying the single track efficiency of the four tracks in our final state. This correction improves the model visualisation in the $\cos(\theta)$ variables significantly.

Afterwards, an iterative, data-driven method, is used on top of the PID efficiency correction to emend the simulated data for the mismodelling of the track multiplicity and the B^0 momentum distributions.

For this, in the first step, an estimation of the physical parameters entering the `PDF` is obtained from a fit to the data sample using the uncorrected simulated data sample to compute the normalisation weights and this information on the physics is propagated to the simulation. This first step is mandatory, as part of the data-simulation kinematic differences are genuine and caused by the polarisation and different waves present in data, which were not generated in the simulated data sample. Therefore, the latter must be corrected for the physics before performing the iterative reweight.

After, in the second step, the sweighted data distributions for the two variables of interest are used as target to train a multivariate method which will produce a set of weights to correct the corresponding simulated data sample distributions. Finally, the corrected simulated data sample is used to obtain a new set of normalisation weights and the final fit is repeated. The summary of the iterative procedure reads:

1. A first fit to data is performed, using the normalisation weights computed from the uncorrected simulated data sample. This allows to obtain a first estimation on the values of the physical parameters.

2. The simulated data sample is corrected for physics by adding a weight computed from the ratio of the fitting `PDF` evaluated on the current estimate of the physical parameters over the generation model used in the simulation.

3. The `GBReweighter` method from the scikit-learn package [91] is used to obtain a set of weights accounting for data/simulation differences. The nominal sweighted data sample is used as target in the B^0_P and `nTracks` variables.

4. The simulated data is corrected for these data/simulation differences and a new set of normalisation weights is computed.

5. The final fit is repeated using the updated normalisation weights.

The whole chain is applied separately to each fitting category. Steps 2 to 5 are repeated 3 times, as the variation in the physical parameters becomes much smaller than their statistical uncertainty from the second iteration onwards (see Figure 5.13). The final results of the analysis correspond to those from the last iteration, and their difference

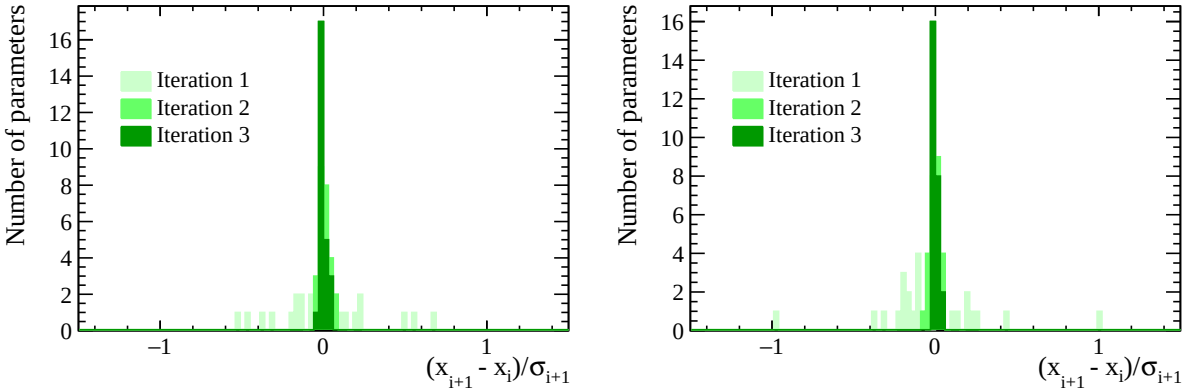

Figure 5.13: Evolution of the pull like distribution of the fit parameters with the number of iterations of the iterative reweight, for the B^0 sample on the right and the $\overline{B}^0$ sample on the left. The pull variable is built comparing the value of a given parameter (x) in the i^{th} and the $(i+1)$ iterations, divided by its statistical uncertainty (σ).

with respect to the previous one is assigned as the systematic uncertainty due to the finite number of iterations in the iterative procedure and are labelled as *IterativeRW* in the summary tables.

5.2.7 Summary tables of the systematic uncertainties

The systematic uncertainties are evaluated for all the fit parameters, their results being shown in Tables 5.14, 5.15, 5.16. The value of the statistical uncertainty is shown as reference in the first column. In order to correctly account for the correlations among the parameters, the systematic uncertainties for the derived quantities (*CP* averages and asymmetries of the observables) are evaluated for each of these derived quantities in the same way as the fit parameters, this is, computing the value of the relevant observable in each pseudoexperiment and analysing their distribution. The resulting systematic uncertainties are shown in Tables 5.17 and 5.18. The total systematic uncertainty is obtained from the sum in quadrature of the individual sources of systematic uncertainties detailed in the paragraphs above, accounting for 100% correlation of the common systematic uncertainties for B^0 and $\overline{B}^0$.

The estimated effect from having a pollution from $B^0 \to a_1(1260)^- K^+$ decays results in the dominant systematic uncertainty on the parameters describing the VV waves. This is understandable since only these waves and the $a_1(1260)^-$ amplitude are sensitive to the angle ϕ, so any deviation induced by the $a_1(1260)^-$ contribution should have a larger impact on the VV than on any S-wave, since these are isotropic in ϕ. The largest systematics regarding the S-wave parameters are due to both the choice of constants used in the mass propagators and the effect of the experimental resolution on the invariant masses and helicity angles.

Table 5.14: Summary table of the systematic uncertainties, fit parameters, B^0 sample. The statistical uncertainty (*Stats.*) is shown for reference. (Negligible values are represented by $-$).

Parameter	*Stats.*	*Ang.Barriers*	*sWeights*	*negWeights*	*normWeights*	*IterativeRW*
$Re(A^0_{V1V})$	0.057	0.0034	0.0031	0.0280	0.011	0.0002
$Im(A^0_{V1V})$	0.051	0.0014	0.0022	0.0077	0.016	0.0002
$Re(A^{\|\|}_{V1V})$	0.038	0.0025	0.0015	0.0230	0.010	–
$Im(A^{\|\|}_{V1V})$	0.036	0.0044	0.0012	0.0150	0.010	0.0013
$Re(A^{\perp}_{V1V})$	0.035	0.0016	0.0011	0.0092	0.008	0.0001
$Im(A^{\perp}_{V1V})$	0.039	0.0043	0.0013	0.0081	0.010	0.0006
$Re(A^0_{V2V})$	0.050	0.0028	0.0011	0.0042	0.014	0.0007
$Im(A^0_{V2V})$	0.055	0.0017	0.0013	0.0084	0.016	0.0001
$Re(A^{\|\|}_{V2V})$	0.031	0.0009	0.0008	0.0067	0.007	0.0009
$Im(A^{\|\|}_{V2V})$	0.030	0.0006	0.0010	0.0085	0.006	0.0015
$Re(A^{\perp}_{V2V})$	0.029	0.0004	0.0006	0.0053	0.006	0.0005
$Im(A^{\perp}_{V2V})$	0.030	0.0014	0.0006	0.0041	0.007	0.0001
$Re(A_{V2S})$	0.049	0.0031	0.0016	0.0093	0.017	0.0011
$Im(A_{V2S})$	0.050	0.0006	0.0015	0.0027	0.021	0.0007
$Re(A_{S1V})$	0.074	0.0044	0.0029	0.0370	0.024	0.0008
$Im(A_{S1V})$	0.048	0.0130	0.0015	0.0380	0.017	0.0007
$Re(A_{S2V})$	0.065	0.0022	0.0029	0.0081	0.020	–
$Im(A_{S2V})$	0.083	0.0045	0.0051	0.0140	0.028	0.0032
$Re(A_{S3V})$	0.072	0.0120	0.0042	0.0120	0.030	0.0008
$Im(A_{S3V})$	0.081	0.0087	0.0052	0.0170	0.028	0.0014
$Re(A_{S1S})$	0.049	0.0055	0.0021	0.0240	0.013	0.0011
$Im(A_{S1S})$	0.043	0.0029	0.0017	0.0071	0.009	0.0011
$Re(A_{S2S})$	0.055	0.0083	0.0036	0.0062	0.015	0.0006
$Im(A_{S2S})$	0.056	0.0025	0.0024	0.0035	0.014	0.0009
$Re(A_{S3S})$	0.055	0.0110	0.0040	0.0071	0.016	0.0002
$Im(A_{S3S})$	0.055	0.0054	0.0036	0.0086	0.013	0.0012

Table 5.15: Summary table of the systematic uncertainties, fit parameters, $\overline{B}^0$ sample. The statistical uncertainty (*Stats.*) is shown for reference.

Parameter	*Stats.*	*Ang.Barriers*	*sWeights*	*negWeights*	*normWeights*	*IterativeRW*
$Re(A^0_{V1V})$	0.042	0.0020	0.0011	0.0083	0.011	0.0008
$Im(A^0_{V1V})$	0.039	0.0016	0.0021	0.0170	0.011	0.0001
$Re(A^{\parallel}_{V1V})$	0.033	0.0024	0.0013	0.0100	0.009	0.0007
$Im(A^{\parallel}_{V1V})$	0.027	0.0021	0.0016	0.0095	0.007	0.0008
$Re(A^{\perp}_{V1V})$	0.027	0.0008	0.0012	0.0064	0.007	0.0002
$Im(A^{\perp}_{V1V})$	0.033	0.0012	0.0014	0.0074	0.009	0.0005
$Re(A^0_{V2V})$	0.042	0.0007	0.0019	0.0060	0.013	0.0004
$Im(A^0_{V2V})$	0.043	0.0034	0.0011	0.0031	0.014	0.0002
$Re(A^{\parallel}_{V2V})$	0.027	0.0003	0.0008	0.0033	0.007	0.0007
$Im(A^{\parallel}_{V2V})$	0.026	0.0019	0.0005	0.0028	0.006	0.0006
$Re(A^{\perp}_{V2V})$	0.025	0.0003	0.0006	0.0028	0.006	0.0006
$Im(A^{\perp}_{V2V})$	0.027	0.0011	0.0011	0.0021	0.007	0.0013
$Re(A_{V2S})$	0.043	0.0018	0.0009	0.0016	0.018	0.0018
$Im(A_{V2S})$	0.042	0.0028	0.0014	0.0031	0.017	0.0010
$Re(A_{S1V})$	0.064	0.0048	0.0035	0.0170	0.023	0.0011
$Im(A_{S1V})$	0.036	0.0083	0.0012	0.0190	0.017	0.0003
$Re(A_{S2V})$	0.054	0.0046	0.0025	0.0041	0.020	0.0002
$Im(A_{S2V})$	0.078	0.0045	0.0028	0.0056	0.032	0.0011
$Re(A_{S3V})$	0.065	0.0170	0.0025	0.0072	0.028	0.0013
$Im(A_{S3V})$	0.063	0.0130	0.0031	0.0150	0.025	0.0014
$Re(A_{S1S})$	0.037	0.0047	0.0018	0.0045	0.013	0.0001
$Im(A_{S1S})$	0.041	0.0030	0.0047	0.0067	0.012	0.0007
$Re(A_{S2S})$	0.046	0.0130	0.0033	0.0054	0.015	0.0006
$Im(A_{S2S})$	0.043	0.0045	0.0012	0.0024	0.011	0.0005
$Re(A_{S3S})$	0.042	0.0020	0.0022	0.0047	0.012	0.0006
$Im(A_{S3S})$	0.050	0.0074	0.0043	0.0068	0.014	0.0006

Table 5.16: Summary table of the systematic uncertainties common for the B^0 and $\overline{B}^0$ models, fit parameters. (Negligible values are represented by $-$).

Parameter	*Props.*	*Resolution*	*Fit method*	$a_1(1260)^-$	*Symm. ($\pi\pi$)*
$Re(A^0_{V1V})$	0.018	0.018	0.0023	0.059	0.003
$Im(A^0_{V1V})$	0.005	0.013	0.0076	0.035	0.025
$Re(A^{\|\|}_{V1V})$	0.017	0.011	0.0042	0.043	0.005
$Im(A^{\|\|}_{V1V})$	0.012	0.019	0.0013	0.039	0.017
$Re(A^{\perp}_{V1V})$	0.017	0.013	0.0019	0.030	0.001
$Im(A^{\perp}_{V1V})$	0.018	0.025	0.0018	0.029	0.016
$Re(A^0_{V2V})$	0.006	0.023	0.0024	0.031	0.002
$Im(A^0_{V2V})$	0.007	0.042	0.0030	0.041	$-$
$Re(A^{\|\|}_{V2V})$	0.003	0.020	0.0011	0.007	0.003
$Im(A^{\|\|}_{V2V})$	0.002	0.023	0.0002	0.006	0.004
$Re(A^{\perp}_{V2V})$	0.002	0.015	0.0001	0.003	0.005
$Im(A^{\perp}_{V2V})$	0.002	0.015	0.0005	0.005	0.003
$Re(A_{V2S})$	0.006	0.048	0.0041	0.021	0.014
$Im(A_{V2S})$	0.005	0.042	0.0014	0.023	0.003
$Re(A_{S1V})$	0.103	0.017	0.0012	0.033	0.013
$Im(A_{S1V})$	0.110	0.018	0.0008	0.029	0.023
$Re(A_{S2V})$	0.038	0.024	0.0055	0.031	0.010
$Im(A_{S2V})$	0.063	0.039	0.0052	0.068	0.049
$Re(A_{S3V})$	0.058	0.042	0.0003	0.018	0.008
$Im(A_{S3V})$	0.080	0.018	0.0020	0.069	0.034
$Re(A_{S1S})$	0.024	0.013	0.0001	0.023	0.031
$Im(A_{S1S})$	0.063	0.009	0.0005	0.010	0.022
$Re(A_{S2S})$	0.013	0.015	0.0061	0.009	0.012
$Im(A_{S2S})$	0.019	0.026	0.0001	0.043	0.004
$Re(A_{S3S})$	0.027	0.012	0.0001	0.006	0.011
$Im(A_{S3S})$	0.026	0.020	0.0044	0.025	0.037

Table 5.17: Table (I) of the systematic uncertainties for the derived quantities. The abbreviations $S1, S2$ and $S3$ stand for $f_0(500), f_0(980)$ and $f_0(1370)$, respectively. Negligible values are represented by a dash (−).

	Systematic uncertainty	$\lvert A^0_{\rho K^*}\rvert^2$	$\lvert A^{\lVert}_{\rho K^*}\rvert^2$	$\lvert A^{\perp}_{\rho K^*}\rvert^2$	$\lvert A^0_{\omega K^*}\rvert^2$	$\lvert A^{\lVert}_{\omega K^*}\rvert^2$	$\lvert A^{\perp}_{\omega K^*}\rvert^2$	$\lvert A_{\omega(K\pi)}\rvert^2$	$\lvert A_{S1K^*}\rvert^2$	$\lvert A_{S2K^*}\rvert^2$	$\lvert A_{S3K^*}\rvert^2$
CP averages	Centrifugal barrier factors	–	–	–	–	0.0001	–	0.001	0.01	0.01	0.04
	Hypatia parameters	–	–	–	–	–	–	–	–	–	–
	$B^0_s \to K^*(892)^0\overline{K}^*(892)^0$ bkg.	0.01	0.01	0.01	0.001	0.0004	0.0002	0.001	0.01	0.02	0.01
	Simulation sample size	0.01	0.01	0.01	0.002	0.0007	0.0003	0.005	0.02	0.06	0.04
	Data-Simulation corrections	–	–	–	–	0.0002	–	–	–	–	–
CP asym.	Centrifugal barrier factors	–	–	0.004	–	–	–	0.01	–	0.003	0.01
	Hypatia parameters	–	0.002	0.002	–	0.01	–	0.01	–	0.002	–
	$B^0_s \to K^*(892)^0\overline{K}^*(892)^0$ bkg.	0.03	0.011	0.013	–	0.13	0.1	0.01	0.02	0.005	0.01
	Simulation sample size	0.02	0.014	0.011	0.1	0.17	0.4	0.14	0.04	0.022	0.03
	Data-Simulation corrections	–	0.001	–	–	0.01	–	0.01	–	–	–
Common ($B^0, \overline{B}^0$)	Mass propagators parameters	0.01	0.033	0.040	0.002	0.0003	0.0001	0.002	0.07	0.170	0.12
	Masses and angles resolution	0.01	0.023	0.040	0.010	0.0028	0.0010	0.024	0.03	0.050	0.10
	Fit method	0.01	0.007	0.007	0.004	0.0005	0.0010	0.001	0.01	0.029	–
	$a_1(1260)^-$ pollution	0.06	0.070	0.019	0.003	0.0005	0.0002	0.003	0.05	0.130	0.10
	Symmetrised ($\pi\pi$) PDF	0.04	0.030	0.021	–	0.0008	0.0003	0.004	0.03	0.080	0.06

	Systematic uncertainty	$\lvert A_{S1(K\pi)}\rvert^2$	$\lvert A_{S2(K\pi)}\rvert^2$	$\lvert A_{S3(K\pi)}\rvert^2$	$\delta^0_{\rho K^*}$	$\delta^{\lVert}_{\rho K^*}$	$\delta^{\perp}_{\rho K^*}$	$\delta^0_{\omega K^*}$	$\delta^{\lVert}_{\omega K^*}$	$\delta^{\perp}_{\omega K^*}$	$\delta_{\omega(K\pi)}$
CP averages	Centrifugal barrier factors	0.003	0.02	0.003	–	0.001	0.002	0.03	0.01	–	0.01
	Hypatia parameters	0.001	0.01	0.001	–	0.001	0.002	0.01	0.01	–	–
	$B^0_s \to K^*(892)^0\overline{K}^*(892)^0$ bkg.	0.008	0.01	0.004	0.02	0.018	0.007	0.04	0.02	0.1	0.01
	Simulation sample size	0.006	0.03	0.007	0.02	0.009	0.008	0.15	0.07	0.1	0.10
	Data-Simulation corrections	–	–	0.001	–	0.001	–	–	–	–	–
CP asym.	Centrifugal barrier factors	–	0.010	0.02	–	0.004	0.001	0.02	0.01	0.03	0.02
	Hypatia parameters	0.01	0.004	0.01	–	0.001	0.001	0.01	0.01	0.01	–
	$B^0_s \to K^*(892)^0\overline{K}^*(892)^0$ bkg.	0.05	0.007	0.03	0.03	0.024	0.009	0.05	0.02	0.06	0.02
	Simulation sample size	0.04	0.020	0.06	0.02	0.009	0.009	0.15	0.07	0.15	0.13
	Data-Simulation corrections	–	0.001	–	–	–	–	–	0.01	0.01	–
Common ($B^0, \overline{B}^0$)	Mass propagators parameters	0.012	0.027	0.024	0.03	0.009	0.008	0.04	0.05	0.09	0.04
	Masses and angles resolution	0.010	0.026	0.011	0.03	0.020	0.017	0.30	0.30	0.50	0.17
	Fit method	0.003	0.021	0.005	–	0.001	0.001	0.03	0.05	0.04	0.01
	$a_1(1260)^-$ pollution	0.018	0.040	0.019	0.17	0.060	0.050	0.60	0.06	0.05	0.12
	Symmetrised ($\pi\pi$) PDF	0.029	0.025	0.019	0.02	0.010	0.012	–	0.04	0.30	0.05

Table 5.18: Table (II) of the systematic uncertainties for the derived quantities. The abbreviations $S1, S2$ and $S3$ stand for $f_0(500), f_0(980)$ and $f_0(1370)$, respectively. Negligible values are represented by a dash (−).

	Systematic uncertainty	δ_{S1K^*}	δ_{S2K^*}	δ_{S3K^*}	$\delta_{S1(K\pi)}$	$\delta_{S2(K\pi)}$	$\delta_{S3(K\pi)}$	$f^0_{\rho K^*}$	$f^{\parallel}_{\rho K^*}$	$f^{\perp}_{\rho K^*}$	$f^0_{\omega K^*}$	$f^{\parallel}_{\omega K^*}$
CP averages	Centrifugal barrier factors	0.01	–	0.01	0.01	0.001	0.02	0.001	0.001	0.002	–	–
	Hypatia parameters	–	–	–	–	0.001	0.01	0.001	0.001	0.001	–	–
	$B^0_s \to K^*(892)^0\overline{K}^*(892)^0$ bkg.	0.05	–	0.01	0.02	0.002	0.01	0.005	0.003	0.005	0.02	0.02
	Simulation sample size	0.02	0.01	0.02	0.02	0.009	0.03	0.004	0.004	0.004	0.06	0.05
	Data-Simulation corrections	–	–	–	–	0.001	–	–	–	–	0.01	–
CP asym.	Centrifugal barrier factors	0.01	0.001	0.001	0.004	0.003	0.02	–	0.001	0.002	0.01	0.01
	Hypatia parameters	–	0.002	0.002	0.004	0.001	0.01	–	0.003	0.002	0.01	0.01
	$B^0_s \to K^*(892)^0\overline{K}^*(892)^0$ bkg.	0.04	0.005	0.011	0.023	0.002	0.01	0.03	0.007	0.011	0.03	0.06
	Simulation sample size	0.03	0.022	0.022	0.025	0.012	0.03	0.02	0.010	0.009	0.12	0.14
	Data-Simulation corrections	–	0.001	–	0.003	–	–	–	0.001	0.001	–	0.01
Common $(B^0,\overline{B}^0)$	Mass propagators parameters	0.19	0.031	0.070	0.200	0.018	0.06	0.011	0.005	0.006	0.01	0.01
	Masses and angles resolution	0.02	0.027	0.017	0.026	0.026	0.05	0.010	0.016	0.018	0.14	0.12
	Fit method	–	0.004	0.001	0.002	0.001	–	0.003	0.001	0.002	0.01	0.05
	$a_1(1260)^-$ pollution	0.09	0.040	0.040	0.040	0.050	0.04	0.015	0.040	0.031	0.02	0.01
	Symmetrised $(\pi\pi)$ PDF	0.03	0.029	0.022	0.035	0.006	0.05	0.004	–	0.004	0.04	0.05

	Systematic uncertainty	$f^{\perp}_{\omega K^*}$	$\delta^{\parallel-\perp}_{\rho K^*}$	$\delta^{\parallel-0}_{\rho K^*}$	$\delta^{\perp-0}_{\rho K^*}$	$\delta^{\parallel-\perp}_{\omega K^*}$	$\delta^{\parallel-0}_{\omega K^*}$	$\delta^{\perp-0}_{\omega K^*}$	$\mathcal{A}_{\rm T}^{\rho K^*,1}$	$\mathcal{A}_{\rm T}^{\rho K^*,2}$	$\mathcal{A}_{\rm T}^{\omega K^*,1}$	$\mathcal{A}_{\rm T}^{\omega K^*,2}$
CP averages	Centrifugal barrier factors	–	0.001	–	–	–	–	–	0.0002	–	0.001	0.001
	Hypatia parameters	–	0.001	–	–	–	–	–	0.0002	–	0.001	0.001
	$B^0_s \to K^*(892)^0\overline{K}^*(892)^0$ bkg.	0.01	0.018	0.02	0.02	0.1	–	0.1	0.0017	0.002	0.004	0.002
	Simulation sample size	0.03	0.009	0.02	0.02	0.2	0.2	0.2	0.0013	0.002	0.012	0.012
	Data-Simulation corrections	–	0.001	–	–	–	–	–	–	–	–	–
CP asym.	Centrifugal barrier factors	–	0.004	0.007	0.004	0.03	0.02	0.04	0.0003	0.001	0.001	0.001
	Hypatia parameters	0.1	0.001	0.002	0.002	0.02	0.01	0.02	0.0001	–	0.001	0.001
	$B^0_s \to K^*(892)^0\overline{K}^*(892)^0$ bkg.	0.2	0.024	0.020	0.026	0.06	0.04	0.13	0.0017	0.004	0.005	0.003
	Simulation sample size	0.1	0.011	0.027	0.023	0.14	0.17	0.20	0.0013	0.002	0.015	0.017
	Data-Simulation corrections	–	–	0.002	0.002	0.02	0.01	0.01	–	–	0.001	–
Common $(B^0,\overline{B}^0)$	Mass propagators parameters	–	0.004	0.028	0.024	0.07	0.06	0.09	0.0006	0.001	0.002	–
	Masses and angles resolution	0.08	0.031	0.029	0.040	0.60	0.40	0.60	0.0020	0.005	0.026	0.019
	Fit method	0.03	0.003	0.005	0.004	0.02	0.02	0.03	0.0001	–	0.005	0.001
	$a_1(1260)^-$ pollution	0.01	0.024	0.035	0.032	0.24	0.32	0.40	0.0040	0.004	0.012	0.001
	Symmetrised $(\pi\pi)$ PDF	0.03	0.005	0.001	0.001	0.35	0.02	0.29	0.0007	0.001	0.018	0.003

5.3 Results

The 1-dimensional projections of the maximum likelihood fit to the selected data sample using the PDF previously described are shown in Figures 5.14 and 5.15, for the B^0 and $\overline{B}^0$ samples, respectively. The full simulated data sample (combination of PHSP+SVV_HELAMP2) is reweighted with the physical parameters found in data and used to visualise the fit results. The amplitudes of the different partial waves contributing to the considered final states are also plotted separately, following the colour and line style codes shown in Figures 5.14 and 5.15.

The numerical results obtained for the fit parameters $(Re(A_i), Im(A_i))$ are reported in Table 5.19, together with their statistical and total systematic uncertainties. The latter are obtained from the sum in quadrature of the individual sources of systematic uncertainties described in Section 5.2.

The results for the *CP* averaged amplitudes and their *CP* asymmetries, together with their strong and weak phase differences as defined in Section 1.2.2, are shown in Table 5.20. As anticipated, the corresponding systematic and statistical uncertainties are obtained accounting for all the correlations among the fit parameters.

Finally, the triple product asymmetries for both VV modes are computed from their expressions detailed in Equation 1.15 and are found to be:

$$\mathcal{A}^{\rho K^*,1}_{T-fake} = 0.0416 \pm 0.0050 \pm 0.0054, \quad \mathcal{A}^{\rho K^*,2}_{T-fake} = -0.0037 \pm 0.0062 \pm 0.0070,$$
$$\mathcal{A}^{\omega K^*,1}_{T-fake} = 0.042 \pm 0.043 \pm 0.037, \quad \mathcal{A}^{\omega K^*,2}_{T-fake} = -0.005 \pm 0.021 \pm 0.023,$$

$$\mathcal{A}^{\rho K^*,1}_{T-true} = -0.0210 \pm 0.0050 \pm 0.0022, \quad \mathcal{A}^{\rho K^*,2}_{T-true} = -0.0032 \pm 0.0062 \pm 0.0047,$$
$$\mathcal{A}^{\omega K^*}_{T-true} = 0.022 \pm 0.043 \pm 0.016, \quad \mathcal{A}^{\omega K^*,2}_{T-true} = -0.014 \pm 0.021 \pm 0.017.$$

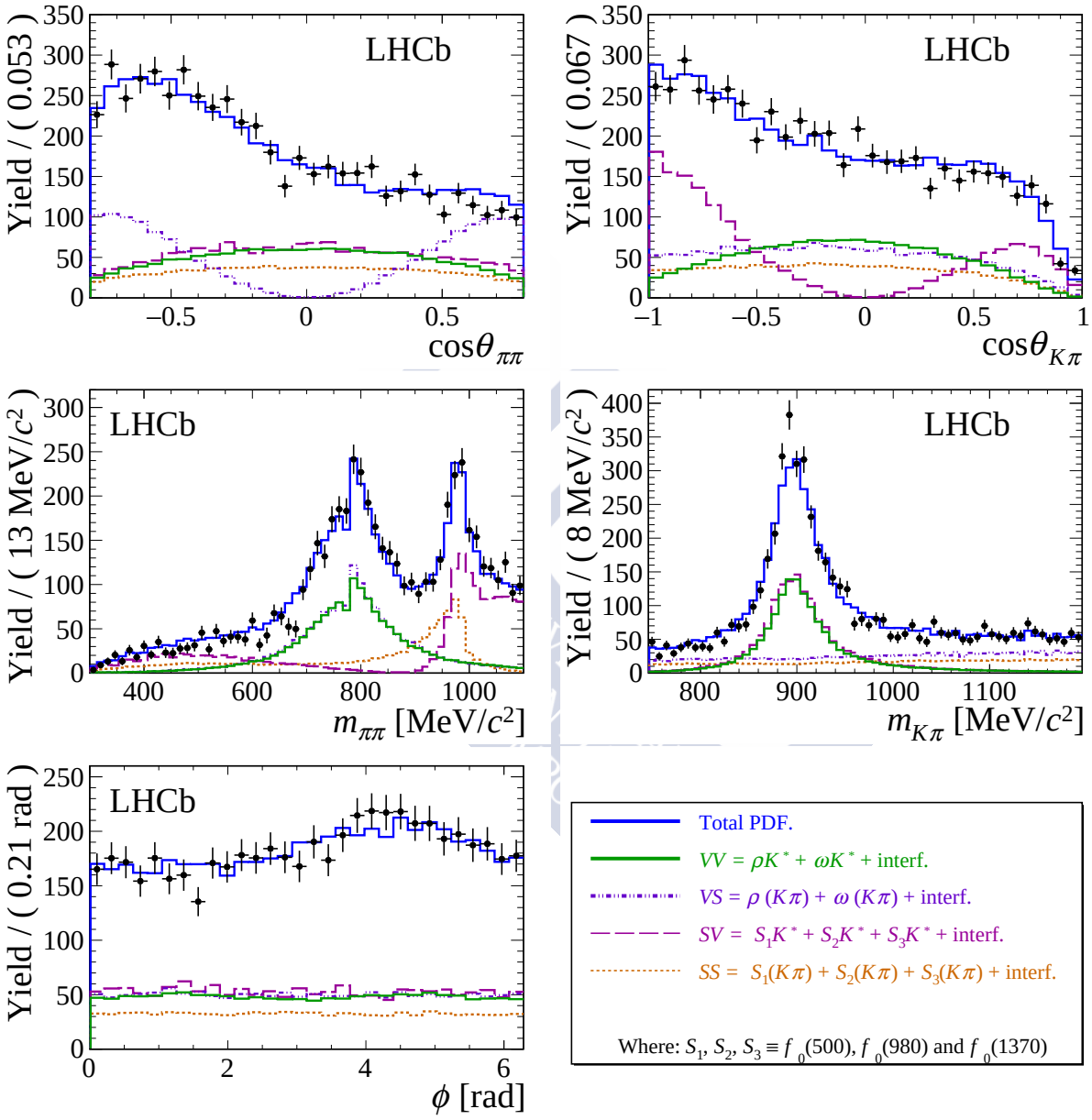

Figure 5.14: Result of the 5D fit in the B sample.

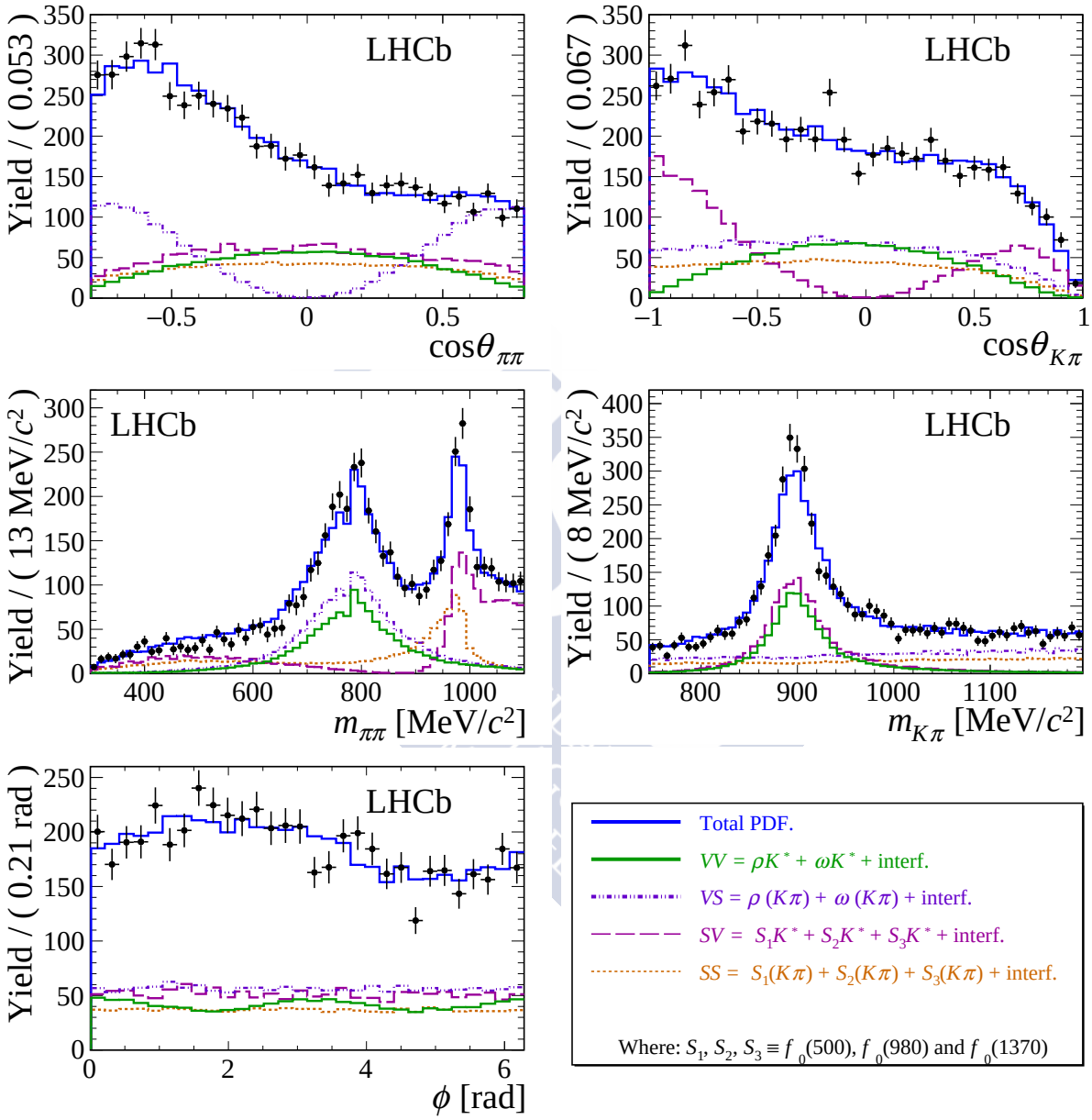

Figure 5.15: Result of the 5D fit in the $\overline{B}$ sample.

Table 5.19: Numerical results for the fit parameters obtained in the B^0 (left) and $\overline{B}^0$ (right) samples. The total systematic uncertainty is obtained from the sum in quadrature of the individual sources of systematic uncertainties.

B				$\overline{B}$			
Parameter	Value	Stat.	Syst.	Parameter	Value	Stat.	Syst.
$Re(A^0_{V1V})$	0.095	0.057	0.071	$Re(A^0_{V1V})$	-0.034	0.042	0.066
$Im(A^0_{V1V})$	0.74	0.051	0.049	$Im(A^0_{V1V})$	0.28	0.039	0.050
$Re(A^{\|\|}_{V1V})$	0.61	0.038	0.054	$Re(A^{\|\|}_{V1V})$	0.56	0.033	0.050
$Im(A^{\|\|}_{V1V})$	0.6	0.036	0.064	$Im(A^{\|\|}_{V1V})$	0.59	0.027	0.062
$Re(A^{\perp}_{V1V})$	-0.64	0.035	0.039	$Re(A^{\perp}_{V1V})$	-0.53	0.027	0.038
$Im(A^{\perp}_{V1V})$	-0.62	0.039	0.047	$Im(A^{\perp}_{V1V})$	-0.52	0.033	0.047
$Re(A^0_{V2V})$	0.11	0.05	0.042	$Re(A^0_{V2V})$	0.058	0.042	0.042
$Im(A^0_{V2V})$	-0.13	0.055	0.062	$Im(A^0_{V2V})$	-0.064	0.043	0.061
$Re(A^{\|\|}_{V2V})$	-0.061	0.031	0.024	$Re(A^{\|\|}_{V2V})$	0.019	0.027	0.023
$Im(A^{\|\|}_{V2V})$	-0.053	0.030	0.026	$Im(A^{\|\|}_{V2V})$	-0.056	0.026	0.025
$Re(A^{\perp}_{V2V})$	-0.013	0.029	0.018	$Re(A^{\perp}_{V2V})$	0.0097	0.025	0.018
$Im(A^{\perp}_{V2V})$	0.048	0.030	0.018	$Im(A^{\perp}_{V2V})$	0.039	0.027	0.017
$Re(A_{V2S})$	-0.1	0.049	0.056	$Re(A_{V2S})$	-0.097	0.043	0.056
$Im(A_{V2S})$	-0.17	0.050	0.053	$Im(A_{V2S})$	-0.069	0.042	0.052
$Re(A_{S1V})$	-0.49	0.074	0.12	$Re(A_{S1V})$	-0.46	0.064	0.12
$Im(A_{S1V})$	-0.57	0.048	0.12	$Im(A_{S1V})$	-0.54	0.036	0.12
$Re(A_{S2V})$	1.5	0.065	0.06	$Re(A_{S2V})$	1.4	0.054	0.060
$Im(A_{S2V})$	0.56	0.083	0.12	$Im(A_{S2V})$	0.6	0.078	0.12
$Re(A_{S3V})$	-1.1	0.072	0.082	$Re(A_{S3V})$	-0.97	0.065	0.081
$Im(A_{S3V})$	-0.36	0.081	0.12	$Im(A_{S3V})$	-0.48	0.063	0.12
$Re(A_{S1S})$	-0.3	0.049	0.055	$Re(A_{S1S})$	-0.47	0.037	0.049
$Im(A_{S1S})$	-0.18	0.043	0.069	$Im(A_{S1S})$	-0.066	0.041	0.071
$Re(A_{S2S})$	-1.1	0.055	0.032	$Re(A_{S2S})$	-1	0.046	0.033
$Im(A_{S2S})$	-0.21	0.056	0.056	$Im(A_{S2S})$	-0.14	0.043	0.056
$Re(A_{S3S})$	-0.15	0.055	0.039	$Re(A_{S3S})$	-0.0086	0.042	0.035
$Im(A_{S3S})$	0.43	0.055	0.058	$Im(A_{S3S})$	0.27	0.052	0.058

Table 5.20: Numerical fit results for the *CP* averages and asymmetries (top) and strong and weak phase differences (bottom) of the partial waves amplitudes and among the VV polarisation fractions. The first and second uncertainties correspond to the statistical and total systematic, respectively. The total systematic uncertainty is obtained from the sum in quadrature of the individual sources of systematic uncertainties, accounting for 100% correlation of the common systematic uncertainties for B^0 and $\overline{B}^0$.

Parameter	*CP* average	*CP* asymmetry
$\lvert A^0_{\rho K^*}\rvert^2$	$0.316 \pm 0.039 \pm 0.074$	$-0.75 \pm 0.07 \pm 0.17$
$\lvert A^{\lvert\lvert}_{\rho K^*}\rvert^2$	$0.701 \pm 0.038 \pm 0.084$	$-0.049 \pm 0.053 \pm 0.019$
$\lvert A^{\perp}_{\rho K^*}\rvert^2$	$0.668 \pm 0.036 \pm 0.068$	$-0.187 \pm 0.051 \pm 0.026$
$\lvert A^0_{\omega K^*}\rvert^2$	$0.019 \pm 0.010 \pm 0.012$	$-0.61 \pm 0.37 \pm 0.39$
$\lvert A^{\lvert\lvert}_{\omega K^*}\rvert^2$	$0.0050 \pm 0.0029 \pm 0.0031$	$-0.30 \pm 0.54 \pm 0.28$
$\lvert A^{\perp}_{\omega K^*}\rvert^2$	$0.0020 \pm 0.0019 \pm 0.0015$	$-0.21 \pm 0.86 \pm 0.41$
$\lvert A_{\omega(K\pi)}\rvert^2$	$0.026 \pm 0.011 \pm 0.025$	$-0.47 \pm 0.33 \pm 0.45$
$\lvert A_{f_0(500)K^*}\rvert^2$	$0.532 \pm 0.048 \pm 0.098$	$-0.056 \pm 0.091 \pm 0.042$
$\lvert A_{f_0(980)K^*}\rvert^2$	$2.42 \pm 0.13 \pm 0.25$	$-0.022 \pm 0.052 \pm 0.023$
$\lvert A_{f_0(1370)K^*}\rvert^2$	$1.29 \pm 0.09 \pm 0.20$	$-0.094 \pm 0.071 \pm 0.037$
$\lvert A_{f_0(500)(K\pi)}\rvert^2$	$0.174 \pm 0.021 \pm 0.039$	$0.30 \pm 0.12 \pm 0.09$
$\lvert A_{f_0(980)(K\pi)}\rvert^2$	$1.184 \pm 0.079 \pm 0.073$	$-0.083 \pm 0.066 \pm 0.023$
$\lvert A_{f_0(1370)(K\pi)}\rvert^2$	$0.139 \pm 0.028 \pm 0.039$	$-0.48 \pm 0.17 \pm 0.15$
$f^0_{\rho K^*}$	$0.164 \pm 0.015 \pm 0.022$	$-0.622 \pm 0.085 \pm 0.086$
$f^{\lvert\lvert}_{\rho K^*}$	$0.435 \pm 0.016 \pm 0.042$	$0.188 \pm 0.037 \pm 0.022$
$f^{\perp}_{\rho K^*}$	$0.401 \pm 0.016 \pm 0.037$	$0.050 \pm 0.039 \pm 0.015$
$f^0_{\omega K^*}$	$0.68 \pm 0.17 \pm 0.16$	$-0.13 \pm 0.27 \pm 0.13$
$f^{\lvert\lvert}_{\omega K^*}$	$0.22 \pm 0.14 \pm 0.15$	$0.26 \pm 0.55 \pm 0.22$
$f^{\perp}_{\omega K^*}$	$0.096 \pm 0.094 \pm 0.091$	$0.34 \pm 0.81 \pm 0.37$
Parameter	Strong phases, $\frac{1}{2}(\delta_{\overline{B}} + \delta_B)$ [rad]	Weak phases, $\frac{1}{2}(\delta_{\overline{B}} - \delta_B)$ [rad]
$\delta^0_{\rho K^*}$	$1.57 \pm 0.08 \pm 0.18$	$0.123 \pm 0.084 \pm 0.036$
$\delta^{\lvert\lvert}_{\rho K^*}$	$0.795 \pm 0.030 \pm 0.068$	$0.014 \pm 0.030 \pm 0.026$
$\delta^{\perp}_{\rho K^*}$	$-2.365 \pm 0.032 \pm 0.054$	$0.000 \pm 0.032 \pm 0.013$
$\delta^0_{\omega K^*}$	$-0.86 \pm 0.29 \pm 0.71$	$0.03 \pm 0.29 \pm 0.16$
$\delta^{\lvert\lvert}_{\omega K^*}$	$-1.83 \pm 0.29 \pm 0.32$	$0.59 \pm 0.29 \pm 0.07$
$\delta^{\perp}_{\omega K^*}$	$1.58 \pm 0.43 \pm 0.63$	$-0.25 \pm 0.43 \pm 0.16$
$\delta_{\omega(K\pi)}$	$-2.32 \pm 0.22 \pm 0.24$	$-0.20 \pm 0.22 \pm 0.14$
$\delta_{f_0(500)K^*}$	$-2.28 \pm 0.06 \pm 0.22$	$-0.002 \pm 0.064 \pm 0.045$
$\delta_{f_0(980)K^*}$	$0.385 \pm 0.038 \pm 0.066$	$0.018 \pm 0.038 \pm 0.022$
$\delta_{f_0(1370)K^*}$	$-2.757 \pm 0.051 \pm 0.089$	$0.076 \pm 0.051 \pm 0.025$
$\delta_{f_0(500)(K\pi)}$	$-2.80 \pm 0.09 \pm 0.21$	$-0.206 \pm 0.088 \pm 0.034$
$\delta_{f_0(980)(K\pi)}$	$-2.982 \pm 0.032 \pm 0.057$	$-0.027 \pm 0.032 \pm 0.013$
$\delta_{f_0(1370)(K\pi)}$	$1.76 \pm 0.10 \pm 0.11$	$-0.16 \pm 0.10 \pm 0.04$
$\delta^{\lvert\lvert-\perp}_{\rho K^*}$	$3.160 \pm 0.035 \pm 0.044$	$0.014 \pm 0.035 \pm 0.026$
$\delta^{\lvert\lvert-0}_{\rho K^*}$	$-0.772 \pm 0.085 \pm 0.061$	$-0.109 \pm 0.085 \pm 0.034$
$\delta^{\perp-0}_{\rho K^*}$	$-3.931 \pm 0.085 \pm 0.065$	$-0.123 \pm 0.085 \pm 0.035$
$\delta^{\lvert\lvert-\perp}_{\omega K^*}$	$-3.41 \pm 0.52 \pm 0.73$	$0.84 \pm 0.52 \pm 0.16$
$\delta^{\lvert\lvert-0}_{\omega K^*}$	$-0.97 \pm 0.41 \pm 0.57$	$0.57 \pm 0.41 \pm 0.17$
$\delta^{\perp-0}_{\omega K^*}$	$2.44 \pm 0.51 \pm 0.82$	$-0.28 \pm 0.51 \pm 0.24$

USC
UNIVERSIDADE
DE SANTIAGO
DE COMPOSTELA

6

Conclusions

In this thesis the first full amplitude analysis of $B^0 \to (\pi^+\pi^-)(K^+\pi^-)$ events in the two-body invariant mass ranges of $300 < m(\pi^+\pi^-) < 1100\,\text{MeV}/c^2$ and $750 < m(K^+\pi^-) < 1200\,\text{MeV}/c^2$ using LHCb data is presented. The analysed data sample corresponds to $3\,\text{fb}^{-1}$ of proton-proton collision data collected at $\sqrt{s}$ =7 and $\sqrt{s}$ =8 TeV during the detector operation periods in 2011 and 2012, respectively. The results of this work [92] have been submitted for publication to the Journal of High Energy Physics and are available on the free access site arXiv (`arXiv:1812.07008`) and the LHCb public pages (`LHCB-PAPER-2018-042`).

A model accounting for 14 contributions is described and used to fit selected $B^0 \to (\pi^+\pi^-)(K^+\pi^-)$ candidates in order to extract the relative strength of each considered amplitude with respect to the reference contribution, the VS wave $B^0 \to \rho^0(K^+\pi^-)$. Most of these amplitudes and phase differences had never been measured before. The high dimensionality of this amplitude fit, done in 5 dimensions and with 26 free parameters, and the use of background subtracted data samples motivated the use of the MultiNest algorithm for the first time in an amplitude analysis at LHCb. This work is also among the first to use a GPU based fit. Special emphasis is placed on the study of the $B^0 \to \rho(770)^0 K^*(892)^0$ decay channel, for which the polarisation fractions (f^λ) and the phase differences ($\delta^{\lambda_i - \lambda_j}$) are measured and their mean values and asymmetries computed. Triple product asymmetries are also derived from this set of observables.

Theoretical predictions of the VV related observables for the $B^0 \to \rho^0 K^{*0}$ mode are available, computed in both, pQCD and QCDF frameworks. However, the contributions of a a doubly Cabibbo suppressed tree, a gluonic penguin and an electroweak penguin diagrams to the decay rate, challenge the computability of the observables, making the

experimental input of great relevance. The results presented in this thesis could be used to place constraints on similar observables for other decay modes, being of particular interest for those of them also receiving a contribution from the electroweak penguin amplitude.

The relevance of this particular amplitude is hinted by the remarkably small value of the longitudinal polarisation measured for the $B^0 \to \rho^0 K^{*0}$ mode, as well as by the significant *CP* asymmetry found for this observable:

$$\tilde{f}^0_{\rho K^*} = 0.164 \pm 0.015 \pm 0.022 \quad \text{and} \quad \mathcal{A}^0_{\rho K^*} = -0.62 \pm 0.09 \pm 0.09\,,$$

where the first uncertainty is statistical and the second, systematic. The significance of the *CP* asymmetry is obtained by dividing the value of the asymmetry by the sum in quadrature of the statistical and systematic uncertainties and is found to be in excess of 5 standard deviations. This is the first significant observation of *CP* asymmetry in angular distributions of $B^0 \to VV$ decays. For completeness of the results, a determination of the equivalent parameters for the $B^0 \to \omega K^*(892)^0$ mode is also made, resulting in

$$\tilde{f}^0_{\omega K^*} = 0.68 \pm 0.17 \pm 0.16 \quad \text{and} \quad \mathcal{A}^0_{\omega K^*} = -0.13 \pm 0.27 \pm 0.13\,.$$

The phase differences between the perpendicular and parallel polarisation, $\delta^{||-\perp}_{\rho K^*}$, are found to be very close to π and 0, for the *CP* averaged and *CP* difference values, respectively. These are in good agreement with theoretical predictions computed in both QCDF and pQCD frameworks.

To conclude, a comparison of theoretical predictions for the $B^0 \to \rho(770)^0 K^*(892)^0$ mode with the results obtained from this analysis is shown in Table 6.1. It should be noted that the theoretical predictions involving the *CP* averaged value of $\delta^{\perp}_{\rho K^*}$ have been shifted by π on account of the different phase conventions used in the theoretical and experimental works.

Table 6.1: Comparison of theoretical predictions for the $B^0 \to \rho(770)^0 K^*(892)^0$ mode with the results obtained from this analysis.

	Observable	QCDF [16]	pQCD [21]	This work
$f^0_{\rho K^*}$	*CP* average	$0.22^{+0.03+0.53}_{-0.03-0.14}$	$0.65^{+0.03+0.03}_{-0.03-0.04}$	$0.164 \pm 0.015 \pm 0.022$
	CP asymmetry	$-0.30^{+0.11+0.61}_{-0.11-0.49}$	$0.0364^{+0.0120}_{-0.0107}$	$-0.62 \pm 0.09 \pm 0.09$
$f^\perp_{\rho K^*}$	*CP* average	$0.39^{+0.02+0.27}_{-0.02-0.07}$	$0.169^{+0.027}_{-0.018}$	$0.401 \pm 0.016 \pm 0.037$
	CP asymmetry	–	$-0.0771^{+0.0197}_{-0.0186}$	$0.050 \pm 0.039 \pm 0.015$
$\delta^{\parallel-0}_{\rho K^*}$	*CP* average [rad]	$-0.7^{+0.1+1.1}_{-0.1-0.8}$	$-1.61^{+0.02}_{-3.06}$	$-0.77 \pm 0.09 \pm 0.06$
	CP difference [rad]	$0.30^{+0.09+0.38}_{-0.09-0.33}$	$-0.001^{+0.017}_{-0.018}$	$-0.109 \pm 0.085 \pm 0.034$
$\delta^{\parallel-\perp}_{\rho K^*}$	*CP* average [rad]	$\equiv \pi$	$3.15^{+0.02}_{-4.30}$	$3.160 \pm 0.035 \pm 0.044$
	CP difference [rad]	$\equiv 0$	$-0.003^{+0.025}_{-0.024}$	$0.014 \pm 0.035 \pm 0.026$

USC
UNIVERSIDADE
DE SANTIAGO
DE COMPOSTELA

A

Resumo da tese en Galego

A.1 Introdución

O Modelo Estándar da Física de Partículas (SM) é simétrico ante a transformación Carga-Paridade (CP), excepto para o sector dos quarks e da interacción feble. Tendo en conta esta simetría, resulta chamativo que o universo actual non presente cantidades máis parecidas de materia e antimateria e que estea, ata onde alcanza o noso coñecemento, amplamente dominado pola materia. En 1967, o físico soviético Andrei Sajarov estableceu tres condicións que permitirían explicar as diferentes taxas de produción de materia e antimateria nalgún momento da evolución do universo. Unha delas é a violación da simetría combinada da conxugación de carga (C) e paridade (P).

Todas as medidas de violación CP realizadas ata a actualidade están ben descritas, dentro do SM, pola matriz de Cabibbo-Kobayashi-Maskawa (CKM). Non obstante, a magnitude da asimetría observada neste modelo, non é suficiente para explicar o desequilibrio entre materia e antimateria no universo e, polo tanto, é esperable que existan mecanismos de ruptura da simetría CP non contidos no SM.

O experimento LHCb do CERN, un dos catro principais do Large Hadron Collider (LHC), foi especificamente deseñado para explorar a violación da simetría CP mediante o estudo de decaementos de partículas que conteñan quarks b ou quarks c. Mentres que ATLAS e CMS, os dous grandes experimentos de propósito xeral do CERN, optaron por realizar pescudas directas de nova física a través do estudo da produción de novas partículas; LHCb emprega unha técnica complementaria, baseada en realizar medidas de alta precisión, para tratar de detectar efectos indirectos de nova física.

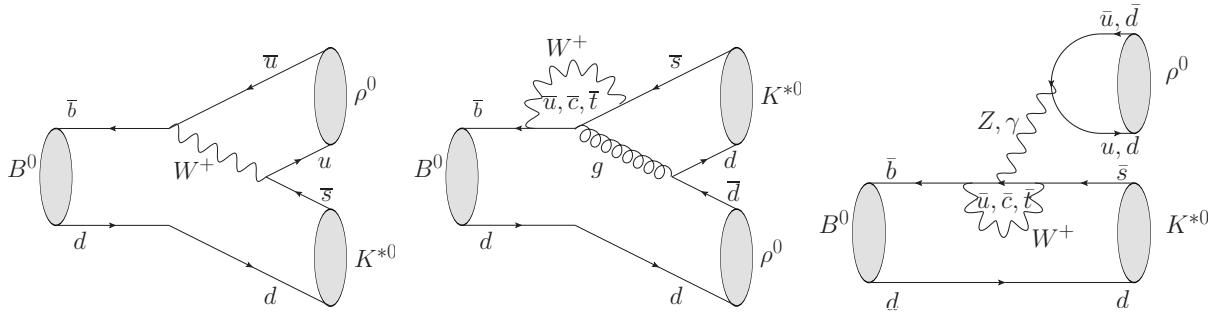

Figure A.1: Esquemas dos diagramas de Feynman que dominan o decaemento $B^0 \to \rho^0 K^{*0}$. De esquerda a dereita: diagrama "tree" dobremente suprimido por Cabibbo, diagrama "penguin" gluónico e diagrama "penguin" electrofeble.

Entre os resultados máis destacables de LHCb, atópase a medida da violación *CP* directa na canle $B^0 \to \pi^- K^+$. Este decaemento, que se corresponde cun análogo escalar da familia da canle que se quere estudar, presenta os efectos máis espectaculares de violación *CP* directa de todas as estudadas.

Dentro das canles obxecto de estudo no LHCb, unha de particular interese é a desintegración vectorial do mesón B^0, constituído por un antiquark b e un quark d, nun mesón vectorial ρ^0 (que é unha mestura $(u\bar{u} - d\bar{d})/2$), e dun mesón vectorial K^{*0} (formado polos quarks $d\bar{s}$).

Esta desintegración, que en adiante se designará como $B^0 \to \rho^0 K^{*0}$, ocorre maioritariamente a través de tres procesos representados polos diagramas de Feynman que se mostran na Figura A.1. A existencia de, como mínimo, dúas amplitudes distintas é unha condición necesaria para unha posible observación de violación *CP* directa a través de diferenzas nas anchuras parciais de desintegración en reaccións conxugadas. Neste caso, unha das contribucións provén dun diagrama de tipo "tree" (onde o quark b verifica a transición $b \to \bar{u}us$); mentres que as outras se correspondes con diagramas que proceden a través de "loops" (gluónico e electrofeble) que median a transformación $b \to \bar{d}ds$. O efecto de violación *CP* directa podería ser significativo xa que, ao estar a amplitude "tree" moi suprimida (tecnicamente "doubly Cabbibbo suppressed"), as tres amplitudes, "tree" e "loop" (ou "penguin") agárdanse da mesma orde, o que amplifica os efectos de interferencias.

Adicionalmente, a desintegración $B^0 \to \rho^0 K^{*0}$ presenta a vantaxe de que, debido á natureza vectorial dos mesóns do estado final, a distribución angular das partículas resultantes depende de tres amplitudes ortogonais, o que permite estudar efectos de polarización na desintegración. Para levar a cabo este tipo de medidas, precísase realizar unha complexa análise angular que require unha estatística notable, polo que non existían, ata o momento, medidas precisas en demasiadas canles.

A.2 Dispositivo experimental

O Gran Colisor de Hadróns (*Large Hadron Collider (LHC)*), situado no Laboratorio Europeo para a Física de Partículas (CERN), é o acelerador de partículas máis potente de todos os que o ser humano leva construído ata a actualidade. Atópase nun anel de 27 km de circunferencia ás aforas de Xenebra (Suíza), no que antes foran as instalacións do Gran Colisor de electróns e positróns (*Large Electron Positron collider (LEP)*), e foi deseñado para operar con colisións protón-protón (pp) a unha enerxía nominal de 14 TeV no centro de masas. Os seus obxectivos principais son comprobar as predicións do Modelo Estándar (SM) e buscar sinais de nova física alén del.

O proceso de aceleración dos feixes de protóns involucra varios pre-aceleradores secundarios, de forma que, en condicións nominais de funcionamento, ao LHC chegan protóns de 450 GeV (procedentes do Super Sincrotrón de Protóns) que finalmente serán acelerados ata os 7 TeV. Manter protóns a esta enerxía nas órbitas do colisor require un campo magnético de 8.33 T que se consegue con imáns supercondutores colocados no interior dun criostato que contén helio superfluído a 1.9 K. Para poder acelerar dous feixes de protóns en sentidos opostos, dentro do anel existen dúas liñas con campos magnéticos tamén opostos. Os datos mencionados son os nominais do deseño do acelerador, non obstante, os datos empregados para a análise presentada nesta tese obtivéronse durante os anos 2011 e 2012, nos que as colisións pp ocorrían a 3.5 e 4 TeV, respectivamente.

Existen catro puntos de cruce dos feixes, onde a traxectoria dos protóns é desviada un ángulo pequeno cara a liña contraria. Durante o funcionamento nominal do LHC, circulan por cada liña 2808 paquetes con 10^{11} protóns cada un, atravesándose cada 25 ns. Os grandes detectores situados nestes puntos son: ALICE (*A Large Ion Collider Experiment*), CMS (*Compact Muon Solenoid*), ATLAS (*A Toroidal LHC Apparatus*) e LHCb (*Large Hadron Collider beauty*).

O LHCb [50] foi deseñado cun propósito específico: o estudo da violación da simetría *CP* e dos decaementos raros, en ambos casos, mediante decaementos de partículas co quark *bottom*. Por este motivo, neste experimento resulta esencial reconstruír con precisión tanto o vértice primario (PV, lugar da colisión entre protóns onde se producen os quarks b) coma o vértice secundario (SV, onde decae o hadrón co quark b). Para poder acadar unha excelente identificación dos vértices, LHCb require funcionar cunha luminosidade instantánea menor que a nominal do LHC, polo que se desenfocan os feixes de protóns no punto de interacción. Desta forma, garántese que o número promedio de colisións pp inelásticas cada vez que acontece un cruce de paquetes estea en torno a 2.

Este espectrómetro de brazo único, conta cunha cobertura angular de 10 mrad a 300 (250) mrad no plano de curvatura magnético (plano de curvatura non magnético) [50]. Na Figura A.2 pode verse a distribución do detector. Para fixar un sistema de referencia escóllese, por convenio, un sistema co eixo z positivo cara a dereita e na dirección do feixe. A xustificación para que o detector estea focalizado nesta rexión atópase ao analizar a distribución do ángulo polar co que son producidos os pares $b\bar{b}$, xa que, a altas enerxías, ambos quarks tenden a producirse dentro do mesmo cono cara adiante ou cara atrás e,

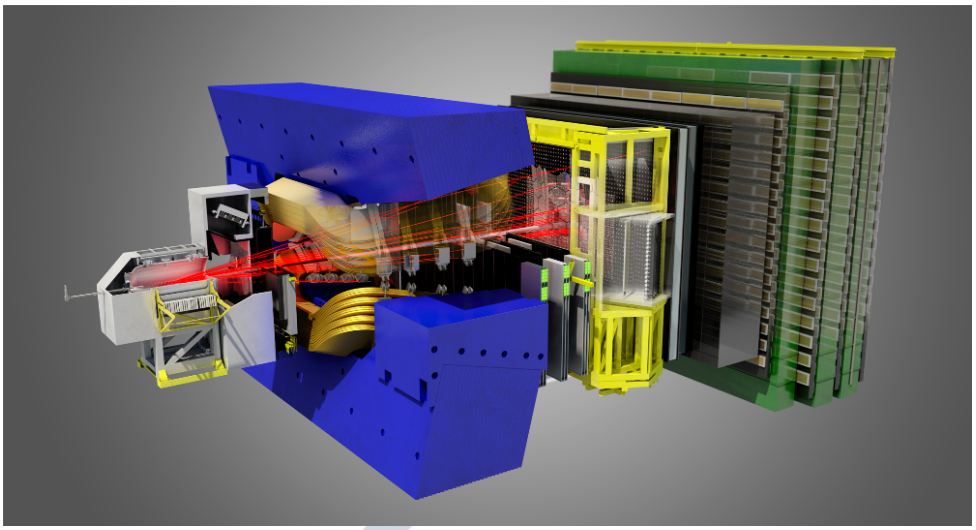

Figure A.2: Vista lateral do LHCb.

polo tanto, a xeometría a baixo ángulo do detector optimiza a aceptancia de partículas producidas por eses pares. As principais compoñentes do LHCb durante o período de funcionamento entre 2010 e 2012, listadas en orde dende o punto de interacción, son:

- Un localizador de vértices (*Vertex Locator*, VELO) que proporciona información sobre os vértices onde se producen e decaen os hadróns. Pola súa especial relevancia para a análise será visto con máis detalle na seguinte sección.

- Un imán de dipolo que proporciona un campo integrado de 4 Tm para poder medir os momentos das partículas cargadas. A magnetización do imán invértese periodicamente para estudar a violación da simetría *CP* e para minimizar e controlar os erros sistemáticos do detector.

- Un sistema de trazado [60] composto por un detector de micropistas de silicio situado antes do imán (*Tracker Turiciensis*, TT) e por tres estacións de trazado (*T Stations*, T1, T2 e T3) despois do imán. A súa función é a de reconstruír as trazas de partículas cargadas dentro do detector.

- Dous contadores por Imaxe de Aneis Cherenkov (*Ring Imaging Cherenkov*, RICH1 e RICH2, antes e despois do imán) cuxo obxectivo é identificar hadróns cargados (principalmente pións e kaóns) nun rango de momentos que vai dos 2 aos 100 GeV/c.

- Un sistema de calorímetros (*Scintillator Pad Detector*, SPD; *PreShower*, PS; *Electromagnetic CALorimeter*, ECAL e *Hadronic CALorimeter*, HCAL) empregado para identificar electróns e hadróns en función de enerxías e posicións.

- Un sistema de detección de muóns (formado por unha combinación de *Multi Wire Proportional Chambers*, MWPC e *Gas Electron Multiplier*, GEM) cuxo obtectivo é medir os seus momentos.

Aínda tendo en conta a relativamente baixa multiplicidade coa que traballa o LHCb, estímase que ocorren da orde de 10^7 colisións pp cada segundo, polo que a cantidade de datos que se xera é demasiado elevada como para poder almacear información de todos os eventos. En consecuencia, precísase dispoñer dun sistema de clasificación que decida, en tempo real, se se garda ou non a información do suceso. Este sistema denominado *trigger* identifica sinais característicos propios dos decaementos de partículas co quark b: un momento transverso (p_T) relativamente alto e un vértice secundario separado do primario. Isto equivale a pedir que os produtos do decaemento teñan un alto parámetro de impacto (IP), que se define como a mínima distancia entre a traza e o PV. O primeiro nivel do *trigger* emprega a información do VELO, do calorímetro e do sistema de identificación de muóns para preseleccionar da orde de 10^6 eventos por segundo; finalmente, o segundo nivel, reduce esta cifra a uns 2000, que será dos que se garde información para a súa posterior reconstrución e análise.

A.3 Fenomenoloxía do $B^0 \to \rho^0 K^{*0}$

Como se indicou na Sección A.1, a fenomenoloxía da canle de desintegración $B^0 \to \rho^0 K^{*0}$ vén definida polos diagramas de Feynman que contribúen ao proceso e pola natureza vectorial das resonancias intermedias que se producen antes de chegar ao estado final $B^0 \to (\pi^+\pi^-)(K^+\pi^-)$. O feito de que varios procesos (representados polos distintos diagramas) contribúan ao decaemento permite a existencia de interferencias entre as distintas amplitudes físicas. En consecuencia, esta canle será sensible a efectos de violación da simetría *CP*, que se manifestarán como distintos valores dos parámetros físicos que gobernan o decaemento das desintegracións dos mesóns B^0 e $\overline{B}^0$, respectivamente. O principal obxectivo da análise presentada nesta tese será determinar estas diferenzas. Para describir a desintegración $B^0 \to \rho^0 K^{*0}$ cómpre ter en conta todas as posibles resonancias intermedias polas que se pode chegar ao estado final $B^0 \to (\pi^+\pi^-)(K^+\pi^-)$. O listado das canles consideradas atópase na Táboa A.1. Para dous destes procesos, ambas resonancias intermedias teñen carácter vectorial, o cal, como se anticipou, ten implicacións na fenomenoloxía da desintegración.

A conservación do momento angular dá lugar á fenomeloxía relacionada coa natureza vectorial das resonancias intermedias. A partícula nai, o mesón B^0, ten un comportamento pseudo-escalar, polo que o valor do seu momento angular intrínseco (*spin*) é 0. No sistema de referencia propio, no que esta partícula está en repouso, o momento angular total (J) do sistema resultante é nulo, $J = 0$. A lei de conservación desta magnitude implica que o momento angular orbital (L) do sistema composto polas dúas resonancias vectoriais ten que acoplar co *spin* do sistema (S) de forma que se siga cumprindo a condición $J = 0$ no estado final. Isto implica que L poderá tomar unicamente tres valores, que terán

que coincidir cos tres acoplos posibles para o *spin* total do sistema formado por dúas partículas de *spin* 1: $S = 0, 1, 2$. Estas tres configuracións dan lugar ás tres amplitudes que contribúen á anchura parcial de desintegración no caso do decaemento dunha partícula pseudo-escalar a dúas vectoriais. Resulta conveniente expresar estas amplitudes en función da orientación relativa entre a polarización das partículas vectoriais e a súa dirección de movemento. Deste xeito, as amplitudes denomínanse lonxitudinal ou transversas con respecto a esta dirección. A amplitude lonxitudinal ten paridade positiva, mentres que das amplitudes transversas, unha ten paridade positiva (as polarizacións dos vectores son paralelas entre si) e outra, negativa (polarizacións perpendiculares). Estas tres amplitudes denótanse por $A^0, A^{||}$ e $A^{\perp}$, respectivamente. Non obstante, como xa se mencionou, a anchura parcial de desintegración para o proceso $B^0 \to (\pi^+\pi^-)(K^+\pi^-)$ ten que incluír todas as resonancias intermedias. No caso de amplitudes escalares, unicamente unha configuración de momento angular é posible, polo que cada nova resonancia contribúe cunha única amplitude.

Tendo en conta o anterior e seguindo o formalismo detallado en [29], a anchura parcial de desintegración para este proceso virá dada pola expresión:

$$\begin{aligned} \frac{d^5\Gamma}{dm_{12}^2 dm_{34}^2 d\cos\theta_{12} d\cos\theta_{34} d\phi} &\propto |A_T(\theta_{12}, \theta_{34}, \phi, m_{12}, m_{34})|^2 = \\ &= \left| \sum_{i=1}^{14} A_i \cdot g_i \cdot M_i \right|^2 = \sum_{i=1}^{14} \sum_{j=1}^{14} (A_i \cdot g_i \cdot M_i)(A_j \cdot g_j \cdot M_j)^*, \end{aligned} \tag{A.1}$$

onde os índices i e j corren sobre a primeira columna da Táboa A.1, os A_i son os parámetros físicos, as funcións g_i son combinacións de harmónicos esféricos que describen a dependencia angular e as funcións M_i conteñen a dependencia de Γ nas parellas de masa invariante de dous corpos, que variarán en función das resonancias que se estean a considerar. Os ángulos dos que dependen as funcións g_i defínense na base de helicidade, empregando como sistema de referencia aquel no que a resonancia nai está en repouso. A súa definición ilústrase na Figura A.3.

A análise realízase nas ventás de masa invariante correspondentes a $300 < m(\pi^+\pi^-) < 1100\,\mathrm{MeV}/c^2$ e $750 < m(K^+\pi^-) < 1200\,\mathrm{MeV}/c^2$. Na primeira das combinacións, o espectro de masas contén as resonancias vectoriais ρ^0 e ω e as escalares $f_0(500)$, $f_0(980)$ e $f_0(1370)$. Doutra banda, a resonacia dominante no espectro de masa $K\pi$ é a vectorial K^{*0}, aínda que tamén é preciso incluír a compoñente escalar denotada por $(K^+\pi^-)_0$. A forma da resonancia ρ^0 descríbese coa función Gounaris-Sakurai, a do $f_0(980)$ coa Flattè, a do $(K\pi)_0$ cunha modificación da función LASS e o resto das resonancias seguen unha Breit-Wigner. As correspondentes expresións matemáticas para cada unha destas función poden consultarse na Sección 1.2.2.

Os parámetros do axuste correspóndense cos A_i da Ecuación A.1. A magnitude dunha das contribucións fíxase a un valor arbitrario, establecendo a referencia con respecto da cal se miden o resto de contribucións. Como se indicou anteriormente, o obxectivo da análise

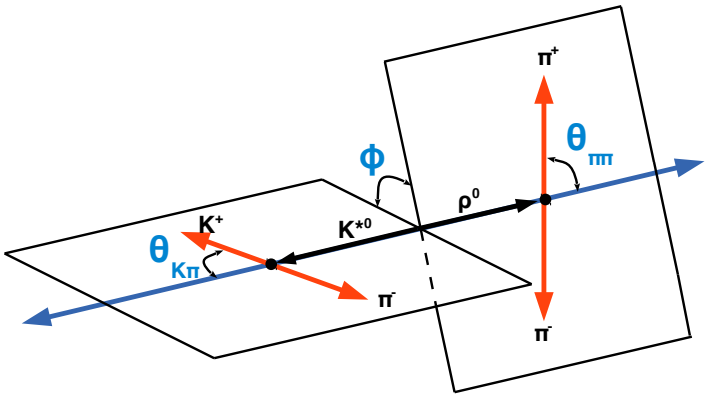

Figure A.3: Definicion dos ángulos de helicidade no decaemento $B^0 \to \rho^0 K^{*0}$, onde se particularizan os índices da Ecuación A.1 para o estado final considerado: $i = 1, 2, 4 \equiv \pi$ e $i = 3 \equiv K$.

é medir asimetrías *CP*, para o que cómpre ter en conta a paridade das amplitudes que contribúen á anchura parcial de desintegración e aplicala para describir o decaemento dos mesóns $\overline{B}^0$. No caso estudado, estes cambios correspóndese con realizar a transformación $A^\perp \to -A^\perp$ para as amplitudes transversas (unha para cada canle vectorial, $B^0 \to \rho^0 K^{*0}$ e $B^0 \to \omega K^*(892)^0$).

As asimetrías *CP*, obtéñense de combinar adecuadamente os valores dos parámetros físicos A_i obtidos en candaseu axuste aos datos correspondentes aos decaementos dos mesóns B^0 (A_i) e $\overline{B}^0$ $(\overline{A}_i)$. Similarmente, poden obterse as amplitudes promediadas en sabor $(B^0 + \overline{B}^0)$ para cada contribución e as diferenzas de fase entre todas as contribucións.

Para as canles VV defínense, ademais, as fracións de polarización

$$f_{VV}^\lambda = \frac{|A_{VV}^\lambda|^2}{|A_{VV}^0|^2 + |A_{VV}^{||}|^2 + |A_{VV}^\perp|^2}\,, \qquad \lambda = 0, ||, \perp \tag{A.2}$$

coas correspondentes observables promediadas en sabor, $\tilde{f}$, e as asimetrías, $\mathcal{A}$,

$$\tilde{f}_{VV}^\lambda = \frac{1}{2}(f_{VV}^\lambda + \overline{f}_{VV}^\lambda)\,, \qquad \mathcal{A}_{VV}^\lambda = \frac{\overline{f}_{VV}^\lambda - f_{VV}^\lambda}{\overline{f}_{VV}^\lambda + f_{VV}^\lambda}\,, \tag{A.3}$$

ademais das diferenzas de fase, medidas con respecto á canle de referencia $B^0 \to \rho^0(K\pi)$,

$$\delta_{VV}^0 \equiv (\delta_{VV}^0 - \delta_{\rho(K\pi)}) = \arg(A_{VV}^0 / A_{\rho(K\pi)}). \tag{A.4}$$

Para poder comparar coas predicións teóricas existentes, resulta conveniente definir tamén as diferenzas de fase entre as tres amplitudes que contribuen ás desintegracións VV,

$$\delta_{VV}^{||-0,\perp-0} \equiv (\delta_{VV}^{||,\perp} - \delta_{VV}^0) = \arg(A_{VV}^{||,\perp} / A_{VV}^0). \tag{A.5}$$

Table A.1: Dependencia nas funcións dos ángulos de helicidade e da masa invariante de dous corpos das distintas amplitudes que contribúen á desintegración do $B^0 \to \rho^0 K^{*0}$.

i	Tipo	A_i	$g_i(\theta_{12}, \theta_{34}, \phi)$	$M_i(m_{12}, m_{34})$
1		$A^0_{\rho K^*}$	$\cos\theta_{12}\cos\theta_{34}$	$M_\rho(m_{12})M_{K^*z}(m_{34})$
2	V_1V	$A^{\|\|}_{\rho K^*}$	$\frac{1}{\sqrt{2}}\sin\theta_{12}\sin\theta_{34}\cos\phi$	$M_\rho(m_{12})M_{K^*}(m_{34})$
3		$A^{\perp}_{\rho K^*}$	$\frac{i}{\sqrt{2}}\sin\theta_{12}\sin\theta_{34}\sin\phi$	$M_\rho(m_{12})M_{K^*}(m_{34})$
4		$A^0_{\omega K^*}$	$\cos\theta_{12}\cos\theta_{34}$	$M_\omega(m_{12})M_{K^*}(m_{34})$
5	V_2V	$A^{\|\|}_{\omega K^*}$	$\frac{1}{\sqrt{2}}\sin\theta_{12}\sin\theta_{34}\cos\phi$	$M_\omega(m_{12})M_{K^*}(m_{34})$
6		$A^{\perp}_{\omega K^*}$	$\frac{i}{\sqrt{2}}\sin\theta_{12}\sin\theta_{34}\sin\phi$	$M_\omega(m_{12})M_{K^*}(m_{34})$
7	V_1S	$A^0_{\rho(K\pi)}$	$\frac{1}{\sqrt{3}}\cos\theta_{12}$	$M_\rho(m_{12})M_{(K\pi)}(m_{34})$
8	V_2S	$A^0_{\omega(K\pi)}$	$\frac{1}{\sqrt{3}}\cos\theta_{12}$	$M_\omega(m_{12})M_{(K\pi)}(m_{34})$
9	S_1V	$A^0_{f_0(500)K^*}$	$\frac{1}{\sqrt{3}}\cos\theta_{34}$	$M_{f_0(500)}(m_{12})M_{K^*}(m_{34})$
10	S_2V	$A^0_{f_0(980)K^*}$	$\frac{1}{\sqrt{3}}\cos\theta_{34}$	$M_{f_0(980)}(m_{12})M_{K^*}(m_{34})$
11	S_3V	$A^0_{f_0(1370)K^*}$	$\frac{1}{\sqrt{3}}\cos\theta_{34}$	$M_{f_0(1370)}(m_{12})M_{K^*}(m_{34})$
12	S_1S	$A^0_{f_0(500)(K\pi)}$	$\frac{1}{3}$	$M_{f_0(500)}(m_{12})M_{(K\pi)}(m_{34})$
13	S_2S	$A^0_{f_0(980)(K\pi)}$	$\frac{1}{3}$	$M_{f_0(980)}(m_{12})M_{(K\pi)}(m_{34})$
14	S_3S	$A^0_{f_0(1370)(K\pi)}$	$\frac{1}{3}$	$M_{f_0(1370)}(m_{12})M_{(K\pi)}(m_{34})$

A partir deste conxunto de parámetros poden obterse as diferenzas de fase promediadas en sabor, $\frac{1}{2}(\delta_{\overline{B}} + \delta_B)$, e as diferenzas, $\frac{1}{2}(\delta_{\overline{B}} - \delta_B)$.

Finalmente, as denominadas asimetrías de produtos triples (TPA) [17,32], obtéñense a partir das cantidades

$$\mathcal{A}_T^1 = f_\perp f_0 \sin(\delta_\perp - \delta_0), \quad \mathcal{A}_T^2 = f_\perp f_{||} \sin(\delta_\perp - \delta_{||}), \tag{A.6}$$

mediante a súa combinación nas correspondentes *TPA* verdadeiras (*true*, orixinadas por unha violación da simetría *CP*) e falsas (*fake*, provocadas por fases fortes):

$$\mathcal{A}^k_{T-true} = \frac{\mathcal{A}^k_T - \overline{\mathcal{A}}^k_T}{2}, \qquad \mathcal{A}^k_{T-fake} = \frac{\mathcal{A}^k_T + \overline{\mathcal{A}}^k_T}{2}. \tag{A.7}$$

A.4 Selección de candidatos $B^0 \to (\pi^+\pi^-)(K^+\pi^-)$

A primeira parte da selección de eventos está baseada na topoloxía do decaemento $B^0 \to (\pi^+\pi^-)(K^+\pi^-)$. As partículas do estado final agrúpanse en parellas, sempre e cando

teñan cargas opostas, para formar as resonancias intermedias. As trazas correspondentes teñen que aproximarse o suficiente no espazo como para que se puidesen ter orixinado nun vértice común e cada unha delas ten que ter un momento transverso maior que 500 MeV/c. Para que as características da desintegración sexan compatibles co tempo de vóo característico dun mesón B^0, requírese que os produtos da mesma teñan unha significancia do seu parámetro de impacto maior que 16, o que garante que se orixinaran nun punto do espazo desprazado de calquera vértice primario. Os últimos requirementos cinemáticos sobre as resonancias intermedias consisten en esixir que o momento das mesmas estea dentro do volume fiducial do detector e en que a súa masa invariante caia dentro das ventás definidas na análise, $300 < m(\pi^+\pi^-) < 1100\,\mathrm{MeV}/c^2$ e $750 < m(K^+\pi^-) < 1200\,\mathrm{MeV}/c^2$. Unha vez os produtos intermedios foron illados, aínda queda por garantir que se orixinaran conxuntamente na desintegración dun mesón B. Para isto, as catro trazas do estado final combínanse nun único vértice, onde se require que a calidade do axuste do mesmo sexa boa. Nun segundo requerimento, os mesóns B^0 reconstruidos teñen que ter unha dirección de vóo compatible co vector que une os vértices definidos pola interacción protón-protón e polas catro trazas iniciais. Finalmente, a masa invariante dos candidatos a mesóns B ten que estar comprendida no rango $5190 < m(\pi^+\pi^-K^+\pi^-) < 5700\,\mathrm{MeV}/c^2$.

A segunda fase da selección usa información sobre a identificación das partículas que orixinaron as trazas mencionadas no apartado anterior. Para isto, combínase a información procedente de varios subdetectores de LHCb nunha única variable (`ProbNN`) que lle asigna a cada partícula a súa probabilidade de ser dun ou doutro tipo. Nesta análise búscase identificar pións e kaóns, polo que se requiren valores da probabilidade correspondente, `ProbNNpi` ou `ProbNNk`, maiores do 30%.

Feita esta selección, a mostra de datos a analizar consta de tres compoñentes diferenciadas: eventos de sinal, eventos do fondo "combinatorio" e unha minoría de casos que conteñen partículas mal identificadas ou doutras desintegracións que non son a estudada. Estes últimos, elimínanse mediante vetos específicos no seu espazo de fases. Doutra banda, para minimizar o número de eventos que proveñen da combinación aleatoria de catro trazas, empregaranse técnicas de análise multivariable (TMVA, das siglas en inglés), en concreto, unha do tipo "Boosted Decision Tree (BDT)". Estas técnicas permiten beneficiarse das correlacións entre as variables analizadas para distinguir, en base a estas correlacións, os eventos de sinal dos eventos producidos pola combinación aleatoria de trazas. En concreto, a BDT utiliza información sobre o momento do mesón B^0 e máis detalles da topoloxía do evento, como a distancia espacial entre as trazas no punto no que se definiu o vértice da desintegración. A Figura A.4 amosa o diferente comportamento da variable obtida como resultado da BDT para as mostras de sinal e e de fondo combinatorio.

O último paso da selección consiste na realización do axuste do modelo de masa invariante de catro corpos ao devandito espectro. O modelo empregado inclúe as contribucións do sinal buscado, o $B^0 \to \rho^0 K^{*0}$, da correspondente desintegración do mesón B_s^0 ao mesmo estado final, $B_s^0 \to (\pi^+\pi^-)(K^-\pi^+)$, e a orixinada polo fondo combinatorio, que foi previamente reducida mediante do uso da BDT. Debido á fenomenoloxía dos decaemen-

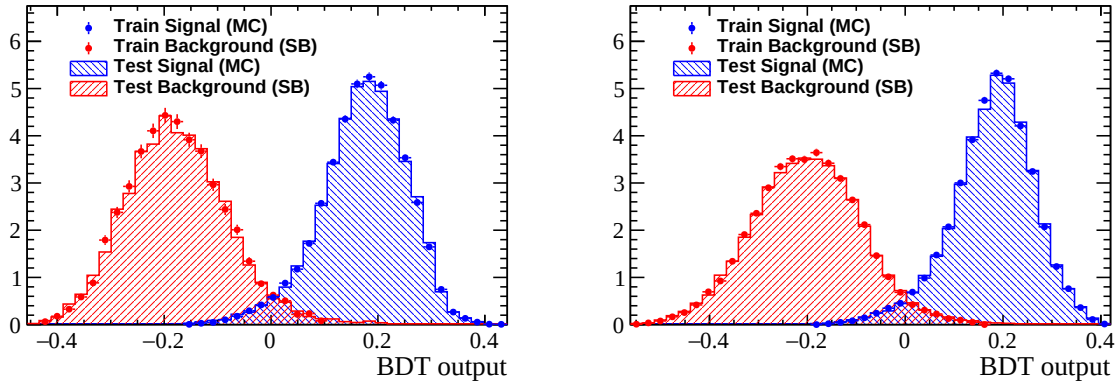

Figure A.4: Resposta da BDT nas mostras de simulación xeradas coas condicións de 2011 (esquerda) e 2012 (dereita). As distribucións representadas en azul correspóndese coas de sinal e as vermellas, coas do fondo.

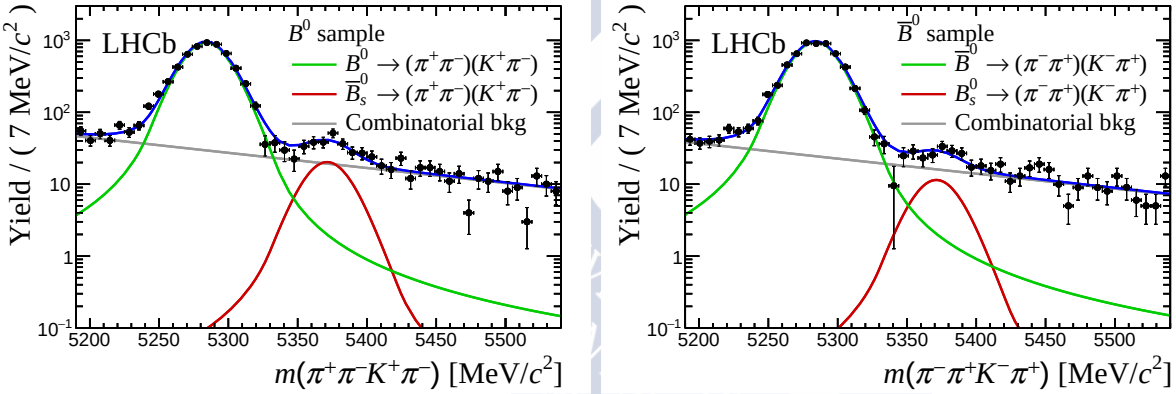

Figure A.5: Axuste do modelo de masa invariante de catro corpos aos correspondentes espectros da masa invariante dos candidatos a B^0 (esquerda) e a $\overline{B}{}^0$ (dereita).

tos, a descrición matemática dos picos do B^0 e do B^0_s realizáse coa función Hypatia, onde os parámetros empregados, salvo o correspondente á masa da resonancia, coinciden para ambos picos. A distribución de masa dos eventos do fondo combinatorio descríbese cunha función exponencial decrecente cuxo único parámetro se determina no axuste aos datos, conxuntamente coa abundancia de cada contribución. Como consecuencia das distintas categorías de sabor e aceptancia coas que se traballa, este axuste realizáse simultaneamente en oito submostras de datos. Os resultados correspondentes aparecen recollidos na Táboa A.2.

Table A.2: Resultados numéricos do axuste simultáneo nas oito categorías nas que se dividen os datos da análise.

Estado final	Ano	*Trigger*	B^0	$\overline{B}{}^0_s$	Combinatorio
$(\pi^+\pi^-)(K^+\pi^-)$	2011	TIS	985 ± 34	20 ± 9	249 ± 23
		TOSnoTIS	615 ± 27	7 ± 5	134 ± 17
	2012	TIS	2451 ± 54	62 ± 13	487 ± 35
		TOSnoTIS	1422 ± 41	30 ± 9	250 ± 24
Estado final	Ano	*Trigger*	$\overline{B}{}^0$	B^0_s	Combinatorio
$(\pi^+\pi^-)(K^-\pi^+)$	2011	TIS	1013 ± 34	4 ± 7	204 ± 22
		TOSnoTIS	620 ± 26	6 ± 4	69 ± 12
	2012	TIS	2521 ± 53	46 ± 13	437 ± 32
		TOSnoTIS	1439 ± 40	12 ± 7	220 ± 23

A.5 Análise de amplitudes en $B^0 \to (\pi^+\pi^-)(K^+\pi^-)$

As medidas dos parámetros físicos que se estableceron como obxectivo deste traballo obtéñense como resultado dun axuste simultáneo en catro mostras de datos empregando cinco observables (tres ángulos e dúas masas) da análise. Para realizar este axuste final son aspectos de crucial importancia: a parametrización da aceptancia do detector, o efecto dos cortes de selección aplicados na mostra de datos e os modelos fenomenolóxicos empregados para describir as resonancias nos espectros de masa de dous corpos. A maiores, o estudo dos efectos sistematicos introducidos ao longo da análise terán que ser tidos en conta para estimar as correspondentes incertezas.

Por primeira vez nunha análise da colaboración LHCb empregáse o algoritmo MultiNest [75–77] para realizar o axuste dos datos. O seu uso está motivado pola alta dimensionalidade do axuste e polas características que teñen as mostras de datos empregadas (*background subtracted*, empregando a técnica *sPlot* para eliminar eventos de fondo).

As proxeccións en cada unha das dimensións do axuste poden verse nas Figuras A.6 e A.7, para as mostras do B^0 e $\overline{B}{}^0$, respectivamente. A visualización do modelo consíguese repesando as mostras de datos simulados polas amplitudes físicas medidas na mostra de datos reais. Desta forma, consíguense visualizar proxeccións 1D do modelo multidimensional tendo en conta as correlacións entre as variables da análise. Nas figuras pode verse a proxección do modelo total (liña azul) sobre os datos (puntos negros). O resto de contribucións debuxadas (ver lenda correspondente nas Figuras A.6 e A.7) correspóndense coas ondas parciais recollidas na Táboa A.1.

Os resultados numéricos dos parámetros do axuste $(Re(A_i), Im(A_i))$ aparecen na Táboa A.3, xunto cos valores correspondentes ás súas incertezas estatística e sistemática. A partir destes resultados, seguindo as definicións da Sección A.3, poden obterse os val-

ores buscados para os promedios e as asimetrías *CP* dos módulos e fases das contribucións á amplitude total de desintegración. Estes valores, xunto coas observables definidas especificamente para as canles de desintegración VV, poden verse na Táboa A.4. Todas as correlacións entre os parámetros do axuste foron tidas en conta á hora de estimar as incertezas estatística e sistemática destes parámetros.

Finalmente, a partir das fraccións de polarización e das diferenzas de fase correspondentes, poden calcularse os valores das TPA, a partir das expresións que foron introducidas na Sección A.3, resultando:

$$\begin{aligned}
\mathcal{A}_{T-fake}^{\rho K^*,1} &= 0.0416 \pm 0.0050 \pm 0.0054, & \mathcal{A}_{T-fake}^{\rho K^*,2} &= -0.0037 \pm 0.0062 \pm 0.0070,\\
\mathcal{A}_{T-fake}^{\omega K^*,1} &= 0.042 \pm 0.043 \pm 0.037, & \mathcal{A}_{T-fake}^{\omega K^*,2} &= -0.005 \pm 0.021 \pm 0.023,
\end{aligned}$$

$$\begin{aligned}
\mathcal{A}_{T-true}^{\rho K^*,1} &= -0.0210 \pm 0.0050 \pm 0.0022, & \mathcal{A}_{T-true}^{\rho K^*,2} &= -0.0032 \pm 0.0062 \pm 0.0047,\\
\mathcal{A}_{T-true}^{\omega K^*} &= 0.022 \pm 0.043 \pm 0.016, & \mathcal{A}_{T-true}^{\omega K^*,2} &= -0.014 \pm 0.021 \pm 0.017.
\end{aligned}$$

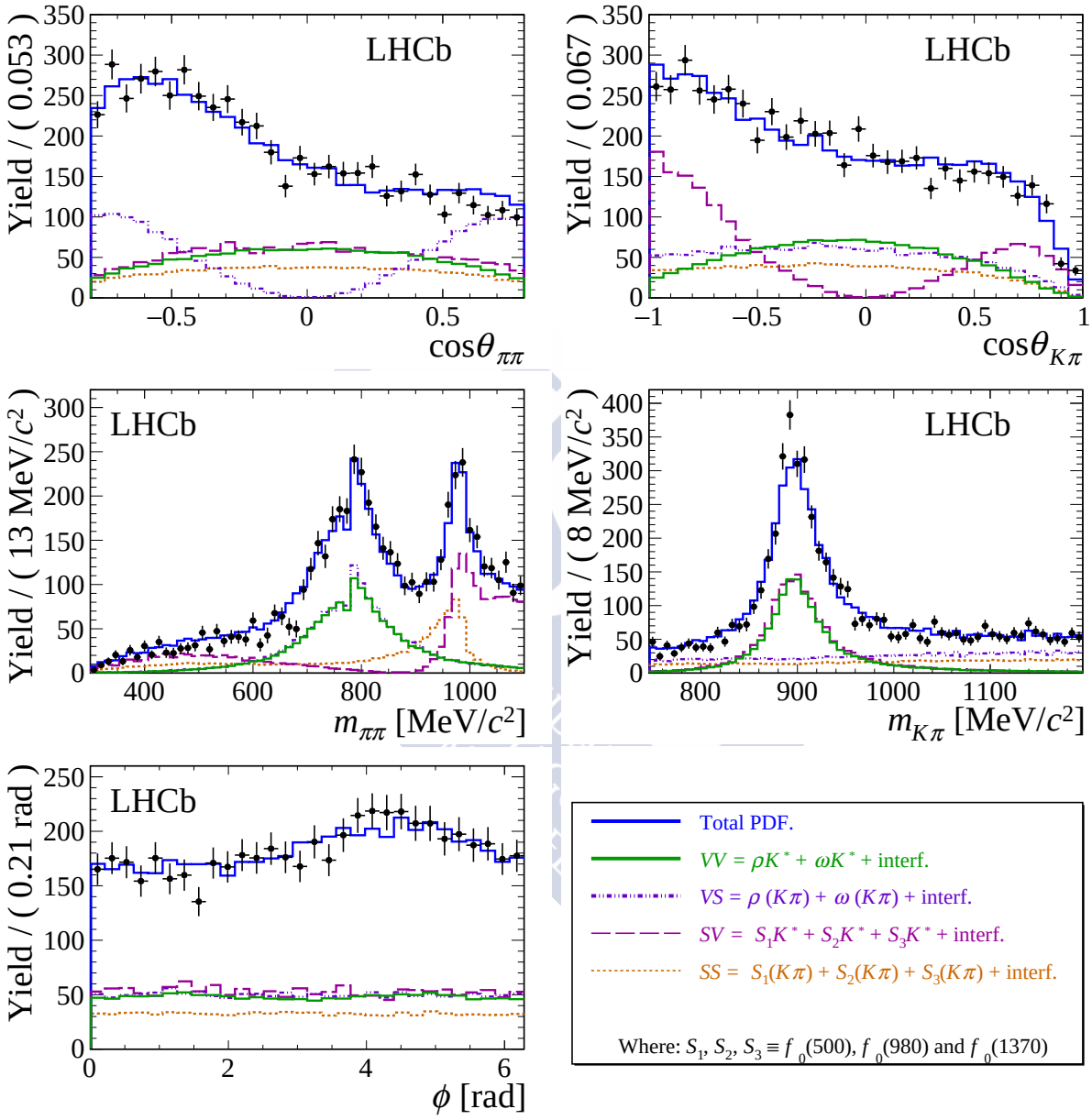

Figure A.6: Proxeccións do axuste multidimensional na mostra de datos do B^0.

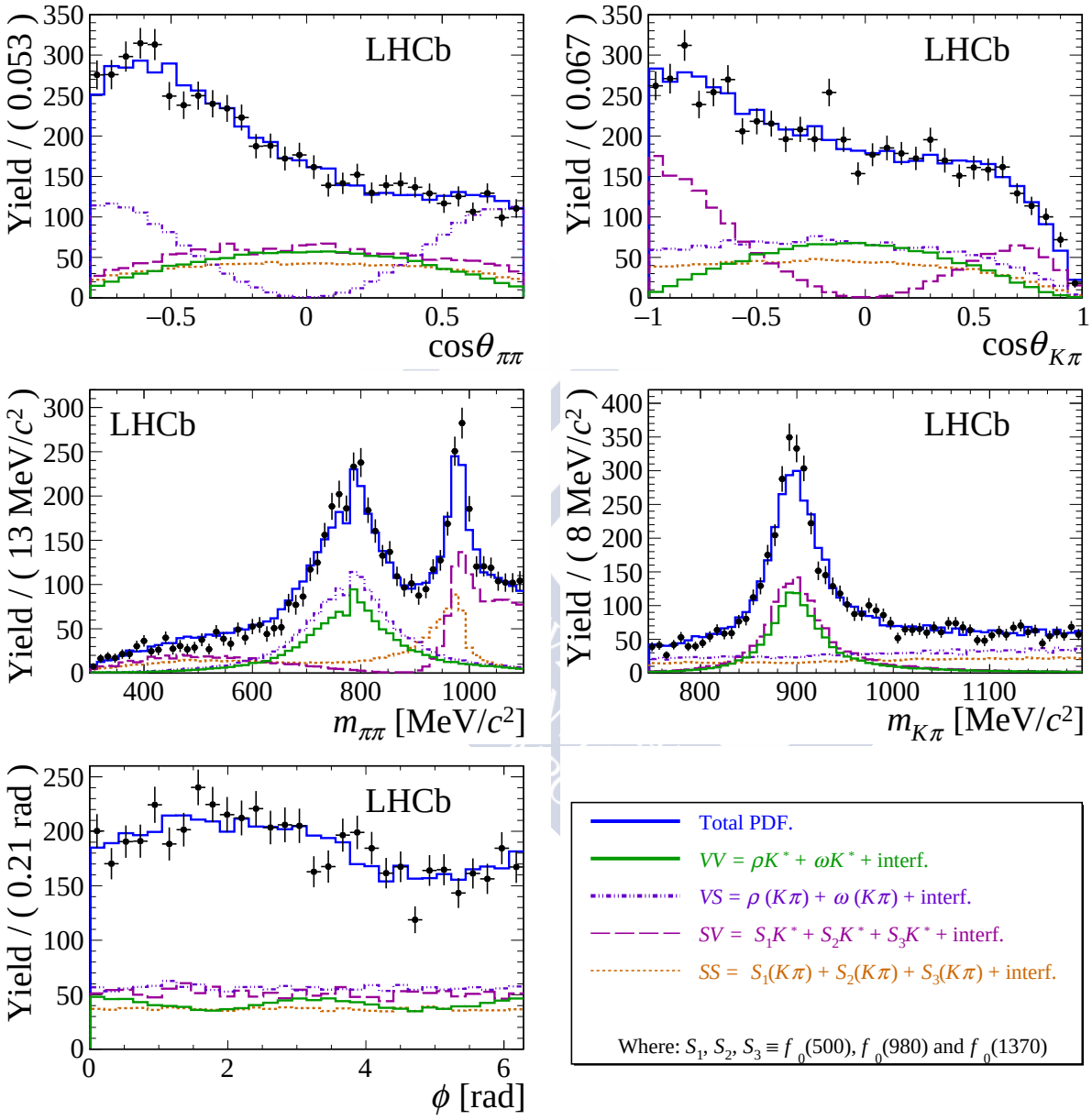

Figure A.7: Proxeccións do axuste multidimensional na mostra de datos do $\overline{B}^0$.

Table A.3: Resultados numéricos do axuste multimensional ás mostras de datos B^0 e $\overline{B}^0$. As incertezas estatística e sistemática asociadas a cada parámetro denótanse por *Stat.* e *Syst.*, respectivamente.

B			
Parámetro	Valor	*Stat.*	*Syst.*
$Re(A^0_{V1V})$	0.095	0.057	0.071
$Im(A^0_{V1V})$	0.74	0.051	0.049
$Re(A^{\|\|}_{V1V})$	0.61	0.038	0.054
$Im(A^{\|\|}_{V1V})$	0.6	0.036	0.064
$Re(A^{\perp}_{V1V})$	−0.64	0.035	0.039
$Im(A^{\perp}_{V1V})$	−0.62	0.039	0.047
$Re(A^0_{V2V})$	0.11	0.05	0.042
$Im(A^0_{V2V})$	−0.13	0.055	0.062
$Re(A^{\|\|}_{V2V})$	−0.061	0.031	0.024
$Im(A^{\|\|}_{V2V})$	−0.053	0.030	0.026
$Re(A^{\perp}_{V2V})$	−0.013	0.029	0.018
$Im(A^{\perp}_{V2V})$	0.048	0.030	0.018
$Re(A_{V2S})$	−0.1	0.049	0.056
$Im(A_{V2S})$	−0.17	0.050	0.053
$Re(A_{S1V})$	−0.49	0.074	0.12
$Im(A_{S1V})$	−0.57	0.048	0.12
$Re(A_{S2V})$	1.5	0.065	0.06
$Im(A_{S2V})$	0.56	0.083	0.12
$Re(A_{S3V})$	−1.1	0.072	0.082
$Im(A_{S3V})$	−0.36	0.081	0.12
$Re(A_{S1S})$	−0.3	0.049	0.055
$Im(A_{S1S})$	−0.18	0.043	0.069
$Re(A_{S2S})$	−1.1	0.055	0.032
$Im(A_{S2S})$	−0.21	0.056	0.056
$Re(A_{S3S})$	−0.15	0.055	0.039
$Im(A_{S3S})$	0.43	0.055	0.058

$\overline{B}$			
Parámetro	Valor	*Stat.*	*Syst.*
$Re(A^0_{V1V})$	−0.034	0.042	0.066
$Im(A^0_{V1V})$	0.28	0.039	0.050
$Re(A^{\|\|}_{V1V})$	0.56	0.033	0.050
$Im(A^{\|\|}_{V1V})$	0.59	0.027	0.062
$Re(A^{\perp}_{V1V})$	−0.53	0.027	0.038
$Im(A^{\perp}_{V1V})$	−0.52	0.033	0.047
$Re(A^0_{V2V})$	0.058	0.042	0.042
$Im(A^0_{V2V})$	−0.064	0.043	0.061
$Re(A^{\|\|}_{V2V})$	0.019	0.027	0.023
$Im(A^{\|\|}_{V2V})$	−0.056	0.026	0.025
$Re(A^{\perp}_{V2V})$	0.0097	0.025	0.018
$Im(A^{\perp}_{V2V})$	0.039	0.027	0.017
$Re(A_{V2S})$	−0.097	0.043	0.056
$Im(A_{V2S})$	−0.069	0.042	0.052
$Re(A_{S1V})$	−0.46	0.064	0.12
$Im(A_{S1V})$	−0.54	0.036	0.12
$Re(A_{S2V})$	1.4	0.054	0.060
$Im(A_{S2V})$	0.6	0.078	0.12
$Re(A_{S3V})$	−0.97	0.065	0.081
$Im(A_{S3V})$	−0.48	0.063	0.12
$Re(A_{S1S})$	−0.47	0.037	0.049
$Im(A_{S1S})$	−0.066	0.041	0.071
$Re(A_{S2S})$	−1	0.046	0.033
$Im(A_{S2S})$	−0.14	0.043	0.056
$Re(A_{S3S})$	−0.0086	0.042	0.035
$Im(A_{S3S})$	0.27	0.052	0.058

Table A.4: Resultados numéricos, xunto coas correspondentes incertezas estatística e sistemática, dos promedios en sabor e as asimetrías *CP* dos módulos e fases das contribucións á amplitude total de desintegración. As medidas das fraccións de polarización e das diferenzas de fase entre as amplitudes VV inclúense ao final da táboa.

Parámetro	Promedio *CP*	Asimetría *CP*
$\lvert A^0_{\rho K^*}\rvert^2$	$0.316 \pm 0.039 \pm 0.074$	$-0.75 \pm 0.07 \pm 0.17$
$\lvert A^{\lvert\lvert}_{\rho K^*}\rvert^2$	$0.701 \pm 0.038 \pm 0.084$	$-0.049 \pm 0.053 \pm 0.019$
$\lvert A^{\perp}_{\rho K^*}\rvert^2$	$0.668 \pm 0.036 \pm 0.068$	$-0.187 \pm 0.051 \pm 0.026$
$\lvert A^0_{\omega K^*}\rvert^2$	$0.019 \pm 0.010 \pm 0.012$	$-0.61 \pm 0.37 \pm 0.39$
$\lvert A^{\lvert\lvert}_{\omega K^*}\rvert^2$	$0.0050 \pm 0.0029 \pm 0.0031$	$-0.30 \pm 0.54 \pm 0.28$
$\lvert A^{\perp}_{\omega K^*}\rvert^2$	$0.0020 \pm 0.0019 \pm 0.0015$	$-0.21 \pm 0.86 \pm 0.41$
$\lvert A_{\omega(K\pi)}\rvert^2$	$0.026 \pm 0.011 \pm 0.025$	$-0.47 \pm 0.33 \pm 0.45$
$\lvert A_{f_0(500)K^*}\rvert^2$	$0.532 \pm 0.048 \pm 0.098$	$-0.056 \pm 0.091 \pm 0.042$
$\lvert A_{f_0(980)K^*}\rvert^2$	$2.42 \pm 0.13 \pm 0.25$	$-0.022 \pm 0.052 \pm 0.023$
$\lvert A_{f_0(1370)K^*}\rvert^2$	$1.29 \pm 0.09 \pm 0.20$	$-0.094 \pm 0.071 \pm 0.037$
$\lvert A_{f_0(500)(K\pi)}\rvert^2$	$0.174 \pm 0.021 \pm 0.039$	$0.30 \pm 0.12 \pm 0.09$
$\lvert A_{f_0(980)(K\pi)}\rvert^2$	$1.184 \pm 0.079 \pm 0.073$	$-0.083 \pm 0.066 \pm 0.023$
$\lvert A_{f_0(1370)(K\pi)}\rvert^2$	$0.139 \pm 0.028 \pm 0.039$	$-0.48 \pm 0.17 \pm 0.15$
$f^0_{\rho K^*}$	$0.164 \pm 0.015 \pm 0.022$	$-0.622 \pm 0.085 \pm 0.086$
$f^{\lvert\lvert}_{\rho K^*}$	$0.435 \pm 0.016 \pm 0.042$	$0.188 \pm 0.037 \pm 0.022$
$f^{\perp}_{\rho K^*}$	$0.401 \pm 0.016 \pm 0.037$	$0.050 \pm 0.039 \pm 0.015$
$f^0_{\omega K^*}$	$0.68 \pm 0.17 \pm 0.16$	$-0.13 \pm 0.27 \pm 0.13$
$f^{\lvert\lvert}_{\omega K^*}$	$0.22 \pm 0.14 \pm 0.15$	$0.26 \pm 0.55 \pm 0.22$
$f^{\perp}_{\omega K^*}$	$0.096 \pm 0.094 \pm 0.091$	$0.34 \pm 0.81 \pm 0.37$
Parámetro	Fases fortes, $\frac{1}{2}(\delta_{\overline{B}} + \delta_B)$ [rad]	Fases febles, $\frac{1}{2}(\delta_{\overline{B}} - \delta_B)$ [rad]
$\delta^0_{\rho K^*}$	$1.57 \pm 0.08 \pm 0.18$	$0.123 \pm 0.084 \pm 0.036$
$\delta^{\lvert\lvert}_{\rho K^*}$	$0.795 \pm 0.030 \pm 0.068$	$0.014 \pm 0.030 \pm 0.026$
$\delta^{\perp}_{\rho K^*}$	$-2.365 \pm 0.032 \pm 0.054$	$0.000 \pm 0.032 \pm 0.013$
$\delta^0_{\omega K^*}$	$-0.86 \pm 0.29 \pm 0.71$	$0.03 \pm 0.29 \pm 0.16$
$\delta^{\lvert\lvert}_{\omega K^*}$	$-1.83 \pm 0.29 \pm 0.32$	$0.59 \pm 0.29 \pm 0.07$
$\delta^{\perp}_{\omega K^*}$	$1.58 \pm 0.43 \pm 0.63$	$-0.25 \pm 0.43 \pm 0.16$
$\delta_{\omega(K\pi)}$	$-2.32 \pm 0.22 \pm 0.24$	$-0.20 \pm 0.22 \pm 0.14$
$\delta_{f_0(500)K^*}$	$-2.28 \pm 0.06 \pm 0.22$	$-0.002 \pm 0.064 \pm 0.045$
$\delta_{f_0(980)K^*}$	$0.385 \pm 0.038 \pm 0.066$	$0.018 \pm 0.038 \pm 0.022$
$\delta_{f_0(1370)K^*}$	$-2.757 \pm 0.051 \pm 0.089$	$0.076 \pm 0.051 \pm 0.025$
$\delta_{f_0(500)(K\pi)}$	$-2.80 \pm 0.09 \pm 0.21$	$-0.206 \pm 0.088 \pm 0.034$
$\delta_{f_0(980)(K\pi)}$	$-2.982 \pm 0.032 \pm 0.057$	$-0.027 \pm 0.032 \pm 0.013$
$\delta_{f_0(1370)(K\pi)}$	$1.76 \pm 0.10 \pm 0.11$	$-0.16 \pm 0.10 \pm 0.04$
$\delta^{\lvert\lvert-\perp}_{\rho K^*}$	$3.160 \pm 0.035 \pm 0.044$	$0.014 \pm 0.035 \pm 0.026$
$\delta^{\lvert\lvert-0}_{\rho K^*}$	$-0.772 \pm 0.085 \pm 0.061$	$-0.109 \pm 0.085 \pm 0.034$
$\delta^{\perp-0}_{\rho K^*}$	$-3.931 \pm 0.085 \pm 0.065$	$-0.123 \pm 0.085 \pm 0.035$
$\delta^{\lvert\lvert-\perp}_{\omega K^*}$	$-3.41 \pm 0.52 \pm 0.73$	$0.84 \pm 0.52 \pm 0.16$
$\delta^{\lvert\lvert-0}_{\omega K^*}$	$-0.97 \pm 0.41 \pm 0.57$	$0.57 \pm 0.41 \pm 0.17$
$\delta^{\perp-0}_{\omega K^*}$	$2.44 \pm 0.51 \pm 0.82$	$-0.28 \pm 0.51 \pm 0.24$

A.6 Conclusións

Nesta tese preséntanse os resultados dunha análise de amplitudes de eventos $B^0 \to (\pi^+\pi^-)(K^+\pi^-)$. A análise realízase nas ventás de masa invariante definidas por $300 < m(\pi^+\pi^-) < 1100\,\mathrm{MeV}/c^2$ e $750 < m(K^+\pi^-) < 1200\,\mathrm{MeV}/c^2$. A mostra de datos empregada correspóndese con $3\,\mathrm{fb}^{-1}$, recollidos polo detector LHCb durante os anos 2011 e 2012 con enerxía no centro de masas de $\sqrt{s}$ =7 e $\sqrt{s}$ =8 TeV, respectivamente.

O modelo empregado describe 14 amplitudes complexas que contribúen á anchura total de desintegración da canle $B^0 \to (\pi^+\pi^-)(K^+\pi^-)$, de maneira que se pode obter a relevancia de cada contribución con respecto da amplitude da onda VS, $B^0 \to \rho^0(K^+\pi^-)$, escollida como referencia. Os resultados presentados nesta tese correspóndense coa primeira determinación das magnitudes e fases para a maioría destas amplitudes. A complexidade do axuste multidimensional e as características das mostras de datos empregadas para a análise motivaron o uso do algoritmo MultiNest por primeira vez nunha análise da colaboración LHCb. Este traballo tamén se atopa entre os primeiros na colaboración en empregar unha GPU para a paralelización do cálculo necesario para a minimización do axuste.

Como se indicou anteriormente, o decaemento $B^0 \to \rho^0 K^{*0}$ recibe contribucións de tres procesos diferentes, representados por un diagrama de Feynman tipo *tree* e por dous diagramas tipo *loop*, un gluónico e un electrofeble. A complexidade da amplitude total e as características do diagrama *loop* electrofeble dificultan enormemente o cálculo teórico de predicións, tanto para esta canle en particular como para calquera proceso ao que contribúa o *loop* electrofeble. Os resultados obtidos nesta tese poden empregarse para comprobar parte das hipóteses nos marcos de traballo de pQCD e QCDF, e, tamén, como punto de partida para realizar predicións para os valores das fraccións de polarización e das súas diferenzas de fase noutras canles.

Conclúese coa comparación, na Táboa A.5, entre os resultados experimentais obtidos [92] e as predicións teóricas para os promedios e asimetrías *CP* das fraccións de polarización e diferenzas de fase do modo de desintegración $B^0 \to \rho(770)^0 K^*(892)^0$.

Table A.5: Resultados da análise comparados coas predicións teóricas en pQCD e QCDF para os promedios e asimetrías das fraccións de polarización e diferenzas de fase do modo de desintegración $B^0 \to \rho(770)^0 K^*(892)^0$.

	Observable	QCDF [16]	pQCD [21]	Este traballo
$f^0_{\rho K^*}$	*CP* average	$0.22^{+0.03+0.53}_{-0.03-0.14}$	$0.65^{+0.03+0.03}_{-0.03-0.04}$	$0.164 \pm 0.015 \pm 0.022$
	CP asymmetry	$-0.30^{+0.11+0.61}_{-0.11-0.49}$	$0.0364^{+0.0120}_{-0.0107}$	$-0.62 \pm 0.09 \pm 0.09$
$f^\perp_{\rho K^*}$	*CP* average	$0.39^{+0.02+0.27}_{-0.02-0.07}$	$0.169^{+0.027}_{-0.018}$	$0.401 \pm 0.016 \pm 0.037$
	CP asymmetry	–	$-0.0771^{+0.0197}_{-0.0186}$	$0.050 \pm 0.039 \pm 0.015$
$\delta^{\parallel-0}_{\rho K^*}$	*CP* average [rad]	$-0.7^{+0.1+1.1}_{-0.1-0.8}$	$-1.61^{+0.02}_{-3.06}$	$-0.77 \pm 0.09 \pm 0.06$
	CP difference [rad]	$0.30^{+0.09+0.38}_{-0.09-0.33}$	$-0.001^{+0.017}_{-0.018}$	$-0.109 \pm 0.085 \pm 0.034$
$\delta^{\parallel-\perp}_{\rho K^*}$	*CP* average [rad]	$\equiv \pi$	$3.15^{+0.02}_{-4.30}$	$3.160 \pm 0.035 \pm 0.044$
	CP difference [rad]	$\equiv 0$	$-0.003^{+0.025}_{-0.024}$	$0.014 \pm 0.035 \pm 0.026$

REFERENCES

[1] S. L. Glashow, *Partial Symmetries of Weak Interactions*, Nucl. Phys. **22** (1961) 579. (Cited on page 1.)

[2] S. Weinberg, *A model of leptons*, Phys. Rev. Lett. **19** (1967) 1264. (Cited on page 1.)

[3] A. Salam, *Weak and Electromagnetic Interactions*, Conf. Proc. **C680519** (1968) 367. (Cited on page 1.)

[4] D. J. Gross and F. Wilczek, *Ultraviolet behavior of non-abelian gauge theories*, Phys. Rev. Lett. **30** (1973) 1343; H. D. Politzer, *Reliable perturbative results for strong interactions?*, Phys. Rev. Lett. **30** (1973) 1346; D. J. Gross and F. Wilczek, *Asymptotically free gauge theories. i*, Phys. Rev. D **8** (1973) 3633; H. D. Politzer, *Asymptotic freedom: An approach to strong interactions*, Physics Reports **14** (1974) 129 . (Cited on page 1.)

[5] Particle Data Group, C. Patrignani *et al.*, *Review of Particle Physics*, Chin. Phys. **C40** (2016) 100001. (Cited on pages 1, 6, 17, 18, 54, 68, and 71.)

[6] C. S. Wu *et al.*, *Experimental test of parity conservation in beta decay*, Phys. Rev. **105** (1957) 1413. (Cited on page 1.)

[7] BaBar collaboration, B. Aubert *et al.*, *Direct CP violating asymmetry in $B^0 \to K^+\pi^-$ decays*, Phys. Rev. Lett. **93** (2004) 131801, `arXiv:hep-ex/0407057`. (Cited on page 1.)

[8] Belle collaboration, Y. Chao *et al.*, *Improved measurements of partial rate asymmetry in $B \to hh$ decays*, Phys. Rev. **D71** (2005) 031502, `arXiv:hep-ex/0407025`. (Cited on page 1.)

[9] M. Prim, *Angular Analysis of $B \to \phi K^*$ Decays and Search for CP Violation at the Belle Experiment*, dr., KIT, 2013, KIT, Diss., 2013. (Cited on page 3.)

[10] A. Pich, *The Standard model of electroweak interactions*, in *2004 European School of High-Energy Physics, Sant Feliu de Guixols, Spain, 30 May - 12 June 2004*, pp. 1–48, 2005. `arXiv:hep-ph/0502010`. (Cited on page 3.)

[11] *Figure from the wikimedia commons and licensed under the creative commons attribution 3.0 unported licence. online at* ***http://en.wikipedia.org/wiki/File:Standard_Model_of_Elementary_Particles.svg***, . (Cited on page 4.)

[12] *Quark model review,* ***http://pdg.lbl.gov/2018/reviews/rpp2018-rev-quark-model.pdf*** *(PDG)*, . (Cited on page 4.)

[13] P. W. Higgs, *Broken symmetries, massless particles and gauge fields*, Phys. Lett. **12** (1964) 132. (Cited on page 5.)

[14] N. Cabibbo, *Unitary Symmetry and Leptonic Decays*, Phys. Rev. Lett. **10** (1963) 531, [,648(1963)]; M. Kobayashi and T. Maskawa, *CP-Violation in the Renormalizable Theory of Weak Interaction*, Progress of Theoretical Physics **49** (1973) 652. (Cited on page 5.)

[15] A. D. Sakharov, *Violation of cp invariance, c asymmetry, and baryon asymmetry of the universe.*, JETP Lett. (USSR)(Engl. Transl.), 5: 24-7(Jan. 1, 1967). (Sun Jan 01 00:00:00 EST 1967). (Cited on page 7.)

[16] M. Beneke, J. Rohrer, and D. Yang, *Branching fractions, polarisation and asymmetries of $B \to VV$ decays*, Nucl. Phys. **B774** (2007) 64, arXiv:hep-ph/0612290. (Cited on pages 8, 9, 11, 125, and 144.)

[17] A. Datta and D. London, *Triple-product correlations in $B \to V_1 V_2$ decays and new physics*, Int. J. Mod. Phys. **A19** (2004) 2505, arXiv:hep-ph/0303159. (Cited on pages 9, 14, and 134.)

[18] Belle collaboration, P. Vanhoefer *et al.*, *Study of $B^0 \to \rho^+\rho^-$ decays and implications for the CKM angle ϕ_2*, Phys. Rev. **D93** (2016) 032010, Addendum ibid. **94** (2016) 099903, arXiv:1510.01245; BaBar collaboration, B. Aubert *et al.*, *Study of $B^0 \to \rho^+\rho^-$ decays and constraints on the CKM angle α*, Phys. Rev. **D76** (2007) 052007, arXiv:0705.2157. (Cited on page 9.)

[19] LHCb collaboration, R. Aaij *et al.*, *First measurement of the CP-violating phase $\phi_s^{d\bar{d}}$ in $B_s^0 \to (K^+\pi^-)(K^-\pi^+)$ decays*, JHEP **03** (2018) 140, arXiv:1712.08683. (Cited on page 9.)

[20] LHCb collaboration, R. Aaij *et al.*, *Measurement of CP violation in $B_s^0 \to \phi\phi$ decays*, Phys. Rev. **D90** (2014) 052011, arXiv:1407.2222; CDF collaboration, T. Aaltonen *et al.*, *Measurement of polarization and search for CP violation in $B_s^0 \to \phi\phi$ decays*, Phys. Rev. Lett. **107** (2011) 261802, arXiv:1107.4999. (Cited on page 9.)

[21] Z.-T. Zou *et al.*, *Improved estimates of the $B_{(s)} \to VV$ decays in perturbative QCD approach*, Phys. Rev. **D91** (2015) 054033, arXiv:1501.00784. (Cited on pages 9, 125, and 144.)

[22] S. Baek *et al.*, *Polarization states in $B \to \rho K^*$ and new physics*, Phys. Rev. **D72** (2005) 094008, arXiv:hep-ph/0508149. (Cited on page 9.)

[23] A. Datta *et al.*, *Methods for measuring new-physics parameters in B decays*, Phys. Rev. **D71** (2005) 096002, arXiv:hep-ph/0406192. (Cited on page 9.)

[24] Heavy Flavor Averaging Group, Y. Amhis *et al.*, *Averages of b-hadron, c-hadron, and τ-lepton properties as of summer 2016*, Eur. Phys. J. **C77** (2017) 895, arXiv:1612.07233, updated results and plots available at https://hflav.web.cern.ch. (Cited on page 10.)

[25] BaBar collaboration, J. P. Lees *et al.*, *B^0 meson decays to $\rho^0 K^{*0}$, $f_0 K^{*0}$, and $\rho^- K^{*+}$, including higher K^* resonances*, Phys. Rev. **D85** (2012) 072005, arXiv:1112.3896. (Cited on page 9.)

[26] Belle collaboration, S.-H. Kyeong *et al.*, *Measurements of charmless hadronic $b \to s$ penguin decays in the $\pi^+\pi^- K^+\pi^-$ final state and first observation of $B^0 \to \rho^0 K^+\pi^-$*, Phys. Rev. **D80** (2009) 051103, arXiv:0905.0763. (Cited on page 9.)

[27] BaBar collaboration, B. Aubert *et al.*, *Observation of B meson decays to ωK^* and improved measurements for $\omega\rho$ and ωf_0*, Phys. Rev. **D79** (2009) 052005, arXiv:0901.3703. (Cited on page 9.)

[28] Belle collaboration, P. Goldenzweig *et al.*, *Evidence for neutral B meson decays to ωK^{*0}*, Phys. Rev. Lett. **101** (2008) 231801, arXiv:0807.4271. (Cited on page 9.)

[29] M. Jacob and G. C. Wick, *On the general theory of collisions for particles with spin*, Annals of Physics **7** (1959) 404 . (Cited on pages 11 and 132.)

[30] L. Collaboration, *Measurement of the CP-violating phase Φ_s in $\overline{B}^0_s \to J/\Psi\pi^+\pi^-$ decays*, Physics Letters B **713** (2012) 378 . (Cited on page 12.)

[31] M. Suzuki, *Helicity conservation in inclusive nonleptonic decay $B \to VX$: Test of long distance final state interaction*, Phys. Rev. **D66** (2002) 054018, arXiv:hep-ph/0206291. (Cited on page 12.)

[32] M. Gronau and J. Zupan, *Isospin-breaking effects on α extracted in $B \to \pi\pi$, $\rho\rho$, $\rho\pi$*, Phys. Rev. **D71** (2005) 074017, arXiv:hep-ph/0502139. (Cited on pages 14 and 134.)

[33] A. Weinstein, *CLEO internal note: Breit Wigners and Form Factors, CBX 99-55 (1999)*, . (Cited on page 16.)

[34] J. Bressieux *et al.*, *Evidence for the resonant character of the $Z(4430)^- \to \psi(2S)\pi^-$ mass peak observed in $B^0 \to \psi(2S)K^+\pi^-$ decays, and determination of the $Z(4430)^-$ spin-parity*, LHCb-ANA-2013-053. (Cited on page 16.)

[35] G. J. Gounaris and J. J. Sakurai, *Finite-width corrections to the vector-meson-dominance prediction for $\rho \to e^+e^-$*, Phys. Rev. Lett. **21** (1968) 244. (Cited on page 17.)

[36] S. M. Flatté, *Coupled-channel analysis of the $\pi\eta$ and $K\bar{K}$ systems near $K\bar{K}$ threshold*, Phys. Lett. **63B** (1976) 224. (Cited on page 18.)

[37] S. M. Flatté, *On the nature of 0^+ mesons*, Physics Letters B **63** (1976) 228. (Cited on page 18.)

[38] S. Stone and L. Zhang, *Measurement of resonant and CP components in* $\overline{B}{}^0_s \to J/\psi\pi^+\pi^-$ *decay*, , Linked to LHCb-PAPER-2013-069. (Cited on page 18.)

[39] D. Aston *et al.*, *A study of* $K^-\pi^+$ *Scattering in the reaction* $K^-p \to K^-\pi^+n$ *at* 11 GeV/c, Nucl. Phys. **B296** (1988) 493. (Cited on pages 18 and 20.)

[40] K. M. Watson, *The effect of final state interactions on reaction cross sections*, Phys. Rev. **88** (1952) 1163. (Cited on page 19.)

[41] J. R. Pelaez and A. Rodas, *Pion-kaon scattering amplitude constrained with forward dispersion relations up to 1.6 GeV*, Phys. Rev. **D93** (2016) 074025, arXiv:1602.08404. (Cited on page 19.)

[42] LHCb collaboration, R. Aaij *et al.*, *LHCb detector performance*, Int. J. Mod. Phys. **A30** (2015) 1530022, arXiv:1412.6352. (Cited on page 25.)

[43] CERN, *Cern home page*, https://home.cern. (Cited on pages 25 and 28.)

[44] E. Mobs, *The CERN accelerator complex. Complexe des accélérateurs du CERN*, , General Photo. (Cited on page 26.)

[45] https://home.cern/science/accelerators/large-electron-positron-collider. (Cited on page 27.)

[46] X. Cid Vidal and R. Cid Manzano, *Taking a closer look at lhc*, https://www.lhc-closer.es/taking_a_closer_look_at_lhc/0.lorentz_force. (Cited on page 27.)

[47] ALICE Collaboration, *ALICE: Technical proposal for a Large Ion collider Experiment at the CERN LHC*, LHC Tech. Proposal, CERN, Geneva, 1995. (Cited on page 27.)

[48] ATLAS, W. W. Armstrong *et al.*, *ATLAS: Technical proposal for a general-purpose p p experiment at the Large Hadron Collider at CERN*, . (Cited on page 27.)

[49] CMS Collaboration, *Technical proposal*, , Cover title : CMS, the Compact Muon Solenoid : technical proposal. (Cited on page 27.)

[50] *LHCb : Technical Proposal*, Tech. Proposal, CERN, Geneva, 1998. (Cited on pages 27, 31, and 129.)

[51] R. Aaij *et al.*, *Performance of the LHCb Vertex Locator*, JINST **9** (2014) P09007, arXiv:1405.7808. (Cited on page 32.)

[52] LHCb Collaboration, *LHCb VELO Upgrade Technical Design Report*, . (Cited on page 33.)

[53] R. Arink *et al.*, *Performance of the LHCb Outer Tracker*, JINST **9** (2014) P01002, arXiv:1311.3893. (Cited on page 33.)

[54] G. A. Cowan, *Performance of the lhcb silicon tracker*, Nuclear Instruments and Methods in Physics Research Section A: Accelerators, Spectrometers, Detectors and Associated Equipment **699** (2013) 156 , Proceedings of the 8th International "Hiroshima" Symposium on the Development and Application of Semiconductor Tracking Detectors. (Cited on pages 33 and 34.)

[55] LHCb Collaboration, *LHCb Tracker Upgrade Technical Design Report*, Tech. Rep. CERN-LHCC-2014-001. LHCB-TDR-015, Feb, 2014. (Cited on page 34.)

[56] M. Adinolfi *et al.*, *Performance of the LHCb RICH detector at the LHC*, Eur. Phys. J. **C73** (2013) 2431, arXiv:1211.6759. (Cited on pages 34 and 35.)

[57] LHCb Collaboration, *LHCb PID Upgrade Technical Design Report*, Tech. Rep. CERN-LHCC-2013-022. LHCB-TDR-014, Nov, 2013. (Cited on page 35.)

[58] R. Aaij *et al.*, *Performance of the LHCb calorimeters*, LHCb-DP-2013-004, in preparation. (Cited on page 35.)

[59] F. Archilli *et al.*, *Performance of the muon identification at LHCb*, JINST **8** (2013) P10020, arXiv:1306.0249. (Cited on page 36.)

[60] LHCb Collaboration, *LHCb trigger system technical design report*, . (Cited on pages 36 and 130.)

[61] The LHCb Collaboration, CERN, *Upgrade Software and Computing*, Tech. Rep. CERN-LHCC-2018-007. LHCB-TDR-017, CERN, Geneva, Mar, 2018. (Cited on page 38.)

[62] T. Sjöstrand, S. Mrenna, and P. Skands, *A brief introduction to PYTHIA 8.1*, Comput. Phys. Commun. **178** (2008) 852, arXiv:0710.3820. (Cited on page 38.)

[63] T. Sjöstrand, S. Mrenna, and P. Skands, *PYTHIA 6.4 physics and manual*, JHEP **05** (2006) 026, arXiv:hep-ph/0603175. (Cited on page 38.)

[64] I. Belyaev *et al.*, *Handling of the generation of primary events in Gauss, the LHCb simulation framework*, J. Phys. Conf. Ser. **331** (2011) 032047. (Cited on page 38.)

[65] D. J. Lange, *The EvtGen particle decay simulation package*, Nucl. Instrum. Meth. **A462** (2001) 152. (Cited on page 38.)

[66] P. Golonka and Z. Was, *PHOTOS Monte Carlo: A precision tool for QED corrections in Z and W decays*, Eur. Phys. J. **C45** (2006) 97, arXiv:hep-ph/0506026. (Cited on page 38.)

[67] Geant4 collaboration, J. Allison *et al.*, *Geant4 developments and applications*, IEEE Trans. Nucl. Sci. **53** (2006) 270; Geant4 collaboration, S. Agostinelli *et al.*, *Geant4: A simulation toolkit*, Nucl. Instrum. Meth. **A506** (2003) 250. (Cited on page 38.)

[68] M. Clemencic *et al.*, *The LHCb simulation application, Gauss: Design, evolution and experience*, J. Phys. Conf. Ser. **331** (2011) 032023. (Cited on page 38.)

[69] L. Breiman, J. H. Friedman, R. A. Olshen, and C. J. Stone, *Classification and regression trees*, Wadsworth international group, Belmont, California, USA, 1984. (Cited on page 41.)

[70] Y. Freund and R. E. Schapire, *A decision-theoretic generalization of on-line learning and an application to boosting*, J. Comput. Syst. Sci. **55** (1997) 119. (Cited on page 42.)

[71] A. Hoecker *et al.*, *TMVA: Toolkit for Multivariate Data Analysis*, PoS **ACAT** (2007) 040, `arXiv:physics/0703039`. (Cited on page 42.)

[72] M. Pivk and F. R. L. Diberder, *A statistical tool to unfold data distributions*, Nuclear Instruments and Methods in Physics Research Section A: Accelerators, Spectrometers, Detectors and Associated Equipment **555** (2005) 356 . (Cited on pages 43 and 67.)

[73] T. du Pree, *Search for a strange phase in beautiful oscillations*, PhD thesis, Vrije Universiteit Amsterdam, 2010, CERN-THESIS-2010-124. (Cited on pages 44 and 80.)

[74] J. Buchner *et al.*, *X-ray spectral modelling of the AGN obscuring region in the CDFS: Bayesian model selection and catalogue*, Astronomy and Astrophysics **564** (2014) A125, `arXiv:1402.0004`. (Cited on page 45.)

[75] F. Feroz and M. P. Hobson, *Multimodal nested sampling: an efficient and robust alternative to Markov Chain Monte Carlo methods for astronomical data analysis*, Mon. Not. Roy. Astron. Soc. **384** (2008) 449, `arXiv:0704.3704`. (Cited on pages 45, 86, and 137.)

[76] F. Feroz, M. P. Hobson, and M. Bridges, *MultiNest: an efficient and robust Bayesian inference tool for cosmology and particle physics*, Mon. Not. Roy. Astron. Soc. **398** (2009) 1601, `arXiv:0809.3437`. (Cited on pages 45, 86, and 137.)

[77] F. Feroz, M. P. Hobson, E. Cameron, and A. N. Pettitt, *Importance nested sampling and the MultiNest algorithm*, `arXiv:1306.2144`. (Cited on pages 45, 86, and 137.)

[78] D. Martínez Santos *et al.*, *Ipanema-β: tools and examples for HEP analysis on GPU*, `arXiv:1706.01420`. (Cited on page 46.)

[79] A. Fowlie and M. H. Bardsley, *Superplot: a graphical interface for plotting and analysing MultiNest output*, Eur. Phys. J. Plus **131** (2016) 391, arXiv:1603.00555. (Cited on page 46.)

[80] L. Anderlini *et al.*, *The PIDCalib package*, Tech. Rep. LHCb-PUB-2016-021. CERN-LHCb-PUB-2016-021, CERN, Geneva, Jul, 2016. (Cited on pages 47 and 64.)

[81] A. Rogozhnikov, *Reweighting with Boosted Decision Trees*, J. Phys. Conf. Ser. **762** (2016) , arXiv:1608.05806, https://github.com/arogozhnikov/hep_ml. (Cited on page 47.)

[82] T. Oliphant, *Guide to NumPy*, Trelgol Publishing, 2006. (Cited on page 48.)

[83] M. Feindt, *A Neural Bayesian Estimator for Conditional Probability Densities*, arXiv:physics/0402093. (Cited on page 52.)

[84] M. Adinolfi *et al.*, *Performance of the LHCb RICH detector at the LHC*, The European Physical Journal C **73** (2013) 2431. (Cited on page 53.)

[85] D. M. Santos and F. Dupertuis, *Mass distributions marginalized over per-event errors*, Nuclear Instruments and Methods in Physics Research Section A: Accelerators, Spectrometers, Detectors and Associated Equipment **764** (2014) 150 . (Cited on page 64.)

[86] T. Skwarnicki, *A study of the radiative cascade transitions between the Upsilon-prime and Upsilon resonances*, PhD thesis, Institute of Nuclear Physics, Krakow, 1986, DESY-F31-86-02. (Cited on page 64.)

[87] LHCb, R. Aaij *et al.*, *Measurement of CP asymmetries and polarisation fractions in $B_s^0 \to K^{*0}\bar{K}^{*0}$ decays*, JHEP **07** (2015) 166, arXiv:1503.05362. (Cited on pages 66 and 99.)

[88] ARGUS collaboration, H. Albrecht *et al.*, *Exclusive Hadronic Decays of B Mesons*, Z. Phys. **C48** (1990) 543. (Cited on page 71.)

[89] A. Klöckner *et al.*, *PyCUDA and PyOpenCL: A scripting-based approach to GPU run-time code generation*, Parallel Computing **38** (2012) 157 . (Cited on page 86.)

[90] E. O. Lebigot, *Uncertainties: a python package for calculations with uncertainties*, . (Cited on page 94.)

[91] F. Pedregosa *et al.*, *Scikit-learn: Machine learning in Python*, Journal of Machine Learning Research **12** (2011) 2825. (Cited on page 110.)

[92] LHCb collaboration, M. Vieites Díaz *et al.*, *Study of the $B^0 \to \rho(770)^0 K^*(892)^0$ decay with an amplitude analysis of $B^0 \to (\pi^+\pi^-)(K^+\pi^-)$ decays*, Submitted to: JHEP (2018) arXiv:1812.07008. (Cited on pages 123 and 143.)